Order Number 9312183

Millimeter and infrared studies of young stellar objects in dark cloud L1641

Chen, Hua, Ph.D.

University of Hawaii, 1992

U·M·I
300 N. Zeeb Rd.
Ann Arbor, MI 48106

MILLIMETER AND INFRARED STUDIES OF YOUNG STELLAR OBJECTS IN DARK CLOUD L1641

A DISSERTATION SUBMITTED TO THE GRADUATE DIVISION OF THE UNIVERSITY OF HAWAI'I IN PARTIAL FULFILLMENT OF THE REQUIREMENTS FOR THE DEGREE OF

DOCTOR OF PHILOSOPHY

IN

ASTRONOMY

DECEMBER 1992

By

Hua Chen

Dissertation Committee:

Alan Tokunaga, Chairperson

George Herbig

Klaus Hodapp

John Learned

Gareth Wynn-Williams

Dedicated to my father

who inspired me to wonder about the sky

and to my mother

who taught me to be down to earth.

ACKNOWLEDGMENTS

The first person I would like to thank is my advisor Alan Tokunaga. Keeping the big picture in mind while paying attention to details -- these are the two things that impress me most about Alan. The many hours of discussion and arguments and the personal friendship are things I shall benefit from my whole career. I would also like to thank Drs. George Herbig, Klaus Hodapp, John Learned, and Gareth Wynn-Williams for serving as my thesis committee members, and for many stimulating discussions in the course of this project. I especially thank George for always reminding me to keep an open mind.

Besides the committee members, Dr. Y. Fukui deserves a special thank you for his active involvement in my thesis work. The excellent work of his group studying L1641 was an important reason I choose the dark cloud for this project. His expertise in millimeter astronomy and enthusiasm in general continuously encouraged me throughout this project. I would also like to thank Drs. Ji Yang, T. Iwata, A. Mizuno, and H. Ogawa, and all the colleagues at Nagoya University for their help and friendship during my three visits to Nagoya.

I thank Drs. Karen and Steve Strom for the very insightful discussions and for their hospitality during my visit to Amherst. I am also grateful to Drs. E. Ladd, R. Wainscoat, K. Tatematsu, and T. Umemoto for many helpful discussions, and for allowing me to use their data prior to publication.

The observations carried out for this thesis used various telescopes and facilities in the United States and Japan. I would like to thank the IPAC staff for their superb work in providing us with the *IRAS* coadded images and the ADDSCAN data. My thanks also go to the supporting scientists and telescope operators at the University of Hawaii 2.2 m telescope, the Infrared Telescope Facility, the United Kingdom Infrared Telescope, and

the Nobeyama Radio Observatory. Without their help, this project would never have been possible.

During the course of this project, I was financially supported in part by a fellowship from the East-West Center, Honolulu; a NASA grant (NAGW-2278); and the Grant-in-Aid for specially supported research No. 01065002; and the Monbusho International Scientific Research Program: Joint Research No. 02044064 for the Ministry of Education, Science and Culture, Japan.

Six years ago, before seeing me board the airplane for Honolulu, my parents expressed the hope that I would find many new stars. Making them proud has been my biggest motivation during all these years. Although nothing can compensate for their sacrifice and loneliness, I dedicate this thesis to my loving Mom and Dad for their generosity and support. As to the new stars, I am still looking . . . . My mother-in-law deserves a special thanks for her help when it was very much needed.

Finally, and most importantly, I want to thank my wife Hong for being understanding, and my son Stephen for being a good boy. This thesis, like a Chinese song says, is half mine, and half yours.

ABSTRACT

To understand the physical process of star formation, we address three questions: (1) what are the critical indicators of evolutionary states of young stellar objects? (2) when and how are dense cores dissipated? and (3) how are young stars distributed in a single molecular cloud? We selected 224 *IRAS* sources from the *IRAS* coadded images in dark cloud L1641. The *IRAS* data analysis suggested that the 122 sources inside L1641 are probably young stellar objects, while the sources outside L1641 are probably infrared cirrus. In ^{13}CO and HCO^+ millimeter observations, we found that most of the *IRAS* sources with CO outflows are associated with molecular dense cores, while most nonoutflow sources are not. This can be explained if dense cores are dissipated by the outflows before the driving sources become pre-main-sequence stars. Using near-IR array detectors, we imaged 59 *IRAS* sources in *H* and *K'*, some of them also were imaged in narrow-band *L* and *M*. The most important result from the imaging is the detection of small groupings of 10-40 near-IR sources near 14 *IRAS* sources. These groupings, defined as stellar density enhancements (SDEs), are statistically significant compared to background stars. Most of the near-IR sources within the SDEs are low-mass pre-main-sequence stars physically associated with the *IRAS* sources. The SDEs probably result from pile-up of young stars due to continuous star formation within the dense cores, a phenomenon seen in the early stage of star formation. Our images showed that the young stars in L1641 can be characterized by a range of stellar densities, from a large cluster (the Trapezium Cluster) to the SDEs and to individual stars. The previously proposed cluster and isolated star formation modes are probably the high and low ends of the continuous distribution. With the near-IR imaging, we were able to identify the probable near-IR counterparts for 55 of the 59 *IRAS* sources. Forty-five of them are class I sources, and the other 10 sources are class II sources.

TABLE OF CONTENTS

LIST OF TABLES

LIST OF FIGURES

CHAPTER 1
INTRODUCTION

1.1. STAR FORMATION: WHAT DO WE KNOW?

In the last 10 years, a wealth of information has been accumulated in the field of star formation, in a wide range of wavelengths (from X-ray, optical, near-IR, far-IR to millimeter) and spatial scales (10^{14-18} cm). In this section, we briefly review the major advances made during the last 10 years. This review also serves as a background introduction to the work presented in this thesis.

In the study of star formation and early stellar evolution, low-mass stars (<3 $M_\odot$) attracted more attention than high-mass (>3 $M_\odot$) stars for the following reasons (Lada 1991): (1) since majority of the stars in the Galaxy is low-mass stars, the data sample of low-mass stars is much larger than that of high-mass stars; (2) low-mass stars have a much slower evolution time-scale and an observable pre-main-sequence stage; and (3) low-mass stars are considerably less destructive to their natal environment, so the relationship between the young stars and their environment can be studied. For these reasons, in this thesis we will concentrate on the formation and early evolution of low-mass stars. The term "star formation" is denoted to mean "low-mass star formation" unless specified.

1.1.1. *Dense Cores in Molecular Clouds*

The Hα emission features of T Tauri stars was among the first evidences that led the observational study of young stars. Thanks to the optical spectroscopic observations pioneered by Herbig (1962) and Cohen & Kuhi (1979), it is now well-established that T

Tauri stars are low-mass pre-main-sequence stars with an age of 10^{5-6} yr. The close association of T Tauri stars with the interstellar molecular gas strongly suggests that young stars are being formed in giant molecular clouds (GMCs). In fact, within 1 kpc from the sun, all the GMCs show sign of star formation (Blitz 1991).

Only a portion of the GMCs can directly turn into stars, because otherwise the number of young stars would be much more than that observed (Zuckerman and Plamer 1981). Using the $C^{18}O$ J = 1-0 and NH_3 (J,K) = (1,1) lines, Myers and his co-workers (Myers, Linke & Benson 1983; Myers & Benson 1983; Benson & Myers 1989) observed ~100 visually opaque regions in nearby molecular clouds, and discovered the dense molecular cores. The typical properties of dense cores are summarized by Fuller (1991), as shown in Table 1.1. The close association of the cores with known T Tauri stars indicates that they are the site of recent star formation. Dynamic analyses by Myers & Benson (1983) show that the dense cores are in the early stage of collapse or in near-critical equilibrium, and that they may directly give birth to young stars.

Traditionally the dense cores are defined as the concentrations seen in high-excitation molecular lines, such as CS, NH_3, HCO^+ and HCN, while the concentrations seen in low-excitation lines, such as CO and ^{13}CO, are defined as clumps. Although the dense cores are usually more compact and denser than the clumps, it is unclear whether they are physically different. In this thesis, we define both of them as dense cores.

1.1.2. IRAS *Sources*

Since young stellar objects (YSOs) are being formed in the dense molecular cores, most of their emission will be absorbed and reemitted in infrared by the surrounding dust. The model of accreting protostar, as first suggested by Larson (1969a, 1969b), also predicted that a protostar will first reveal itself as a high-luminosity infrared source. This

led to an extensive infrared search for protostars (Wynn-Williams 1982). One important step in the search for protostars was the launch of the *Infrared Astronomical Satellite* (*IRAS*) which surveyed the 95% of sky in four far-IR bands (centered at 12, 25, 60, and 100 μm). Many sources in the *IRAS Point Source Catalog* (*PSC*) are YSOs (Beichman 1987). The search for *IRAS* sources in dense cores turned out to be fruitful: nearly 50% of the NH_3 dense cores mapped by Myers & Benson (1983) are associated with *IRAS* sources (Beichman et al. 1986). One-third of the *IRAS* sources are associated with visible T Tauri stars, and the other two-third has no optical counterpart. The dense cores with invisible sources are colder and more massive. Beichman et al. (1986) suggested that some of the invisible *IRAS* sources are probably "protostars". The more recent studies in ρ Oph (Wilking, Lada, & Young 1989), L1641 (Strom et al. 1989b) and Taurus (Kenyon et al. 1990) also showed that *IRAS* sources are closely associated with active star-forming regions.

IRAS color-color diagram based on *IRAS* 12-25 and 25-60 μm flux density ratios has been widely used to classify the *IRAS* sources, because various YSOs (sources in dense cores, pre-main-sequence stars, and main-sequence stars) occupy the specific regions in the diagram (Beichman 1985, Emerson 1990).

1.1.3. *CO Molecular Outflows*

The discovery of CO molecular outflow from embedded YSOs set another milestone (Snell et al. 1980, Bally & Lada 1983). In CO J = 1-0 line observations of some YSOs at 2.3 mm, the emission line showed an asymmetric profile with a high-velocity wing (10-30 km s^{-1}). The blue and red-shifted wings are often spatially separated, resulting in bipolar-shaped contour maps of the integrated wing emission with the YSO at the center.

It is generally accepted that this is the result of high-velocity material flowing outward from the polar regions of the embedded YSOs (Lada 1985).

The red and blue lobes of CO molecular outflows have a spatial scale of a few pc. The dynamic time scale (flow linear extent / flow velocity) is typically a few times 10^4 yr (Fukui 1989). The mechanical energy of outflowing material is roughly correlated with the luminosity of the central sources, suggesting that they are physically related. Nearly 200 CO outflows have been detected as the results of the extensive (biased and unbiased) CO surveys (Lada 1985, Fukui 1989). Almost all of them are associated with *IRAS* sources with luminosities ranging from 1 to 10^6 $L_\odot$, indicating that both high- and low-mass young stars have the outflows. The high detection rate of CO outflows from YSOs suggests that most, if not all, young stars undergo a stage of outflow. Because CO molecular outflow is more likely to be associated with embedded sources than with T Tauri stars, Lada (1985) suggested that CO outflow represents the earliest observable stage of star formation, prior to the pre-main-sequence stage.

1.1.4. *Spectral Energy Distribution*

Both millimeter and *IRAS* observation of YSOs provide information on a relatively large scale because of the large beam sizes (20"-3') of the telescopes. They trace the molecular and dust environment of the newly formed young stars. More detail information of YSOs themselves comes from optical and near-IR observations. Because most embedded sources are highly obscured, near-IR broad-band photometry can play an important role. The shape of spectral energy distribution (SED) of a young stellar object depends both on the nature and distribution of the surrounding dust. A SED is a plot of λf_λ vs. λ in log-log space, and the spectral index is defined as α = dlog λf_λ / dlog λ, where f_λ is flux density at wavelength λ. Lada (1988) classified the near-IR sources into

three main classes according to their SEDs: class I: the SED is broader than that of a single-temperature blackbody and α is positive; class II: the SED is also broader than the blackbody with $-2 < \alpha < 0$; and class III: the SED is compatible with the blackbody with $\alpha < -2$. A theoretical model (Adams, Lada & Shu 1987) successfully explained the above classification as a continuous evolution of the circumstellar dust. They suggested that class I sources are probably the protostars, class II sources are classical T Tauri stars, and class III sources are weak-line T Tauri stars. The typical SEDs of the three classes, along with a sub-class IID, are displayed in Figure 1.1.

1.1.5. *A Star Formation Scenario*

The time scale and spatial scales of the star forming phenomena are illustrated in Figure 1.2. They provided the comprehensive information for theorists to construct the model of the physical process of star formation. At present the best-known star formation scenario is the inside-out model by Shu and his co-workers (Shu, Adams & Lizano 1987). The model proposed that young stars are formed through the following four stages (Shu 1991, see also Figure 1.1):

(1) *dense core*: the sphere of the gas and dust slowly contracts under its own gravity against the frictional support provided by the ions and magnetic fields via the process of ambipolar diffusion. The evolution of the core is an isothermal, quasi-static and has a density profile given by

$$\rho(r) = \frac{a^2}{2\pi G r^2} \tag{1.1}$$

where a is the isothermal sound speed.

(2) *gravitational collapse*: when the contracting configuration becomes sufficiently central concentrated, the core gravitationally collapses from inside out. The central region collapses first, forming a central accreting protostar, an optically thick and geometrically thin accretion disk. The regions at progressively larger radii collapse as they lose pressure support from below, forming a spherical infalling envelope of gas and dust. The accretion rate and the accretion luminosity can be written as

$$\dot{M} = \frac{0.975\, a^3}{G} \tag{1.2}$$

$$L_{acc} = \frac{G\, M_* \dot{M}}{R_*} \tag{1.3}$$

where M_* and R_* are the mass and the radii of the accreting star, respectively.

(3) *bipolar outflow*: almost simultaneously, a powerful wind breaks out along the rotational poles. This wind is responsible for transporting outward the angular momentum brought in by infalling material. The time scales of (2) and (3) are about 10^5 yr;

(4) *pre-main-sequence stars*: the continuous depletion of the gas and dust shell by outflowing material will eventually halt the infall, and dissipate the dense cores surrounding the central source. The star then for the first time becomes optically visible.

1.2. THE SCIENTIFIC GOALS OF THE THESIS

Although the progress discussed in the last section have greatly advanced our knowledge, there are still many questions to be answered before we can fully understand the physical process of star formation. In this thesis I like to address three questions.

For a young stellar object deeply embedded in molecular dense cores, its spectrum is usually not a single-temperature black-body. It is generally difficult to estimate their age by placing them in the H-R diagram. On the other hand, a YSO will change its dust and gas environment through the infall and outflow during the process of star formation. It may be possible to characterize their evolutionary state by comparing the properties of the molecular gas (in millimeter), cold dust (in *IRAS* bands) and the hot dust (in near-IR band) adjacent to the sources. *Our first goal is to find critical observational indicators of the evolutionary state of YSOs.* Eventually the evolutionary indicators may result in an evolutionary diagram of YSOs, similar to the H-R diagram for optical stars.

A natural outcome of the inside-out model is that young stellar object will gradually change its molecular environment at the early stage of its formation. *Our second goal is to study the evolution of the molecular dense cores during early star formation, and to understand from observations when and how the molecular dense cores are dissipated.*

Although the inside-out model has successfully reconciled many observations, it is mostly based on a single (or binary) star forming in an isolated molecular dense core. Recent observations show that this is not the only way to form stars. While most stars in Taurus seem to be formed in isolation, young stars in other molecular clouds, such as ρ Oph (Wilking, Lada, & Young 1989) and L1630 (E. Lada 1990), are mostly formed in clusters. Lada (1991) referred these two cases as the isolated star formation mode and the clustering mode, respectively. *Our third goal is to understand how young stars are distributed within a single molecular cloud?* We also like to know wether different spatial distributions of young stars indicate different star formation mechanisms.

1.3. L1641: AN ACTIVE STAR FORMING REGION

To accomplish the goals set in the last section, it is best to study all YSOs in a single molecular cloud. Such studies have at least two advantages: (1) all sources in the sample have similar global environment and star formation history. The analysis therefore should be more straight forward; and (2) all sources have the same distance, the selection effect due to the distance can be minimized.

This thesis reports on a millimeter, far-infrared and near-IR study of *IRAS* sources in a nearby dark cloud Lynds 1641. The L1641 was first identified as a dark cloud in the Orion region, occupying nearly six square degrees of the sky with the Dec. between -6^{o} and -10^{o} (Lynds 1962). A CO molecular survey by Kutner et al. (1977) found that it is actually part of the Orion A giant molecular cloud (Figure 1.3). When observed in ^{13}CO J = 1-0, the entire L1641 is very filamentary and clumpy. Bally et al. (1987) detected more than 100 individual high-density condensations. Takaba et al. (1986) searched the northern part of L1641 and found at least four clumps in a 20' × 30' region.

There are 123 sources listed in the *PSC* in the direction of L1641 (the *IRAS* sources with only 100 μm detections have been excluded to avoid the contamination of the infrared cirrus). Strom et al. (1989) showed that 93 of them might be point source physically associated with the L1641. Many of these sources have rising spectral energy distributions in the far-IR, indicating that they are embedded YSOs. However, as to be discussed in Chapter 2, the *PSC* source selection was mostly based on single *IRAS* scans, and was therefore limited in sensitivity. By co-adding single *IRAS* scans at the same position, we can increase the signal-to-noise ratio by a factor of 2-3. These co-added *IRAS* data have the advantages over the *PSC* data by allowing us (1) to improve the detection quality of *PSC* sources; and (2) to find new detections. The *IRAS* data sample used in this thesis is based on the co-added *IRAS* data.

In an unbiased CO survey with the Nagoya 4 m telescope, Fukui and his co-workers (Fukui et al. 1986; Fukui 1989) detected eight CO molecular outflows. More recently, Morgan et al. (1991) detected several additional outflows. All of these CO molecular outflows in L1641 are associated with *IRAS* sources. Since the CO molecular outflow defines a unique stage during the early star formation, the comprehensive surveys for CO outflows in L1641 allow us to characterize the evolutionary state of YSOs by comparing the *IRAS* sources with and without CO outflows.

When observed in optical wavelengths, Most optically bright objects, or massive stars, are located in the northern part of Ori A (north of Dec = -6^{o}). It was suggested that star formation in Orion had been triggered by a series of supernovas (Cowie, Songaila & York 1977). One important member in this region is the Trapezium Cluster (Herbig 1962). It has about 150 stars within a 3' × 3' region in the I band (Herbig & Terndrup 1986). When observed at 2.2 μm, McCauhrean (1988) detected over 500 stars within a 5' × 5' region centered on Trapezium OB star.

In contrast, the L1641 (south of Dec = -6^{o}) is much darker in the optical. The most prominent object is NGC 1999, a reflection nebula illuminated by a possible Ae Star, V380 Ori. There are several Herbig-Haro objects, such as HH 1-2, HH 33/40, Haro 13a and Haro 14a. Optical CCD images of these sources showed jet-like structures that are probably driven by newly formed stars (Mundt et al. 1984, Strom et al. 1986). Many stars are extensively observed in Hα (at 6563 Å) to search for pre-main-sequence stars (Herbig & Bell 1988; Wiramihardja et al. 1989, Wouterloot & Brand 1992). In the catalog compiled by Herbig & Bell, there are 30 stars showing Hα emission feature in the L1641.

Nakajima et al. (1986) surveyed a 1.4 square degree region of L1641 in near-IR, and detected about 100 sources with a limiting magnitude of K = 9.5 mag. Only 15 of them were identified as pre-main-sequence stars. To identify the near-IR counterparts of the

PSC sources, Strom et al. (1989) mapped the vicinity of the *IRAS* sources with a limiting magnitude of K = 14 mag. These existing near-IR data were obtained using a single detector with a very limited sensitivity. The advance of two-dimensional near-IR array detectors provides a much more sensitive (down to K = 17 mag) and efficient way of observing dark cloud like L1641. The near-IR studies to be presented in Chapters 4 and 5 were carried out using the near-IR cameras.

In summary, the extensive studies at different wavelengths indicate that L1641 is an active star formation region. The diversity of the YSOs in L1641 make it suitable for a comparative study.

1.4. THESIS OUTLINE

The flow-chart in Figure 1.4 outlines the structure of the thesis.

In Chapter 2, we present an *IRAS* source sample selected from *IRAS* co-added images in L1641. We discuss the source selection and the flux determination. We also use the *IRAS* data to investigate the nature of these sources. Finally 122 *IRAS* sources are selected as possible YSOs for the follow-up studies.

To address the problem of dense core dissipation, in Chapter 3, we present two sets of molecular line observations, (1) a moderate-resolution (3') ^{13}CO J = 1-0 mapping of 40 sources; and (2) the high-resolution (20") ^{13}CO J = 1-0 and HCO^+ J = 1-0 observations of 28 sources. From these observations we conclude that the most sources with CO outflows are associated with dense cores, and most of the sources without outflows are not associated with dense cores. The most plausible explanation is the dense core dissipation by either accretion or outflow of the embedded sources at the early stage of star formation. Part of result presented in this chapter has been published in *Astrophysical Journal* (Chen, Fukui, & Yang 1992a)

In Chapter 4, we present a near-IR (1.6-4.8 μm) imaging of 59 *IRAS* sources. The images provide the most sensitive and extensive census of the near-IR sources in the vicinity of *IRAS* sources in L1641. The most interesting result from our imaging is the discovery of stellar density enhancements (SDEs) in 14 of the 59 sources. We will show that most of the near-IR sources in the SDEs are YSOs associated with the *IRAS* sources. It is also shown that the spatial distribution of young stars in the L1641 can be characterized by a range of stellar density, from a large cluster (the Trapezium Cluster) to the SDEs and to individual stars. The previously proposed isolated and cluster star formation modes may be the low and high ends of this continuous distribution. These conclusions are supported by a detailed optical and near-IR imaging of 3 *IRAS* sources in Chapter 5. The work presented in Chapter 5 has been accepted for publication in *Astrophysical Journal* (Chen et al. 1992b)

In Chapter 6 we discuss in detail the association of the SDEs with molecular dense cores, and the formation of the SDEs. We also discuss the implications of SDEs to star formation theory. Finally, in Chapter 7, we conclude this thesis with a summary of observational results obtained in this project, and what we have learned from these results. Some open questions and possible follow-up studies are discussed.

Now, sit back, and enjoy your journey.

TABLE 1.1 OBSERVED AND DERIVED PROPERTIES OF CORES

	$C^{18}O$		NH_3	
	Range	Typical	Range	Typical
Map half-power diameter (pc)	0.2 - 0.7	0.3	0.05 - 0.2	0.1
Log number density (cm^{-3})	3.5 - 4.4	4.1	4 - 5	4.5
FWHM line width (km s^{-1})	0.4 - 0.9	0.5	0.2 - 0.4	0.3
Gas Mass within FWHM ($M_\odot$)	3 - 60	15	0.3 - 10	1
Free fall time (10^5 yr)	2 - 6	3	1 - 4	2
Kinetic Temperature (K)	5 - 17	10	9 - 12	10
Velocity Gradient (km s^{-1} pc^{-1})	0 - 3	1	0 - 3	1

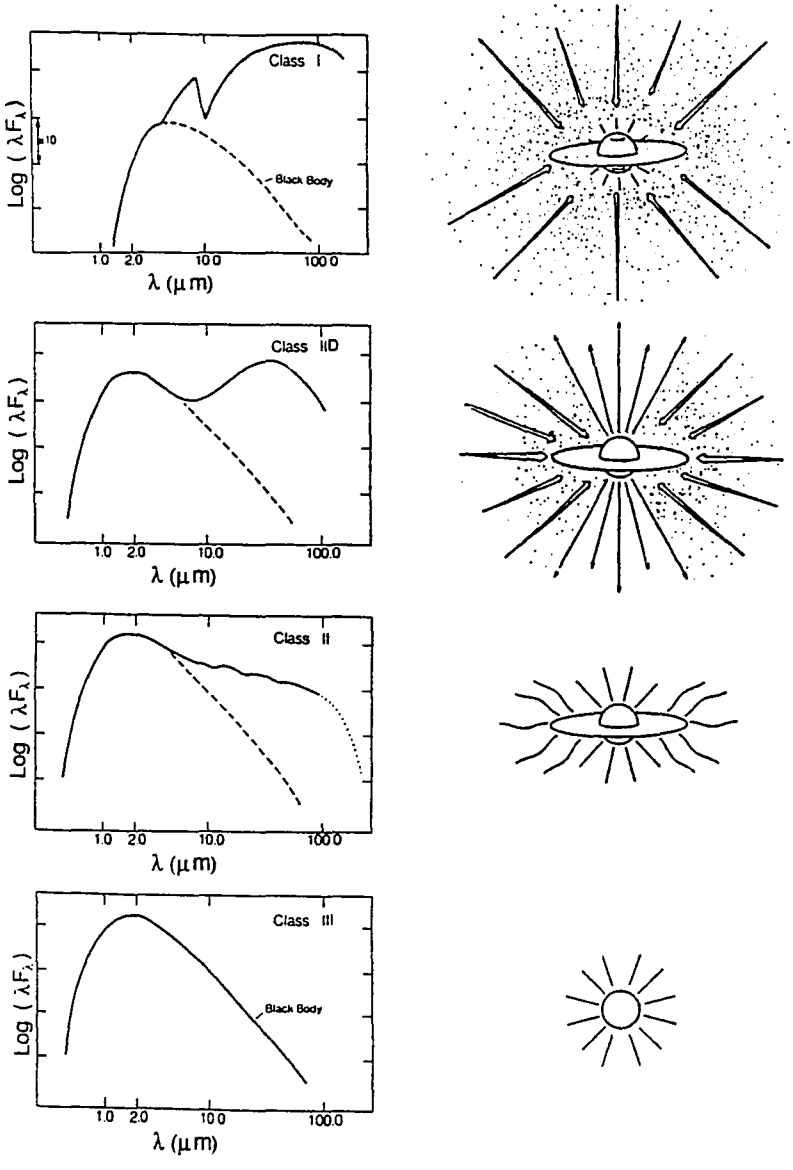

Figure 1.1 The proposed four stages that young stars should go through during their formation and early evolution, based on the model of Shu et al. (1987). The spectral energy distributions of young stars at the corresponding stages are also shown (Lada 1987). The four stages are: (1) an accreting protostar (class I SED), (2) an accreting protostar with a well-developed outflow (class IID), (3) the T Tauri phase (class II), and (4) the naked T Tauri or post-T Tauri phase (class III). This figure is adopted from Wilking (1989).

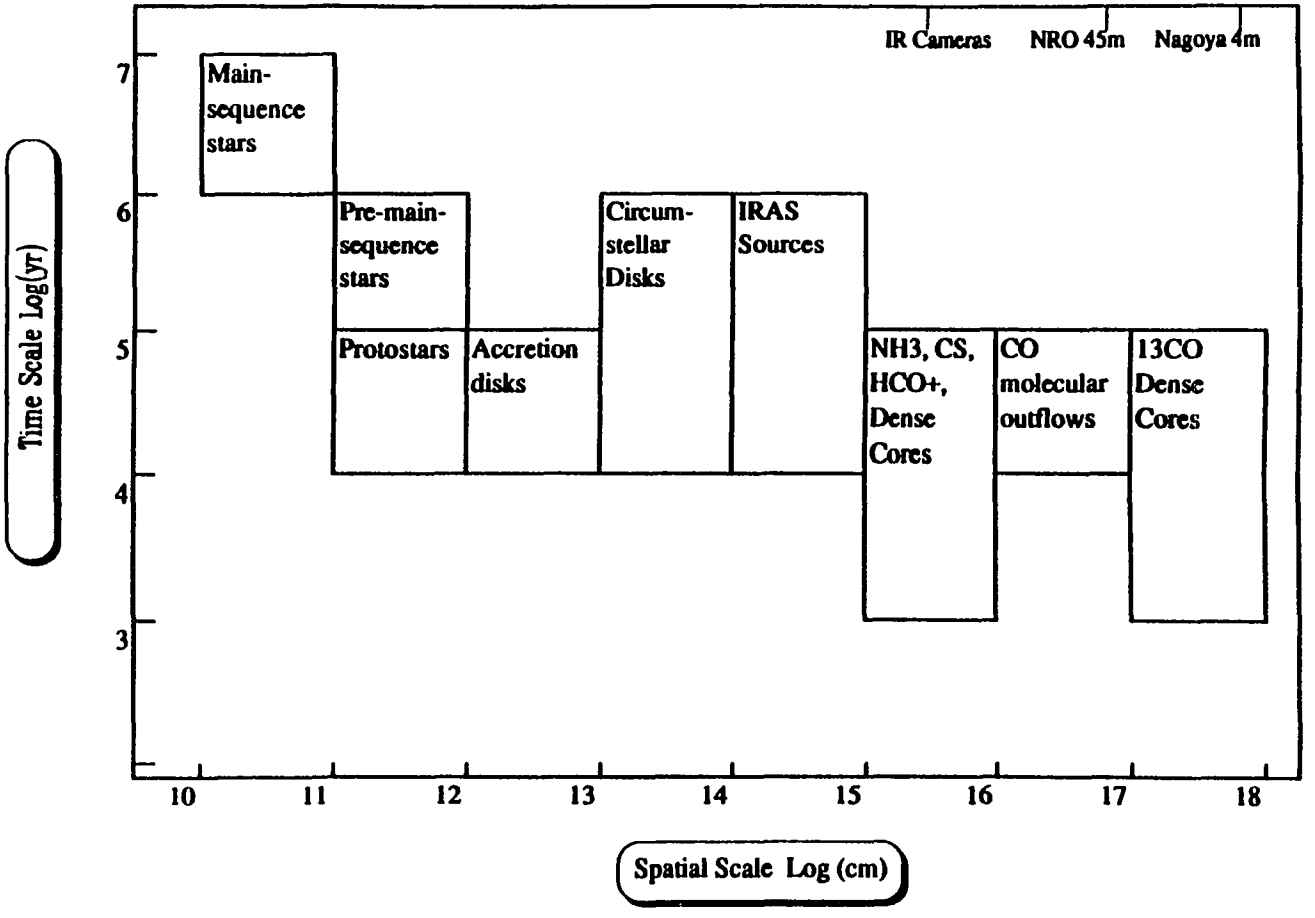

Figure 1.2 The time and spatial scales of the phenomena related to star formation. The spatial resolutions of the observations used in this thesis are indicated on the top.

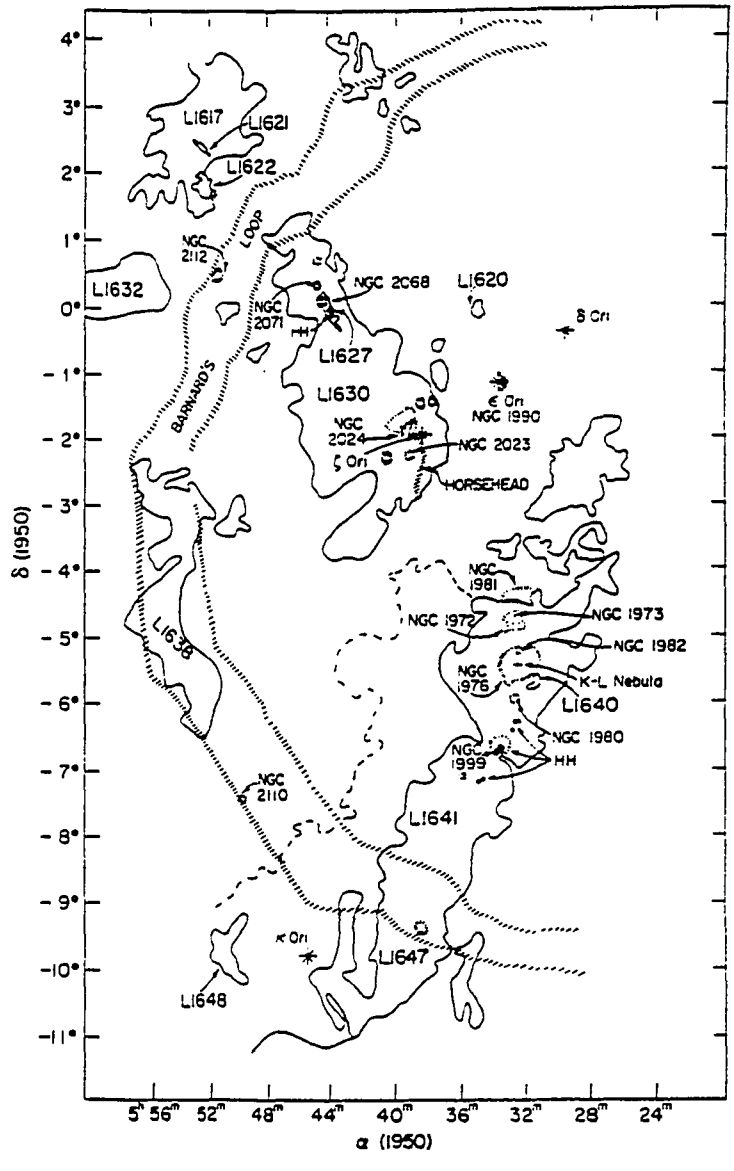

Figure 1.3 The CO map of Orion molecular complex. The dark cloud L1641, as a part of Orion A giant molecular cloud, is located near the bottom of the figure. This figure is adopted from Kutner (1977).

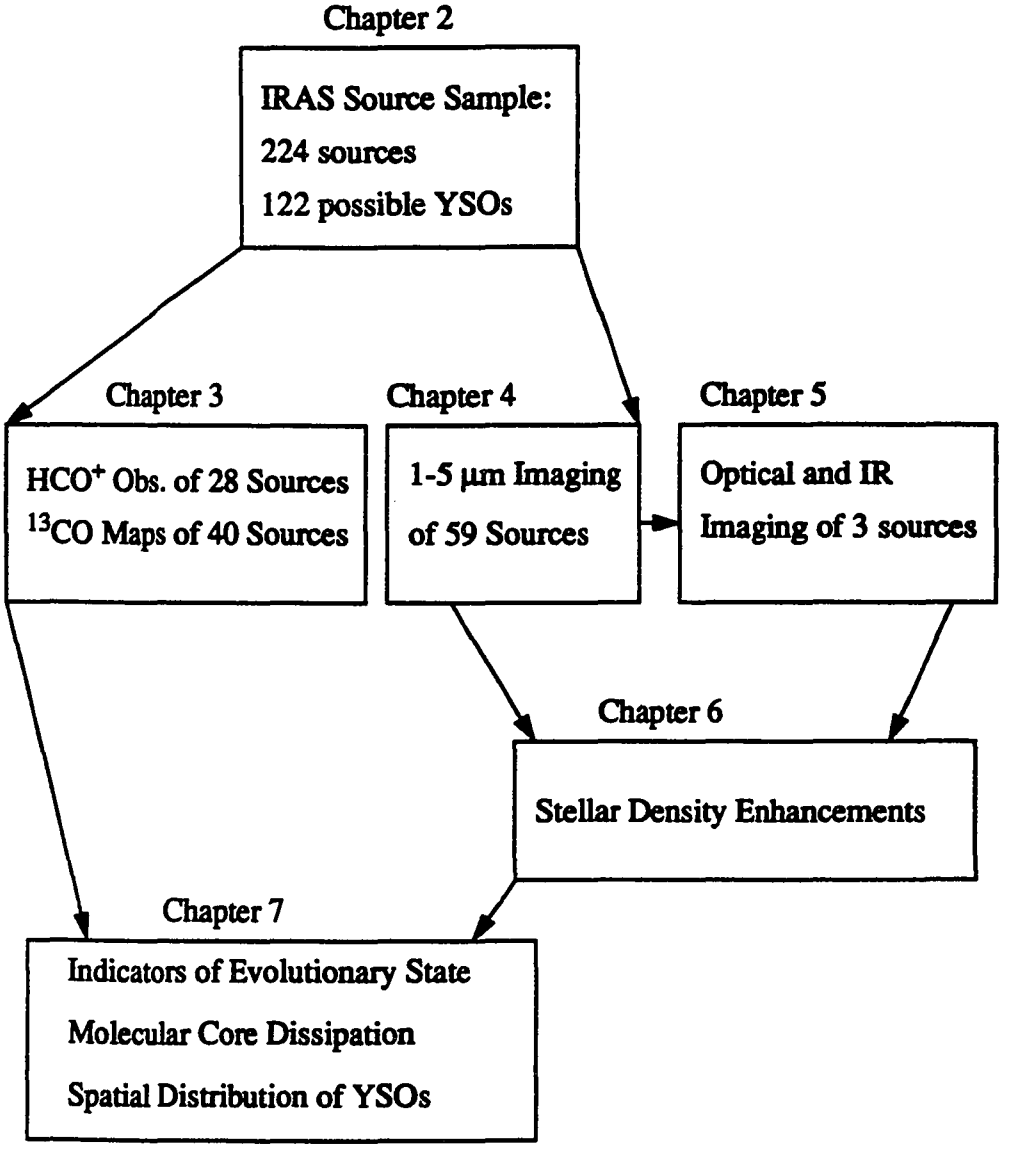

Figure 1.4 The outline of the thesis.

CHAPTER 2

AN *IRAS* SAMPLE FROM COADDED IMAGES OF L1641[1]

2.1. INTRODUCTION

In the early studies of *IRAS* sources, much attention has been drawn to the sources that are associated with known star forming activity, such as molecular dense cores, CO outflows, and T Tauri stars (Emerson et al. 1984, Beichman et al. 1986). These studies did not systematically study all the *IRAS* sources in a single molecular cloud and therefore conclusions on the evolutionary state of the *IRAS* sources were complicated by different environment and evolutionary history of the sources. A different approach is to study all the sources listed in *IRAS Point Source Catalog* (*PSC*, Beichman et al. 1988) within one molecular cloud, such as has been done for L1641 (Strom et al. 1989) and Taurus (Kenyon et al. 1990). In this case, sources at different evolutionary stages will allow us to understand the star formation process in a larger context. In addition, because all sources are located within one molecular cloud at a known distance, the analysis is relatively simpler. The availability of *IRAS* coadded images makes it feasible to select an unbiased *IRAS* sample with a sensitivity 2-3 times higher than that of *PSC*. The enhanced sensitivity will allow us to detect new sources, and to improve the detections for the sources that have only upper limits in *PSC*. The recent study of molecular cloud ρ Oph is a good example of this approach (Wilking et al. 1989).

In this chapter, we report on a study of *IRAS* sources in L1641 using the coadded images. In section 2.2, we explain the *IRAS* source selection and flux density

---

[1] The IRAS data were obtained using the facilities of Infrared Processing and Analysis Center (IPAC). IPAC is funded by NASA as part of the IRAS extended mission program under contract to JPL.

determination. Three physical parameters (*IRAS* color, far-infrared luminosity, and ^{13}CO column density) of the sources are obtained in section 2.3. Using these parameters, we discuss the nature of the *IRAS* sources in section 2.4. In section 2.5 we examine the potential evolutionary indicators of YSOs. The major results are summarized in section 2.6.

2.2. SOURCE SAMPLE

L1641 was identified by Lynds (1962) as a dark cloud with an optical obscuration level of 4 (approximately A_V = 4 mag). Figure 2.1 shows the ^{13}CO molecular gas distribution of L1641 (Fukui and Mizuno 1991). The lower contour level is 3.0 K km s^{-1}, an approximate 3 σ detection of the ^{13}CO integrated intensity. This contour level gives a ^{13}CO column density of 3×10^{15} cm^{-2} under the typical interstellar conditions (T_{ex} = 15 K, and Δv = 1.0 km s^{-1}). This corresponds to a visual extinction of A_V = 3 mag using the $N(^{13}CO)$-A_V relationship given by Dickman and Herbst (1990), and it encompasses the dark cloud boundary defined by Lynds. Following Strom et al. (1989), we focus on the region with R.A. between 5^h30^m and 5^h45^m and declination between -6°0' and -9°45', which covers the entire L1641 dark cloud, as shown in Figure 2.1.

2.2.1. *Source Selection*

The *IRAS* time-ordered data set can be re-binned into a position-ordered data set or a two-dimensional image. Several such images in the same area can be combined into a co-added image with sensitivity 2-3 times higher than that of *PSC*. We obtained the co-added images from the Infrared Processing and Analysis Center (IPAC) in two main fields. The two fields (2.25° x 2.25° each) cover the entire L1641 cloud (see Fig. 2.1),

and they are the same regions studied by Strom et al. (1989b). Each image contains 540 × 540 pixels at 12 and 25 μm, 270 × 270 at 60 μm and 135 × 135 at 100 μm. This yields a scale of 15" pixel^{-1} at 12 and 25 μm, 30" pixel^{-1} at 60 μm and 60" pixel^{-1} at 100 μm. For comparison, coadded images were also obtained in two nearby areas, also indicated in Figure 2.1. The scale for the control areas is 30" pixel^{-1} at all four wavelengths.

Three tests were used to select sources from the co-added images:

(1) *Pixel signal-to-noise ratio* The images were divided by their corresponding noise frames, and the pixels with signal-to-noise ratio < 3 were rejected.

(2) *Source significance* Aperture photometry was obtained on the pixels that passed test (1). The aperture on the sources was three pixels in diameter and the annular aperture on the sky was 2 pixels wide around the source aperture. The sources with total flux less than 3 times that of surrounding annular regions were rejected.

(3) *Source Positions* For that has passed tests (1) and (2), the pixel with the maximum value within a 1' × 1' box was taken as the source position. Areas that do not have a well-defined peak inside the box were rejected. This process rejected the signal peaks that occurred only in the in-scan direction as a result of ridge-like emission features.

We obtained 312 detections by applying the above three tests to the coadded images (in both main regions and control regions) at 12, 25 and 60 μm. The source positions were determined by their peak emission at 12 μm (or 25 μm if there is no detection at 12 μm). These positions were used to determine the source fluxes.

2.2.2. *Flux Density Determination*

The *IRAS* fluxes of the sources were determined using the Addscan data obtained from IPAC. At each source position, an IPAC program ADDSCAN extracted 10-12

single scans in the in-scan direction, which is approximately the North-South direction in L1641, from the *IRAS* database. They were combined to construct the Addscans in four different ways: simple co-adding (scan code No. 999); mean of the scans (code 1001); median of the scans (code 1002), and noise-weighted co-adding (code 1003). Of the four Addscans, the noise-weighted scan (code 1003) usually has the highest signal-to-noise ratio. It was therefore used in most cases. The other scans were used only if one of the following problems was encountered with the noise-weighted scan: i) the baseline was bad; ii) spikes appeared in the profile; and iii) adjacent sources affected the scan profile.

The combined scans were then compared to the point source template. For each addscan, we used the IPAC program SCANPI to calculate four flux estimators in each band: the peak value within a given aperture; the integrated flux between the zero points; the integrated flux within the given aperture, and the amplitude of the fitted point source template. To select the appropriate flux estimator, we divided all the sources into point sources and extended sources. The spatial-intensity profiles of the sources were fitted by the point source template to obtain the *FWHM* of the fitted template, <*W50*>, which is used to describe the angular size of the sources. For this study, sources with <W50> <1'.1 at 12 μm were classified as the point sources, and those with <W50> >1'.1 as the extended sources. For sources that seemed to be multiple sources or were not detected at 12 μm, the same classification was carried out at 25 μm. Note this criteria corresponds to the correlation coefficiency flags of A, B, C and D in the *PSC* (Beichman et al. 1988). We used a more restrictive criteria here to separate the point sources from the slightly extended sources. As shown below, there are indeed many differences between the point and the extended sources.

Once a source was classified as a point or an extended source, the flux estimator was chosen according to its angular size. For the point sources, the four estimators described above are usually consistent to each other, and, in most cases, the amplitude of the fitted

point source template was assigned to the source flux. For the extended sources, integrated fluxes were chosen. The flux uncertainty was determined by the rms deviation of the residuals after the baseline fitting by the SCANPI.

2.2.3. *Source Sample*

The final selection criterion was that the sources have at least one clear detection at 12, 25 or 60 μm (with signal-to-noise ratio >5). We excluded sources that were only detected in 100 μm band because most of these sources are probably infrared cirrus. Of 312 sources selected from the coadded images, we rejected 73 sources having the signal-to-noise ratio < 5 in all three bands, one source that is coincident with a galaxy (Strom et al. 1989b), and 14 other sources that are probably foreground or background stars as determined by Strom et al. (1989b). After excluding these sources, we were left with 224 sources (98 point sources and 126 extended sources).

The association of the *IRAS* sources with the molecular cloud L1641 was examined. The spatial distribution of all the sources is superimposed onto the ^{13}CO contour map of the L1641 in Figure 2.2. 122 sources (79 point, and 43 extended) are located inside the ^{13}CO contour (3.0 K km s^{-1}), and are therefore considered to be associated with the L1641. Note that most point sources (filled circles in the left panel) are located within the contour, while the extended sources (open circles in the right panel) are almost randomly distributed. As to be discussed in section 2.4, most of the sources located outside the molecular cloud are probably either infrared cirrus or foreground stars. The complete data sample of the 224 *IRAS* sources can be found in Appendix A (Table A1), and Table 2.1 shows only the 122 sources that are located inside the L1641.

2.2.4. *Comments on the Sample*

(1) Of the 123 sources in the *IRAS PSC* (Strom et al. 1989), 106 were found by the process described above. For the 17 *PSC* sources that were not detected, 3 are probably caused by source confusion. The other 14 sources are not associated with a peak of emission, instead they are often located in a ridge that is extended in the cross-scan direction, and five of them are classified as spurious sources by Strom et al. (1989). In our sample, there are 27 newly-detected point sources (15 of them inside molecular cloud). The average flux density of the newly detected point sources is 0.34 Jy at 12 μm, about a factor of two lower than the upper limit of 12 μm flux of *PSC* (0.5 Jy at 3 σ). We attribute these new detections to the enhanced sensitivity of the *IRAS* coadded images.

(2) For the 106 *PSC* sources, we have compared the positions determined from coadded images with the positions given in *PSC*. The coadded source positions agree well with the *PSC* position in the in-scan direction with 77 % of the sources having a position difference < 15". The position discrepancy is much larger in the cross-scan direction with 75% of the sources having position difference < 45". Such a large position discrepancy was also found by Schwartz, Gyuludaghian & Wilking (1991) in IC 1396. At least two factors may cause the discrepancy: (i) the *PSC* positions were based on 2-3 bands, while the coadded positions were mainly determined by the 12 μm peak; and (ii) the *PSC* positions were determined by point source template. If a source is not a well-defined point source, the position will be different from the peak position. The second possibility is supported by the fact that most of the sources that have large position difference were classified as extended sources in this study.

(3) It is very difficult to draw a uniform detection limit because (i) the noise level varies from source to source; and (ii) some sources might be confused by the nearby

sources. For the isolated sources, we estimate a 5 σ upper limit of 0.2, 0.2, 0.7 and 7 Jy at 12, 25, 60 and 100 μm respectively. The flux errors can be as high as 50-100% in the confused regions, especially in the 60 and 100 μm bands.

(4) Although we classified the sources into point and extended sources, it is subject to source confusion within the *IRAS* beam. We cannot be absolutely certain that all sources classified as point or extended are in fact single-sources. However, as shown in section 2.4, many differences between the point sources and the extended sources do indicate that they are different in nature.

(5) Our source selection is biased against evolved stars that have relatively little far-infrared emission. Since our major interest is to study the stars at early evolutionary stage, the above bias is not critical. Of the 30 emission-line stars in the region (Herbig and Bell 1988), twelve of them (40%) are detected in this study. The sample is also biased against the sources that can only be detected at 100 μm. Most of these sources are likely to be infrared cirrus, although there is a possibility that we might miss YSOs at an extremely young age. It is beyond the scope of this thesis to discuss these sources.

2.3. THE PHYSICAL PROPERTIES

2.3.1. *Color Temperature*

If cold dusts are in thermal equilibrium and the dust emissivity is proportional to ν^n, a color temperature between wavelengths λ_1 and λ_2 can be calculated as:

$$T[\lambda_1,\lambda_2] = \frac{\frac{hc}{k}\left(\frac{1}{\lambda_1}-\frac{1}{\lambda_2}\right)}{\ln\frac{f(\lambda_1)}{f(\lambda_2)} + (n+3)\ln\frac{\lambda_1}{\lambda_2}} \quad \text{(K)} \qquad (2.1)$$

where $f(\lambda)$ is source flux density, and h, c and k are the Planck constant, the speed of light, and the Boltzman constant, respectively (Emerson 1988a). For the dust emissivity dependence on frequency, we adopted the result of Draine and Lee (1984) which gave $n = 2$ for both graphite and silicate. As to be discussed in section 2.4, the *IRAS* emission the *IRAS* sources located inside the L1641 is mostly thermal emission, so equation (2.1) can be applied. For each of these sources, a color temperature, T[12,25], is obtained using the ratio of 12 and 25 μm flux densities, and is listed in Table 2.1. Equation (2.1) may not be valid for the sources located outside of L1641, because their emission at 12 and 25 μm is probably dominated by the non-thermal emission from very small grains (VSGs) heated by the interstellar UV photons.

2.3.2. *Far-Infrared Luminosity*

Given the *IRAS* flux densities in the four *IRAS* bands, and assuming that the dust emission spectrum f_λ is proportional to λ, the source infrared luminosity between 7 and 135 μm can be calculated as (Emerson 1988b):

$$L = 3.2 \times 10^{-5} D^2 (20.65 f_{12} + 7.54 f_{25} + 4.58 f_{60} + 1.76 f_{100}) \ L_\odot \qquad (2.2)$$

where D is the distance to the source in parsecs, f_λ is the flux density in Jy at λ. To account for the luminosity beyond the observable bands, we use a method suggested by Myers et al. (1988). Assuming that blackbody radiation peaked at the longest observable wavelength λ_{max} with flux density f_{max}, the luminosity longward of λ_{max} can be written as:

$$\Delta L = 3.9 \times 10^{-5} D^2 f_{max} / \lambda_{max} \ (L_{\odot}) \qquad (2.3)$$

The total far-infrared luminosities of the *IRAS* sources, $L_{FIR} = L + \Delta L$, are given in Table 2.1.

2.3.3. ^{13}CO *Column Density*

We made CO and ^{13}CO millimeter observations to obtain the gas column density toward the *IRAS* sources. The CO (J = 1-0) and ^{13}CO (J = 1-0) line emission at 115 and 110 GHz were observed using the 4 m millimeter telescope in Nagoya University during March 26 - 27, 1990. The telescope has a beamsize of 2'.7. A SIS receiver was used and the system temperature was about 400 K (double-side band). For each of the *IRAS* sources selected in the two main fields, a single-point observation was made at the *IRAS* position. Ori A was observed during the observations for the temperature calibration. The rms noise is typically 1.0 K and 0.35 K for CO and ^{13}CO, respectively.

The data reduction was carried out using the Nagoya data reduction system. After the baseline removal, a gaussian fit to the line profile gave three parameters: the peak temperature, the line width and the line center. Using these parameters we estimated the ^{13}CO column density toward each *IRAS* source. The CO line is usually optically thick so that the CO antenna temperature gives directly measure of the gas excitation temperature. With the assumptions that both CO and ^{13}CO are in thermal equilibrium with the same excitation temperature, the ^{13}CO line is optically thin, and the line profile is gaussian, we calculate the ^{13}CO column density from:

$$N(^{13}\mathrm{CO}) = 2.49 \times 10^{14} \frac{T_{ex}\, \tau_0\, \Delta v}{1-\exp(-5.31/T_{ex})} \qquad (\mathrm{cm}^{-2}) \qquad (2.4)$$

where T_{ex} is the excitation temperature of CO and ^{13}CO gas in K, and Δv is the ^{13}CO line width (FWHM) in km s^{-1} (see Appendix B for the derivation of equation (2.4)). The optical depth of ^{13}CO at line center, τ_0, can be obtained by using the peak temperatures of CO and ^{13}CO and assuming $X(CO) / X(^{13}CO) = 89$. Note that for T_{ex} = 20 K, the ^{13}CO line will become optically thick ($\tau_0 > 1$) when the column density reaches 2×10^{16} cm^{-2}, and the ^{13}CO line will not be a good measure of the gas density such as at the center of the densest cores in our sample. The ^{13}CO column densities $N(^{13}CO)$ of the *IRAS* sources are presented in Table 2.1.

2.4. THE NATURE OF THE SOURCES

2.4.1. *Point Sources vs. Extended Sources*

Figure 2.2 shows the spatial distribution of the point sources and the extended sources in L1641. The point sources are clearly associated with the molecular cloud (as defined by the ^{13}CO integrated intensity contour map), and 80% of them are located inside the molecular cloud. On the other hand, the distribution of the extended sources appears to be random, and only 37% of the extended sources are located inside the L1641 boundary. Table 2.2 shows the association of the sources with the L1641. Using the contingency table statistical test (see Appendix C), we find that the distributions of the point sources and the extended sources are different at a >> 99.9% level of confidence.

The color-color diagram using *IRAS* flux densities at 12, 25 and 60 μm is often used for the first-order classification of the *IRAS* sources (Beichman 1985, Emerson 1988b). We plotted the point sources and the extended sources in Figures 2.3a and 2.3b, respectively. It is clear that the point sources and the extended sources are distributed

differently in the color-color diagrams. Most of the point sources are spread widely across the diagram, and 50% of them are located inside the boxes defined by known T Tauri stars and molecular dense cores. In contrast, almost all the extended sources are located in a region appropriate for hot cirrus defined by Beichman (1985). This result, together with the concentration of the point sources within the molecular cloud, suggests that most of the point sources are probably YSOs, and most of the extended sources are not.

2.4.2. *Emission Mechanism of the Dust*

The location of the *IRAS* sources in the color-color diagram yield some clues into the dust emission mechanism. The point sources are spread widely in the diagram, indicating a large range of the dust temperature. This can be understood if the heating sources are embedded sources whose temperature varies from source to source, depending on the luminosity of the sources, dust properties (particle size and composition) and the spatial distributions of the surrounding dust.

On the other hand, the extended sources are located in a small region of the color-color diagram characteristic of hot cirrus emission. The cirrus emission is believed to arise from the non-thermal emission from very small grains (VSGs) that are heated by UV photons in the interstellar radiation field (Boulanger et al. 1988). Since the VSGs have very small size (~ 10 Å) and heat capacity, they can attain a temperature up to 1000 K when heated by a single UV photon. With this stochastic heating and cooling the VSGs cannot be in thermal equilibrium (Sellgren 1984). The high temperature of the VSGs cause them to dominate the emission at both 12 and 25 μm. The ratio of the two flux densities therefore is insensitive to the thermal equilibrium temperature. The hot VSGs have little emission at longer wavelengths at which the thermal emission from the

colder and larger grains dominates. Figures 2.4a and 2.4b show the 12-25 μm vs. 60-100 μm color-color diagrams of the sources inside and outside the L1641 respectively. In Figure 2.4b, the sources located outside the L1641 (most of them are extended) vary by a factor of >10 in the 60-100 μm flux density ratio, while their 12-25 μm flux density ratio only changes by a factor of 2.

For the large-scale *IRAS* emission in the California Nebula, Boulanger et al. (1988) developed an analytical model for VSG emission. Assuming that the far-infrared emission comes from a mixture of the VSGs (~ 10 Å) and the larger grains (~ 0.5 μm) heated by the interstellar radiation field, they calculated the *IRAS* colors as a function of equilibrium temperature of the large grains (T_{eq}). As shown in Figure 2.4b, the theoretical calculation (solid line) matches our observations very well.

The same analysis was carried out for the sources inside L1641 (most of them are point sources). As shown in Figure 2.4a, most of these sources have a 12-25 μm flux ratio lower than what the model predicted (solid line). This indicates that the thermal emission from the large grains overpowers the non-thermal emission from the VSGs. The probable heating sources are the embedded YSOs.

In summary, the spatial distribution of the sources and the *IRAS* color-color diagram show that the sources inside and outside L1641 are significantly different. The color-color diagram shows the sources within L1641 are self-heated probably YSOs, while the sources outside have a spatial distribution and *IRAS* color typical of infrared cirrus. Since our main objective is to study the YSOs in L1641, the following discussion will concentrate on the sources that are located inside L1641, i.e. the 122 sources presented in Table 2.1.

2.5. DISCUSSION

How might one characterize the evolutionary state of a YSO from physical observations? The infrared emission from a YSO may arise from the central object, a disk system and a dust shell. Its spectral energy distribution may not resemble a single-temperature blackbody, and it is therefore difficult to place a YSO in the luminosity-temperature diagram. Using his protostar model, Adams (1990) attempted to use the relation between the luminosity and visual extinction to determine the evolutionary state of a YSO by placing it in a L_{FIR}-A_V diagram. However, because of light scattering and possible IR excess of YSOs, it is very difficult to determine the extinction in the near-IR (1-5 μm) and to compare the observations with the model. This motivates us to look for other observational parameters to characterize the YSOs. In the following, we use the sample in Table 2.1 to discuss possible evolutionary indicators. For simplicity we divide the sources in Table 2.1 into three groups: (1) outflow sources (the 11 *IRAS* sources known to be associated with CO outflow); (2) T Tauri stars (the 9 sources associated with known T Tauri stars); and (3) other sources (those not associated with known CO outflows or known T Tauri stars).

2.5.1. $N(^{13}CO)$ *as an Evolutionary Indicator*

The ^{13}CO column density measures the number of ^{13}CO molecules in the line of sight if the emission line J=1-0 is optically thin. Figure 2.5a shows the histograms of $N(^{13}CO)$ for the three groups. The outflow sources have $N(^{13}CO)$ significantly higher than the non-outflow sources. To see if the high column density toward the outflow sources is due to a local enhancement associated with the *IRAS* source or just a chance overlap, we have made the following observations: (1) By mapping a group of the *IRAS*

sources in ^{13}CO, we find that 7 of 9 outflow sources are located inside dense cores, compared with only 4 of 31 nonoutflow sources (Chapter 3); and (2) High-angular resolution HCO^+ and ^{13}CO observations with about 20" beamsize show that the column densities of these two molecules are correlated with each other, and both column densities are well correlated with the *IRAS* colors (Chapter 3). This indicates that the molecular gas is physically associated with the *IRAS* sources. It is possible that N(^{13}CO) may underestimate the gas column density if ^{13}CO J=1-0 line becomes saturated. However because Figure 2.5a shows that outflow sources are usually associated with higher N(^{13}CO) than the non-outflow sources, and therefore more likely to be saturated, the line saturation should not change the general trend in Figure 2.5a.

The association of the outflow sources with dense gas indicates that the outflow sources are YSOs still embedded in their parental dense cores. The significant difference shown in Figure 2.5a between the outflow sources and non-outflow sources suggest that the embedded YSOs have disrupted the core when the energetic outflow is terminated. The outflow from the YSO and the accretion to the YSO therefore are the prime candidates for dissipating of the dense cores.

2.5.2. IRAS *Color Temperature as an Evolutionary Indicator*

As discussed in the previous section, the 12 and 25 μm emission from the sources located inside L1641 (most of them are point sources) are probably the thermal emission from dust heated by the embedded sources. Since the color temperatures T[12, 25] is usually much higher than the color temperature obtained at longer wavelengths, T[12,25] measures the dust closer to the central embedded sources. T[12,25] is capable of sampling the dust with a scale of 10^{14} cm (equilibrium radius) for an *IRAS* source with a luminosity of 10 $L_\odot$.

Figure 2.5b displays the histograms of T[12,25] for the outflow sources, the T Tauri stars and all other sources. As a group, the outflow sources are the coldest. The average T[12,25] of outflow sources is 137 K, compared with 180 K for all of the non-outflow sources. The outflow sources appear to be much more deeply embedded in the dust shell than the pre-main sequence stars, and their emission is degraded to longer wavelengths.

2.5.3. *Far-IR Luminosity as an Evolutionary Indicator*

Because the emission of the central sources is absorbed by the surrounding dust and reemitted at longer wavelengths, the far-infrared luminosity obtained in section 2.3.2 should account for most of the source luminosity. If we include the luminosity contribution at the shorter wavelengths (shorter than 5 μm), the luminosity would likely increase by a factor no more than two (Beichman et al. 1986). If disk reprocessing exists, the source luminosity may be overestimated by a factor of two (Wilking, Lada, & Young 1989). Since the two corrections can compensate each other, and we have no reliable information on either of them, it is assumed here that the luminosity derived in section 2.3.2 represents the total luminosity of the YSO within a factor of two.

Figure 2.5c shows the luminosity histograms for detected outflows, T Tauri stars and the other sources. It is clear that outflow sources tend to be more luminous than the nonoutflow sources. The average luminosity of outflow sources is 81 $L_{\odot}$, while that of the non-outflows is only 7 $L_{\odot}$. There is no significant difference in the luminosity distribution of T Tauri stars and the other nonoutflow sources.

The fact that the outflow sources are more luminous has also been observed in other low-mass star formation regions, such as Taurus (Myers et al. 1988) and ρ Oph (Wilking, Lada, & Young 1989). There are three possible explanations: (1) this might be a selection effect in the sense that the CO outflow is easier to detect around a more

luminous source; (2) the outflow sources are more massive stars than the non-outflow sources, and (3) the outflow sources are at a younger evolutionary stage and have significant luminosity from accretion or deuterium burning. With the present data, we cannot conclusively discriminate among the possibilities. However we show in the following that (1) and (2) are less likely, and we therefore favor (3).

(i) The unbiased Nagoya survey for CO outflow has a lower limit of 10^{-3} $L_{\odot}$ in mechanical luminosity. Using the correlation between the outflow mechanical luminosity and the star luminosity (Lada 1985), the survey should be capable of detecting any CO outflow from our *IRAS* source with luminosity greater than 1 $L_{\odot}$. 85% of our sources are brighter than that luminosity. Unless an outflow is smaller than the beamsize of Nagoya telescope (2'.7, or 0.4 pc), the outflow survey should be complete for 85% of our sources.

(ii) CO outflows have been detected around both high-mass and low-mass YSOs (Fukui 1989). It is unlikely that in L1641 only high-mass stars are associated with CO outflows.

(iii) L1641 is a low-mass star formation region. The major young stellar population is believed to be T Tauri type low-mass stars (Cohen & Kuhi 1979, Fukui et al. 1989, see also Chapters 4 and 5).

(iv) The average luminosity of the outflow sources is about 80 $L_{\odot}$. It can be easily accounted for if most of the YSO luminosity is obtained from the accretion. Since $L_{acc} = GM\dot{M}R^{-1}$, a 1 $M_{\odot}$ star can have L_{acc} = 70 $L_{\odot}$ for an accretion rate of 10^{-5} $M_{\odot}$ yr^{-1} and protostar radius of 4 $R_{\odot}$. The most luminous outflow source L1641-N has a luminosity of 220 $L_{\odot}$, and this could be the result of multiple heating sources of *IRAS* luminosity, as suggested by the near-IR images (Chapter 5).

We have also compared the luminosity distribution of the *IRAS* sources in L1641 with those in Ophiuchus and in Taurus-Auriga (Figure 2.6). The data in Ophiuchus were

taken from Wilking, Lada & Young (1989) and data in Taurus were taken from Kenyon et al. (1990). Because L1641 is 3 times further away from the sun than both Ophiuchus and Taurus-Auriga, our detection limit is about 10 times higher. This may explain the lack of low-luminosity sources ($L/L_{\odot} < 1$) in L1641. It is significant however that there are more brighter sources ($L/L_{\odot} > 10$) in L1641 than in the other two molecular clouds. It is possible that the YSOs in L1641 are more massive than those in Oph and Taurus-Auriga. It is also possible that the source confusion in L1641 may be more significant due to its distance, and the *IRAS* luminosities might be the result of more than one sources.

2.5.4. *Comparison of the Three Indicators*

The average physical parameters of outflow sources, T Tauri stars, and the other sources are summarized in Table 2.3. The similar beamsizes of the *IRAS* telescope and the Nagoya telescope allow us to compare the three parameters discussed in the previous section, as shown in Figures 2.7a-c. In all three figures, outflow sources are again significantly different from the rest of the *IRAS* sources, and they can be identified as an earlier stage of stellar evolution. This stage can be characterized by high luminosity, low color temperature, and association with dense gas and with a CO outflow. The difference of the three parameters for the outflow and non-outflow sources can be understood as the removal of a parental dense core surrounding the outflow source.

Note that the 9 T Tauri stars in the three figures are virtually indistinguishable from the majority of the sources inside L1641. They share almost the same color, have similar luminosity, and are associated with similar amount of molecular gas. It is possible that most of these non-outflow sources are also the pre-main-sequence stars like T Tauri stars.

Although the outflow sources are significantly different, we have noticed that there is no obvious correlation among the three physical parameters for the non-outflow sources. The large scatter may be attributed to (1) the *IRAS* sources may be multiple sources and cannot be resolved by the *IRAS* beam; (2) the ^{13}CO column density may be contaminated by the gas emission in the line of sight due to its relatively low excitation density. The high-spatial resolution millimeter observations (Chapter 3) and imaging with near-IR cameras (Chapter 4 and 5) should help us to overcome the above limitations.

2.6. SUMMARY

1. From the *IRAS* coadded images, we have selected 224 (98 point and 126 extended) sources in star forming region L1641 in an unbiased manner. There are 122 sources inside L1641 (presented in Table 2.1).

2. There are significant differences between the point sources and the extended sources. The two groups occupy different locations in the *IRAS* color-color diagram. The point sources are associated with ^{13}CO molecular gas of L1641, while the extended sources are randomly distributed. The point sources are heated by the embedded objects, while the extended sources are probably heated by the interstellar radiation field. The emission from the extended sources is likely to be dominated by the VSGs. We conclude that most of the extended sources could be infrared cirrus, and most point sources are probably embedded YSOs.

3. For the sources associated with the L1641, we find the outflow sources are significantly different from the non-outflow sources. They are colder, more luminous and are associated higher column density. Such differences can be explained if the outflow sources are embedded proto-stellar objects still in the accretion phase.

4. The three parameters (T[12,25], L_{fir}, and $N(^{13}CO)$) allow us to separate outflow sources from non-outflow sources. Further high resolution observations are needed to define a more detailed evolutionary sequence.

5. This study provides an unbiased *IRAS* source sample within a single molecular cloud for further study. In the following chapters we will present the follow-up millimeter observations (Chapter 3) and near-IR imaging (Chapters 4, and 5) of these sources.

TABLE 2.1. 122 *IRAS* SOURCES INSIDE L1641

No	SN	α (1950) 5^h		δ (1950)			f_{12} (Jy)		f_{25} (Jy)		f_{60} (Jy)		f_{100} (Jy)		L_{FIR} ($L_\odot$)	p-e	$N(^{13}CO)$ ($10^{16}cm^{-2}$)	ID	YSO type	Ref
[1]	[2]	[3]		[4]			[5]		[6]		[7]		[8]		[9]	[10]	[11]	[12]	[13]	[14]
4		35^m	0^s	-6^o	21'	7"	0.37	D	0.57	C	3.9	C	16.1	U	3.0	e	0.11			
7	4	34	31	-6	23	22	0.6	U	0.65	E	3.7	E	39	F	11.5	e	1.15			
8	6	33	56	-6	24	7	1.08	D	21.9	A	213	A	601	A	238	p	5.22	L1641-N	O	1
12	8	35	15	-6	25	37	0.37	D	0.36	D	1.94	E	35	U	1.8	e	0.13			
17	9	33	4	-6	26	22	3.07	C	5.0	U	22	U	16	U	7.8	e	1.20			
18	11	33	58	-6	26	37	0.70	D	3.00	D	15.0	C	200	F	58.5	e	3.77	MSSB-8	O	2
22		34	36	-6	27	15	0.2	F	0.33	E	3.0	E	10	F	4.0	e	0.27			
25	12	33	3	-6	28	37	1.15	A	8.60	A	36.0	A	101	A	44.3	p	2.52	V801 Ori	T	3
26		35	17	-6	30	22	1.31	C	2.16	A	10.8	B	18	E	11.4	e	0.19			
27	13	35	3	-6	31	52	0.73	E	0.90	D	6.2	E	43	U	5.0	e	0.20			
29		33	39	-6	33	37	3.92	A	4.88	A	26.5	B	57.4	C	32.2	e	2.61			
30		35	52	-6	33	52	1.28	C	1.26	D	6.3	C	12	H	7.8	e	0.00			
31	16	34	37	-6	35	7	1.07	B	1.07	B	4.9	U	37	U	2.8	p	1.60	BE Ori	T	3
32	17	34	15	-6	35	37	0.33	A	0.76	B	4.8	U	110	U	1.3	p	1.04	V846 Ori		4
33	18	34	52	-6	36	37	1.06	C	1.07	D	4.0	F	20	F	8.6	p	0.63	BF Ori	T	3
34	19	33	16	-6	37	37	0.22	F	0.36	D	6.8	D	18	U	4.2	e	1.30			
36	22	34	11	-6	39	52	5.58	A	6.05	B	18.0	C	120	D	48.4	e	0.53	MSSB-18	O	2
37	23	34	4	-6	40	37	5.87	A	8.12	A	13.2	E	192	U	20.7	e	0.99			
39	25	32	42	-6	42	15	0.30	D	0.32	E	3.0	C	37	U	2.3	e	0.64			
41		32	32	-6	42	37	0.24	D	0.3	C	2.47	B	11	H	4.2	p	0.65			
42	26	34	27	-6	43	22	0.40	F	0.9	F	7.6	G	32.0	D	11.8	p	1.01			
44		32	54	-6	43	52	1.14	B	1.56	B	5.7	B	11.8	F	7.5	e	0.43			
46	27	35	20	-6	44	7	2.10	A	2.92	A	5.0	D	20.2	D	11.7	p	0.27	HD 37357		4
47	28	33	58	-6	44	37	8.58	B	7.35	C	27.0	C	150	U	31.9	p	3.92	V380 Ori	OA	1,3
49	30	33	30	-6	45	7	0.96	B	1.94	B	29.7	A	155	B	51.9	p	2.93			

TABLE 2.1. - *Continued*

No	SN	α (1950)		δ (1950)			f_{12}		f_{25}		f_{60}		f_{100}		L_{FIR}	p-e	$N(^{13}CO)$	ID	YSO	Ref
[1]	[2]	[3]		[4]			[5]		[6]		[7]		[8]		[9]	[10]	[11]	[12]	[13]	[14]
50	31	33	58	-6	46	22	1.80	C	10.0	H	60.0	B	280	B	99.6	p	4.90			
51	32	33	56	-6	47	7	0.70	D	5.00	E	80.7	C	262	A	97.5	p	4.66	MSSB-21	O	2
53		34	44	-6	48	45	2.40	B	3.98	A	9.2	D	37.8	U	10.9	e	0.63			
56	33	35	24	-6	48	52	0.38	U	0.59	C	3.13	C	14.6	U	2.0	p	0.83			
62	34	35	41	-6	50	52	2.82	A	3.11	A	7.1	B	55.9	A	22.6	p	0.99			
65		35	14	-6	53	15	0.85	U	0.85	U	5.3	C	10.0	D	4.3	e	0.14			
68		34	38	-6	55	45	1.70	A	2.37	A	7.4	D	23.3	U	7.9	e	0.46			
70		33	15	-6	58	22	0.34	E	1.1	F	8.3	A	56.0	B	18.1	e	0.21			
71	35	35	29	-6	58	22	0.24	U	0.51	C	5.3	C	12	H	5.1	p	1.75	T456		4
72	37	34	59	-6	59	52	0.74	C	1.34	B	2.4	D	34	U	3.2	p	1.64			
73	36	36	16	-6	59	52	2.14	B	5.31	A	20.5	A	44.7	B	24.5	p	0.46			
75	39	36	21	-7	2	22	0.57	C	5.34	A	26.1	A	107	E	39.8	p	1.96	L1641-C	O	1
78		34	43	-7	3	52	0.38	E	0.36	H	4.3	U	7.3	U	1.0	p	1.47			
79	40	35	53	-7	3	52	53.7	A	124	A	169	A	127	A	241	p	1.02	V883 Ori	E	3
81		36	54	-7	7	15	0.51	U	0.39	U	4.5	B	29.6	C	9.0	e	0.59			
83	42	35	44	-7	10	7	0.39	E	0.98	B	4.0	C	21.0	U	3.3	p	2.25	Haro 14a		4
85	44	36	42	-7	12	7	0.5	D	3.11	A	9.6	C	20	H	10.8	p	0.87			
87	*	36	41	-7	12	37	0.49	C	2.93	A	9.6	C	18	H	10.2	p	0.80			
89	47	36	18	-7	14	7	2.22	B	3.18	B	3.1	C	44.1	U	6.9	p	0.66	Haro 2-249	T	1
91		34	19	-7	16	22	0.21	U	0.43	D	1.3	E	11.8	E	3.7	e	0.85			
95	49	36	30	-7	18	7	1.05	B	3.57	B	9.8	B	46.0	U	8.9	p	0.33	V599 Ori		4
96		36	8	-7	18	22	0.89	B	1.42	A	8.3	B	23.4	C	10.9	e	1.36			
97		37	12	-7	20	22	0.29	D	0.31	D	2.0	E	15.2	E	5.1	e	0.75			
99	51	36	26	-7	22	37	0.79	D	1.43	C	5.3	C	18	H	8.4	p	1.75			
101	52	37	25	-7	24	52	0.54	U	0.50	E	3.9	U	15.1	U	0.5	p	1.20			
102		35	53	-7	25	37	0.88	B	1.28	A	4.8	B	6.1	U	4.7	e	0.73			
104	54	36	56	-7	28	7	0.89	B	4.62	A	68.1	A	123	B	58.2	p	1.83	H4 -255	OT	1,3
105	55	38	2	-7	28	52	29.6	A	88.5	A	182	A	219	A	212	p	1.40	L1641-S	OE	1,3
106	57	36	29	-7	29	7	0.45	U	0.45	D	1.5	U	39.4	U	0.5	p	1.26			

TABLE 2.1. - *Continued*

No	SN	α (1950)		δ (1950)			f_{12}		f_{25}		f_{60}		f_{100}		L_{FIR}	p-e	$N(^{13}CO)$	ID	YSO	Ref
[1]	[2]	[3]		[4]			[5]		[6]		[7]		[8]		[9]	[10]	[11]	[12]	[13]	[14]
108	59	37	27	-7	31	37	0.30	U	8.99	A	129	A	220	A	104	p	1.60	L1641-S3	O	1
113	61	36	44	-7	34	52	1.54	A	2.17	A	6.2	B	14.1	E	9.2	e	0.50			
116		36	55	-7	36	22	0.78	B	1.76	A	5.8	B	11.5	D	7.1	e	0.59			
119	62	38	4	-7	38	52	0.11	U	0.78	B	2.0	D	18.4	U	1.5	p	1.38			
120	63	37	34	-7	39	7	0.45	D	0.81	C	1.4	U	24.7	U	1.5	p	0.76			
123		35	20	-7	39	45	0.74	B	0.84	B	4.7	B	21.6	C	8.7	e	0.20			
124		34	46	-7	39	52	0.34	D	0.22	U	1.2	U	6.9	U	0.9	p	0.54			
133		35	52	-7	44	7	0.2	U	0.57	C	3.0	C	11	D	4.1	e	0.53			
134	67	38	1	-7	44	37	0.2	U	0.43	D	2.1	D	10	U	1.4	p	1.30			
138		35	15	-7	46	52	0.7	D	1.33	B	1.96	C	15.6	U	2.9	e	0.41			
142		36	28	-7	48	7	0.48	B	0.50	C	4.7	A	37.1	C	12.0	e	0.49			
146	68	37	55	-7	49	52	0.98	B	3.87	A	9.7	B	9.5	U	8.9	p	1.22			
149	69	36	11	-7	51	52	0.13	C	0.31	C	1.5	D	9.6	U	1.2	p	0.20	Haro 7-1	T	3
150	70	38	58	-7	51	52	0.18	C	0.60	C	1.0	E	38.7	U	1.2	p	1.07			
154		35	10	-7	54	37	0.59	C	0.67	D	1.65	E	15.0	F	5.6	e	0.56			
158		38	24	-7	56	15	0.2	U	0.26	U	1.1	D	7.0	U	0.6	p	1.18			
160	72	39	1	-7	56	22	0.37	B	3.44	B	13.1	A	30.9	E	14.8	p	1.23			
161		34	46	-7	57	22	0.18	U	0.32	E	2.2	C	37	C	10.3	e	0.39			
162		36	9	-7	57	52	0.90	B	0.42	D	0.6	H	1.9	U	1.9	e	0.16			
163	73	37	57	-7	57	52	0.96	B	2.48	A	5.6	A	16.2	E	8.9	p	0.90			
168	74	38	59	-7	59	22	0.36	C	0.95	A	3.5	U	32.5	U	1.5	p	1.42			
171	76	40	2	-8	0	7	0.48	C	0.98	B	2.08	D	20	U	2.4	p	0.10			
172		34	17	-8	0	22	0.20	D	0.21	C	0.7	D	10.0	U	0.8	p	0.17			
173		35	20	-8	0	37	0.21	D	0.20	E	2.1	D	8.1	F	3.2	e	0.40			
177	78	38	16	-8	1	52	0.2	U	0.32	C	1.9	D	10.0	U	1.2	p	1.43			
178	77	39	26	-8	1	52	0.80	B	1.69	B	4.9	A	10.0	U	4.8	p	0.93	Haro 7-2	T	3
180		36	32	-8	2	15	0.4	U	0.3	U	7.8	B	52.0	B	15.8	e	0.35			
181	79	39	3	-8	2	22	0.2	U	0.41	C	2.8	U	28.7	U	0.4	p	1.15			
186	81	39	7	-8	5	7	0.89	B	3.18	B	8.2	D	8.7	U	7.6	p	1.35			

TABLE 2.1. - *Continued*

No	SN	α (1950)		δ (1950)			f_{12}		f_{25}		f_{60}		f_{100}		L_{FIR}	p-e	$N(^{13}CO)$	ID	YSO	Ref
[1]	[2]	[3]		[4]			[5]		[6]		[7]		[8]		[9]	[10]	[11]	[12]	[13]	[14]
187	82	38	15	-8	5	22	2.09	A	4.72	A	3.0	H	13.2	U	7.5	p	1.07			
191	83	39	2	-8	7	7	1.87	A	3.62	A	6.0	C	7.0	U	8.1	p	1.59	DL Ori	T	3
193		38	27	-8	7	37	0.57	D	2.19	D	15	H	25	H	13.5	p	1.52			
194	85	38	27	-8	8	7	0.60	D	1.80	D	12	H	20	H	11.1	p	1.37	L1641-S4	O	1
196	86	38	1	-8	8	52	0.4	B	0.6	B	0.78	C	28	U	1.4	p	0.70	Haro 7-4	T	3
198	87	39	12	-8	9	37	0.27	C	1.34	C	2.2	C	11.2	E	4.7	p	1.56			
211	91	37	58	-8	15	37	0.46	B	1.14	A	2.7	C	8.4	E	4.4	p	0.68			
216	93	40	22	-8	18	22	0.94	B	4.41	A	15.1	B	50.0	F	21.7	p	0.42	L1641-S2	O	1
217		38	42	-8	18	45	0.21	U	0.40	B	1.6	B	3.4	D	1.6	e	0.91			
224	94	39	21	-8	22	52	0.37	C	0.62	B	1.0	D	10.5	U	1.5	p	0.91			
228		45	19	-8	28	52	0.13	E	0.10	U	0.28	D	9.1	U	0.4	p	0.00			
229	95	40	46	-8	30	37	0.13	F	0.52	B	1.1	E	5.4	U	1.1	p	0.29			
232	98	40	33	-8	33	52	0.24	U	0.48	D	1.6	D	2.4	H	1.4	p	0.30			
233		40	44	-8	33	52	0.17	U	0.19	E	0.8	U	5.0	U	0.2	p	0.20			
234	97	40	10	-8	34	7	0.16	U	0.23	D	1.0	C	11.3	E	3.3	p	0.54			
235		42	58	-8	35	7	0.21	D	0.21	U	1.1	U	23.8	U	0.5	p	0.29			
237	99	39	11	-8	36	37	0.40	C	1.97	A	5.3	B	15	H	7.3	p	0.62			
240	100	39	19	-8	38	22	0.35	B	0.50	E	0.5	U	7.3	U	1.1	p	0.63			
242		42	11	-8	39	7	0.09	U	0.35	E	0.2	U	8.0	U	0.4	e	0.32			
243	101	40	24	-8	39	52	0.80	A	1.20	E	1.4	E	10	H	4.9	p	0.95			
245	103	40	24	-8	41	22	0.70	A	1.33	A	1.9	B	10	H	5.0	p	0.99			
246	104	39	7	-8	41	37	0.26	D	0.73	B	3.5	B	16.8	B	6.2	p	0.70			
250		41	31	-8	43	22	0.12	U	0.12	U	0.48	E	17	F	4.5	e	0.48			
251	105	39	8	-8	44	22	0.22	U	0.99	B	4.1	C	19.6	U	2.8	p	0.48			
252		39	39	-8	44	37	0.28	C	0.17	U	0.8	U	10.3	U	0.7	p	0.43			
256	106	40	45	-8	45	37	0.17	U	0.77	B	4.0	B	15.5	A	5.7	p	0.97			
257		43	15	-8	46	52	0.12	U	0.14	U	0.7	C	4.6	H	1.4	e	0.19			
258	107	40	46	-8	47	22	0.14	U	0.40	B	3.2	D	15.8	D	5.3	p	0.16			
261		40	5	-8	51	45	0.16	U	0.12	U	0.4	D	6.9	E	1.9	e	0.64			

TABLE 2.1. - *Continued*

No	SN	α (1950)		δ (1950)			f_{12}		f_{25}		f_{60}		f_{100}		L_{FIR}	p-e	$N(^{13}CO)$	ID	YSO	Ref
[1]	[2]	[3]		[4]			[5]		[6]		[7]		[8]		[9]	[10]	[11]	[12]	[13]	[14]
264	108	38	15	-8	54	45	0.16	E	0.22	E	1.5	C	6.8	A	2.6	p	0.00			
266	110	37	32	-8	58	7	0.41	C	0.2	H	0.7	U	7.7	U	0.8	p	0.10			
267	111	38	49	-8	58	45	0.10	U	0.36	B	6.2	A	7.8	D	4.3	p	0.34			
270	113	38	33	-9	7	22	0.95	B	2.14	A	1.9	D	8.3	E	5.4	p	0.64			
276	114/ 115	38	23	-9	20	52	6.15	F	10.0	U	30.0	E	185	F	72.0	e	0.42			
277	116	39	5	-9	21	45	0.99	B	1.71	A	5.9	C	86.9	A	26.5	e	0.44			
280	118	38	44	-9	24	37	0.79	B	3.04	A	19.1	B	40	E	19.5	p	0.09			
281	119	38	13	-9	29	37	1.71	B	1.47	B	7.5	U	105	U	4.2	e	0.34			
288	123	37	52	-9	43	37	0.88	A	1.70	A	1.2	D	9.0	U	2.9	p	0.19	V350 Ori	T	3
289		40	27	-9	46	22	0.2	D	0.5	D	0.5	U	6.7	U	0.8	p	0.48			

Note: column [1] gives the source number; [2] is the corresponding number in Strom's catalog (Strom et al. 1989b); [3] and [4] are the coordinates of the sources at 1950 epoch; [5]-[8] are the source flux densities at 12, 25, 60 and 100 μm respectively. If there is no detection, a 5 σ upper limit is given with a flag U; The uncertainty of the fluxes are flagged in the following convension: A, 4%; B, 4-8%, C, 8-12%; D, 12-16%; F, 20-50%, G, 50%; and H, 100%; [9] is the far-infrared luminosity integrated from 7 μm to infinity in solar units; [10] indicates source type: p for point source and e for extended source; [11] gives the ^{13}CO column density toward the source; [12] gives source identification(1989); [13] shows if the source is associated with a known YSO: O for outflow, A for Ae or Be star, T for T Tauri star, and E for emission-line star; [14] gives references as follows: (1) Fukui (1989), (2) Morgan et al. (1991), (3) Herbig & Bell (1988) and (4) Strom et al. 1989b.

TABLE 2.2. SPATIAL DISTRIBUTIONS OF THE SOURCES

	Point Source	Extended Source	Total
Inside the L1641	79	43	122
Outside the L1641	20	82	102
Total	99	125	224

TABLE 2.3. PHYSICAL PARAMETERS OF SOURCES INSIDE L1641

Groups	No. of Sources	L_{FIR} ($L_\odot$)	$N(^{13}CO)$ (10^{16} cm^{-2})	T[12,25] (K)
Outflow Sources	11	81.0	2.5	138
T Tauri Stars	9	9.7	1.0	174
Other Sources	102	6.4	0.7	181

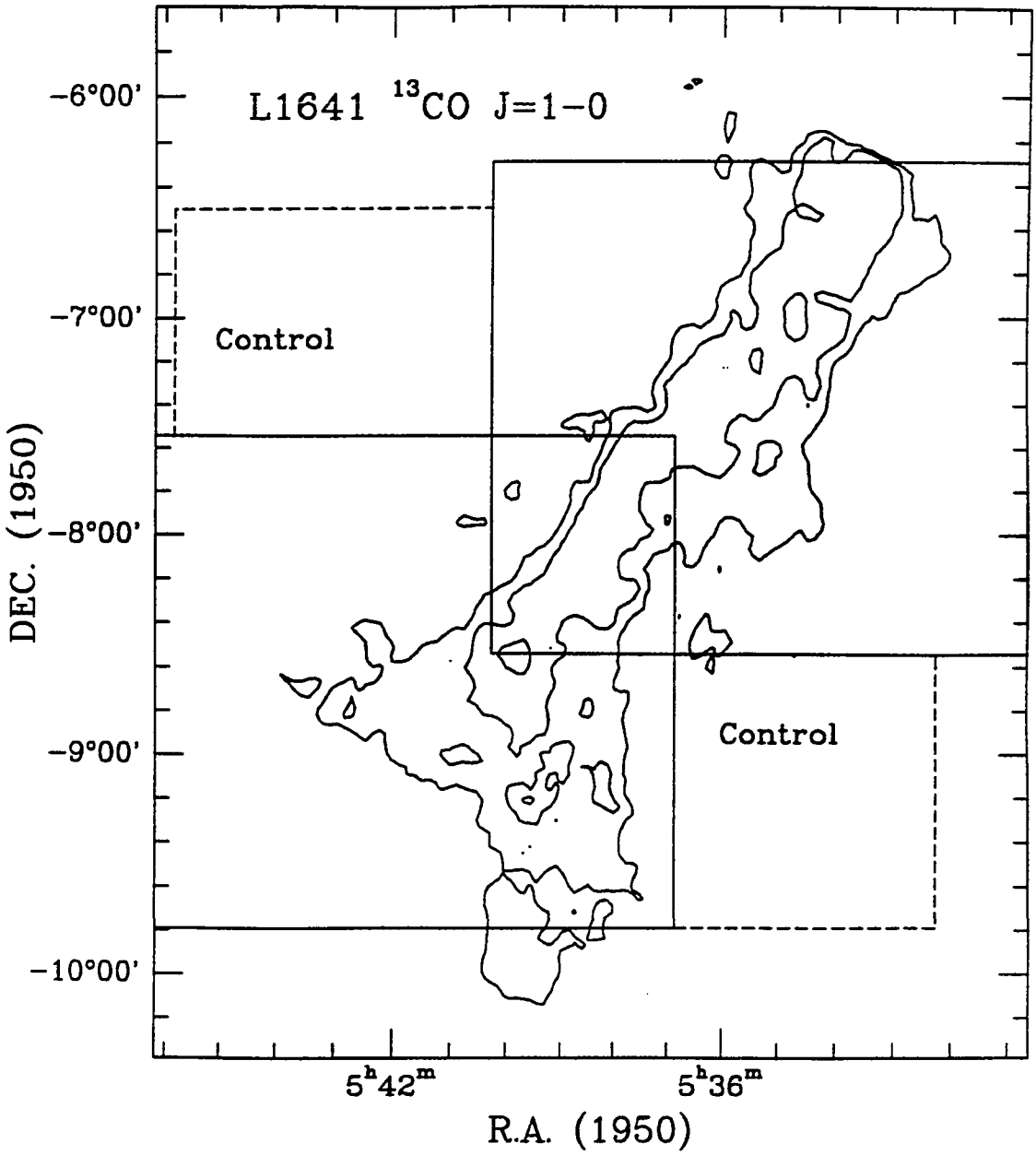

Figure 2.1 The molecular cloud L1641. The contours represent the distribution of the integrated intensity of ^{13}CO molecular gas, based on data from Nagoya survey (Fukui and Mizuno 1991). The contour levels are 3.0 and 7.0 K km s^{-1}. Note the contours were artificially cut off at the northern end for simplicity. The solid boxes show the two main regions of the *IRAS* coadded images. Two smaller control areas are shown by the dotted boxes.

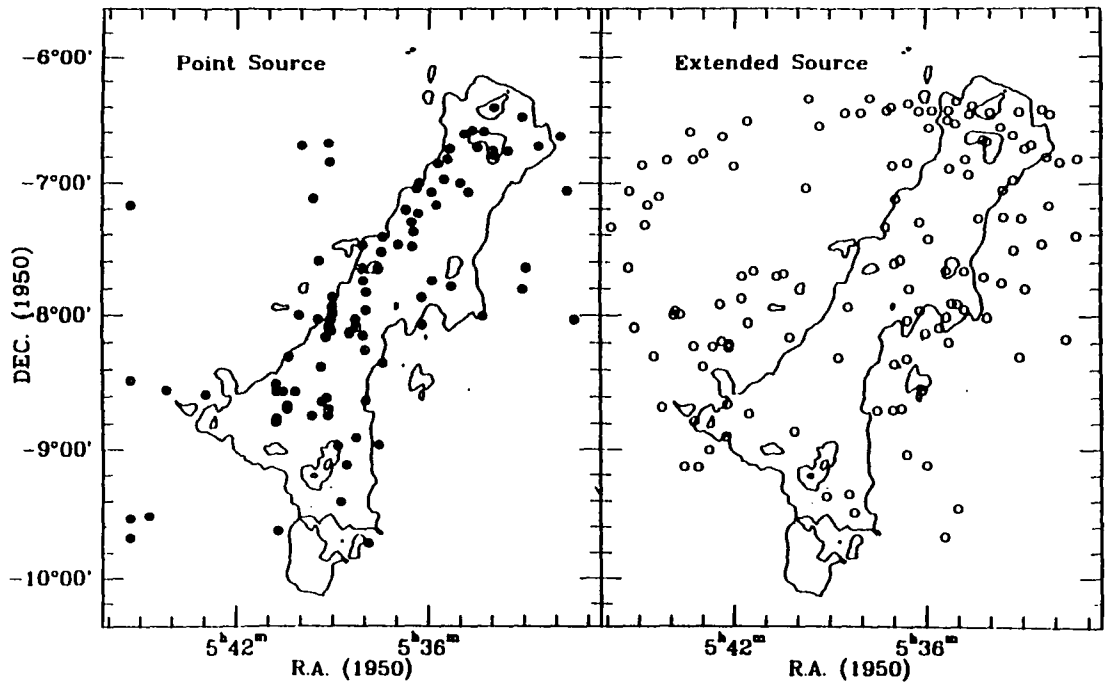

Figure 2.2 *IRAS* sources selected from the coadd images are superimposed on the ^{13}CO integrated intensity map. The point sources (filled circles) and the extended sources (open circles) are shown in the left and right panels, respectively.

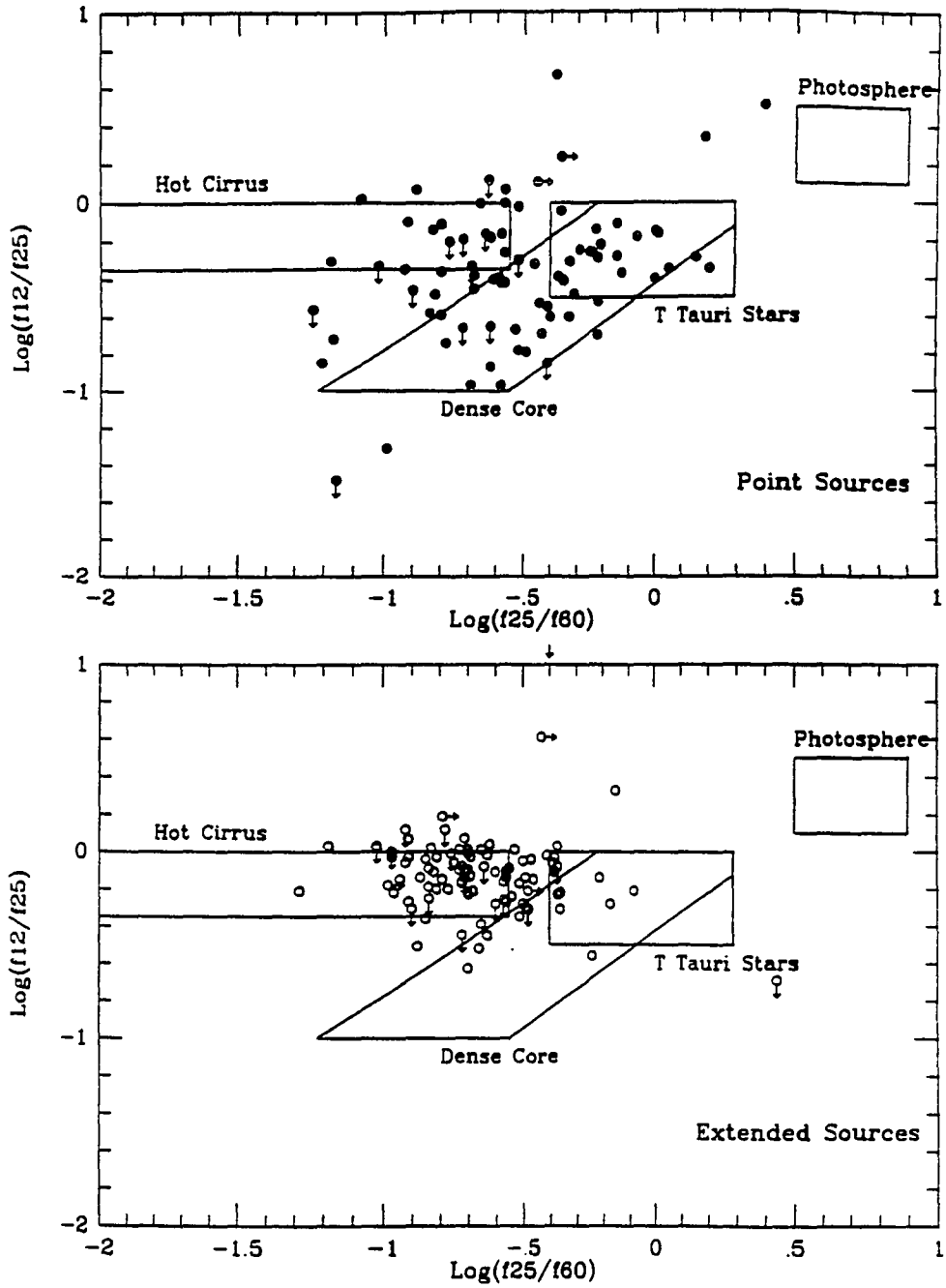

Figure 2.3 The *IRAS* color-color diagram based on 12-25-60 μm flux densities. All the sources plotted here have at least two detections (*SNR* > 5.0) at 12, 25, and 60 μm. The top panel is for the point sources, and bottom one is for the extended sources. The arrows show 5 σ upper limits at 12 μm (vertical arrows) or at 25 μm (horizontal arrows). Following Beichman (1985), the areas that are occupied by various types of sources are indicated.

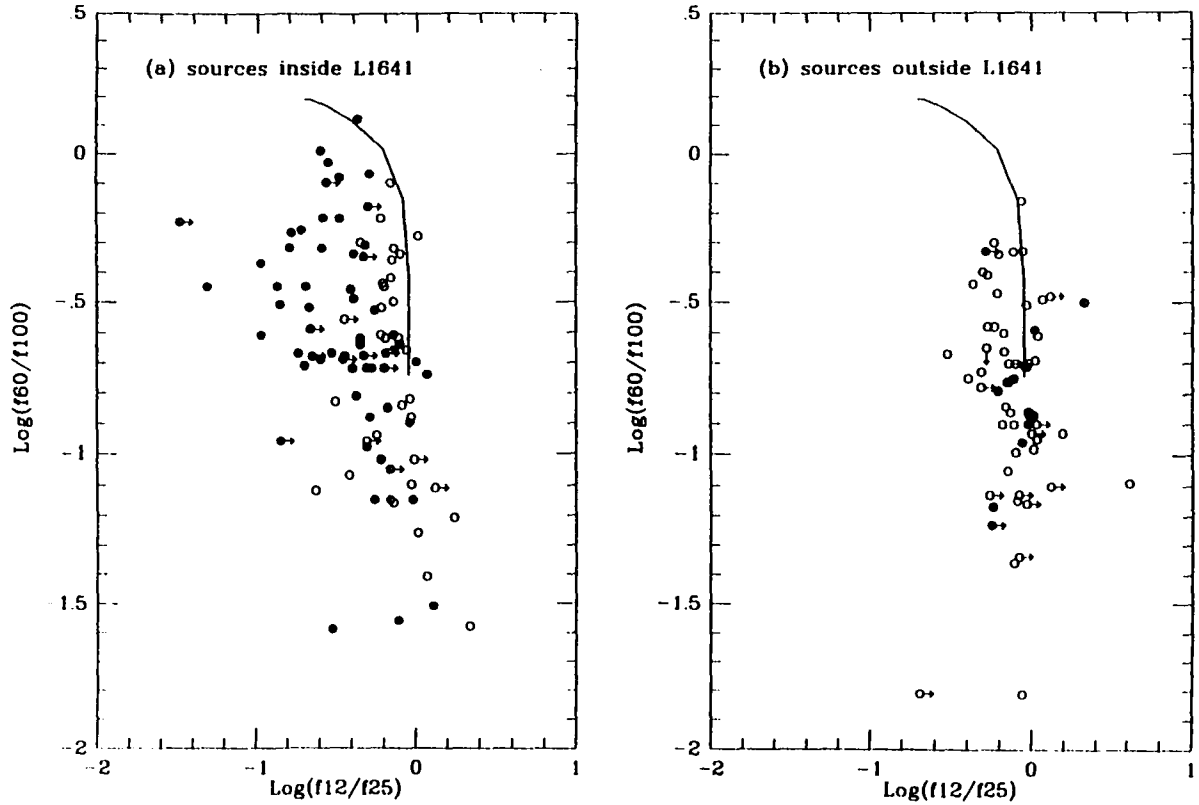

Figure 2.4 The *IRAS* color-color diagram based on 12-25-60-100 μm flux densities. The sources located inside and outside the L1641 are plotted in the left and right panels respectively. The point sources are filled circles and the extended sources are open circles. The solid curves are the expected *IRAS* colors by an analytical model for the small grain emission (Boulanger et al. 1988).

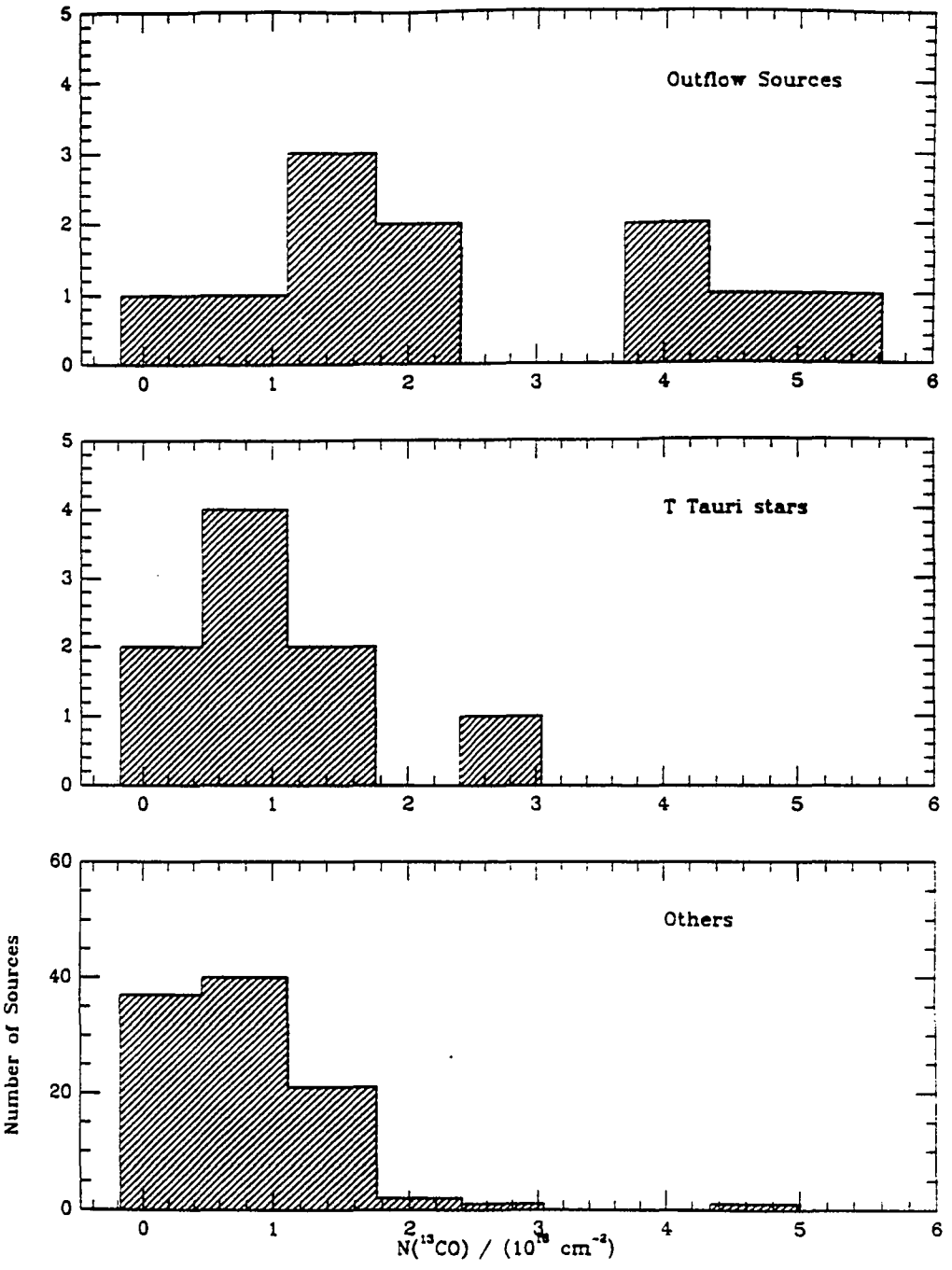

Figure 2.5a The histograms of N(^{13}CO), the ^{13}CO column density. Only the sources that are located inside the L1641 are plotted. Sources are shown in three groups: outflow sources, T Tauri stars and other sources.

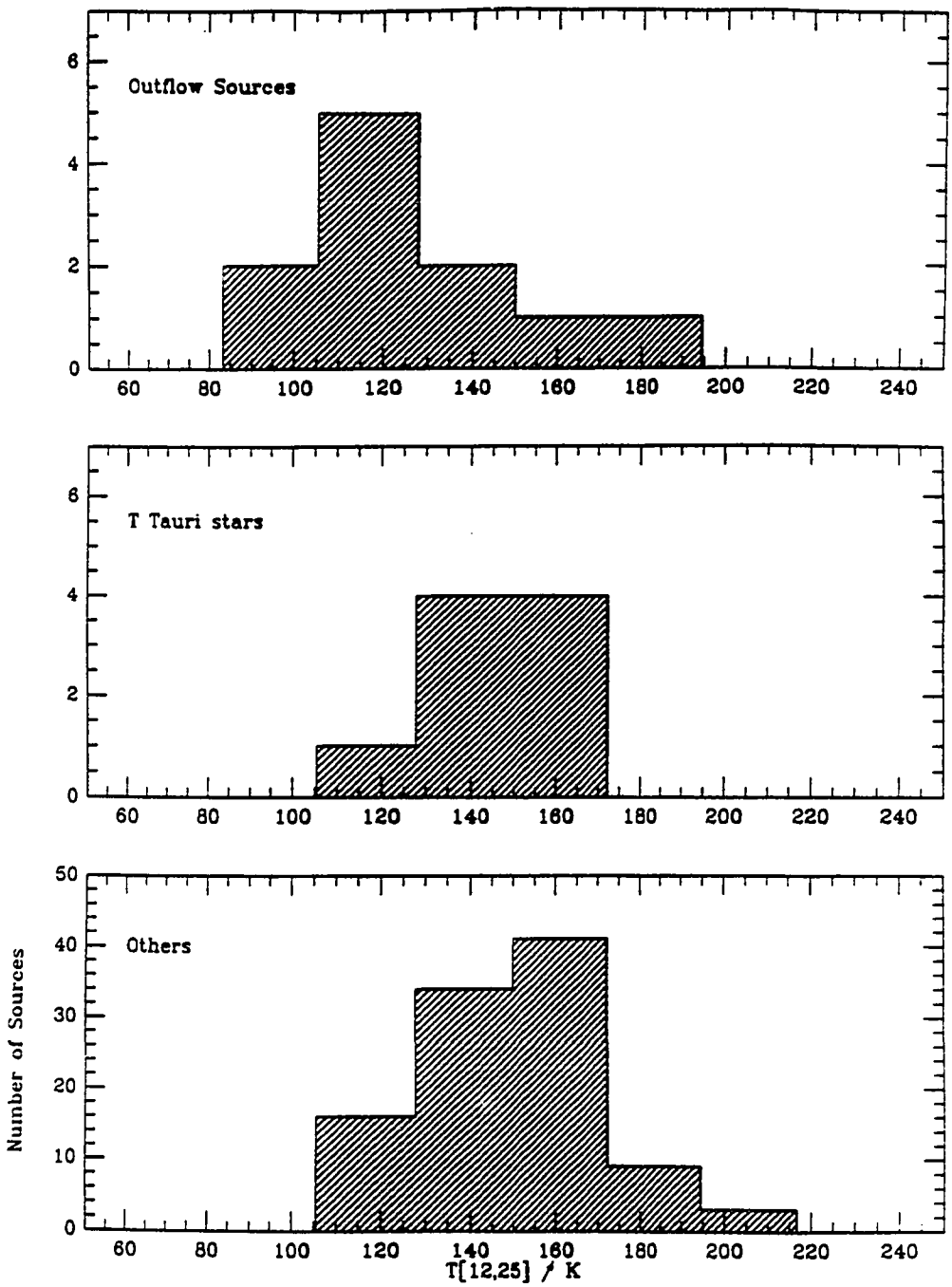

Figure 2.5b The histograms of T[12, 25], the *IRAS* color temperature derived from the 12 and 25 μm flux density ratio. Only the sources that are located inside the L1641 are plotted. Sources are shown in three groups: outflow sources, T Tauri stars and other sources.

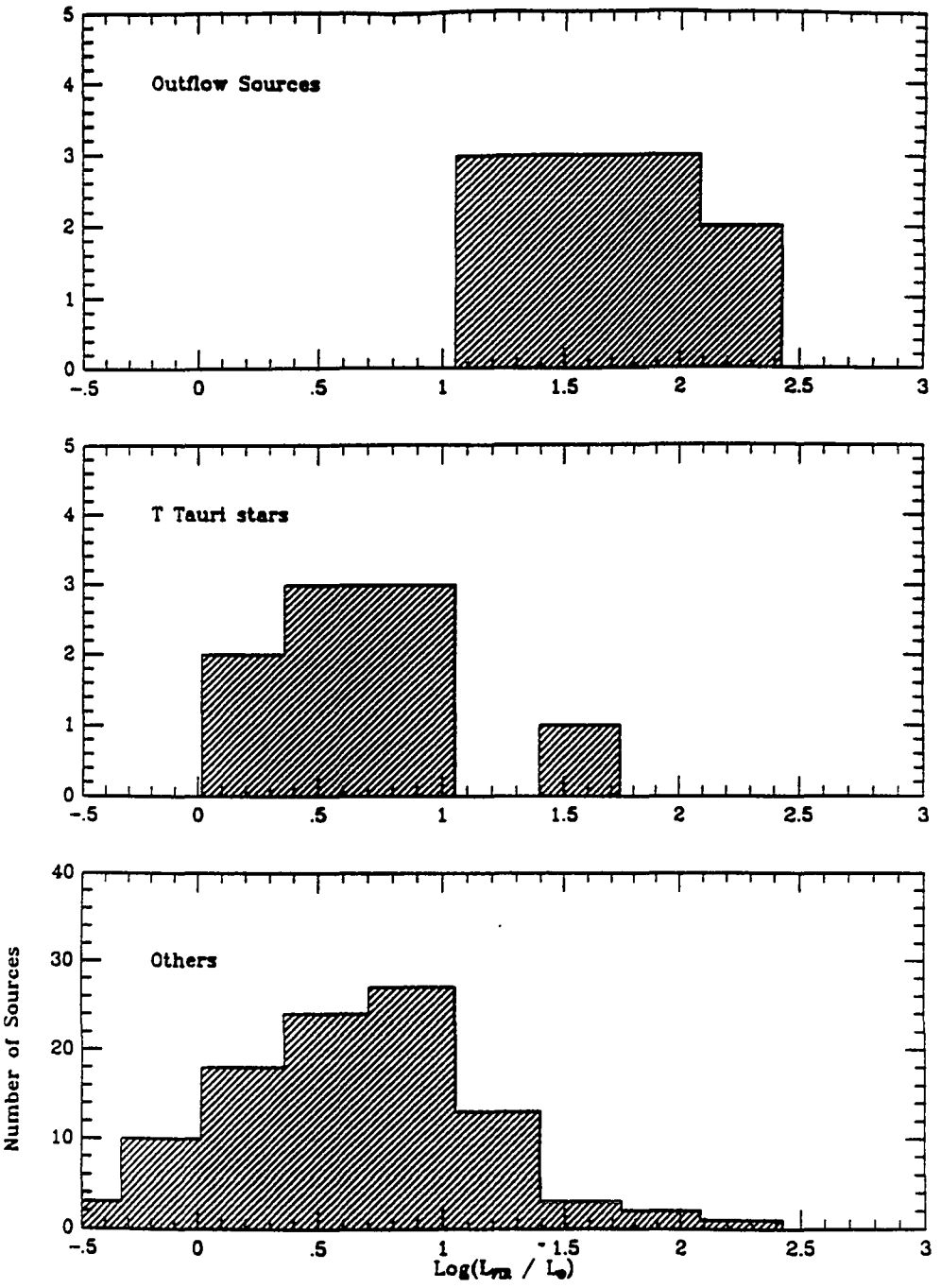

Figure 2.5c The histograms of L_{FIR}, the Luminosity derived from the IRAS observations. Only the sources that are located inside the L1641 are plotted. Sources are shown in three groups: outflow sources, T Tauri stars and other sources.

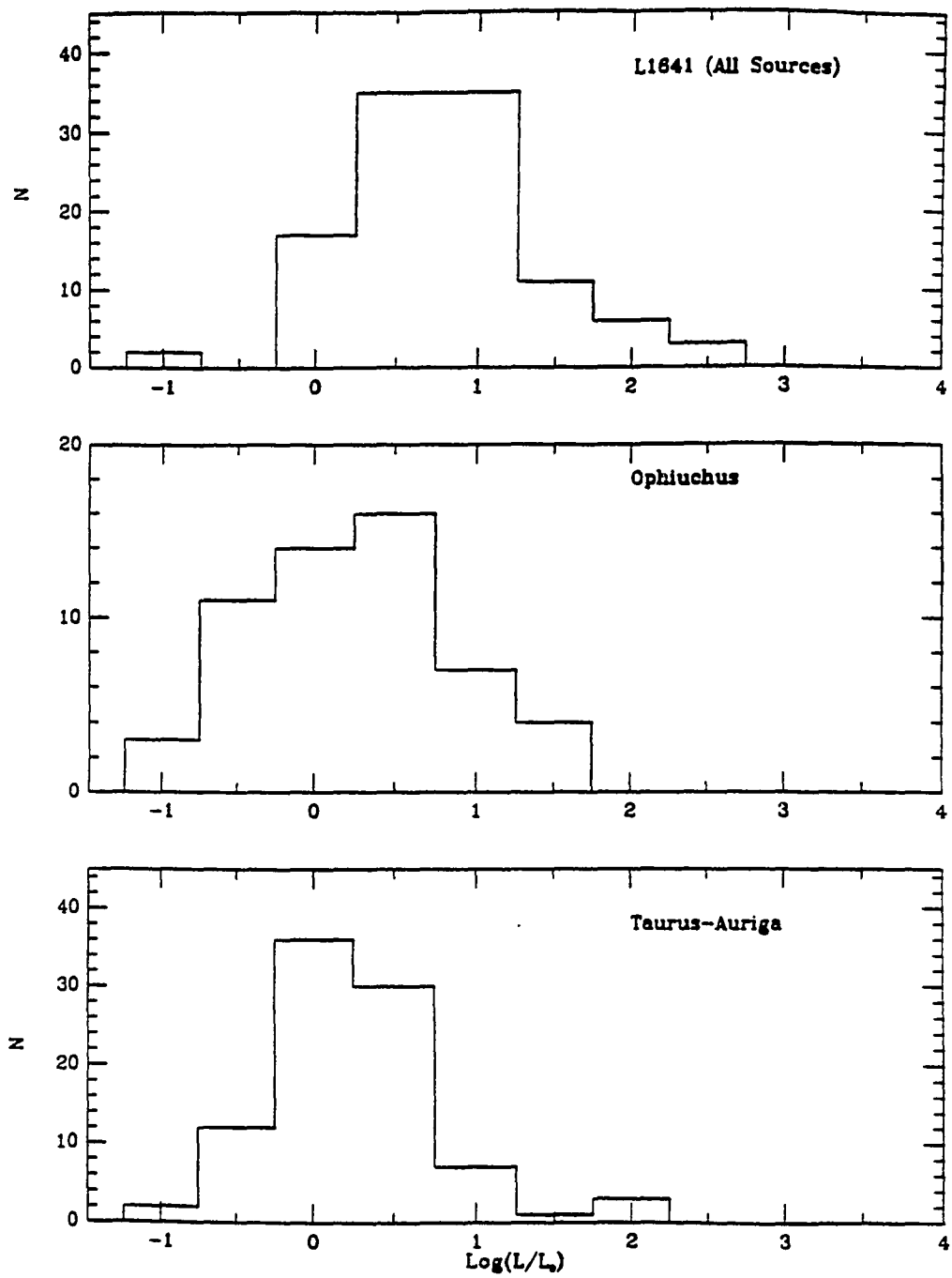

Figure 2.6 The luminosity distributions of *IRAS* sources in L1641 (all the sources inside molecular cloud), in Oph (Wilking, Lada & Young 1989), and in Taurus-Auriga (Kenyon et al. 1990).

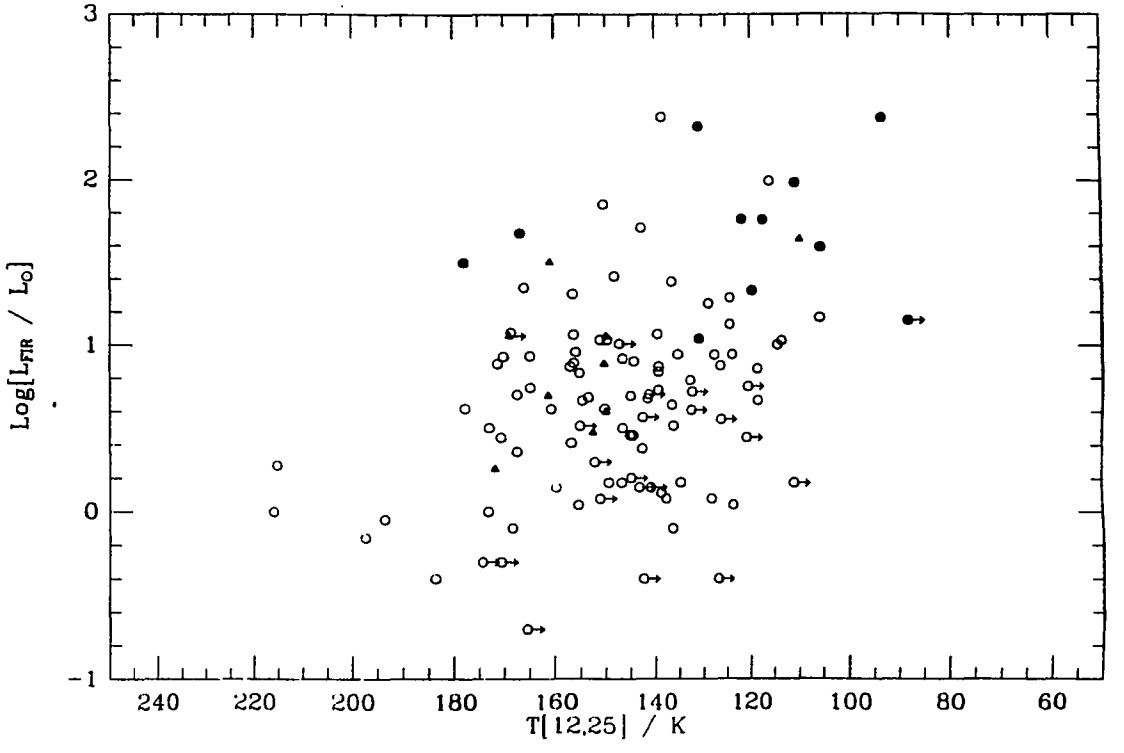

Figure 2.7a Comparison of the indicators of the evolutionary states. T[12,25] vs. L_{FIR} The outflow sources are indicted by the filled circles, T Tauri stars are the triangles, and the other sources are denoted by the open circles. The arrows show the 5 σ upper-limits.

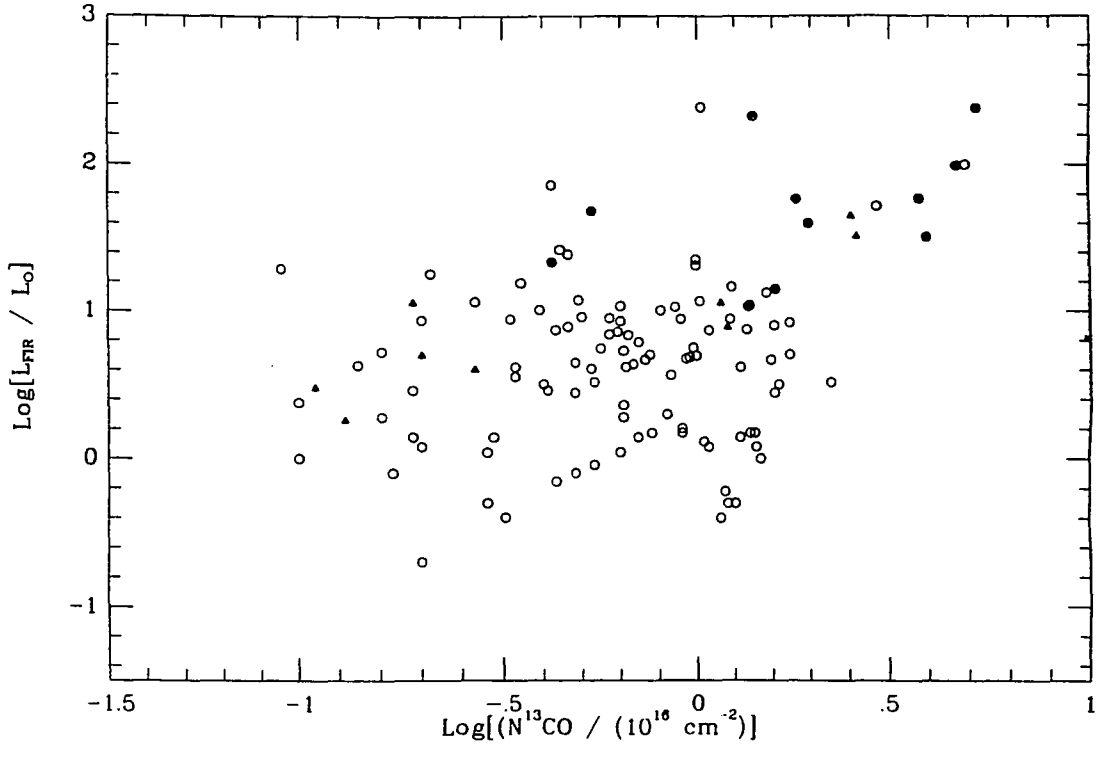

Figure 2.7b Comparison of the indicators of the evolutionary states. $N(^{13}CO)$ vs. L_{FIR}. The outflow sources are indicted by the filled circles, T Tauri stars are the triangles, and the other sources are denoted by the open circles. The arrows show the 5 σ upper-limits.

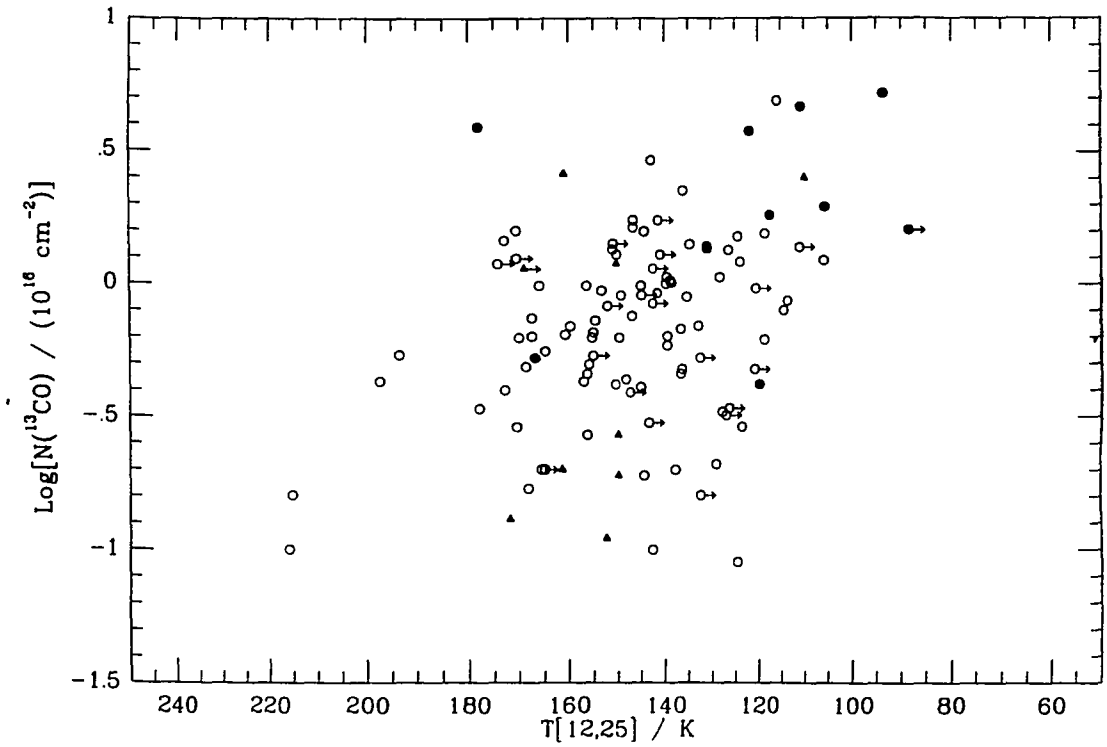

Figure 2.7c Comparison of the indicators of the evolutionary states. T[12,25] vs. $N(^{13}CO)$. The outflow sources are indicted by the filled circles, T Tauri stars are the triangles, and the other sources are denoted by the open circles. The arrows show the 5 σ upper-limits.

CHAPTER 3
DENSE CORE DISSIPATION[1]

3.1. INTRODUCTION

As reviewed in Chapter 1, it is now well-known that low-mass young stellar objects (YSOs) are being formed inside dense molecular cores, and many of them are associated *IRAS* sources (Myers & Benson 1983, Beichman et al. 1986). A natural outcome of the best-known star formation theory (Shu, Adams & Lizano 1987) is that a YSO will gradually change its molecular environment at the early stage of its formation. This makes it of interest to study the evolution of the molecular dense cores. We want to understand when and how the dense molecular cores are dissipated.

The YSO-dense core association can be studied by (1) searching for *IRAS* sources in a sample of dense molecular cores, or (2) searching for dense cores in a sample of *IRAS* sources. Using the first approach, Beichman et al. (1986) found that nearly 50% of the NH_3 dense cores were associated with *IRAS* sources. A statistical study of infrared properties of these sources suggested that some of them are probable protostars in nature. The same conclusion was reached by Fukui et al. (1989) in a study of *IRAS* sources in L1641 (Fukui et al. 1989). The second approach, which we use throughout this chapter, allows us to compare the molecular gas distribution adjacent to various types of *IRAS* sources, and therefore yields some insight into the evolution of the cores during star formation.

---

[1] Part of this work was carried out under common use observation program at the Nobeyama Radio Observatory (NRO). NRO, a branch of the Tokyo Astronomical Observatory, University of Tokyo, is a cosmic radio observing facility for outside users.

CO is the most abundant molecule that has emission line at millimeter wavelengths. Unfortunately, CO J = 1-0 is always optically thick in typical dense molecular cores. The optical depth of the ^{13}CO J = 1-0 transition is much smaller than that of the CO line, allowing us to probe the gas distribution. Although ^{13}CO J = 1-0 may also be saturated at the center of the dense cores, we can use it to study the more extended (~ pc) outer region of the core. The HCO^+ J = 1-0 transition is a much better probe of dense molecular gas. Because the molecule has a much larger dipole moment (4.48 debye, compared to 0.11 debye for ^{13}CO), its collisional excitation requires a much higher gas density (10^{4-5} cm^{-3}) even if the photon trapping is taken into account. The high excitation density of HCO^+ ensures that the line emission comes only from the dense region near the peak of the core, so that the foreground and background contamination can be minimized.

In this chapter, we present two sets of millimeter observations to study the association of molecular gas with *IRAS* sources: (1) a moderate spatial-resolution (2'.7) ^{13}CO mapping of 40 *IRAS* sources with Nagoya 4 m telescope (Nagoya observations, hereafter) and (2) a high-resolution (~20") ^{13}CO and HCO^+ mapping and five-point observations of 28 *IRAS* sources with Nobeyama 45 m telescope (Nobeyama observations). We explain in section 3.2 the details of the observations and data reductions. In section 3.3, we present the results of mapping the *IRAS* sources. We also study the correlation of the molecular column densities with the *IRAS* color. The implications of these results are discussed in section 3.4 with an emphasize on molecular core dissipation. Major conclusions are summarized in section 3.5.

3.2. OBSERVATIONS

3.2.1. *Source Selection*

For Nagoya observations, we selected a sample of 40 *IRAS* sources from Table A1. It includes 9 *IRAS* sources with CO outflows and the other 31 sources randomly selected from Table A1. The sample was selected so that we could study the molecular gas distribution around different types of the *IRAS* sources. The sources are listed in Table 3.1.

For Nobeyama observations, we selected 28 sources from Table A1. The selection was not intended to be statistically complete; the choice of sources was made to achieve a broad range of the *IRAS* colors and *IRAS* luminosities to search for correlation with dense molecular gases. The sources are listed in Table 3.2.

Figure 3.1 shows the spatial distribution of the sources of both samples, superposed on a ^{13}CO integrated intensity map obtained from the Nagoya ^{13}CO survey (Fukui & Mizuno 1991). The strong concentration of the *IRAS* sources within the ^{13}CO integrated intensity contour of ~3 K km s^{-1} suggests that most of these sources are physically associated with the L1641. In the following discussion, for simplicity, the *IRAS* sources that are associated with CO molecular outflows will be referred to as "outflow sources," and sources that have no indication of CO outflow as "nonoutflow sources."

3.2.2. *Observations*

The Nagoya observations were carried out using the 4 m telescope at Nagoya University in March-April, 1989. We employed a SIS receiver with a system temperature of about 400 K at 110 GHz toward the zenith. The half-power beam width

of the telescope is about 2'.7 at this frequency. The acoustic-optical spectrometer has a velocity coverage of 110 km s^{-1} velocity with a 0.1 km s^{-1} resolution. Each *IRAS* source was mapped in the ^{13}CO J = 1-0 line in a 5 × 5 grid with 2' spacing in R.A. and Declination, centered on its *IRAS* position. A 40 s integration yields a rms noise fluctuation of 0.3 K in antenna temperature. Single-point CO J = 1-0 observations were also made at the *IRAS* position to obtain the excitation temperature of CO molecular gas. During the observations, the telescope was periodically switched to the Orion KL source to check system stability.

The Nobeyama observations were carried out in March-April, 1990 using the 45 m telescope of the Nobeyama Radio Observatory. We observed each source in ^{13}CO (J = 1-0) and HCO^+ (J = 1-0) simultaneously. The observations consisted of two parts. For the first part, a five-point map was made centered on each *IRAS* position with an offset of 20" in both R.A. and Declination. For the second part, we made maps of approximately 3' × 3' for three outflow sources (sources 8, 75, and 104) in a 20" grid. The telescope beamsize was 17" and 20" for the ^{13}CO and HCO^+ transitions, respectively. A SIS receiver was used for the ^{13}CO line with a system temperature of 600 K in a single side band at 110 GHz, and the HCO^+ line was observed using a cooled Schottky receiver with a system temperature of 800 K in a single side band at 89 GHz at zenith. The 2048 channel acoustic-optical radio spectrometers had a spectral resolution of 250 kHz (or 0.65-0.85 km s^{-1}). The calibration for atmospheric and ohmic losses was made by the standard chopper wheel technique. We used position switching with the off positions about 1 degree from the sources. The intensity calibration was made by observing the standard source Ori A. For the pointing calibration, the telescope was pointed to the Ori A SiO maser source every 2-3 hours. The peak-to-peak pointing error was about 7".

3.2.3. *Data Reduction*

The data obtained from Nagoya and Nobeyama observations were both reduced using the Nagoya data reduction system. In Nagoya observations 36 of the 40 sources have positive detections in ^{13}CO. In Nobeyama observations, we detected ^{13}CO emission in all 28 sources. The HCO^+ line was detected in 23 sources. Figure 3.2 displays the typical line profiles obtained in both observations. To associate the molecular emission peak with the *IRAS* sources, we used the spectrum with the strongest line to calculate the line parameters. By fitting a gaussian profile to each selected spectrum, we obtained three parameters: the peak temperature T_p, the line width (FWHM) Δv, and the line center V_{LSR}. The line parameters of their associated *IRAS* sources are presented in Table 3.1 and Table 3.2.

Appendix A2 shows how we calculated the column densities of ^{13}CO and HCO^+ using these parameters. Assuming (1) CO is optically thick and ^{13}CO is optically thin, and (2) the two transitions have the same excitation temperature ($T_{ex}(CO) = T_{ex}(^{13}CO)$), from equation (A2.9) the column density of ^{13}CO can be calculated as:

$$N(^{13}CO) = 2.49 \times 10^{14} \frac{T_{ex}\, \tau_0{}^{13}\, \Delta v_{13}}{1 - \exp(-5.31/T_{ex})} \qquad (cm^{-2}) \qquad (3.1)$$

where T_{ex} is the excitation temperature of ^{13}CO molecular gas that can be obtained using the above assumptions, and Δv_{13} is the linewidth (FWHM) of ^{13}CO. The optical depth at the ^{13}CO line peak, $\tau_0{}^{13}$, can be obtained by using the observed peak temperatures of CO and ^{13}CO. Although the CO data were obtained using the 4 m telescope, they can still be incorporated with both moderate- and high-resolution ^{13}CO

observations because CO distribution is much more extended and uniform than the ^{13}CO gas distribution.

If the HCO^+ J = 1-0 line is optically thin, equation (A2.10) gives HCO^+ column density:

$$N(HCO^+) = 1.87 \times 10^{11} \frac{T_{ex}\, T_p\, \Delta v}{1 - \exp(-4.3/T_{ex})} \quad (cm^{-2}) \qquad (3.2)$$

where T_p and Δv are the peak temperature and FWHM of the HCO^+ line, respectively. The HCO^+ excitation temperature T_{ex} is more difficult to determine, and it is likely different from the CO excitation temperature. Fortunately, the HCO^+ column density is not very sensitive to the excitation temperature. Using the *LVG* model (Goldreich & Kwan 1974), we found that for the T_{ex} = 10-20 K, the calculated column density changes only by a factor of 2. We therefore assume a constant T_{ex} = 15 K. The column densities of ^{13}CO and HCO^+ calculated from equations (3.1) and (3.2) are listed in Table 3.1 and 3.2 as $N(^{13}CO)$ and $N(HCO^+)$, respectively.

3.3. RESULTS

3.3.1. *^{13}CO Maps of 40* IRAS *Sources*

As shown in equations (3.1) and (3.2) the column density of molecules is proportional to the integrated intensity (~Tp Δv). We can use the map of the integrated intensity to illustrate the spatial distribution of the molecular gas. In this section, we first discuss the moderate-resolution ^{13}CO maps of 40 *IRAS* sources, and then, in the next section, the high-resolution HCO^+ maps of 3 sources.

For each of the 40 sources mapped in ^{13}CO with Nagoya telescope, we constructed an integrated intensity contour map. The map is centered on the *IRAS* position, and covers a field of ~10' x 10'. The geometry of the maps shows great diversity, from well-defined cores to no systematic structure. To illustrate these results, we classified these contour maps into three categories according to the distance between the *IRAS* sources and the corresponding ^{13}CO emission peaks: (1) inside core (IC): mapfield has a well-defined core and the distance between the peak of the core and the *IRAS* source is smaller than the beamsize of the telescope (2'.7); (2) outside core (OC): a map indicates a well-defined core and the *IRAS* source-core distance >2'.7; (3) no core (NC): no obvious structure in the field, or no detectable ^{13}CO line emission. Figure 3.3 shows the typical map from each of the three groups. In all the contour maps, the lowest contour represents 50% of maximum, and contour step is about 2 σ. The geometric classifications are presented in Table 3.1.

Of the 40 sources we have mapped, there are 11 IC sources, 22 OC sources, and 7 NC sources (4 of them have no ^{13}CO detection). Figure 3.4 show the contour maps of the IC sources. 7 of the 9 outflow sources are associated with a well-defined core. In contrast only 4 of 31 nonoutflow sources are associated with a dense core. Two optically visible stars (sources 287 and 288) have very weak ^{13}CO emission and, show no sign of a core.

Because the relatively low excitation density of the ^{13}CO J = 1-0 line, it is important to understand if the emission we detected is from the gas physically associated with the *IRAS* sources or it is just foreground or background emission. Figure 3.5 displays a histogram of $N(^{13}CO)$ for the three groups. It is clear that the three groups have very different $N(^{13}CO)$ distributions. A Kolmogorov-Smirnov test shows that they belong to the different distributions at a >99% confidence level. The IC sources have higher $N(^{13}CO)$, while the NC sources have little ^{13}CO emission. This suggests that most of

the ^{13}CO emission comes from the cores associated with the *IRAS* sources, rather than from the foreground or background gas.

As shown in Figure 3.4, most of the dense cores have a half-maximum size larger than our mapped area (>10', or 1.5 pc at distance of 480 pc). Using the ^{13}CO column density obtained above, we can estimate a lower limit of the core mass on the order of 100 $M_{\odot}$ (since the masses outside our map are not known). These cores are 3-5 times larger and 5-10 times more massive than the ^{13}CO cores in Taurus observed with the same telescope (Ohashi, 1991). This is consistent with the suggestion that the gravity is more important in constraining the molecular gas in L1641, while the magnetic field plays an important role in Taurus (Strom et al. 1989).

3.3.2. *HCO^+ Mapping of 3* IRAS *Sources*

The high-resolution HCO^+ maps of three sources obtained in Nobeyama observations are displayed in Figure 3.6a-c. In all three maps, the lowest contour represents the 40% of the maximum integrated intensity for each source and the contour interval is about 3 σ. In each field, there is a well-defined core located close to the *IRAS* sources position, as indicated by the cross.

The high-resolution maps allow us to characterize the HCO^+ dense cores. We used the minimum and maximum sizes of the half-maximum contour and took a geometrical average of them to derive radius *R*. Two of the three cores (sources 8 and 104) are larger than the 20" beamsize and do not show structure within the cores. Since the core near source 75 shows 2-3 components, only the main component (SW of the *IRAS* position) was calculated. The number density of molecular gas can then be estimated by assuming a uniform core density and HCO^+ abundance. The latter may vary from source to source, depending on kinetic temperature and density of the gases. For the first-order

analysis in this study, we adopted $X(HCO^+) = 10^{-9}$ derived by Wotten, Snell, & Evans (1980) for three dark clouds with $T_K < 20$ K, although it might be too high for L1641-North. The physical parameters of the three cores are summarized in Table 3.3. We now discuss each source in turn.

Source 8 (L1641-North) is one of the brightest and coldest *IRAS* sources in L1641. It is associated with L1641-North, the most powerful outflow in L1641 (Fukui et. al 1986; Wilking, Blackwell, & Mundy 1990). The near-IR imaging shows a young cluster associated with the *IRAS* source (Strom, Margulis, & Strom 1989a; Chen, Tokunaga, & Hodapp 1991). The contour map (Figure 3.6a) shows a structure similar to that seen by Fukui et al. (1988) in their HCO^+ observations. The core is elongated at 45 degrees northeast, along the same direction as the CO outflow. It is interesting that our high-resolution ^{13}CO contour map shows no well-defined core within the 2'-3' field. Considering that the moderate-resolution map does show a well-peaked ^{13}CO core (Fig. 3.3), we argue that the ^{13}CO line is saturated in the central part of the core, and that the ^{13}CO core has a size >3', which is almost 10 times larger than the HCO^+ core. Such a large structure of 7'-8' was in fact mapped in the ^{13}CO emission by Takaba et al. (1986).

The CO outflow (L1641-Center) associated with source 75 was first identified and mapped with the Nagoya 4 m telescope by Takaba (1986). The blue high-velocity wing is dominant, while the red wing is weaker. This outflow is extended over 6' as mapped with the Nagoya 4 m telescope (Fukui et al. 1992). The recent CO J = 2-1 and 3-2 observations also confirmed the existence of the outflow (Sugitani et al. 1992). Morgan et al. (1991), however, argue that the high-velocity wing is due to the multiple velocity components, not the outflow from the embedded source. We suggest that the area mapped by Morgan et al. (1991), 6' × 6', was not large enough to localize the high-velocity emission. The high-resolution map of this study allows us to explore the central region of the dense gas in much more detail. As shown in Figure 3.6b, within the field of

2' × 2', we detected two molecular condensations. The main clump is located 60" W and 40" S of the *IRAS* position. There is also a weaker clump to the east. The near-IR imaging (see Chapter 5) shows sign of young stellar density enhancement near the *IRAS* position. One source showing bipolar nebulosity is located very close to the main clump, while another very red source (detectable only at 3.6 μm) is near the *IRAS* position. The high-resolution map and the IR images suggest multiple YSOs near source 75. Further high-spatial and spectral resolution interferometer observations are clearly needed.

Source 104 has been identified as emission-line star Haro 4-255. There is another far-infrared source (Haro 4-255 FIR) located about 1' to the northwest of Haro 4-255 (Evans, Leverault, & Harvey 1986; Leverault 1988). Both sources are marked on the HCO^+ map in Figure 3.6c. Although the two sources seem to have different color temperatures at 50-100 μm, it is not clear whether they are the same source or two different sources, because the far-infrared emission may be contaminated by the other source. Our integrated intensity map shows a well-defined core; however, the position-velocity map (Figure 3.7) clearly shows two velocity components separated by 2 km s^{-1}. The major component is close to the *IRAS* position, and the secondary component is close to Haro 4-255-FIR. A recent CS emission line survey of L1641 also indicated two components in this region (Tatematsu & Umemoto 1991). In Figure 3.7, the velocity structure of the main component is much more extended than that of the secondary, showing signs of a high-velocity wing. We therefore suggest that both Haro 4-255 and Haro 4-255 FIR are associated with molecular dense gas. The core in which Haro 4-255 is embedded has more extended velocity structure and is probably the driving source of the CO outflow.

3.3.3. *Correlation Study*

The ^{13}CO column density measures the amount of ^{13}CO molecules in the direction of the *IRAS* sources along the line of sight, and the *IRAS* flux ratio measures the color temperature of the dust adjacent to the *IRAS* sources (section 2.3.1). Assuming normal dust-to-gas ratio, one may expect a correlation between the two parameters. In Figure 3.8, we plot the ^{13}CO column density obtained from Nagoya observations against the *IRAS* 12-25 μm flux ratio. Although the outflow sources appear to have higher N(^{13}CO) and redder *IRAS* color, the scatters are too large to reveal a clear correlation between the two parameters. The complication can be caused by two factors: (1) the beamsize used in Nagoya observations is too large so that the column density we obtained is only an average over the beam. (2) the density required to collisionally excite the ^{13}CO J = 1-0 line emission is only 10^{2-3} cm^{-3}, so the column density we measured is contaminated by the emission of the ^{13}CO molecules in the foreground or background.

Figure 3.9a overcomes the first drawback by comparing the *IRAS* color with ^{13}CO column density obtained within a 17" beam in Nobeyama observations. Figure 3.9b overcomes both drawbacks by comparing the *IRAS* colors with the high-resolution HCO^+ column densities. Both figures clearly show the much improved correlations between the gas column densities and the *IRAS* color. The cold *IRAS* sources (smaller $f12/f25$) tend to be associated with higher gas column densities. This trend is much clearer for HCO^+ than for ^{13}CO, as suggested by the correlation coefficients of the two diagrams, 0.79 and 0.68, for Figures 3.9a and 3.9b, respectively. While the physical implications of these correlations will be discussed in the next section, the correlations suggest that the line emissions we detected, especially in the HCO^+ observations, mostly come from the gases associated with the *IRAS* sources, and that they are not foreground or background emission.

It is also interesting that the ^{13}CO and HCO^+ column densities obtained in Nobeyama observations are also correlated (Figure 3.10). Sources that have large $N(HCO^+)$ also have large $N(^{13}CO)$.

3.4. DISCUSSION

3.4.1. *Core Dissipation During Star Formation*

As shown in the previous section, the correlation of molecular column densities with the *IRAS* color suggests that the molecular gases, especially HCO^+, detected by our observations are associated with the *IRAS* sources. Figures 3.7a-b show that the outflow sources tend to have higher column density than the non-outflow sources. As shown in Table 3.2, 9 of 10 outflow sources have $N(HCO^+)$ higher than 1.2×10^{13} cm^{-2}, while 14 of 18 non-outflow sources have $N(HCO^+)$ lower than that value. Our ^{13}CO mapping also gives a consistent result, showing 7 of 9 outflow sources are associated with large scale ^{13}CO cores, as compared to only 4 of 31 non-outflow sources. All three outflow sources that we mapped in HCO^+ have the dense cores near the *IRAS* source positions. We conclude that most outflow sources are associated with dense molecular cores, and most non-outflow sources are probably not associated with the dense core.

By now we know young stars are born in molecular dense core, and by the time they passed CO outflow stage, they are no longer associated with dense cores. How do they change their molecular environment during this period? There are at least two explanations: (1) proper motion of the YSOs with respect to the dense cores in which they were born, and (2) core dissipation by accretion and outflow of the central embedded sources.

If a young star is first formed at the center of a molecular dense core and moves away from the core when it becomes a T Tauri-type star, we can calculate the star's velocity dispersion with respect to its associated molecular gas:

$$\Delta V = 1.0 \left(\frac{R_{\rm core}}{\rm pc}\right) \left(\frac{10^6 \rm\ yr}{T_{\rm TTS}}\right) \rm\ km\ s^{-1}, \tag{3.3}$$

where $R_{\rm core}$ is the radius of the core (0.1 pc for HCO^+ cores and 1-2 pc for ^{13}CO cores). Taking the average age of T Tauri stars to be 10^6 yr (Cohen & Kuhi 1979), a velocity dispersion of 0.1 km s^{-1} or 1.0-2.0 km s^{-1} is required for a YSO to move away from its HCO^+ core or ^{13}CO core, respectively. The observations of the proper motion of the T Tauri stars with respect to their associated molecular gas yielded only upper limits. The most recent observations in Taurus-Auriga and the Orion Complex (Hartmann et al. 1986) found the velocity dispersion <1.5 km s^{-1}. Such a dispersion is probably not enough for YSOs to escape the ^{13}CO cores, although it remains uncertain whether the proper motion is large enough for YSOs to escape their HCO^+ cores.

The other possibility is core dissipation during the early evolution of the star. Two mechanisms can cause such dissipation: (1) accretion by which a protostar builds up its mass, and (2) enormous mass loss by the YSO as detected by CO line emission. The dissipation may be accomplished when the protostars become the T Tauri-type stars. For a dense core of 3 $M_\odot$, and assuming the age of T Tauri stars to be 10^6 yr, a dissipation rate of 3×10^{-6} $M_\odot$ yr^{-1} is necessary if the core can be dissipated when the central star becomes T Tauri-type star. Because it is comparable with the accretion rate (10^{-5} $M_\odot$ yr^{-1}) and the mass-loss rate of the CO outflow (2×10^{-6} $M_\odot$ yr^{-1}) within the uncertainties, we suggest that the both accretion and outflow can dissipate the molecular cores. It is important to note that for a more massive core (10-100 $M_\odot$) that is capable of

producing more than one star, the core dissipation may require the collective efforts of the young stars within the core. This is probably the case for source 8 (L1641-N).

3.4.2. *Outflow as an Early Stage of Star Formation*

As discussed above, the *IRAS* sources associated with CO outflow are significantly different from non-outflow sources. They tend to be colder and more luminous, and are associated with higher ^{13}CO column density. They are also located inside the dense molecular cores. Table 3.4 summarizes the difference of physical parameters for outflow and non-outflow sources.

These differences can be understood if the sources associated with CO outflow are indeed at the earliest stage of star formation as suggested by Lada (1985) and as shown by a statistical study of molecular outflows in L1641 by Fukui et al. (1989). Theoretical studies suggest that mass outflow is an unavoidable process during the star formation, and it might occurs at the time the mass accretion is taken place (e.g., Shu et al. 1987). The high luminosity of the outflow sources might be a result of such accretion. At this stage, the central source is deeply embedded in a molecular dense core. The heavy extinction of the dust in the cores should (1) shield against the interstellar radiation field, so that the embedded source becomes the main heating source, and (2) degrade the photons from the YSO to far-infrared photons. The heavier the extinction, the colder the sources should appear, as shown in Figure 5.9a.

3.5. SUMMARY

The goal of this chapter is to study the association of the molecular dense cores with various types of *IRAS* sources, in particular, the sources with and without CO molecular

outflow. We present two sets of observations: (1) a moderate resolution ^{13}CO mapping of 40 *IRAS* sources; and (2) the high-resolution ^{13}CO and HCO^+ observations. Our major conclusions are summarized as follows:

(1) In Nagoya observations, we find that 11 sources are associated with molecular cores, including 7 of 9 *IRAS* sources with CO outflow. The outflow sources tend to be located inside the core, while the more-evolved sources have little surrounding ^{13}CO molecular gas.

(2) All three outflow sources mapped in the Nobeyama observations are associated with the well-defined HCO^+ cores near the *IRAS* source position. The the cores have an average size of 0.1 pc, and a mass of 3-30 $M_\odot$.

(3) There is a correlation between molecular column densities and the *IRAS* color defined by the 12-25 μm flux density ratio. The correlation can be best seen when using high-spatial resolution data of HCO^+ J = 1-0.

(4) Based on the above results, we conclude that the outflow sources are associated with molecular dense cores and that most of the non-outflow sources are not associated with a dense core. Such a difference is probably caused by dissipation of the dense cores during the star formation process. Both accretion and the CO outflow are capable of dissipating the cores. The dissipation of a more massive core, however, requires the collective effort of the young stars that were born within the core.

(5) Outflow sources are significantly different from the non-outflow sources. They tend to be colder, more luminous, have higher ^{13}CO column density, and are located inside or near molecular dense cores. We believe these can be explained if the outflow sources are YSOs still in the stage of accretion.

TABLE 3.1. DATA FROM NAGOYA OBSERVATIONS

No.	CO				^{13}CO				τ_{13}	$N(^{13}CO)$		Map
	T_p (K)	rms (K)	V_{LSR} (kms^{-1})	Δv (kms^{-1})	T_p (K)	rms (K)	V_{LRS} (km s^{-1})	Δv (kms^{-1})		(10^{15}cm^{-2})		
2	7.3	0.63	6.4	1.2	1.2	0.28	6.4	1.2	0.18	0.8	±0.2	NC
3	19.0	0.63	7.7	1.4	4.3	0.32	7.9	1.1	0.26	5.5	0.4	IC
7	16.2	0.62	8.4	4.1	6.0	0.29	8.8	2.2	0.46	14.7	0.7	OC
8	26.0	0.69	7.8	4.8	8.3	0.29	7.3	3.2	0.38	43.1	1.5	IC
9	5.2	0.62	6.7	2.8	...					< 0.4		NC
17	17.6	0.54	8.0	3.4	5.3	0.32	8.4	1.6	0.36	9.6	0.6	OC
28	7.2	0.58	7.4	3.3	...					< 0.4		NC
47	25.5	0.69	8.2	3.8	7.3	0.31	8.3	2.9	0.34	33.0	1.4	IC
51	24.4	0.54	8.3	4.4	7.5	0.41	8.5	3.4	0.37	38.8	2.1	IC
56	13.8	0.58	6.8	3.6	2.9	0.44	6.9	3.2	0.24	8.1	1.2	OC
62	12.6	0.60	6.6	3.4	4.1	0.28	6.8	1.8	0.39	6.5	0.4	OC
71	16.9	0.73	5.7	3.5	4.4	0.40	5.9	2.4	0.30	11.3	1.0	IC
73	16.3	0.60	5.0	4.4	3.7	0.27	4.5	4	0.26	15.0	1.1	OC
74	4.9	0.65	6.0	1.8	...					< 0.4		NC
75	14.1	0.68	5.0	5.4	3.9	0.28	4.3	3.6	0.32	13.0	0.9	IC
79	16	0.64	5.5	3.7	4.3	0.25	5.5	2.2	0.31	9.7	0.6	OC
85	14	0.63	5.1	4.2	3.1	0.28	4.7	3.9	0.25	10.8	1.0	OC
95	11.5	0.62	5.3	3.5	2.7	0.32	5.3	3.5	0.27	7.3	0.9	OC
99	14.2	0.60	5.5	4.2	5.0	0.31	5.3	2.8	0.43	13.8	0.8	IC
101	12.9	0.66	5.0	3.8	4.3	0.31	4.5	2.5	0.41	9.6	0.7	OC
104	14.2	0.64	4.9	5.3	4.7	0.30	5.1	3.1	0.40	14.1	0.9	IC
105	11.8	0.63	4.7	5.4	4.1	0.33	4.9	4.4	0.43	15.2	1.2	IC
106	13.6	0.62	5.5	3.5	3.8	0.42	5.4	2.8	0.33	9.6	1.1	OC
108	13.9	0.61	5.0	3.7	4.3	0.34	4.9	2.6	0.37	10.5	0.8	OC
160	12.3	0.63	4.9	3.7	4.4	0.45	5	2.5	0.44	9.7	1.0	OC
163	12.5	0.60	5.2	3.1	2.8	0.46	4.9	2.5	0.25	5.7	0.9	OC
168	12.4	0.67	5.1	3.7	4.2	0.61	4.9	2.9	0.41	10.6	1.5	OC
171	8.9	0.62	3.3	1.5	2.0	0.28	3.4	1.1	0.25	1.4	0.2	OC
177	14.7	0.73	5.3	2.6	4.2	0.38	5.5	2.6	0.34	10.6	0.9	OC
178	13.7	0.65	4.7	3.1	3.8	0.32	4.9	2.2	0.32	7.6	0.6	OC
181	13.4	0.64	5.1	3.2	3.7	0.29	5.1	2.8	0.32	9.2	0.7	OC
194	12.9	0.65	4.9	3.2	5.9	0.31	5.1	1.9	0.61	11.1	0.6	OC
216	16.0	0.72	2.8	2.4	6.6	0.33	3.1	1.49	0.53	11.2	0.6	IC
256	9.0	0.62	3.2	5.0	2.9	0.30	2.5	2.8	0.39	5.5	0.6	OC
258	8.4	0.65	3.4	4.9	3.0	0.28	3	4.1	0.44	8.1	0.7	IC
267	6.7	0.64	3.3	4.2	2.5	0.27	3.1	2.7	0.47	3.8	0.4	OC
277	7.8	0.67	2.8	3.6	2.1	0.29	3.6	2.5	0.31	3.1	0.4	OC
280	8.5	0.73	2.7	4.0	1.6	0.28	2.1	1.1	0.21	1.0	0.2	NC
287	2.4	0.64	5.3	0.8	...					< 0.4		NC
288	6.4	0.67	3.7	2.9	1.4	0.32	4.4	1.3	0.25	0.9	0.2	NC

TABLE 3.2 DATA FROM NOBEYAMA OBSERVATIONS

No.	^{13}CO				CO	HCO^+					
	T_p (K)	rms (K)	Δv (kms^{-1})	V_{LSR} (kms^{-1})	T_p (K)	T_p (K)	rms (K)	Δv (kms^{-1})	V_{LSR} (kms^{-1})	$N(^{13}CO)$ (10^{15}cm^{-2})	$N(HCO^+)$ (10^{12}cm^{-2})
3	3.6	0.44	0.7	7.4	16.8	0.8	0.24	0.3	7.7	2.5	2.5
7	4.5	0.55	1.6	8.8	13.2	...	0.33	...	...	6.6	<6.7
8	7.4	0.57	2.9	6.7	25.7	3.1	0.31	1.9	6.9	33.5	67.7
18	7.0	0.37	2.2	6.1	20.8	1.1	0.23	2.0	7.2	20.6	24.1
25	7.1	0.57	2.0	8.2	24.6	4.0	0.48	1.0	8.8	21.7	43.7
31	3.5	0.50	1.9	6.9	17.6	0.7	0.16	0.9	7.0	7.2	7.0
33a	2.5	0.72	1.5	9.1	13.6	...	0.25	...	...	3.1	<3.9
33b	1.9	0.72	2.2	6.3	13.6	...	0.25	...	...	3.5	<3.9
34a	4.5	0.47	0.8	8.1	21.9	1.0	0.28	1.0	8.8	4.5	11.0
34b	3.2	0.47	1.3	7.1	21.9	0.8	0.28	0.5	7.4	5.2	4.9
37a	5.5	0.41	0.8	8.3	16.5	0.9	0.30	1.5	9.0	4.7	15.6
37b	4.7	0.41	1.0	6.3	16.5	1.2	0.30	0.7	6.9	5.1	10.0
42	3.6	0.28	1.3	6.5	20.4	0.7	0.22	0.5	6.9	5.8	4.0
47	7.7	0.55	1.4	8.2	25.1	0.9	0.32	1.2	9.1	16.7	12.6
49	4.7	0.35	1.4	6.3	27.1	1.7	0.29	0.5	6.3	10.0	9.8
50	8.1	0.39	2.0	8.1	26.2	1.8	0.17	1.5	8.7	26.4	31.0
51	8.7	0.56	3.4	8.0	25.5	2.0	0.34	2.1	9.1	47.9	46.8
56	3.5	0.44	2.0	5.7	13.7	1.3	0.19	1.0	5.7	6.2	14.8
62	2.8	0.68	3.1	6.4	13.8	...	0.25	...	...	7.6	<4.6
68	3.3	0.79	1.0	8.5	16.6	0.8	0.23	0.6	8.5	3.2	4.6
71	5.3	0.39	1.6	4.8	17.7	0.9	0.16	0.9	5.8	9.9	9.2
73	4.7	0.80	2.5	3.3	14.3	...	0.41	...	...	11.3	<6.7
75	5.1	0.50	3.1	2.3	13.3	2.2	0.29	1.0	3.1	15.1	23.8
79	4.7	0.35	1.5	4.8	14.4	0.9	0.27	1.5	5.4	7.0	15.0
96	3.9	0.59	1.7	6.2	14.2	0.7	0.20	0.7	6.6	6.2	5.1
104	5.0	0.50	2.0	3.9	11.6	1.8	0.36	2.2	3.6	9.0	44.8
105	4.5	0.44	3.9	4.1	10.1	1.1	0.31	1.2	5.5	14.0	14.2
108	3.9	0.50	2.7	4.8	13.5	...	0.45	...	...	9.6	<7.3
119	4.9	0.62	2.0	4.5	11.3	...	0.30	...	...	8.4	<5.0
194	3.4	0.82	1.5	5.1	13.5	1.7	0.61	1.4	5.2	4.5	26.4
216	4.8	0.51	1.6	3.0	13.0	2.7	0.33	1.2	3.1	7.3	35.6

TABLE 3.3. PHYSICAL PARAMETERS OF 3 HCO^+ CORES

No.	ID	$N(HCO^+)$ ($10^{13}cm^{-2}$)	Δv (kms^{-1})	R (pc)	$n(H_2)$ ($10^5\ cm^{-3}$)	M ($M_\odot$)
8	L1641-N	6.8	1.94	0.16	1.4	27
75	L1641-C	2.4	0.96	0.09	0.9	3
104	H 4-255	4.5	2.21	0.11	1.4	8

TABLE. 3.4 OUTFLOW SOURCES VS. NONOUTFLOW SOURCES

	Avg. Log(f12/f25)	$N(^{13}CO)$ ($10^{15}\ cm^{-2}$)	L_{FIR} ($L_\odot$)	IC sources / Total
Outflow sources	-0.81	18.9	92	7/9
Non-outflow sources	-0.44	7.9	22	4/31

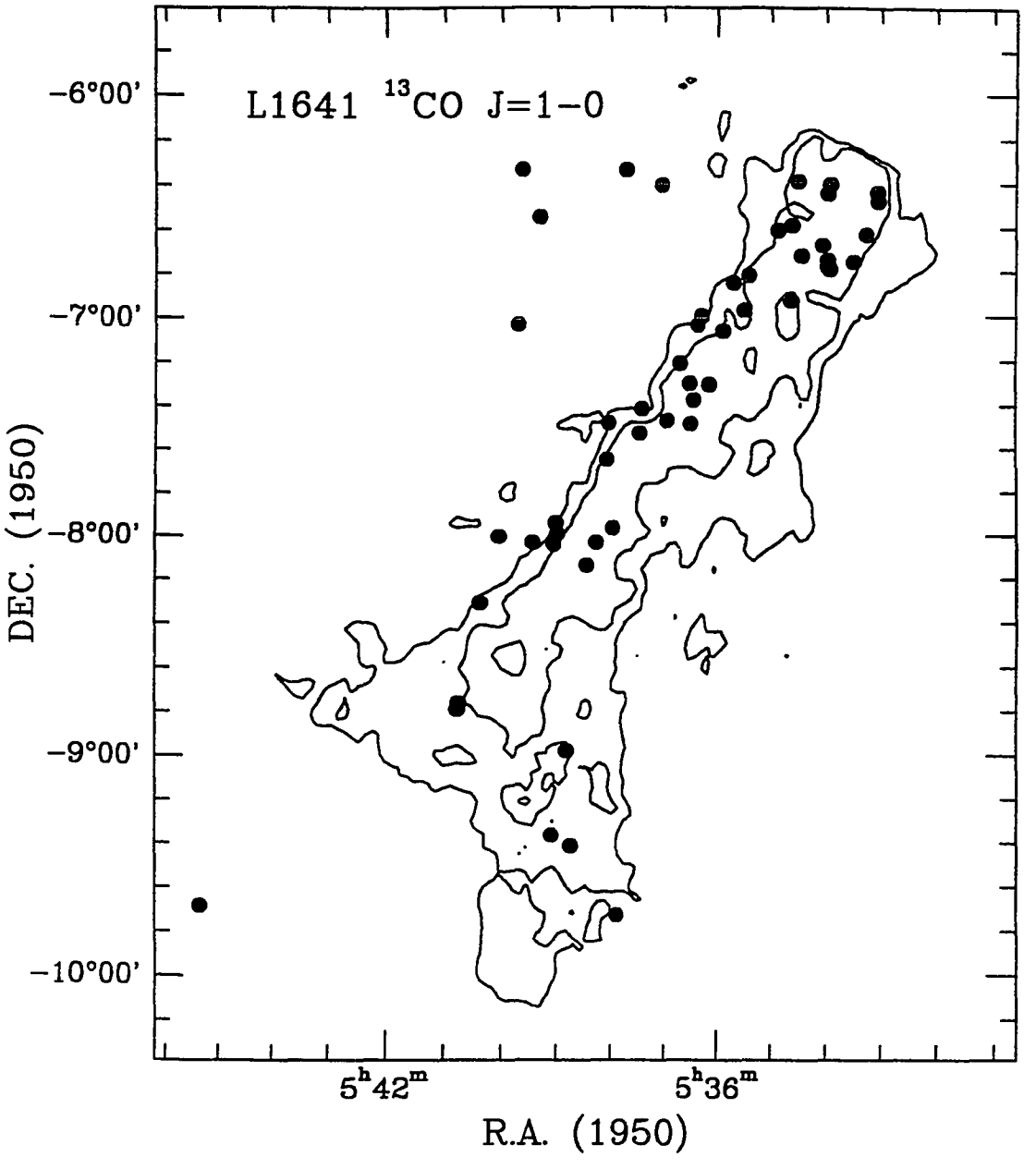

Figure 3.1 The spatial distribution of the two *IRAS* source samples observed in this chapter. The two contours are 3.0 and 7.0 K km s^{-1} integrated intensity of ^{13}CO J = 1-0 line emission (Fukui & Mizuno 1991).

Source 3

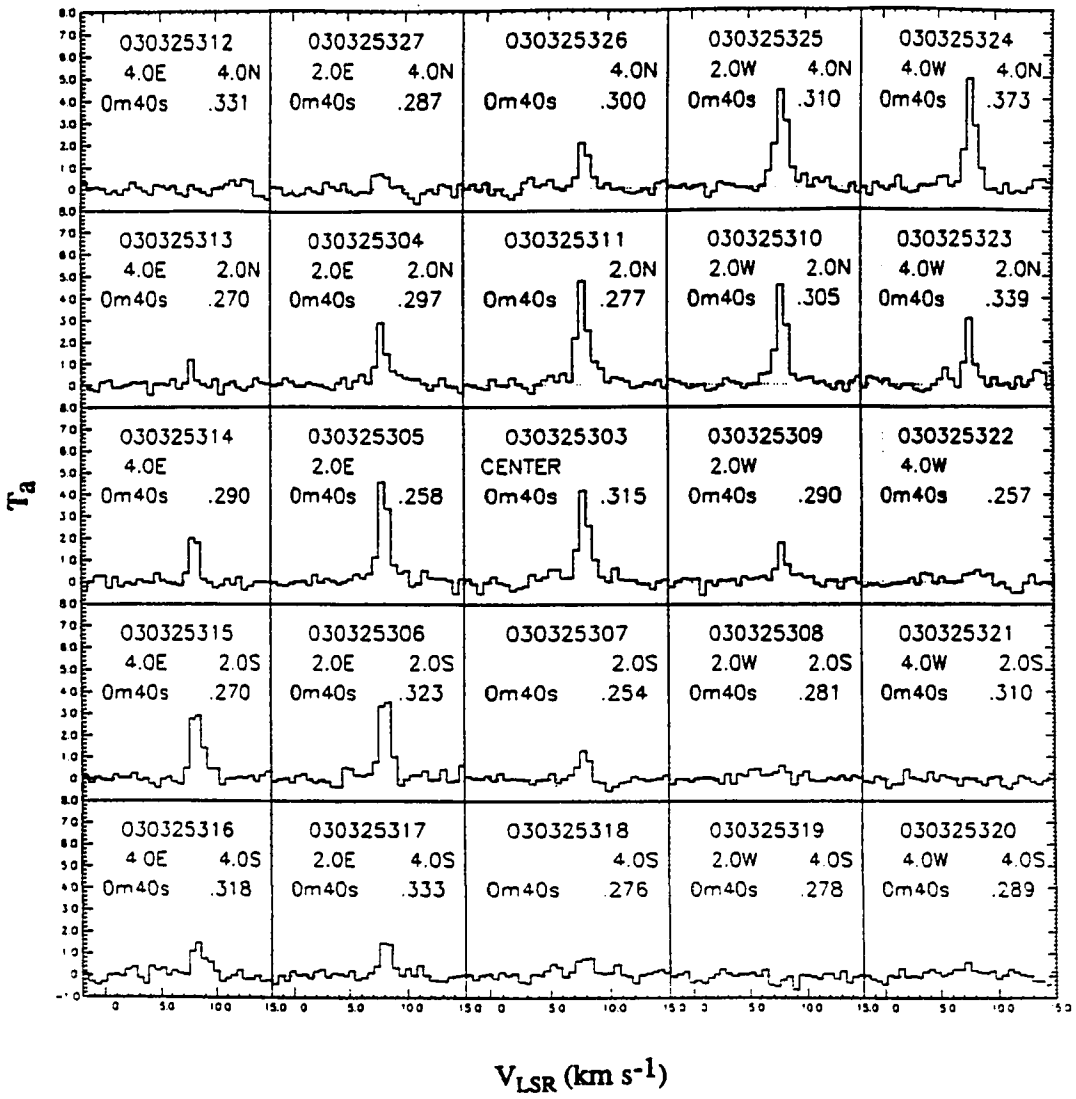

Figure 3.2a Typical line profiles. The ^{13}CO line profile map of source 3 obtained in Nagoya Observations.

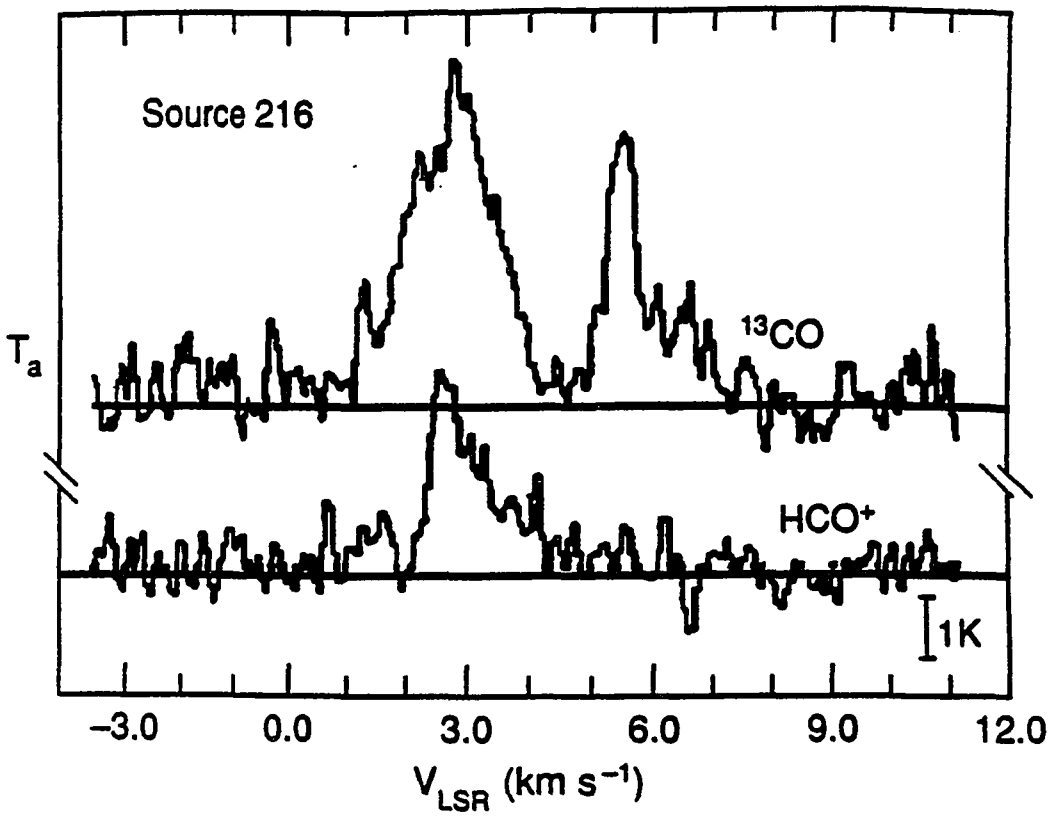

Figure 3.2b Typical line profiles. The line spectra taken at the position of source 216 (L1641-S2) in Nobeyama observations. Note that only the component at 3.0 km s^{-1} was used.

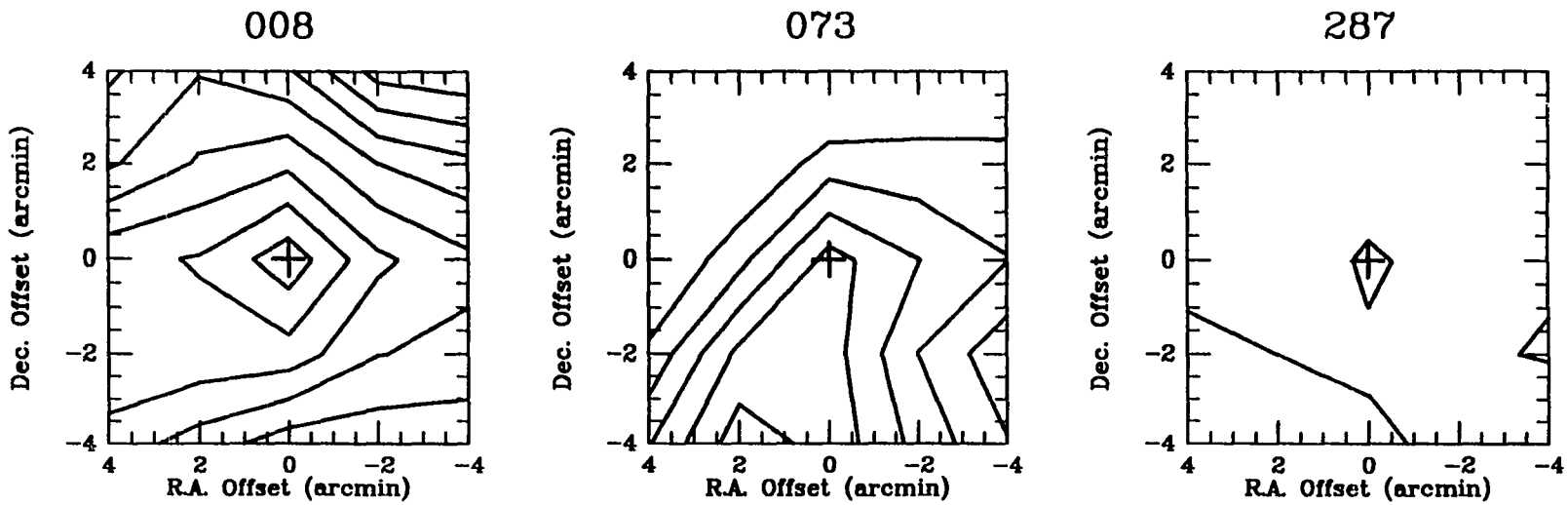

Figure 3.3 The typical integrated intensity maps for three types of sources (see text for classification) obtained in Nagoya observations. (a) IC: source 8; (b) OC: source 73; and (c) NC: source 287. For all the 3 maps, the lowest contour level represents a 50% of the maximum, and contour interval is about 2 σ.

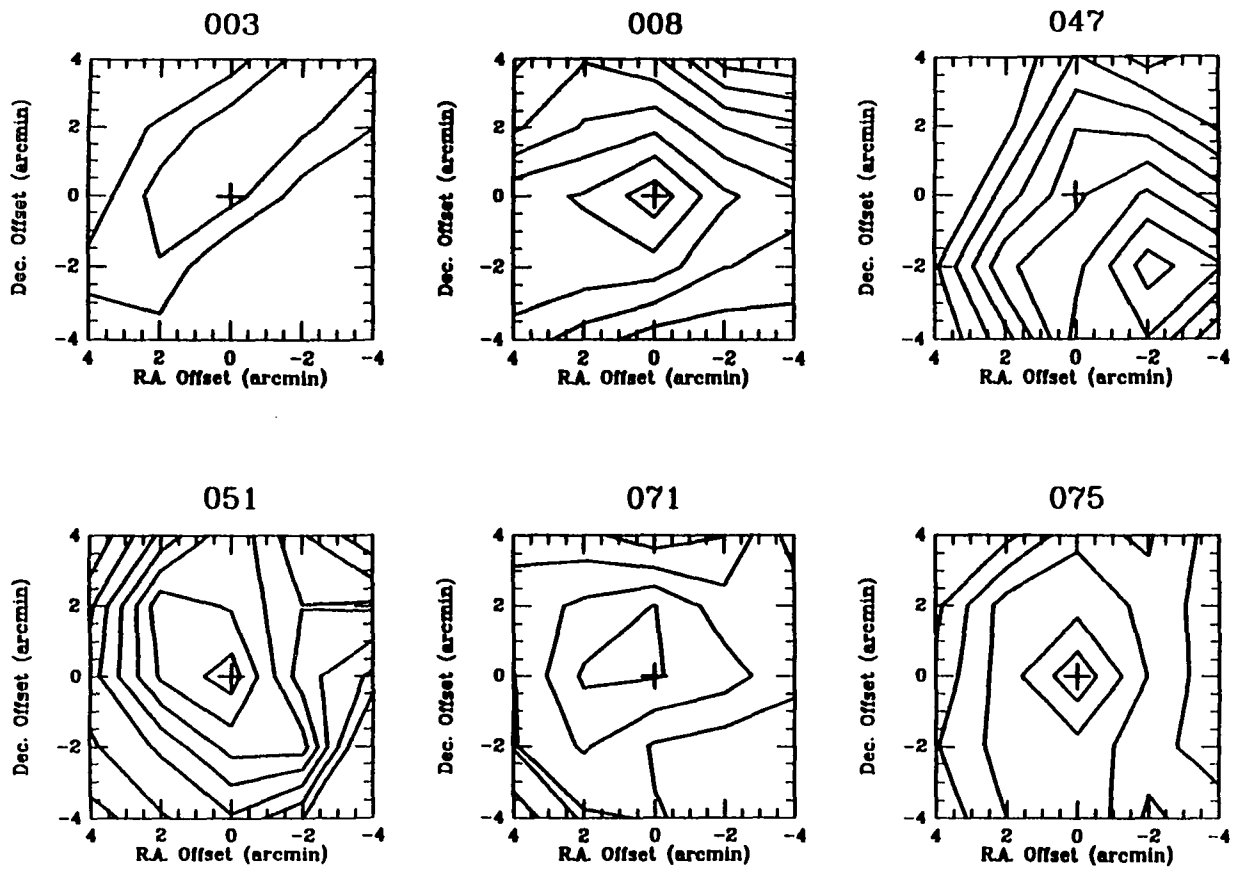

Figure 3.4 The contour maps of the 11 IC sources. The lowest contour represents the 50% of the maximum and the contour level is about 2 σ. The *IRAS* positions are at the centers of maps, and are marked by the cross.

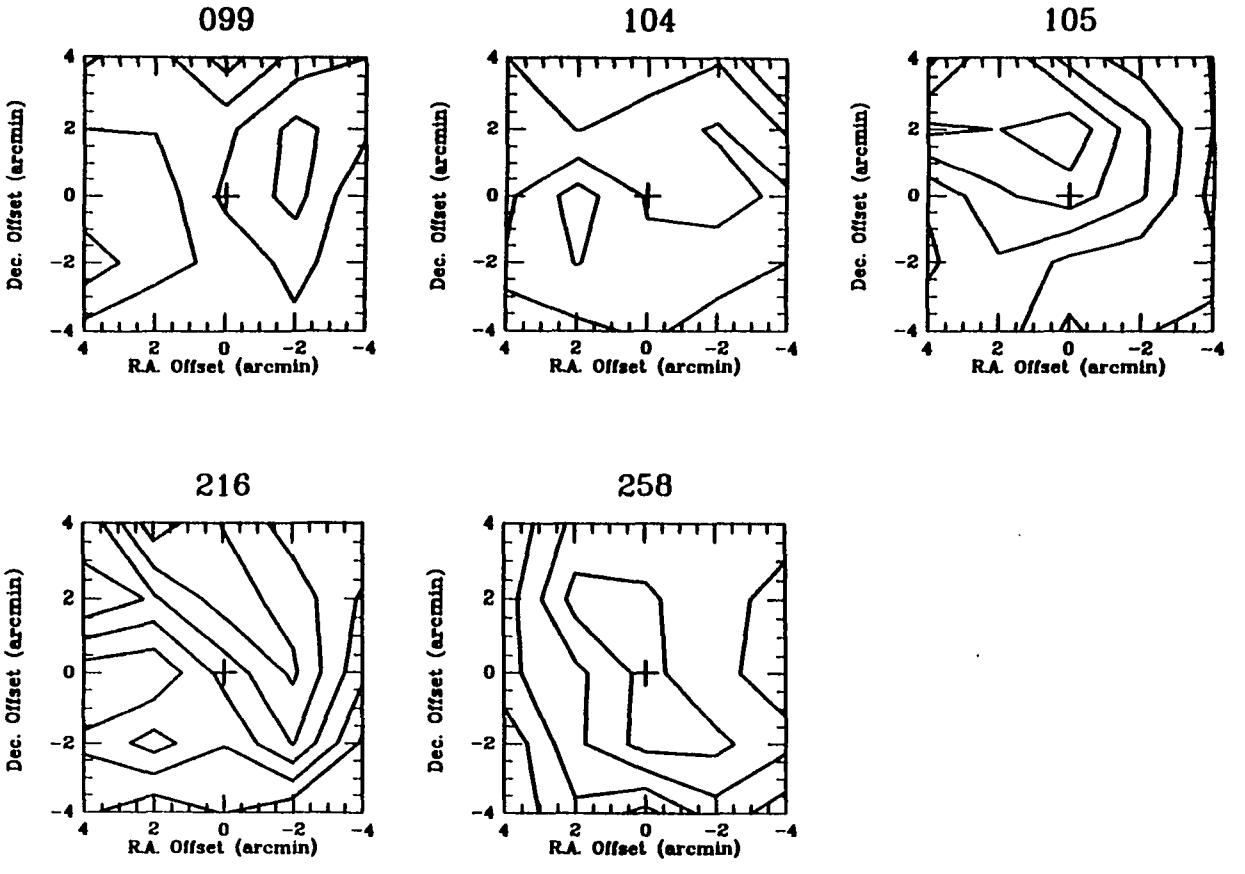

Figure 3.4 - *Continued*

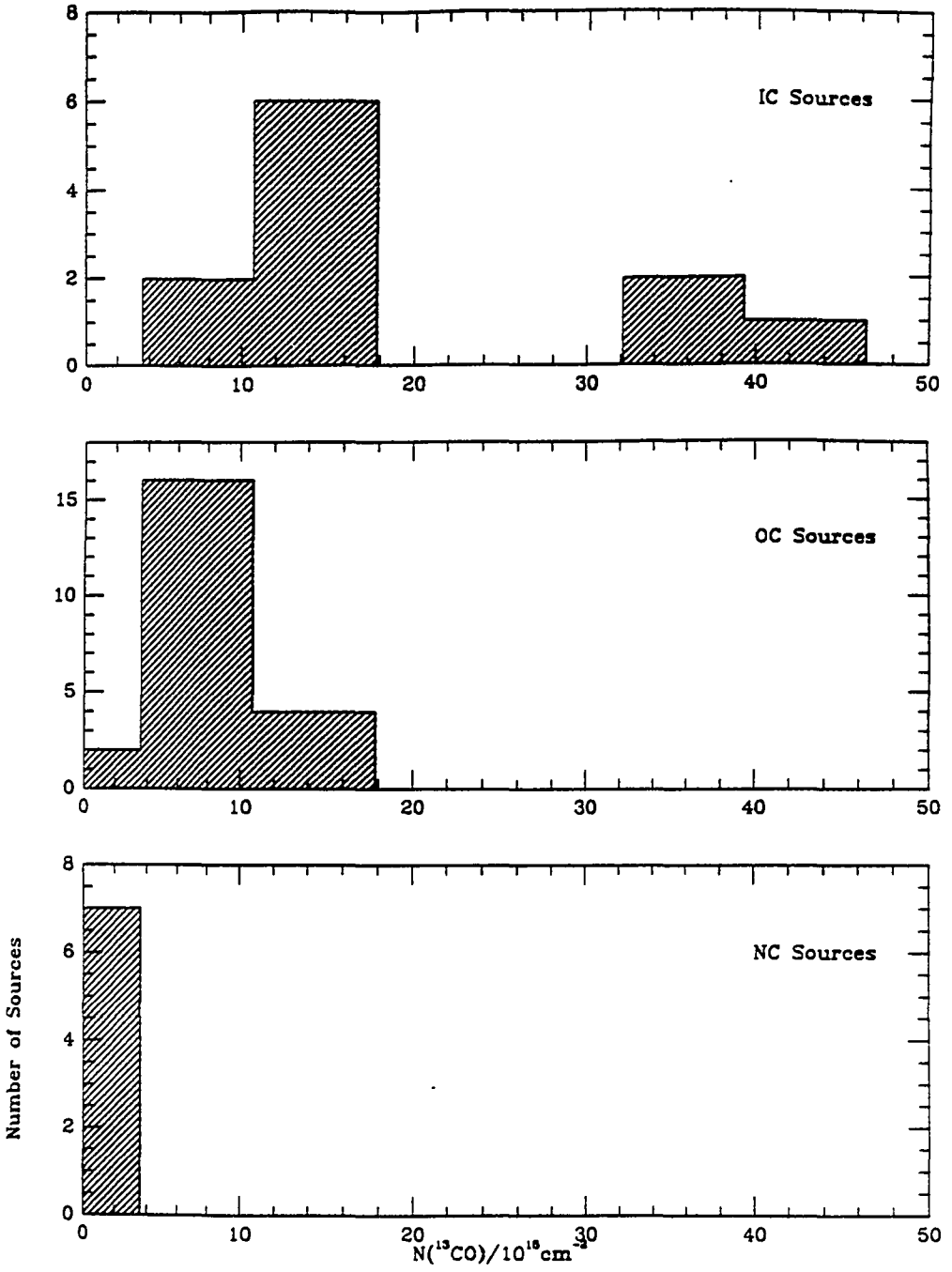

Figure 3.5 The histograms of ^{13}CO column density for IC, OC, and NC sources.

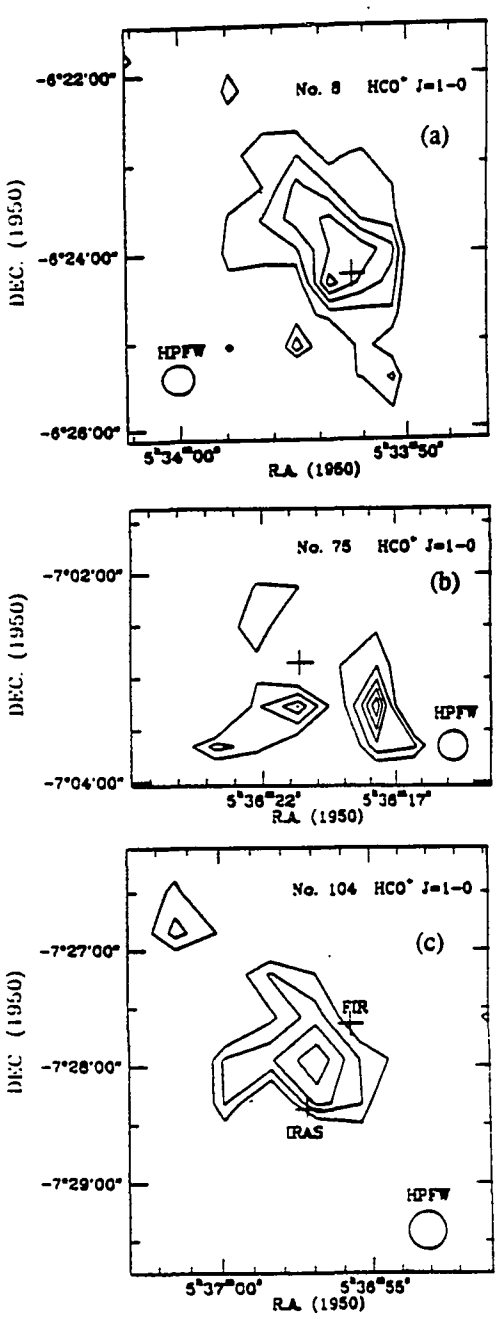

Figure 3.6 Contour maps of HCO^+ integrated intensity of three outflow sources. The lowest contour represents 40% of the maximum, and the intervals are about 3 σ. (a) source 8 (L1641-North); (b) source 75 (L1641-Center); and (c) source 104 (H4-255). The *IRAS* source positions are marked by the crosses.

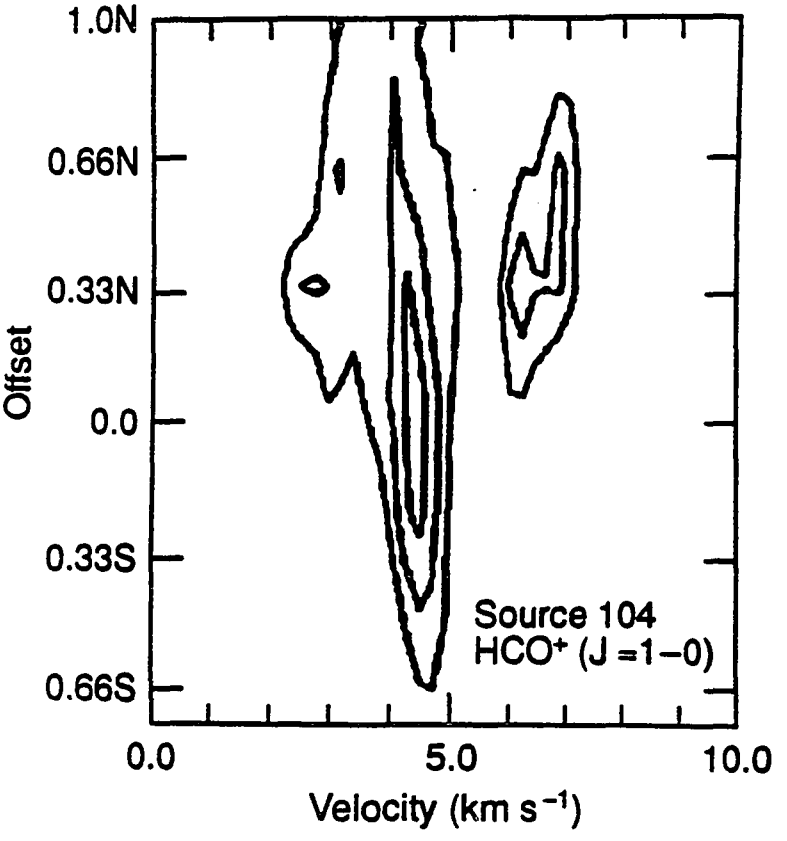

Figure 3.7 The HCO^+ velocity-position diagram of source 104. The north-south cut was made at the *IRAS* position.

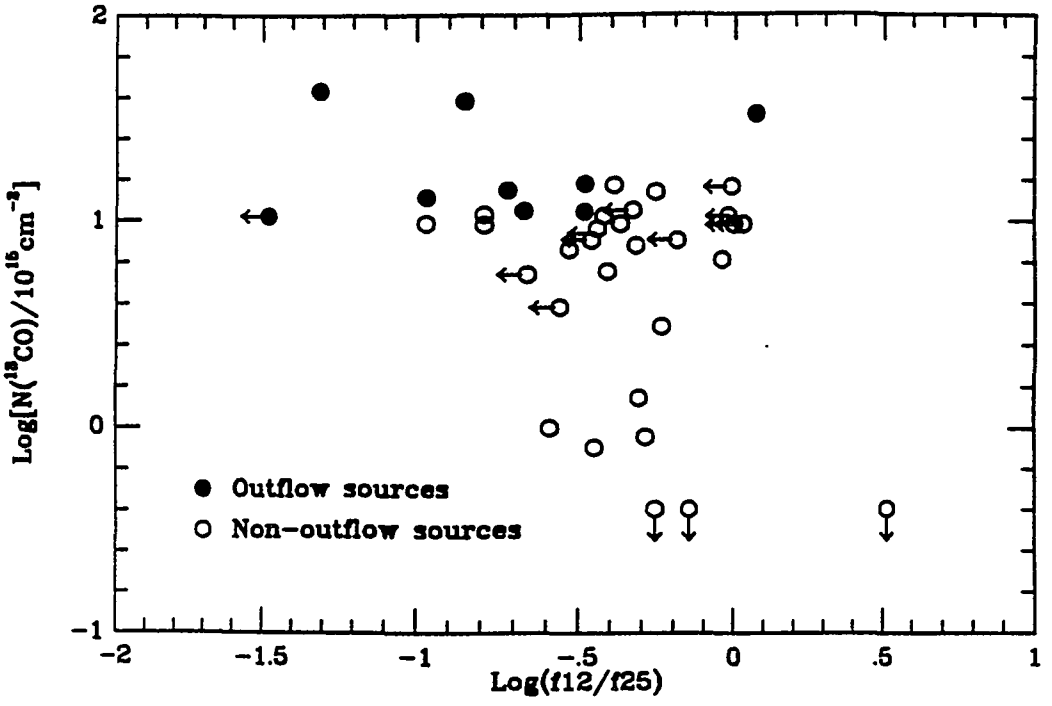

Figure 3.8 *IRAS* 12-25 μm flux density ratio vs. the ^{13}CO column density obtained from the Nagoya observations.

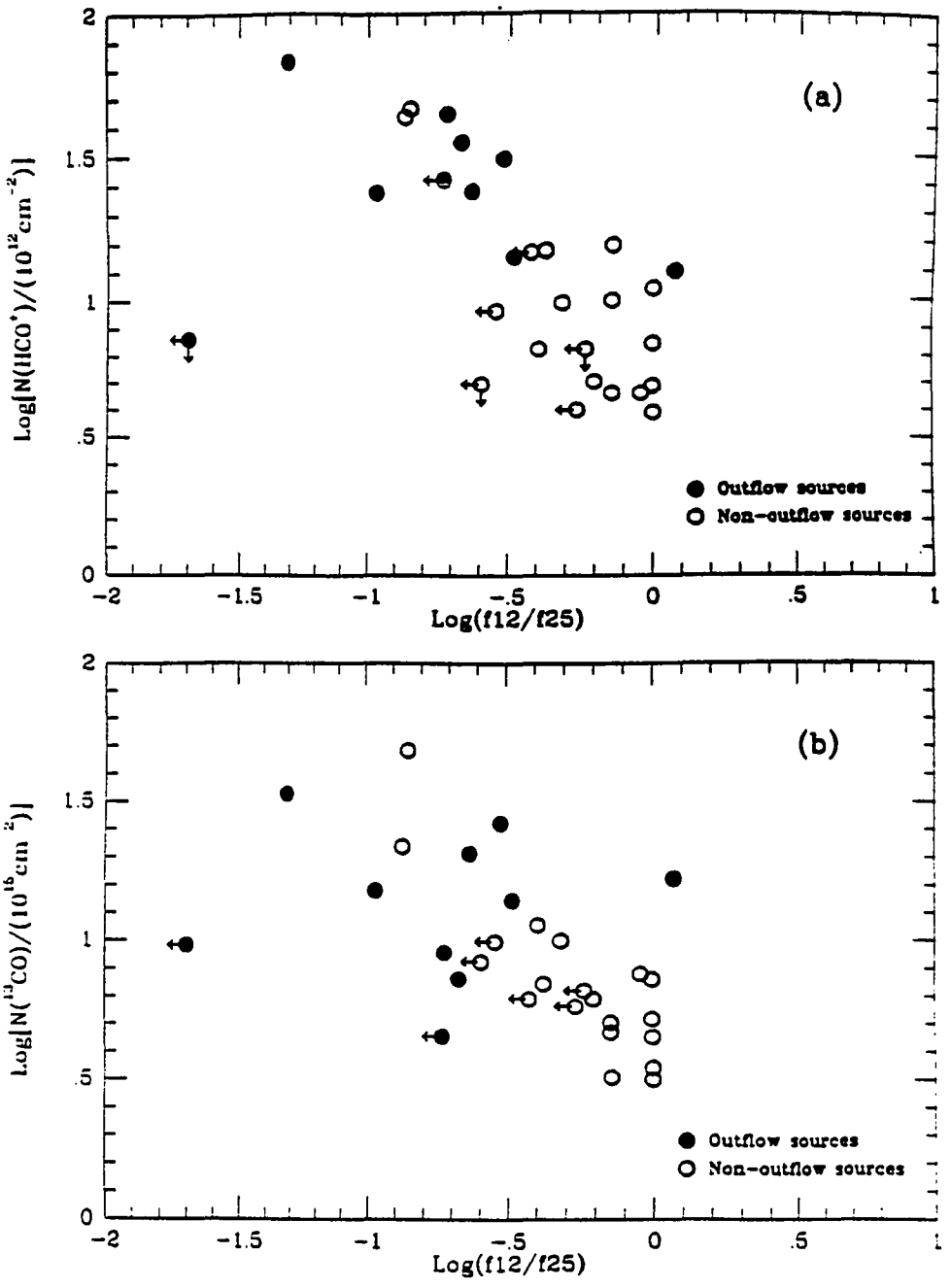

Figure 3.9 The column density vs. *IRAS* color defined by 12 to 25 μm flux density ratio for (a) ^{13}CO column density and (b) HCO^+ from Nobeyama observations. Downward arrows indicate a 3 σ HCO^+ upper limits. The leftward arrows indicate a 5 σ upper limits of 12 μm flux. Sources with no detections at both 12 and 25 μm are not plotted.

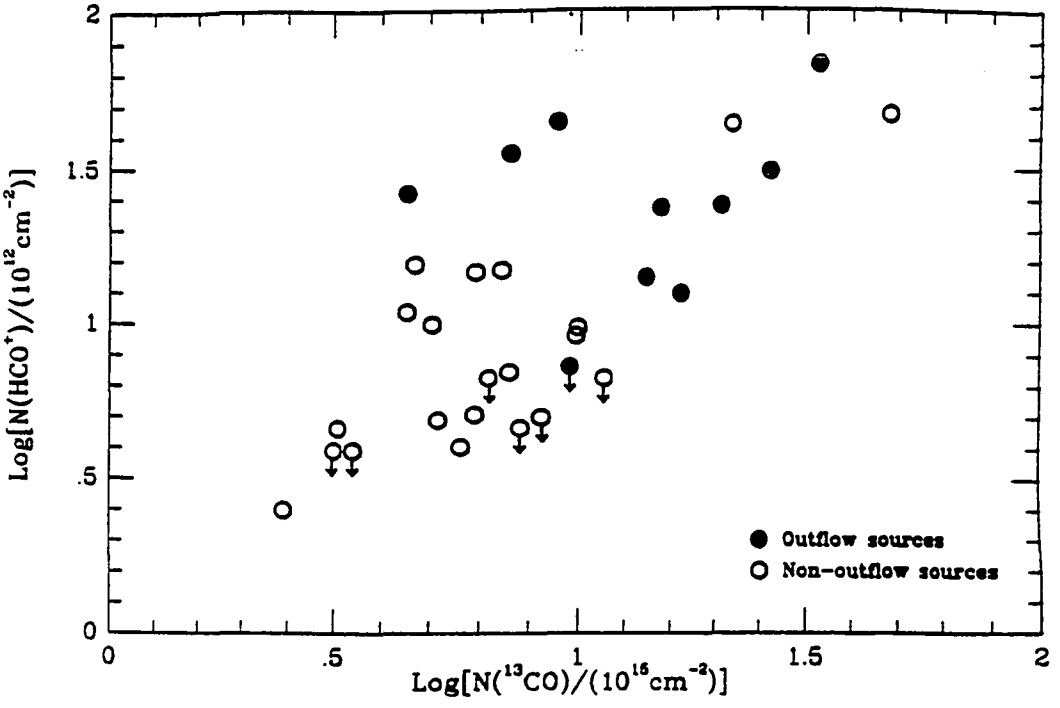

Figure 3.10 Comparison of the ^{13}CO and HCO^+ column densities. The filled circles are the outflow sources, and the open ones are non-outflow sources. Arrows indicate 3 σ upper limits.

CHAPTER 4

NEAR-IR IMAGING OF 59 *IRAS* SOURCES IN L1641[1,2]

4.1. INTRODUCTION

The studies presented in Chapters 2 and 3 were based on the observations at the far-IR and at the millimeter wavelengths. While they provided useful information about the dust and molecular environment of the young stellar objects, the spatial resolutions of these observations (20"-3') were too low for us to study the young stars themselves directly. In this chapter, we report on a high-spatial resolution (0.35"-0.75" pixel^{-1}) deep imaging with the near-IR cameras at 1-5 μm.

There are two motivations for carrying out such imaging. The first motivation is to understand the spatial distribution of young stars within a single molecular cloud. Although it is well known that young stars are being formed in dense molecular cores (Myers and Benson 1983, Beichman et al. 1986, Shu, Adams, & Lizano 1987), the question of how they are formed remains unanswered. Observationally, young stars appear to have two different spatial distributions: (1) young stars in the Taurus dark cloud seem to be formed individually or in small groups of 2-3 stars, and (2) in other molecular clouds, such as ρ Oph and L1630, most young stars are aggregated into large clusters. These two distributions are referred by Lada (1991) as the isolated mode and the clustered mode, respectively. Could young stars have different distributions within in

---

[1] Part of this work is based on the observations carried out at Infrared Telescope Facility, which is operated by the University of Hawaii under contract from the National Aeronautics and Space Administration.

[2] Part of this work is based on the observations carried out at United Kingdom Infrared Telescope, which is operated by the Royal Observatory Edinburgh on behalf of the U.K. Science and Engineering Research Council.

a single molecular cloud? If so, do different distributions indicate different star formation mechanisms? The answers to these questions are of fundamental importance, since the current star formation theories, such as those proposed by Shu et al. (1987) focus mostly on individual star formation in the isolated dense cores.

The second motivation concerns the spectral energy distribution (SED) of YSOs. The SED has been widely used as an indicator of the evolutionary state of young stars (Lada & Wilking 1984, Lada 1991). To obtain a SED between 1-100 μm, one has to combine the near-IR photometry with the *IRAS* fluxes. In crowded regions, it is possible that there are several near-IR sources within the *IRAS* position uncertainty. In such cases, it is important to identify the near-IR counterparts of the *IRAS* sources to construct a meaningful SED.

The advance of near-IR array technology can help us to address the above questions by providing both high-spatial resolution and coverage. It allows us to study details that are unresolved in the *IRAS* observations. In this chapter, we report on an imaging of 59 *IRAS* sources at 1.6-4.8 μm with the near-IR cameras. Of 59 *IRAS* sources we imaged in *H*, *K'*, narrow-band L (*nbL*) and *M*, we found 14 *IRAS* sources are associated with small (but statistically significant) groupings of young stellar objects. These small groupings are defined to be *stellar density enhancements* (SDEs). In section 4.2, we discuss the details of our near-IR imaging and data reduction procedures. We then discuss in section 4.3 (1) the nebulosity presented in the images, and (2) the SDEs. In section 4.4., we use the near-IR infrared images and the photometric data to identify the near-IR counterparts of the *IRAS* sources. The spectral energy distributions (SEDs) are used to determine the evolutionary state of the sources. In section 4.5, we conclude that spatial distribution of young stars in L1641 can be characterized by a range of stellar densities, from a large cluster to SDEs and to individual stars. We also compare the *IRAS* sources in L1641 with those in Perseus and Taurus. Major results are summarized in section 4.6.

4.2. OBSERVATIONS AND DATA REDUCTION

All 59 *IRAS* sources were selected from Table 2.1. They are therefore located inside the dark cloud L1641. Since we are interested in the young stellar objects that are still associated with the dense molecular gas from which they were born, we used the ^{13}CO column density as a selection criterion. We selected 46 sources with $N(^{13}CO) > 10^{16}$ cm^{-2} in Table 2.1. For comparison, 13 other sources with moderate $N(^{13}CO)$ were also selected. All 11 outflow sources were selected. The sources are listed in Table 4.1.

4.2.1. *Observations*

The near-IR imagings were carried out at various telescopes at Mauna Kea, as shown by the observation log in Table 4.2. The images were taken at four wavelengths: *H* (center wavelength at 1.65 μm), *K'* (2.1 μm), narrow-band L (*nbL*; 3.6 μm) and *M* (4.8 μm). The *H* and *M* bands are defined by the standard photometric filters. The *K'* filter was chosen to be at a slightly shorter wavelength than the standard K filter to minimize the thermal background (Wainscoat & Cowie 1992). The *nbL* filter has a 6% bandpass.

The 59 *IRAS* sources were first imaged at *H* and *K'* with the NICMOS 3 camera (Hodapp, Rayner, & Irwin 1992) on the University of Hawaii 2.2 m telescope. The camera has a 256 × 256 HgCdTe detector, and was operated with a scale of 0.75" $pixel^{-1}$, giving a field of view of 197" × 197" per frame. Because all the sources are located in a dark region with few SAO stars, we had to first point the telescope to a nearby optical star (within 30' from each *IRAS* position) selected from the *Guide Star Catalog* (1989), and then slewed to the *IRAS* position. The position uncertainty of the offsetting was typically < 2". For each *IRAS* source, 3-5 images were taken with a 20" offset uniformly

displayed from the center frame. The flat fields were obtained by imaging the dome illuminated by an incandescent light.

Sources that appear to be crowded in *H* and *K'* images were subsequently imaged in the *nbL* at United Kingdom Infrared Telescope (UKIRT) and in *M* at NASA Infrared Telescope Facility (IRTF). The *nbL* and *M* images were taken at selected regions near the *IRAS* positions. Beam switching was used to obtain sky images. The nodding throws were selected to place the sources in both on and off positions. The *nbL* and *M* were acquired without flats. The standard stars were observed near the source locations on the arrays.

The total integration time were 150 s per image at *H* and *K'*, 180 s at *nbL*, and 75 s at *M*. If there were bright sources in a field, a shorter exposure was taken to avoid saturation. The standard stars HD 40335 (for the *H*, *K'*, *nbL*) and π^4 Ori (for *M*) were measured several times each night for the instrumental magnitude and atmospheric extinction correction.

4.2.2. *Data Reduction*

All the images were reduced using IRAF data reduction package. The *H* and *K'* images were first divided by the dome flats. A flat-fielded median sky was then subtracted from them. The resulting images were registered to form an approximately 4' × 4' mosaic image. The *nbL* and *M* images were processed by subtracting the respective sky frames.

Because many sources in our images are very red and our detection is most sensitive in *K'*, the near-IR sources were extracted from the *K'* images using DAOFIND with a detection threshold about 5 times the sky fluctuation. The output source list from each *K'* image was manually checked to eliminate false detections. The counterparts of the *K'*

sources at the other wavelengths were then identified and registered. The positions of the near-IR sources were calculated from the reference pixel in each frame. The positional uncertainty is dominated by the telescope offsetting uncertainty which was < 2". For some sources, we have checked our source positions with the published ones, and found they agree with each other within 1"-2".

To obtain the photometric data, we used APPHOT with a 5"-6" aperture for the isolated point sources. The inner and outer radii of sky annulus were typically 7.5" and 12", respectively. For images that are crowded or that show extended nebulosity, we fitted a point spread function to the sources using DAOPHOT. The 5σ limiting magnitudes for the isolated point sources are approximately H = 17.5, K' = 17.5, nbL = 13.0, and M = 11.0.

4.3. RESULTS

The H and K' images of all 59 sources can be found in Appendix D, along with the discussions of the individual sources. For three sources (sources 8, 18, and 75) that have optical images available, a detailed analysis is presented in Chapter 5. For the discussion in this chapter, we show the H and K' images of two sources (29 and 71) in Figure 4.1. In the following we examine (1) the nebulosity presented in the images, and (2) stellar density enhancements.

4.3.1. *Nebulosity*

As shown in Figure A1 in Appendix D, 26 of the 59 images (44%) of the images have nebulosity, including all the outflow sources. The association of the sources with nebulosity is indicated in Table 4.1. Twelve of them show diffuse nebulosity without a

particular pattern in a scale of 1'-2'. The diffuse nebulosities are probably the light scattered from the embedded sources. This argument is supported by the study to be discussed in the section 5.4 in which we found that several source positions in the vicinity of source 8 have wavelength-dependent shifts. Such shifts were believed to be the result of scattered light from embedded sources (Campbell et al. 1988).

In contrast to the diffuse nebulosity, the nebulosities in the other 14 sources show the elongated structures originating from the embedded sources. The structures can also be explained by the scattered light. The elongated (bipolar or unipolar) structure can be seen if the embedded source is surrounded by an optically thick disk or torus, and the light is mostly scattered through the polar regions into our line of sight. However due to the nature of scattering, the scattered structures tend not to be highly collimated, and scattering cannot explain the highly collimated structures found in some sources. As an example, we show source 36 in Figure 4.2. Near the *IRAS* position, we detected a very elongated bipolar structure originating from a deeply embedded source. The southern lobe ends at several knots. Morphologically, the structure is very similar to the nebulosity near source 51 which is associated with the previously known Herbig-Haro object (HH 1-2). The elongated near-IR structures near source 36 are roughly parallel to the axis of the associated CO molecular bipolar outflow MSSB 18 (Fig. 4.2). The embedded near-IR source is near the center of both the near-IR structures and the CO outflow. We therefore suggest that at least for source 36, the elongated structure and the associated knots are probably the infrared counterpart of the optical jets and HH objects. If this is true, the emission we detected in K' could be mostly due to the H_2 molecular emission excited by the high-velocity outflow from the embedded young star. This can be tested by comparing the images through the narrow-band filter of the S(1) line at 2.12 μm and those in the nearby continuum.

In short, nearly half the sources we imaged show nebulosity, indicating that they are embedded sources. Some of these sources have an elongated nebulosity, and they might be the near-IR counterpart of the optical jets and HH objects.

4.3.2. *Stellar Density Enhancement*

Having studied the nebulosity in the images, we now discuss the stellar distribution in the H and K' images presented in Figure A1. It is obvious that some of the *IRAS* sources have many more bright near-IR sources than the others. Figure 4.1 shows the examples of source distribution in the isolated region (source 29) and in the crowded region (source 72). The most interesting result from our imaging is that we found *stellar density enhancements* (SDEs) in the vicinity of 14 *IRAS* sources. In the following we will first explain how we define the SDE. We then show in turn that (1) the SDEs are statistically significant; (2) the SDEs are physically associated with the *IRAS* sources; and (3) most of the near-IR sources in the SDEs are young stellar objects.

To define an SDE, we need to calculate K'_0, the apparent magnitude of a near-IR source corrected for extinction. Using the standard interstellar extinction law (Reike & Lebofsky 1985), K'_0 can be written as:

$$K'_0 = K' - A_{K'} = K' - 1.78 \times [\,(H - K')_{obs} - (H - K')_0\,] \qquad (4.1)$$

where K' is the observed magnitude, $A_{K'}$ is the interstellar extinction at K', $(H - K')_0$ is the intrinsic color of the star, ranging 0-0.3 for A0-M5 type main-sequence dwarfs, $(H - K')_{obs}$ is the observed $H - K'$ index. Assuming (a) the near-IR sources are main-sequence dwarfs, and (b) the reddening is solely due to the interstellar extinction, we calculated K'_0 for all the near-IR sources detected in the 59 fields. *An image is defined*

to have a stellar density enhancement (SDE) if there are more than 5 sources with K'_0 *< 11 within a 4' × 4' area.* By this definition, 14 of the 59 *IRAS* sources are associated with SDEs, including 7 of 11 sources that are associated with CO molecular outflows. The association of the *IRAS* sources with the SDEs is indicated in Table 4.1.

To see whether the SDEs are statistically significant, we compared our definition with an infrared galactic model by Wainscoat et al. (1992). The model takes into account the contribution of the galactic disk, the bulge, the stellar halo and spiral arms, the molecular ring, and the extragalactic sky. It predicts that we should find 0.5±0.7 star brighter than $K'_0 = 11$ within a 4' × 4' area in the direction of the L1641. The surface density of stars with $K' < 11$ within the SDEs is therefore significantly higher than that of background stars at a > 5 σ level. Since the IRAS sources have higher extinction than the background stars, the correction for extinction will make the SDEs even more significant.

In a separate project, Hodapp & Deane (1992) imaged several much larger regions in L1641 with a sensitivity compatible with our imaging in *K'*. In two 12' × 12' areas that do not contain any *IRAS* source, no SDE can be seen using the same SDE criterion. In a *JHK* survey of a 0.75 square degree region in L1641 with the SQIID camera, Strom (1992, *private communication*) also concluded that the aggregation of near-IR sources could only be found near the *IRAS* sources. Therefore the SDEs we observed in the vicinity of the 14 *IRAS* sources are physically associated with the *IRAS* sources, and they are not in the foreground or the background.

There are a total of 70 stars with $K'_0 < 11$ in the 14 SDEs. What is the nature of these sources? Many of them are detected for the first time, and there is little spectroscopic information available. A detailed optical and infrared analysis of 3 sources (8, 18, 75) with SDEs shows that at least 60% of the near-IR sources in the vicinity of the *IRAS* sources are YSOs (Chapter 5). The near-IR spectroscopic observations of

sources near source 8 (L1641-N) by Hodapp & Deane (1992) also reached the same conclusion. We now use the broad-band photometry to show that most of 70 near-IR sources in the SDEs may also be YSOs.

A G0 main-sequence star should have an apparent magnitude of K'=11.5 at the distance of L1641 (480 pc). Since our SDE selection requires all the sources in the SDEs brighter than $K'_0 = 11$, one might conclude that all these 70 sources are early-type stars with a spectral type earlier than G0. The aggregation of so many early type stars is highly unlikely. Besides, from the optical information of 17 stars near sources 8, 18, and 75, we found that 15 of them have spectral type later than G0 (section 5.3.2).

This dilemma can be solved if these sources are surrounded by circumstellar dust. The circumstellar dust may change the K' magnitude in two ways. First, because the dust is usually colder than the stellar photosphere, its thermal emission peaks at the near-IR wavelengths. This will add additional flux to enhance the K' magnitude. Secondly, the colder dust lowers the effective temperature of the star, and makes the star redder (with higher $H - K'$) than what the interstellar extinction can account for. Equation 4.1 therefore overestimates the interstellar extinction. In either case, the presence of the circumstellar dust strongly suggests that most of the sources in the SDE are the pre-main-sequence (PMS) stars, since the PMS stars like T Tauri stars are known for their infrared excess. This is also consistent with our observations that 10 of 14 SDEs are associated with the infrared nebulosity, indicating that they are embedded sources.

In summary, 14 of 59 *IRAS* sources we imaged are associated with SDEs whose surface density of bright stars is significantly higher than that of the background. The near-IR sources in the SDEs are physically associated with the corresponding *IRAS* sources. Most of these sources are probably PMS stars. It is important to note that we adopted a rather conservative criterion in defining the SDE. It is possible that many other PMS stars are only slightly more luminous than their main-sequence counterparts,

and could not be selected by our criterion. The number of SDEs and the number of stars within each SDE may be much higher. In Chapter 6, we will further discuss the association of the SDEs with molecular dense cores, the formation of the SDEs, and its implication to star formation theory.

4.4. THE EVOLUTIONARY STATE OF THE *IRAS* SOURCES

By plotting the 59 sources in the *IRAS* 12-25-60 μm color-color diagram (Figure 4.3), we found that most of them are located in the regions occupied by the T Tauri stars or dense molecular cores (Beichman 1986). This suggests that they might be YSOs. To determine the evolutionary state of the sources more accurately, we need to compare the *IRAS* data with near-IR data.

Most of the near-IR emission we detected in the imaging comes from the dust heated by the embedded sources. The dust properties and spatial distribution can gradually change at the early stages of star formation. The spectral energy distribution (SED) based on broadband photometry between 1-100 μm measures these changes, and can therefore be an indicator of the evolutionary state of YSOs (Lada 1987; Adams, Lada & Shu 1987). The detection of the SDEs in the previous section complicates the comparison of the *IRAS* data with the near-IR data. Since many of our near-IR images show multiple sources within the *IRAS* position uncertainty, it is important to identify the near-IR counterparts of the *IRAS* sources, the near-IR sources that contribute most of the *IRAS* fluxes. Once the identifications are made, we can combine the near-IR and the *IRAS* data to construct the meaningful SEDs.

Most existing near-IR photometric data in L1641, as compiled by Strom et al. (1989b), were obtained with single detector photometers. The low sensitivity ($K < 14$) and small spatial coverage prevents a reliable identification of the *IRAS* counterparts.

Our near-IR imaging provides a comprehensive census of near-IR sources near the *IRAS* sources with a much higher sensitivity (more than 3 mag deeper in *K'*), a much higher resolution (0.75" pixels^{-1}), and a much larger spatial coverage (a 4' × 4' area centered on each *IRAS* position). In the following we first identify the near-IR counterpart of the *IRAS* sources. Using these identifications, we will examine their evolutionary states.

4.4.1. *Identifying the Near-IR Counterparts of the* IRAS *Sources*

We used the following criteria in the identification: (1) the *IRAS* counterpart should be located within 1' from either the *IRAS* position or the PSC position to account for the position discrepancy (see the discussion in section 2.2.4); (2) the source should be very red; (3) the near-IR flux at the longest detectable wavelength should smoothly match the flux at 12 μm; and (4) where available, optical and millimeter data were taken into account. A detailed description of the identification for the individual sources can be found in Appendix D. The identifications of the 59 *IRAS* sources can be divided into three categories:

(1) *positive identification* For 46 sources, there is a near-IR source that most probably contributes most of the *IRAS* emission. Some sources (i.e. sources 18, 75, and 163) show several near-IR sources with compatible brightness in *K'* within the *IRAS* position uncertainty. However, when imaged at the longer wavelengths (*nbL* and *M*), we detected one source that becomes the brightest source in the field. These red sources were selected as the most probable candidates. A detail analysis for sources 18 and 75 are presented in Chapter 5. The imaging at 3-5 μm is proved to be a very powerful tool in the identification.

(2) *Multiple sources* At least 9 sources show signs of multiple heating sources within the *IRAS* beam. An extreme case can be found near source 8 where several near-

IR sources are very bright even in *M* (see Chapter 5). Although we find the source detectable only at *M* band as the most possible candidate of the *IRAS* source, the other sources may also contribute significant flux in the *IRAS* bands. For these sources, imaging at 10 μm is critical for the identification.

(3) *No identification* For 4 sources (sources 41, 78, 93, 133), we cannot identify any near-IR counterpart of the *IRAS* sources either because the sources in the fields are not red, or because they are too bright to match the *IRAS* flux at 12 μm. The embedded sources may be too faint to be detected by our observations.

The following analysis will be carried out for the 55 sources that have probable near-IR counterparts, although 9 of them may be multiple sources. The 55 near-IR counterparts are indicated in the *K'* images in Figure A4.1. The properties of the identified near-IR counterparts of the *IRAS* sources are compiled in Table 4.3. Column [1] is the *IRAS* source number; columns [2] and [3] give the coordinates of the near-IR sources identified as the counterparts; columns [4] and [5] are the position offsets of the near-IR sources from the *IRAS* coadded positions and the PSC positions, respectively; columns [6]-[9] give the *H*, *K'*, *nbL* and *M* band photometry of the near-IR sources; column [10] indicates whether there is any indication of multiple heating sources; column [11] lists their SED indexes (see below for discussion).

4.4.2. *The Spectral Energy Distributions*

Once the identifications were made, we used the 1.6-100 μm photometric data to plot the spectral energy distributions of the sources in Figure A4.2. Following Lada (1991), we can define a spectral index α as follow:

$$\alpha = \frac{d \log(\lambda f_\lambda)}{d \log(\lambda)} = \frac{\log(25\, f_{25}) - \log(2.1\, f_{2.1})}{\log(25) - \log(2.1)} \qquad (4.2)$$

where f_{25} and $f_{2.1}$ are the flux densities at 25 μm and 2.1 μm. The spectral indexes of the 55 sources are listed in Table 4.3. If we define sources with $\alpha > 0$ as class I sources, and those with $-2 < \alpha < 0$ as class II sources, we have 45 class I sources and 10 class II sources. There are no class III sources (whose spectral index $\alpha < -2.0$) in our sample. Ten of the 11 outflow sources are the class I sources.

The high percentage of class I sources in our sample is probably due to the selection effects. As mentioned in Chapter 2, the *IRAS* selected sample is biased against the class II and III sources because their relatively higher color temperatures. The selection of sources with high ^{13}CO column density for this work imposed another bias against the class II and III sources. The other complication comes from the possible multiple heating sources within the *IRAS* beam. The confusion of *IRAS* flux densities caused by the multiple sources would result in an overestimation of f_{25} and α.

4.5. DISCUSSION

4.5.1. *Young Star Distribution in L1641*

Although L1641 was originally defined as a dark cloud of about 6 square degree (Lynds 1961), the CO survey (Kutner et al. 1977) showed it is part of the Ori A giant molecular cloud that extends from -2^o to -10^o (see Fig 1.3). In the region north of -6^o, the star formation is dominated by the Trapezium Cluster (Herbig 1962). With I-band imaging, Herbig & Terndrup (1986) detected 150 stars in a region of 3' × 3'. When imaged at K using a near-IR camera, McCaughrean (1988) detected over 500 stars at K <

15 within a 5' × 5' region centered on Trapezium OB star in Trapezium Cluster. The star formation in Trapezium Cluster is probably coeval (Zinnecker, McCaughrean & Wilking 1992).

The star formation in the region south of Dec = -6°, however, appears significantly different. The *IRAS* sources in L1641 are almost uniformly distributed throughout the region from -6° to -10° (Strom et al. 1989a, see also Chapter 2). The 11 CO outflow sources are also spread along the ridge of the molecular gas density enhancement, indicating that recent star formation occurs throughout the molecular cloud. Although L1641 is not fully mapped in the near-IR, our imaging of the 59 *IRAS* sources provides thus far the most comprehensive census of star forming activity in the L1641 dark cloud, because the 59 *IRAS* sources represent a large fraction of the YSOs detected by *IRAS* in the L1641.

The young stars we imaged are distributed very differently from the Trapezium Cluster. Forty-five of the 59 sources are individual sources or have only 2-3 near-IR sources in the vicinity. The 14 *IRAS* sources that are associated with SDEs present an intermediate case that is significantly different from either the Trapezium Cluster or the isolated star formation. The SDEs have 10-40 sources in each field down to $K' = 17$. Although extinction toward the *IRAS* sources we imaged might be higher, it does not seem able to account for the difference between the SDEs and the Trapezium Cluster. In summary, the young stars in L1641 are not only in large-scale cluster (the Trapezium Cluster), but also in isolation and in SDEs. This indicates that, at least in case of L1641, young stars can be formed with a range of stellar densities within a single molecular cloud. The previously proposed cluster and isolation modes could be the high and low ends of this continuous surface density distribution, while the SDEs represent an intermediate case.

Although it is unclear what causes the difference between the Trapezium Cluster and the rest of the L1641, the external triggering may play an important role. Star formation in Orion was probably triggered by a series of several tens of supernovas (Cowie, Songaila, & York 1977). As the result, four OB clusters (Ia, Ib, Ic, and Id) were formed sequentially at Dec= 2^{o} and -5.5^{o} (Blaauw 1991). Star formation in the Trapezium Cluster might be consequently triggered by the nearest OB cluster, Ic, with an age of 6×10^{6} yrs, and coevally formed stars into a large cluster. On the other hand, the molecular gas south of Dec = -6^{o} remains undisturbed by the external forces. The low-mass star formation can rise and continue spontaneously under self-gravity whenever and wherever the physical conditions are favorable. External triggering is probably playing a less important role in the formation of SDEs and isolated stars. This is consistent with the fact that the SDEs and isolated stars are evenly distributed throughout the L1641.

4.5.2. *Comparison with* IRAS *Sources in Perseus and Taurus*

How does the star formation in L1641 compare with the star formation in other molecular clouds? In the following, we compare the spectral energy distribution of the 55 *IRAS* sources in L1641 with a group of *IRAS* sources in Perseus and Taurus selected by Ladd, Lada & Myers (1992). The 23 *IRAS* sources in Perseus are mostly deeply embedded sources with the *IRAS* flux density at 60 μm greater than that at 25 μm. This selection criterion is similar to ours, because we have shown in Chapter 3 that the cold *IRAS* sources are usually associated with high ^{13}CO column density. The 29 *IRAS* sources in Taurus were selected by the same criterion, except that their flux densities are a factor of 2.5 higher than those in Perseus to compensate the selection effect due to the different distances.

Following Ladd (1991), we use the mean-frequency to characterize the SED. The mean-frequency is defined as the first moment of frequency weighted by the flux density:

$$\text{Mean frequency} = \int_{\nu_1}^{\nu_2} \nu f_\nu d\nu \Big/ \int_{\nu_1}^{\nu_2} f_\nu d\nu \qquad (4.3)$$

where f_ν is flux at frequency ν, and the integrations should be performed over entire observable frequency range (from ν_1 to ν_2). In this study, we calculate the mean frequency over the wavelength range of 2-135 μm.

Figure 4.4 compares the histograms of the mean-frequency of the 55 sources in our sample with those of Perseus and Taurus. Evidently the distribution of mean-frequency of *IRAS* sources in L1641 is very similar to that in Perseus, and both of them are very different from that in Taurus. The Kolmogorov-Smirnov test shows no significant difference between the histograms for L1641 and Perseus, but the L1641 sample is different from the Taurus sample at 95% level of significance. Since the lower mean-frequency means the SED increasing toward the longer wavelengths, Figure 4.4 indicates that the *IRAS* sources in L1641 and Perseus are more deeply embedded than those in Taurus.

The above difference can be understood if the dense (dust and molecular) cores in L1641 and Perseus are statistically larger and more massive than those in Taurus. It is consistent with the millimeter observations: the 11 ^{13}CO molecular cores we detected in L1641, as discussed in Chapter 3, are a factor of 5-10 more massive than those detected with the same telescope in Taurus (Ohashi 1992). Harju, Walmsley & Wouterloot (1992) reached the same conclusion in their NH_3 survey. Ladd (1991) also showed that the NH_3 cores in Perseus are a factor of six more massive than those in Taurus.

Since the *IRAS* sources in Perseus and Taurus have not been imaged in the same depth and coverage, we do not know if they also are associated with the SDEs. There are however some similarities between the L1641 and Perseus. The spatial distributions of both molecular clouds are highly elongated. Each molecular cloud contains a large cluster (Trapezium cluster in L1641 and NGC 1333 in Perseus). The K imaging of 23 *IRAS* sources in Perseus (Ladd et al. 1992) also showed many young stars not in the cluster. The mixture of the young stars inside and outside the clusters seems to be the characteristics of both clouds. The near-IR imaging of *IRAS* sources in Perseus similar to what we presented here can be very useful for us to understand the role of SDEs in star formation in a broader content.

4.6. SUMMARY

We obtained 1.5 - 4.8 μm images of 59 *IRAS* sources in L1641. Most of them are associated with dense molecular gas. The main results are summarized as follows:

(1) Twenty-six of the 59 sources show nebulosity. Although the diffuse nebulosities are probably the scattered light from the embedded YSOs, some nebulosities show very elongated structures. In particular, the highly elongated bipolar structures originated from source 36 resemble the optical jets with HH objects.

(2) We find that 14 *IRAS* sources are associated with stellar density enhancement, including 7 of 11 outflow sources. Most of the near-IR sources in the SDEs are probably PMS stars physically associated with the *IRAS* sources.

(3) Using 1.6-4.8 μm images and photometric data, we were able to identify the near-IR counterparts for 55 *IRAS* sources, although 9 of them show signs of multiple heating sources within the *IRAS* beamsize. The identifications improved the comparison of near-IR data with *IRAS* data, especially in very crowded regions.

(4) The spatial distribution of young stellar objects in L1641 can be characterized by a range of stellar densities, from a large cluster (the Trapezium Cluster) to the SDEs and to individual stars. The cluster may be a result of external triggering, while the SDEs and individual young stars may be formed in self-gravity in the relatively isolated regions.

(5) The mean-frequency distribution of the *IRAS* sources in L1641 is similar to that in Perseus, and very different from that in Taurus. This may be resulted from the fact that the molecular dense cores in L1641 and Perseus are statistically more massive than those in Taurus.

TABLE 4.1 59 *IRAS* SOURCES IMAGED IN NEAR-IR

No.	ID	Bands imaged	SDE	Nebulosity	No.	ID	Bands imaged	SDE	Nebulosity
8	L1641-N	*HK'nbLM*	Y	diffuse	108	L1641-S3	*HK'nbLM*		spiral
18	MSSB 8	*HK'nbLM*	Y	spiral	119		*HK'*		
25	HH 33	*HK'nbL*		diffuse	120		*HK'*		
29		*HK'nbL*			133		*HK'*		
32	V846 Ori	*HK'*			134		*HK'*		
34		*HK'*			146		*HK'*		
36	MSSB 18	*HK'nbLM*		bipolar	150		*HK'*		
41		*HK'*			160		*HK'M*	Y	elongated
42		*HK'*			163		*HK'nbLM*		spiral
46	HD 37357	*HK'*			168		*HK'*		
47	V380 Ori	*HK'nbL*	Y	diffuse	171		*HK'*		
49		*HK'nbL*			177		*HK'*		
50		*HK'*	Y	diffuse	181		*HK'M*		elongated
51	HH 1-2	*HK'nbL*	Y	elongated	186		*HK'nbL*		
62		*HK'*			187		*HK'*		
71	T456	*HK'*	Y		191		*HK'*		
72		*HK'*			193		*HK'nbL*	Y	diffuse
75	L1641-C	*HK'nbLM*	Y	bipolar	194	L1641-S4	*HK'nbLM*	Y	diffuse
78		*HK'*			198		*HK'M*		bipolar
79	Haro 13a	*HK'*		diffuse	211		*HK'M*	Y	elongated
83	Haro 14a	*HK'*		elongated	216	L1641-S2	*HK'nbLM*		elongated
85		*HK'M*		cone	224		*HK'*		
87		*HK'*		spiral	237		*HK'*		diffuse
93		*HK'*			243		*HK'*	Y	
95	V599	*HK'*			245		*HK'*	Y	
99		*HK'nbL*		diffuse	246		*HK'M*		
101		*HK'*			256		*HK'*		elongated
104	H 4-255	*HK'nbLM*	Y	diffuse	270		*HK'*		
105	Re50	*HK'*		diffuse	280		*HK'*		
106		*HK'*							

TABLE 4.2 OBSERVATION LOG

Date	Telescope	Camera	Format (pixels)	Scale (arcsec pixel^{-1})	Bands	λ (μm)	$\Delta\lambda$ (μm)
12/90	UH 2.2 m	NICMOS3	256 × 256	0.75	*H*, *K'*	1.65, 2.1	0.4, 0.5
1/91	UKIRT	IRCAM	58 × 64	0.61	*nbL*	3.6	6% × 3.6
1/91	UH 2.2 m	NICMOS3	256 × 256	0.75	*H*, *K'*	1.65, 2.1	0.4, 0.5
1/91	IRTF	ProtoCam	58 × 64	0.35	*M*	4.8	0.3
2/92	IRTF	ProtoCam	58 × 64	0.35	*M*	4.8	0.3

TABLE 4.3 NEAR-IR COUNTERPARTS OF THE *IRAS* SOURCES

IRAS	NIR position					NIR-*IRAS*		NIR-PSC		*H*	*K'*	*nbL*	*M*	Multiple	SED
No	α (1950) 5^h		δ (1950)			Δα	Δδ	Δα	Δδ	mag	mag	mag	mag	source	α
[1]	[2]		[3]			[4]		[5]		[6]	[7]	[8]	[9]	[10]	[11]
8	33^m	52.4^s	-6^o	23'	59"	-53"	8"	-4"	3"	>17.5	>17.5	>13.0	8.6	Y	4.2
18	33	57.2	-6	26	38	-12	-2	-41	11	16.3	13.0	9.8	7.8		1.7
25	33	5.9	-6	28	48	43	-11	97	1	13.7	12.6	10.7			2.0
29	33	40.5	-6	34	4.7	22	-28	...	...	10.5	9.8	8.4	...		0.7
32	34	15.1	-6	35	46	1	-9	4	1	10.0	9.4	...	...		-0.2
34	33	15.5	-6	37	48	-8	-11	-21	-35	>17.5	16.1	...	...		2.0
36	34	9.2	-6	40	18	-27	-26	-81	-28	>17.5	15.3	>13.0	>11.0		2.8
42	34	24.8	-6	43	20	-34	2	-95	2	12.5	10.9	...	...		0.4
46	35	21.2	-6	44	11	17	-4	-4	-1	8.0	7.4	...	...		-0.4
47	33	59.5	-6	44	43	23	-6	2	2	7.3	6.4	4.9	...		-0.4
49a	33	30.8	-6	45	12	13	-5	-4	19	16.3	15.2	...	...		2.3
49b	33	29.8	-6	45	25	-2	-18	-19	6	16.8	15.7	...	...		
50	33	59.1	-6	46	29	16	-8	16	4	9.3	8.2	...	...		0.4
51	33	52.9	-6	47	12	-46	-5	5	-13	>17.5	16.3	...	...	Y	3.1
62	35	43.3	-6	50	57	34	-5	7	-1	8.6	7.7	...	...		-0.3
71	35	28.8	-6	58	27	-3	-5	-28	-3	10.2	9.9	...	...		-0.2
72	34	58.8	-7	0	15	-2	-23	-26	-4	11.8	10.7	...	...		0.5
75	36	20.5	-7	2	26	-7	-5	-5	17	>17.5	18.2	10.8	8.2		3.8
79	35	52.7	-7	4	6.2	-5	-14	-9	1	6.8	5.2	...	...		0.3
83	35	42.1	-7	10	10	-29	-3	1	2	13.7	11.9	...	...		0.8
85	36	46.3	-7	12	11	65	-4	52	7	>17.5	14.7	...	8.7		2.3
87	36	40.1	-7	12	41	-14	-4	...	...	11.4	10.7	...	8.0		0.8
95	36	33.4	-7	18	24	52	-17	-8	-2	8.3	7.4	...	...		-0.3
99	36	27.1	-7	22	44	17	-8	16	0	13.6	12.2	10.1	...		1.1
101	37	24.9	-7	25	18	-1	-26	47	-12	>17.5	15.6	...	...	Y	1.9
104	36	54.4	-7	27	56	-24	11	-30	18	12.3	10.8	9.0	7.7		1.0
105	38	2.4	-7	29	0.3	5	-8	-5	-1	11.3	9.6	...	...		1.8
106	36	29.4	-7	29	31	7	-24	-8	-1	11.0	10.2	...	...		-0.1
108	37	29.8	-7	31	51	42	-14	-19	8	>17.5	16.2	>13.0	9.4		3.3
119a	38	4.0	-7	38	41	0	11	-27	18	14.5	13.3	...	...	Y	0.6
119b	38	6.1	-7	38	30	31	22	4	-29	12.7	11.5	...	...		
120	37	34.1	-7	39	4.8	2	2	-4	0	10.1	9.8	...	...		0.0
134	38	0.0	-7	44	37	-15	0	-9	3	15.4	13.3	...	...		1.0
146	37	53.0	-7	49	58	-30	-6	14	6	12.5	10.7	...	...		0.9
150	38	55.0	-7	52	7	-45	-15	-10	0	17.5	14.0	...	...		1.4
160	39	0.2	-7	56	33	-12	-11	14	7	>17.5	15.0	...	8.1		2.4
163	37	56.4	-7	57	54	-10	-2	4	9	16.5	14.8	11.4	8.2		2.3
168	38	57.5	-7	59	30	-22	-8	-14	0	12.7	10.8	...	...		0.4
171a	40	2.1	-8	0	12	1	-5	20	1	11.0	10.4	...	...	Y	0.3
171b	40	2.0	-9	0	18	-1	-11	19	-5	11.5	10.9	...	...		
177	38	13.9	-8	2	5.5	-32	-14	-5	-2	17.2	14.9	...	...		1.5
181	39	3.5	-8	2	35	8	-13	17	-7	>17.5	16.0	...	>11.0		2.0

TABLE 4.3 - *Continued*

IRAS No	NIR position α (1950) 5^h		δ (1950)		NIR-*IRAS* Δα	Δδ	NIR-PSC Δα	Δδ	H mag	K' mag	nbL mag	M mag	Multiple source	SED α
[1]	[2]		[3]		[4]		[5]		[6]	[7]	[8]	[9]	[10]	[11]
186	39	5.9	-8	5	5.5	-17	2	-4	-1	13.3	10.8	8.2	...		0.9
187	38	13.0	-8	5	17	-29	5	1	16	8.8	8.1	...	...		0.0
191	39	1.0	-8	7	18	-14	-11	5	2	11.3	10.5	...	...		0.8
193	38	25.6	-8	7	27	-22	10	-109	-6	>17.5	14.6	12.5	9.6	Y	2.2
194	38	24.8	-8	8	25	-33	-18	3	-5	>17.5	16.4	14.6	12.3		2.7
198	39	11.2	-8	9	47	-12	-10	-55	-3	15.7	14.6	...	>11.0		1.9
211	37	56.9	-8	15	26	-20	11	11	11	14.1	12.1	...	8.2		0.9
216	40	22.9	-8	18	26	14	-5	-6	0	13.2	11.4	8.7	7.3		1.2
224	39	21.1	-8	22	56	2	-4	-17	1	11.3	10.5	...	...		0.1
237	39	10.3	-8	36	52	-10	-15	-13	-1	11.7	9.5	...	...		0.2
243	40	24.2	-8	39	55	3	-3	...	...	10.6	9.3	...	...	Y	-0.1
245a	40	24.4	-8	41	29	6	-7	-52	-8	12.8	11.4	...	...	Y	0.8
245b	40	24.6	-8	41	27	9	-5	-49	-6	13.2	11.6	...	...		
246a	39	6.3	-8	41	36	-11	2	-4	6	15.7	12.7	...	8.8	Y	0.7
246b	39	6.6	-8	41	44	-6	-7	0	-2	14.5	12.0	...	8.8		
256	40	43.5	-8	45	49	-23	-12	3	1	>17.5	16.7	...	...		2.5
270	38	30.7	-9	7	32	-34	-10	10	1	11.3	9.8	...	...		0.4
280	38	41.3	-9	24	47	-41	-10	-14	-1	12.7	12.3	...	...		1.4

Source 29

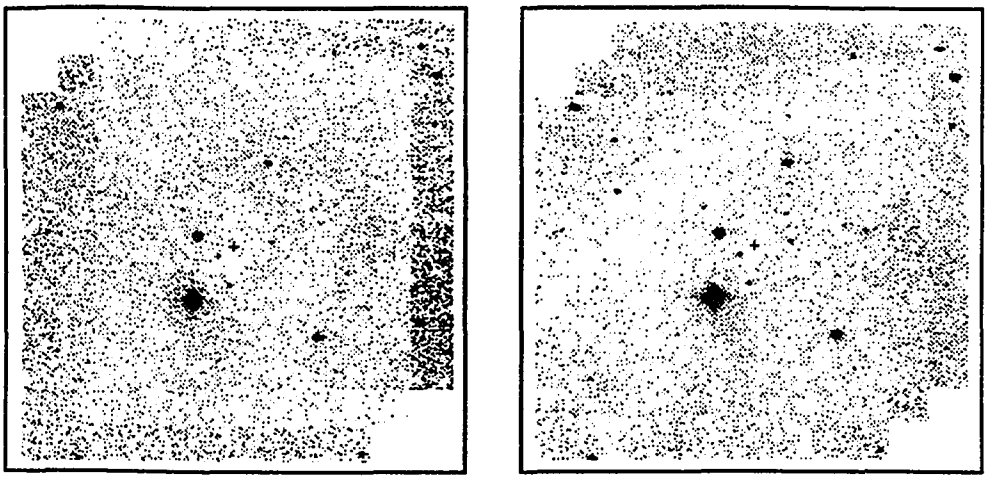

H K'

Source 71

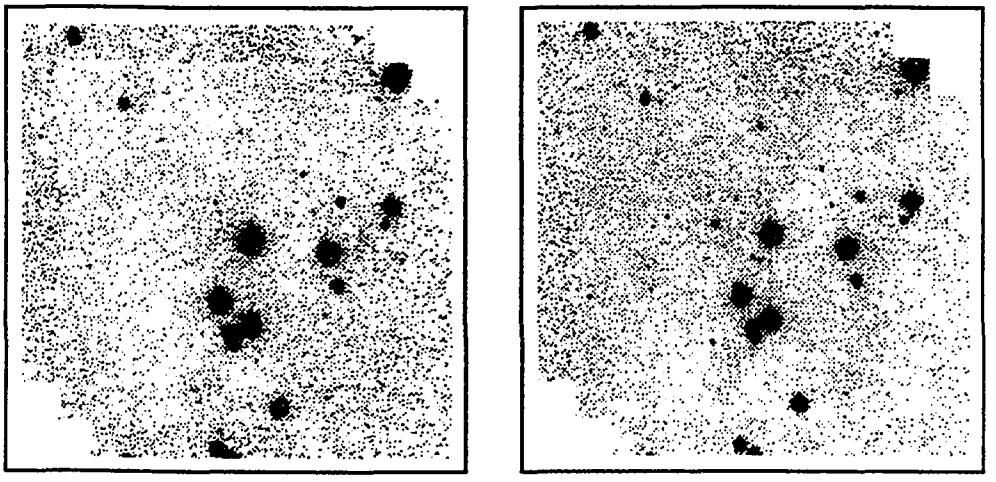

H K'

Figure 4.1. The examples of sources that are in isolation (source 29) and sources that are in the stellar density enhancement (source 71). The *H* and K' images (each covers a 4' x 4' area) are centered on the *IRAS* position (marked by the cross). The spatial resolution is 0.75" pixel^{-1}. The identified the candidates for the *IRAS* counterparts are marked on the *K'* images. North is up, and the east is to the left.

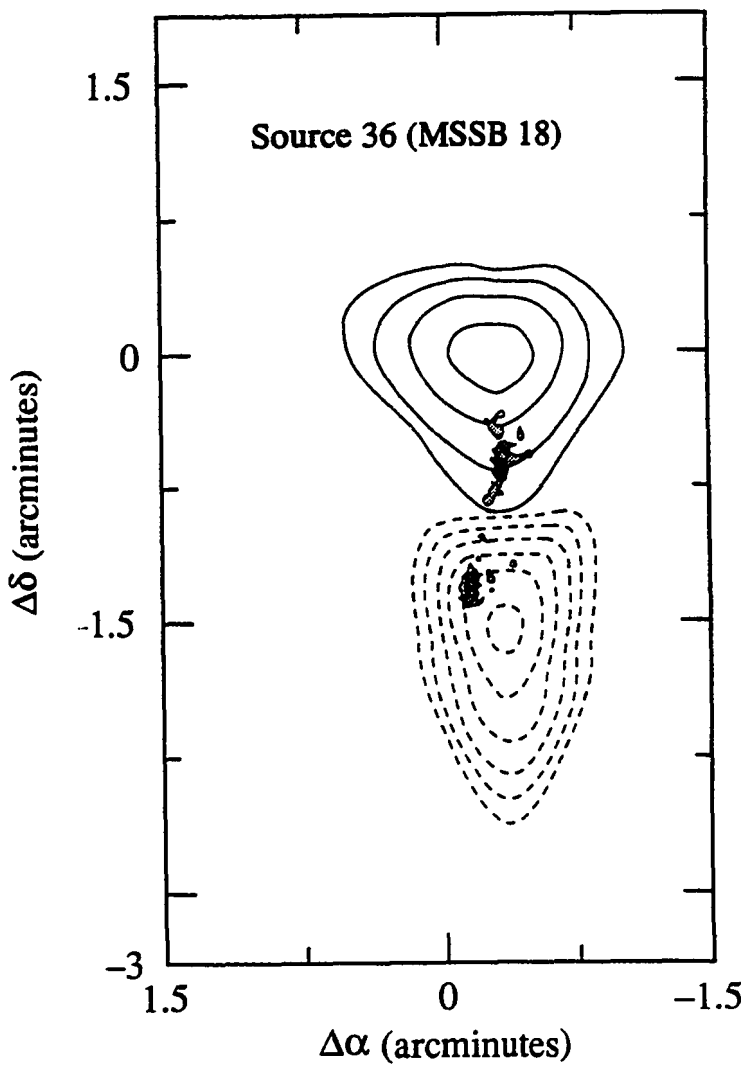

Figure 4.2. The elongated bipolar structure of source 36 overlaid on the CO molecular bipolar outflow MSSB 18 detected by Morgan et al. (1991). The solid contours are the blue-shifted lobes and the dash ones are the red-shifted. The elongated structures seen in *K'* image are showed by the shaded regions. (0,0) is the *IRAS* position.

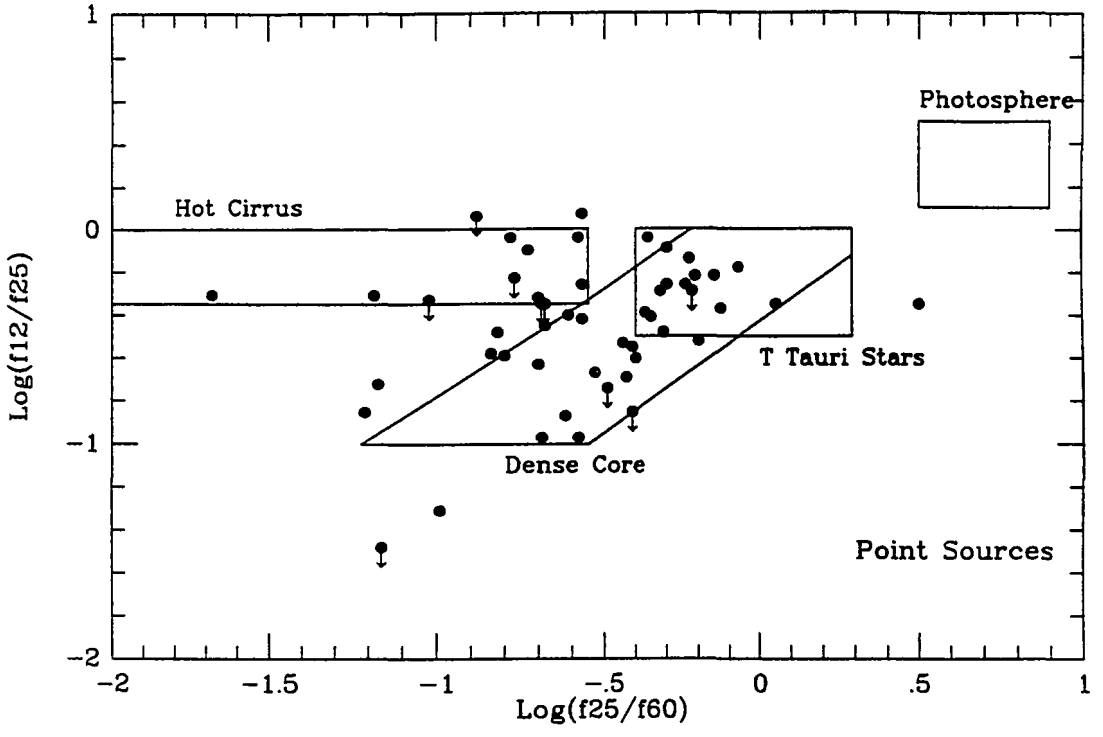

Figure 4.3. The color-color diagram based on the *IRAS* flux densities at 12, 25 and 60 μm. The boxes representing the loci of various sources are from Beichman (1986). For sources not detectable at 12 μm, the downward arrows indicate the 5 σ upper limit.

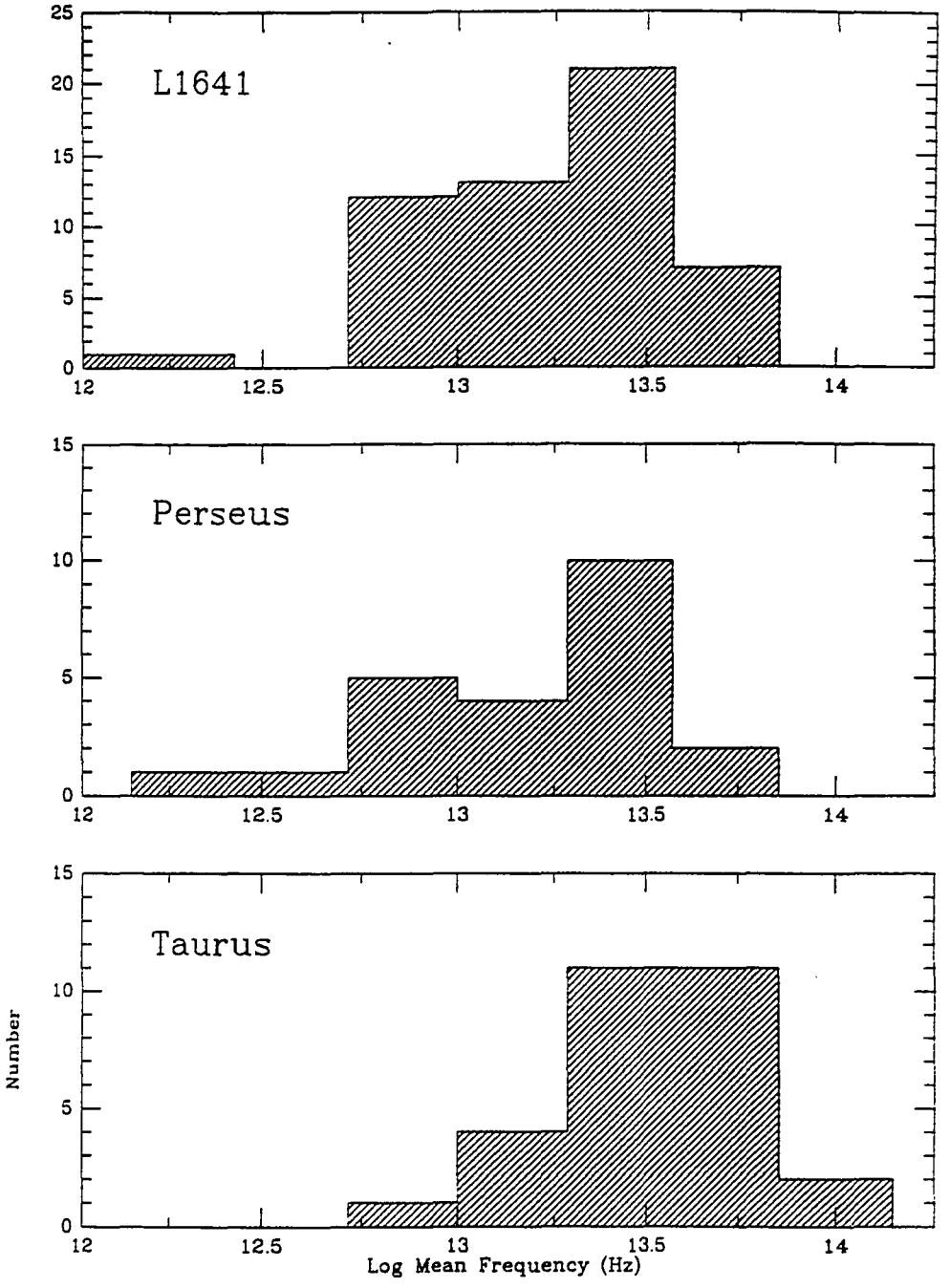

Figure 4.4. The histograms of the mean-frequency distributions of the *IRAS* sources in L1641 (top), in Perseus (middle) and in Taurus (bottom). The data of Perseus and Taurus are from Ladd, Lada & Myers (1992).

CHAPTER 5
IR AND OPTICAL IMAGING OF *IRAS* SOURCES WITH CO OUTFLOW: A SNAPSHOT OF EARLY STAR FORMATION[1,2,3]

5.1. INTRODUCTION

The driving sources of high-velocity CO outflows are young stellar objects (YSOs) with a dynamic age $<10^5$ yr (Lada 1985; Fukui 1989). Observing these sources allows us to study the environment in which protostars are forming and from which the pre-main-sequence (PMS) stars have not yet dispersed. While the analysis of *IRAS* data has provided a great deal of insight into the physical process of star formation, the large *IRAS* beamsize (1'-3') and the extended emission of some sources at mid-IR wavelengths often cause source confusion in crowded regions. Imaging with near-IR provides both high spatial resolution and high sensitivity, and allows us to observe details that are unresolved in the *IRAS* observations.

In this chapter we report on optical (*BVRI*) and infrared (*HK'nbLM*) imaging of three *IRAS* sources with CO outflows. The infrared and optical observations and data analysis are discussed in section 5.2. Using the optical and infrared photometric data, we show in section 5.3 that there are many bright near-IR sources in the vicinity of the *IRAS* sources, and most of them are YSOs. In section 5.4 we discuss the identification of near-IR

---

[1] Part of this work is based on the observations carried out at Infrared Telescope Facility, which is operated by the University of Hawaii under contract from the National Aeronautics and Space Administration.

[2] Part of this work is based on the observations carried out at United Kingdom Infrared Telescope, which is operated by the Royal Observatory Edinburgh on behalf of the U.K. Science and Engineering Research Council.

[3] Part of this work is based on the observations carried out at Kitt Peak National Observatory, National Optical Astronomy Observatories, which is operated by the Association of Universities for Research in Astronomy Inc. (AURA), under cooperative agreement with the National Science Foundation.

counterparts of the *IRAS* sources using 1-5 μm images; in section 5.5, we suggest that the stellar density enhancements found near the 3 IRAS sources result from a continuous star formation with an age span of 1-3 Myr. Major conclusions are summarized in section 5.6.

5.2. OBSERVATIONS AND DATA REDUCTION

5.2.1. *Three* IRAS *Sources*

The three sources reported on here are associated with CO outflows. Source 8 (05338-0624) is associated with the CO outflow L1641-North, first detected by Fukui et al. (1986). Although optically invisible, it is one of the most luminous *IRAS* sources (~220 $L_{\odot}$) in the region. Wilking, Blackwell & Mundy (1989) detected a 2.7 mm continuum source at the *IRAS* position, and near-IR imaging showed that a dense stellar concentration is centered on that position (Strom et al. 1989a, Chen, Tokunaga & Hodapp 1991). Source 18 (05339-0626) was listed in the catalog of Strom et al. (1989b) as source 11 (hereafter Strom 11). Morgan et al. (1991) detected a CO molecular outflow originating from this source. In this chapter, we study Strom 11 and L1641-N separately because they are two discrete *IRAS* sources associated with CO outflow, however, it is not entirely clear whether the outflow from Strom 11 is part of the L1641-N outflow. Source 75 (05363-0702) is associated with a CO outflow L1641-C (Fukui et al. 1986). Although Morgan et al. (1991) argued that the high-velocity wing may be a result of multiple-velocity-components, recent CO J=2-1 and CO J=3-2 observations (Sugitani et al. 1992) have confirmed that there is indeed a high-velocity outflow from the *IRAS* source.

5.2.2. *Observations and Data Reduction*

The infrared data used in this chapter is part of our near-IR imaging of 59 IRAS sources reported in Chapter 4. The detail description of the observations and data reduction can be found in sections 4.2.2 and 4.2.3. The optical data used in this chapter was obtained by Dr. Karen Strom using #1 0.9 m telescope at Kitt Peak National Observatory. The optical observations were taken with the 2048 × 2048 Tektronix CCD camera with a plate scale of 0.77" pixel^{-1}. The "Mould" standard filter set was used with the *B* and *V* filters on the Johnson system and the *R* and *I* filters on the Kron-Cousins system. Standards chosen from the Landolt set of equatorial standards (Landolt 1983) were observed throughout the night to measure the extinction and to establish the zero point and color terms of the magnitude system. The images were reduced using CCDRED package. The photometry on the reduced images was obtained using the APPHOT package. The 5 σ limiting magnitude is $R = 20.0$ and $I = 19.0$.

The positions and the optical and near-IR photometric data for the sources in L1641-N, Strom 11, and L1641-C are presented in Tables 5.1, 5.2, and 5.3, respectively. In the three tables, column 1 gives the near-IR source numbers: the first letter denotes the associated *IRAS* sources (N for L1641-N, S for Strom 11, and C for L1641-C); columns 2 and 3 are the source positions; columns 4-11 give the photometric data.

5.3. RESULTS

5.3.1. *Stellar Density Enhancements*

Figures 5.1, 5.2, and 5.3 display the near-IR images of L1641-N, Strom 11, and L1641-C, respectively. There are many near-IR sources found around each *IRAS* source.

Besides the previously discovered young stellar cluster near L1641-N (Strom et al. 1989a; Chen et al. 1991), we also see stellar density enhancements near Strom 11 and L1641-C. We believe that most of the sources we detected are associated with the *IRAS* sources for the following reasons:

(1) Most near-IR sources in Figures 1-3 are associated with complex nebulosity, which indicates the presence of dust in the immediate vicinity.

(2) Most of the near-IR sources near L1641-N and L1641-C are in or near the molecular dense cores detected in the HCO^+ J=1-0 line (see Chapter 3). Strom 11 was not mapped, but was found to have strong HCO^+ emission at the *IRAS* position.

(3) In an unbiased *K'* survey of L1641, Hodapp et al. (1992) mapped a much larger area (35' × 12') that was centered on L1641-N and Strom 11. Stellar density enhancements and nebulosity are found only near these *IRAS* sources.

In Figure 5.4, we compare the *K'* magnitude distribution of 89 sources detected in Figures 5.1-5.3 with 127 stars that were taken from a 10' × 6' nearby sky area mapped in the unbiased *K'* survey (Hodapp et al. 1992) with a similar detection limit. The Kolmogorov-Smirnov test shows that two samples are different at a 99.9% confidence level. The stars near the *IRAS* sources show a higher frequency of brighter sources than the field star distribution. This difference would be even more significant if the data were corrected for extinction because the sources in the vicinity of the *IRAS* position have higher extinction than the field stars, as indicated by the molecular gas distribution. This provides strong support for our argument that most of the near-IR sources in Figures 5.1-5.3 are physically associated with the *IRAS* sources.

5.3.2. *The Nature of the Sources*

What is the evolutionary state of the near-IR sources associated with the *IRAS* sources? To answer this question, we use the optical and near-IR broadband photometric data to study the extinction and infrared excess of the sources since spectroscopic information is available only for a few optically visible objects due to the high local extinction. The color of an object can be reddened by dust extinction or modified by near-IR emission of circumstellar dust. Where available we use optical photometry for determining the extinction, since photospheric emission dominates the flux at these optical wavelengths, and we use near-IR data as a measure of the circumstellar dust emission.

5.3.2.1. *Optical Sources*

In Figure 5.5 we plot the unreddened apparent V magnitudes (Allen 1973) at the distance of L1641 (480 pc) and the intrinsic $V - I$ colors (Bessell 1989) of B5-M5 main-sequence dwarfs. With extinction, stars would appear to be redder and fainter so as to move downward along the extinction tracks (the dotted lines). The slope of the extinction tracks is determined by the standard extinction law from Rieke & Lebofsky (1985), and each tick mark indicates $A_V = 1$ mag. Also plotted in Figure 5 are the 17 sources detected at V in the vicinity of the *IRAS* sources.

If the sources are main-sequence stars, their extinction and spectral type can be determined by their loci in Figure 5.5. In this case, 15 of the 17 sources would be late-type dwarfs (later than G0) with visual extinction of 2-7 mag. The inferred spectral type and extinction are listed in Table 5.4. For 3 sources (N2, N12, S15) that have been previously classified, the spectral types are much later than those inferred by this method, indicating that the stars are brighter than a main-sequence star of the same spectral type. A similar excessive luminosity was also found in T Tauri stars (Hartigan et al. 1989), and

for classical T Tauri stars it is due both to boundary layer emission and to their higher than main-sequence luminosity. Figure 5.5 suggests that most stars in the figure are late-type dwarfs even if their *V* magnitudes are enhanced by possible boundary layer emission.

Since the boundary layer emission is much smaller in *R* and *I* (Hartigan et al. 1989), the *R* - *I* color more nearly measures stellar photospheric emission. The *H* - K color, on the other hand, measures the relatively colder circumstellar dust emission. In Figure 5.6, we plot 22 sources detected in the *R*, *I*, *H*, and *K'* bands in the *R* - *I* vs. *H* - *K'* color-color diagram. Also plotted in the figure are the intrinsic colors of the main-sequence dwarfs (solid line) and the extinction vector. As shown in the figure 13 out of 22 sources (60%) are above the main-sequence track and cannot be explained by reddening of main-sequence stars. They are probably PMS stars with infrared excess. Of 8 stars that have been observed spectroscopically, six sources (N2, N12, N28, N29, S13, and S15) show Hα emission, suggesting again that they are PMS stars.

5.3.2.2. *Infrared Sources*

Since most of the sources that we detected in *K'* do not have an optical counterpart, we now use Figure 5.7 (*H* - *K'* vs. *K'*) to show that many of these objects are also YSOs. We plotted the intrinsic *H* - K colors (Koornneef 1983) and the apparent K magnitude of main-sequence dwarfs (Allen 1973) with spectral type of B5-M5 at the distance of L1641. The 74 stars that are detectable at *H* and *K'* in the three fields are plotted. If the stars are main-sequence stars and the reddening is due solely to extinction, the extinction correction will move the sources to the upper-left along the extinction tracks (dotted lines) to join the main-sequence track. Consequently 42 of the 74 sources (60%) should

have spectral type earlier than G0. This is in disagreement with our optical data (Fig. 5.5), which shows only 2 of 17 have an inferred spectral type earlier than G0.

This contradiction can be explained if most of these sources are YSOs. It is well-known that T Tauri-type PMS stars are associated with circumstellar dust colder than the stellar photosphere (Bertout 1990). The thermal emission of the circumstellar dust makes PMS stars much more luminous in the near-IR than their main-sequence counterparts. The near-IR excess will also make a star redder than what the extinction law could account for. We therefore argue that *at least 60%* of the near-IR sources in the vicinity of the three *IRAS* positions are YSOs. The infrared excess can also be used to explain the difference between the *K'*-magnitude distribution of these stars and that of the field stars (Fig 5.2).

5.4. IDENTIFYING THE NEAR-IR COUNTERPARTS

The spectral energy distribution (SED) is widely used to identify deeply embedded sources, or class I sources (Lada 1987). Adams, Lada, & Shu (1987) subsequently modeled these sources as proto-stellar objects surrounded by an accretion disk and a cold dust shell. Multiplicity presents a major difficulty when applying this method to the sources we imaged here. Since there are many YSOs nearby, it is important to know whether the SED is dominated by a single source or whether many sources contribute to the SED. Applying the following selection criteria, we have used our infrared images at *H*, *K'*, *nbL*, and *M* to identify the near-IR counterparts of the *IRAS* sources: (1) the near-IR counterparts have to be within 1' of the *IRAS* position. and (2) they should have steeply rising SEDs up to *nbL* or *M*. We now discuss the three *IRAS* sources in turn:

L1641-North This is the most complex region. Figure 5.8 shows the sources in the central 75" x 75" region near the *IRAS* position (the cross). The 2.7 mm continuum

source is also marked (the filled circle). The near-IR source positions at *H*, *K'*, *nbL*, and *M* are shown in different symbols. The positions are determined relative to N12 which is an optical star with low extinction ($A_V \sim 1.5$; see section 3.2.1). N1 is only detectable at *M* and is located within 3" of the *IRAS PSC* position. The *K'* positions of N14 and N15 have a displacement of 2" and 4" to their *nbL* and *M* positions. Such a large wavelength-dependent shift has also been seen in other star-formation regions (Campbell et al. 1988; Heyer et al. 1990; Ressler & Shure 1991) and probably indicates that the shorter wavelength images are scattered light from the embedded YSOs. The extended appearance of N14 and N15 at *K'* and the large-scale nebulosity indicates the presence of a large amount of scattered light. It is interesting to note that the position shifts of N14 and N15 are directed toward the region that corresponds to a dark area in the *K'* image (Fig. 5.1). This may indicate that multiple sources are embedded in this heavily obscured dense core. Although the *K'* position of N18 has a 6" displacement from the nearest *nbL* and *M* sources, it may not be the same source since N15 appears pointlike at *K'*.

We now use Figure 5.8 and the source SEDs (Fig. 5.9a) to identify the near-IR counterpart of the *IRAS* source. N10 is too far from the *PSC* position ($\Delta\alpha$ = 35" , $\Delta\delta$ = 20") and cannot be the counterpart. The fluxes of N11 and N12 decline at wavelength longer than 2.1 μm, and are likely to have little emission in the *IRAS* bands. N13 and N14 are not detected at *M*. N15 is the brightest object at *M*, and the slope between *nbL* and *M* is much steeper than the slope between *M* and 12 μm. This may be an indication that the fluxes at the shorter wavelengths are due to scattered light. Although N15 is a very red source, N1 has a much steeper SED because it can only be detected in *M*. N1 is also located within 2" of the position of the 2.7 mm continuum source detected by Wilking et al. (1989). We identify N1 as the most plausible candidate for the counterpart of the *IRAS* source, although N15 and the source near N18 may also emit significant far-IR flux.

Strom 11 There are *8* sources at the *K'* band that are within 30" from the *IRAS* position. Four of them have optical counterparts and are probably late-type PMS stars (see discussion in section 5.3.2). Of the other 4 sources associated with nebulosity, two sources (S5 and S8) are the reddest. Figure 5.9b shows the SED of the two sources. S5 is not detected in *H* (except for some diffuse scattered light), but it is much brighter at *K'* and *nbL*, and becomes the brightest source at *M*. On the other hand, the SED for S8 rises much more slowly. The redness of S5, and its association with strong nebulosity, makes it the prime candidate for the *IRAS* counterpart. Although S5 is located somewhat far from the *IRAS PSC* position ($\Delta\alpha$ = 36", $\Delta\delta$ = 10"), it is very close ($\Delta\alpha$ = 12", $\Delta\delta$ = 2") to the *IRAS* position determined from *IRAS* coadded image.

L1641-C As shown in our previous discussion, there are many stars in this field with large infrared excesses. Near the *IRAS* position, there are two very red sources of special interest. C21 shows strong bipolar nebulosity. C17 is invisible at *H* and barely visible in *K'*. It quickly becomes the brightest source in *nbL* and *M* bands. The SEDs of both sources are shown in Figure 5.9c. Considering also that C17 lies much closer to the *IRAS* position ($\Delta\alpha$ = 7.5" , $\Delta\delta$ = 4.5") and is a much redder object, it is most likely the counterpart of the *IRAS* source.

If the above identifications are correct, and if the 25 μm *IRAS* flux comes from the single source as we have identified, the spectral index, $d(\log \lambda f_\lambda)/d(\log \lambda)$, over the range 2.1-25 μm is > 4.0, 1.7, and > 3.6 for L1641-N, Strom 11, and L1641-C, respectively. For comparison, the highest spectral index found in Taurus is 3.2 (Myers et al. 1987). However, caution must be exercised because of possible source confusion and scattered light contributions, especially for L1641-N. The definitive identification of the *IRAS* sources will require high spatial resolution imaging at 10 μm and longer wavelengths.

5.5. DISCUSSION

5.5.1. *Spectral Energy Distribution*

The spectral index of YSOs (i.e., the ratio of source flux density at 2.2 μm to that at 12 or 25 μm) has been widely used as an indicator of the evolutionary status of the sources. It is however subject to source confusion and scattered light problems. The group associated with L1641-N shows serious complications due to source confusion. Although we have identified N1 as the most likely counterpart of the *IRAS* source, N15 and the 4.8 μm source near N18 could also contribute to the 12 μm flux as well as that at longer wavelengths. It is therefore uncertain whether the SED between 12 μm and 100 μm is that of a single source or not. Scattered light presents another problem. In Figure 5.8, N14, N15 and N18 show large wavelength-dependent position shifts (4-6 arcsec), suggesting that the K' band positions show only the last scattering front of these embedded sources, as is the case for L1551/IRS5 (Campbell et al. 1988). In such cases, the flux we received at K' is dominated by the scattered light. Because the scattered light will cause overestimation of the source emission in K' band, and the source confusion will cause overestimation of the source emission at 12 μm, the spectral index cannot reliably characterize the YSO. High spatial resolution photometry at longer wavelengths (*nbL*, *M*, and 10 μm) is therefore essential to reduce or eliminate the effect of scattered light and to remove source confusion. Of the three sources we imaged, L1641-N is most affected by source confusion and scattered light.

5.5.2. *Age Span within the Stellar Density Enhancement*

In this study, we detected stellar density enhancement in the vicinity of all three *IRAS* sources associated with CO outflows. We found in section 5.3.2 that at least 60% of the near-IR sources found around the *IRAS* sources are the PMS stars. As mentioned above, two sources (N2 and N12) near L1641-N have been previously classified as K7 and M1-2 stars. S15 near Strom 11 is a M0 star. For these three stars, we use the R - I color and the spectral type to deduce the reddening. We then use the unreddened I and distance modules to obtain the stellar luminosity, allowing us to place them in the H-R diagram. We estimate the ages of the 3 stars to be 1 Myr (N2), 3 Myr (N12), and 0.5 Myr (S15). As a comparison, the dynamical age of both CO outflows, L1641-N and Strom 11, is 4×10^4 yr (Fukui et al. 1986; Morgan et al. 1991). Since these PMS stars are physically associated with the driving sources of CO outflow (section 5.3.1), we conclude that star formation near the three *IRAS* sources is a continuous process with an age span of 1-3 Myr.

In L1641-C we detected many more IR-excess stars than in the other two regions. If more than one source has a CO outflow, and the outflows are not aligned with each other, it would be difficult to detect well-collimated red and blue lobes. This may provide an explanation as to whether the CO high-velocity wing is indeed a molecular outflow (Morgan et al. 1991; Sugitani et al. 1992).

5.5.3. *The Fate of Stellar Density Enhancement*

The optical stars N2, N12, and S15 have relatively low extinction (A_V = 1-3 mag), so they are located toward the surface of the dense molecular gas in which the stellar aggregations are embedded. If N2 was formed at the center of the dense core (near the *IRAS* position), a proper motion of only 0.1 km s^{-1} with respect to the dense core is required to move it to its present location (about 2' from the *IRAS* position) within its

lifetime. The same analysis yields a proper motion of 0.6 km s^{-1} for S15. From the proper motion measurement of 75 T Tauri stars, Jones & Herbig (1979) found velocity dispersions within a subgrouping are on the order of 1-2 km s^{-1}. The radial velocity measurements (Hartmann et al. 1987) of T Tauri stars yield an upper limit of 1.5 km s^{-1}. Within the uncertainty, these observations are consistent with the possibility. It is therefore possible that the optical stars in the observed stellar density enhancements were formed near the *IRAS* positions in the dense cores and have since moved outward to the surface of the cores. If this is true, the stellar density enhancement we observed will become unrecognizable as such unless new stars are being formed continuously. However, this process can continue only if enough material is available or if no high-mass star forms. The stellar density enhancements are a phenomenon found at a very early stage of star formation in L1641. It is indeed found that 60% of *IRAS* sources with CO outflows are associated with stellar density enhancement, compared with only 10% of *IRAS* sources without CO outflow (Chapter 4).

5.6. SUMMARY

We obtained optical and near-IR images of three *IRAS* sources associated with CO outflows in L1641. The main conclusions are summarized as follows:

(1) In the *K'* images we find stellar density enhancements around all three *IRAS* sources. The association of these sources with dense molecular cores and reflection nebulosity suggests that they are physically associated with the *IRAS* sources.

(2) Optical and infrared photometry suggests that *at least 60%* of the near-IR sources are pre-main-sequence stars.

(3) With the near-IR imaging at *K'*, *nbL*, and *M*, we were able to identify the likely counterpart of each *IRAS* source. This yields a meaningful comparison of the near-IR data and *IRAS* data.

(4) Star formation near the three *IRAS* sources is a continuous process with an age span of 0.5-3 Myr.

(5) Stellar density enhancement may be a phenomenon found at the earliest stage of star formation.

TABLE 5.1 NEAR-IR SOURCES AT L1641-N

No.	α (1950)			δ (1950)			*B*	*V*	*R*	*I*	*H*	*K'*	*nbL*	*M*
N1	5	33	52.5	-6	23	59								8.6
N2	5	33	51.9	-6	22	29	15.8	15.0	14.2	13.3	11.3	10.9	...	...
N3	5	33	55.3	-6	22	48					17.5	15.7	...	...
N4	5	34	0.4	-6	22	53			18.1	16.9	15.1	15.0	...	...
N5	5	33	56.1	-6	23	16					15.9	13.7	...	...
N6	5	33	53.9	-6	23	18						16.5	...	...
N7	5	33	54.0	-6	23	36					17.0	15.5	...	...
N8	5	33	58.2	-6	23	41					16.0	15.2	...	...
N9	5	34	1.2	-6	23	42					16.0	15.2	...	...
N10	5	33	54.6	-6	23	42				18.2	11.2	10.3	9.8	8.7
N11	5	33	52.8	-6	23	54					15.1	14.7	...	...
N12	5	33	52.5	-6	23	54	19.2	17.5	16.4	15.0	13.2	12.9	13.5	
N13	5	33	52.8	-6	23	58						15.2	...	
N14	5	33	52.0	-6	24	1						15.4	...	
N15	5	33	53.3	-6	24	2					17.0	15.2	12.4	7.7
N16	5	33	54.2	-6	24	4					15.6	14.6	...	...
N17	5	33	58.0	-6	24	10		19.7	17.7	15.5	11.6	11.1	...	...
N18	5	33	53.4	-6	24	12						15.6	13.1	9.7
N19	5	33	52.1	-6	24	14						15.6	...	...
N20	5	33	51.6	-6	24	19					16.4	15.8	...	...
N21	5	33	51.5	-6	24	22						14.8	12.6	...
N22	5	33	54.6	-6	24	27					16.6	15.5	...	...
N23	5	33	59.9	-6	24	27						16.1	...	...
N24	5	33	51.4	-6	24	40					16.3	14.8	12.6	...
N25	5	33	52.8	-6	24	40			19.2	17.0	14.4	14.3	...	...
N26	5	33	55.3	-6	24	40				18.5	12.4	11.1	...	...
N27	5	33	58.9	-6	24	53		20.0	18.6	16.7	14.3	14.0	...	...
N28	5	34	1.4	-6	24	57	19.0	17.4	15.8	14.0	11.3	11.1	...	...
N29	5	33	57.5	-6	24	58		17.9	16.6	15.5	11.9	10.5	...	...
N30	5	33	54.3	-6	25	10					13.0	11.8	...	...
N31	5	33	55.6	-6	25	17		21.5	19.4	16.7	10.7	9.7	...	...
N32	5	33	55.0	-6	25	19					16.4	15.7	...	...
N33	5	33	56.3	-6	25	32		21.1	19.4	16.7	12.4	11.6	...	...
N34	5	33	49.1	-6	25	47	...	...	...	...	10.0	9.6	...	...

TABLE 5.2 NEAR-IR SOURCES AT STROM 11

No.	α (1950)			δ (1950)			*B*	*V*	*R*	*I*	*H*	*K'*	*nbL*	*M*
S1	5	33	55.6	-6	26	11					13.3	12.3	...	...
S2	5	33	58.9	-6	26	17		19.7	18.0	16.0	13.4	13.2	...	...
S3	5	33	53.1	-6	26	28					15.0	13.7	...	...
S4	5	33	59.7	-6	26	37		18.8	17.6	16.2	14.2	14.0	...	...
S5	5	33	57.2	-6	26	39					16.3	13.0	9.8	7.9
S6	5	33	57.7	-6	26	42						15.1	13.5	
S7	5	34	0.4	-6	26	43		19.0	16.8	15.0	12.6	12.4	...	...
S8	5	33	59.4	-6	26	44					13.0	11.2	9.4	8.3
S9	5	33	58.5	-6	26	53				18.1	13.4	12.9	12.2	
S10	5	33	57.7	-6	27	14					11.5	...	...	...
S11	5	34	1.5	-6	27	20	18.6	17.2	16.0	14.5	12.3	12.2	...	...
S12	5	33	53.2	-6	27	41		18.9	17.1	15.2	12.2	11.8	...	...
S13	5	33	55.6	-6	27	50	18.4	16.8	15.7	14.4	11.2	10.5	...	...
S14	5	33	59.9	-6	28	1			19.0	17.1	13.5	13.2	...	...
S15	5	34	0.5	-6	28	13	16.3	14.7	13.6	12.6	10.7	10.2	...	...

TABLE 5.3 NEAR-IR SOURCES AT L1641-C

No.	α (1950)			δ (1950)			*V*	*R*	*I*	*H*	*K'*	*nbL*	*M*
C1	5	36	14.2	-7	0	56	17.8	16.4	15.1	11.4	10.6	...	...
C2	5	36	26.7	-7	1	0				12.6	11.6	...	...
C3	5	36	17.2	-7	1	7				17.0	16.3	...	...
C4	5	36	23.0	-7	1	11				13.6	12.8	...	...
C5	5	36	13.7	-7	1	12				15.2	13.3	...	...
C6	5	36	21.0	-7	1	33				16.7	15.3	...	...
C7	5	36	22.7	-7	1	38				14.5	13.2	...	...
C8	5	36	22.6	-7	1	43				13.7	12.5	...	...
C9	5	36	27.2	-7	1	44				16.8	15.7	...	...
C10	5	36	24.2	-7	1	56					16.2	...	...
C11	5	36	27.0	-7	1	58		18.7	16.9	12.0	11.5	...	...
C12	5	36	24.7	-7	2	18		19.1	16.9	11.2	10.5	...	...
C13	5	36	18.5	-7	2	19				16.0	14.0	12.1	
C14	5	36	23.1	-7	2	19			18.0	12.4	11.7	...	...
C15	5	36	14.4	-7	2	23			18.6	14.4	13.9	...	...
C16	5	36	22.3	-7	2	26				14.2	13.1	12.6	
C17	5	36	20.5	-7	2	26					17.4	10.8	8.2
C18	5	36	20.0	-7	2	32					14.7	11.5	11.7
C19	5	36	19.4	-7	2	36					17.1	12.6	
C20	5	36	21.6	-7	2	37				14.9	12.9	11.1	
C21	5	36	18.3	-7	2	52				14.3	12.3	10.8	11.0
C22	5	36	24.0	-7	2	52					14.7	...	...
C23	5	36	26.8	-7	3	5					15.5	...	...
C24	5	36	13.2	-7	3	7			19.1	14.2	13.7	...	...
C25	5	36	17.8	-7	3	14				11.9	10.9	...	...
C26	5	36	24.8	-7	3	24				16.7	14.8	...	...
C27	5	36	21.9	-7	3	27					15.4	...	...
C28	5	36	21.7	-7	3	30				15.4	13.1	...	...
C29	5	36	20.7	-7	3	31				16.7	13.9	...	...
C30	5	36	16.0	-7	3	33	21.0	18.4	16.3	12.2	11.7	...	...
C31	5	36	20.2	-7	3	36				13.2	11.7	...	...
C32	5	36	19.8	-7	3	40				15.8	14.8	...	...
C33	5	36	26.6	-7	3	47					15.7	...	...
C34	5	36	26.9	-7	3	48				14.0	12.3	...	...
C35	5	36	25.3	-7	3	49				16.0	14.0	...	...
C36	5	36	16.6	-7	3	56				16.3	15.4	...	...
C37	5	36	22.5	-7	4	8			19.1	18.0	15.4	...	...
C38	5	36	24.4	-7	4	11				14.4	13.9	...	...
C39	5	36	26.7	-7	4	13				16.4	14.2	...	...
C40	5	36	26.4	-7	4	13					15.8	...	...

TABLE 5.4 OPTICAL SOURCES

No.	Identification	Known Spectral type	Emission Line ?	Reference	Inferred Spectral type	Av (mag)
N2	PC 388	K7V	Y	1	G0	2.0
N12		M1-2e	Y	2	K0-2	3.0
N17					K2	2.0
N27					K2-M5	<4.0
N28	PC 398		Y	1	F5	5.5
N29	PC 389		Y	1	K2-M0	2.0
N31					K0	7.0
N33					K0-2	3.3
S2					K0-2	4.5
S4					K2	3.0
S7					F5-G0	6.0
S11					G5	3.5
S12					G0	5.5
S13	PC 390		Y	1	K0	2.5
S15	V990 Ori	M0e	Y	3	G0-5	2.0
C1					K0-2	3.0
C30					G5-K0	7.0

Reference: (1) Parsamian & Charvira 1982, (2) Strom et al. 1989, (3) Strom et al. 1990

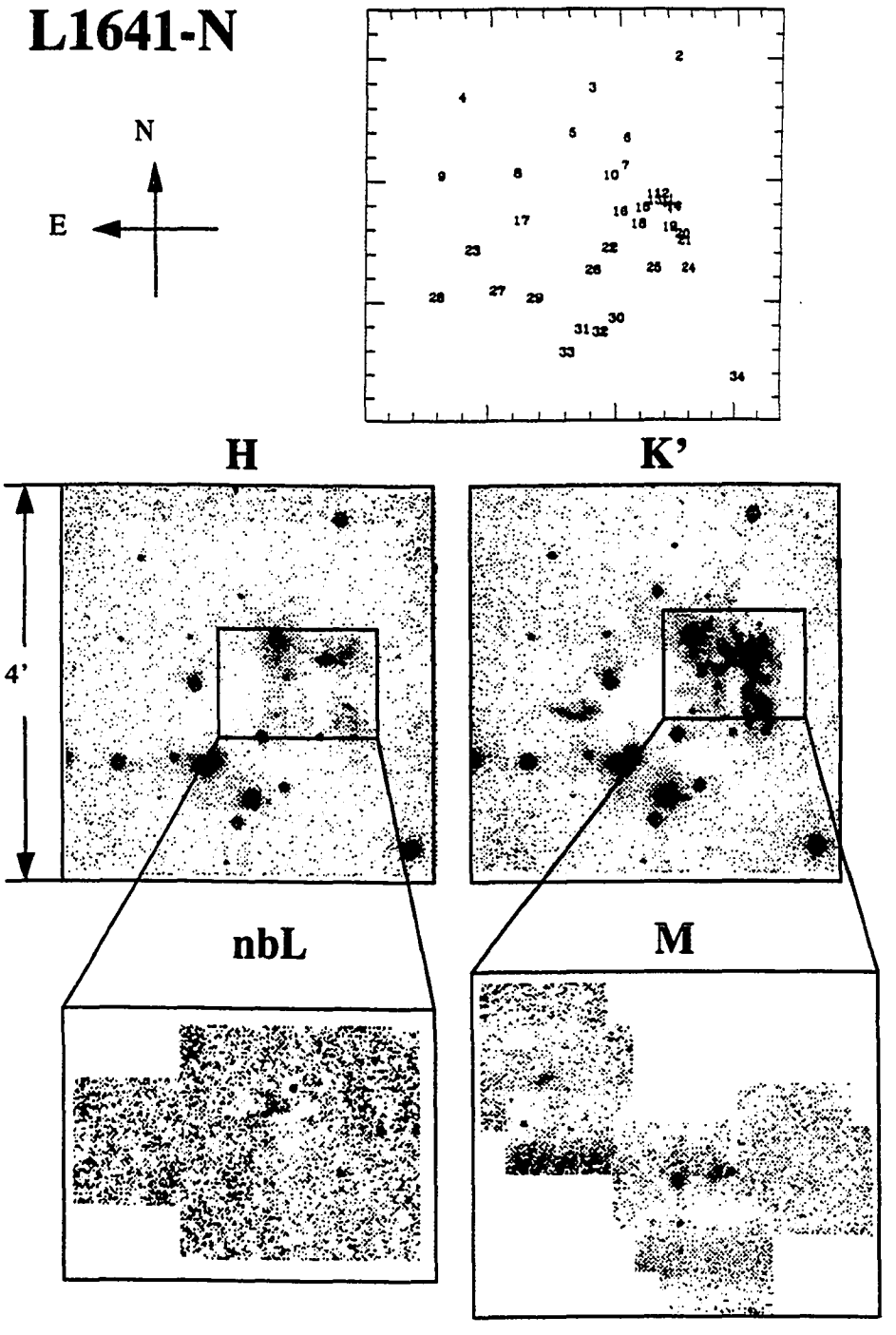

Figure 5.1 *H*, *K'*, *nbL*, and *M* images of L1641-North. The *H* and *K'* images cover a 4' × 4' arcmin region at the same scale. The *nbL* and *M* images cover much smaller areas and are shown at an enlarged scale. The figure on top shows the source numbers used in Table 5.1. The *IRAS PSC* position is marked by the cross.

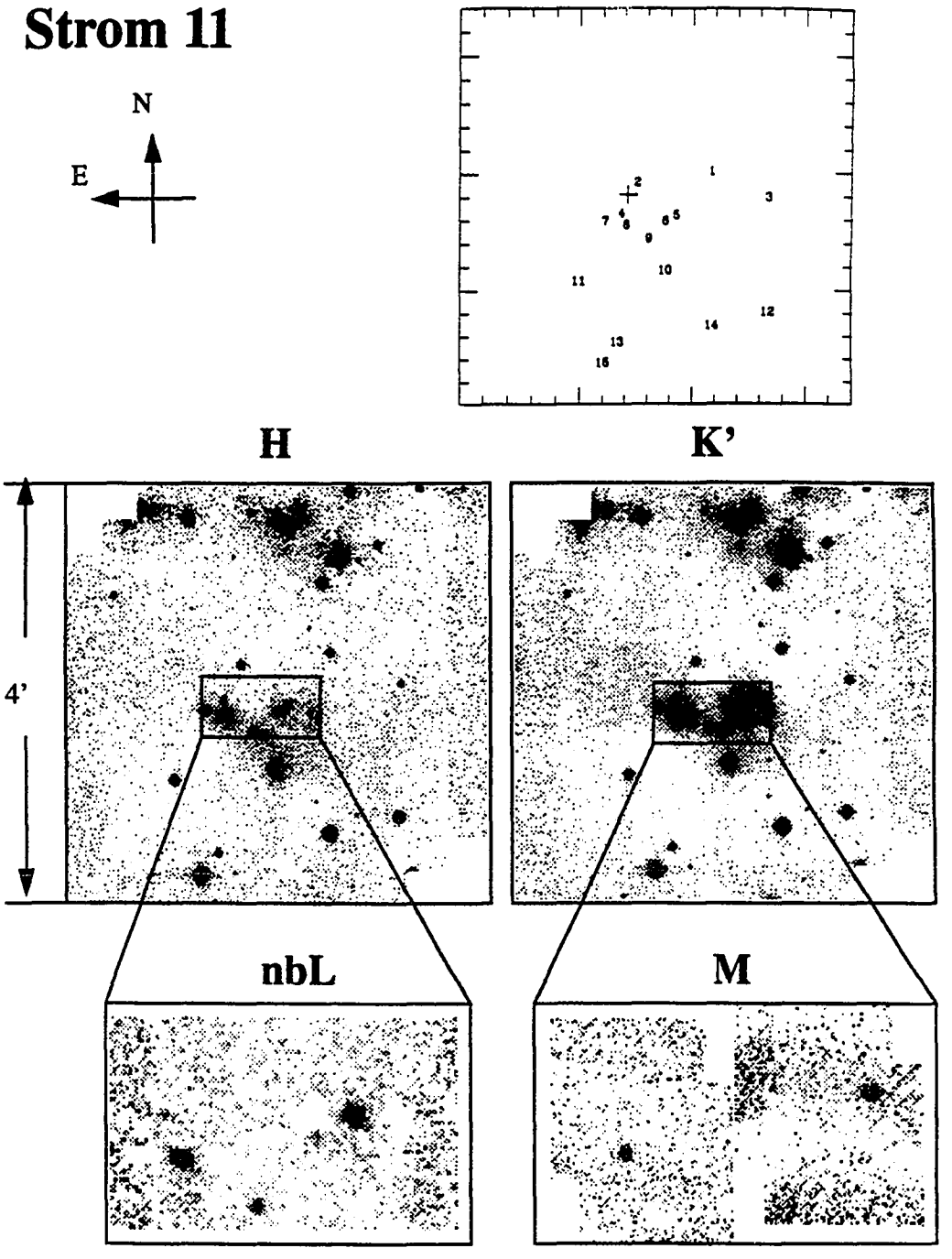

Figure 5.2 *H*, *K'*, *nbL*, and *M* images of Strom 11. The *H* and *K'* images cover a 4' × 4' arcmin region at the same scale. The *nbL* and *M* images cover much smaller areas and are shown at an enlarged scale. The figure on top shows the source numbers used in Table 5.2. The *IRAS PSC* position is marked by the cross.

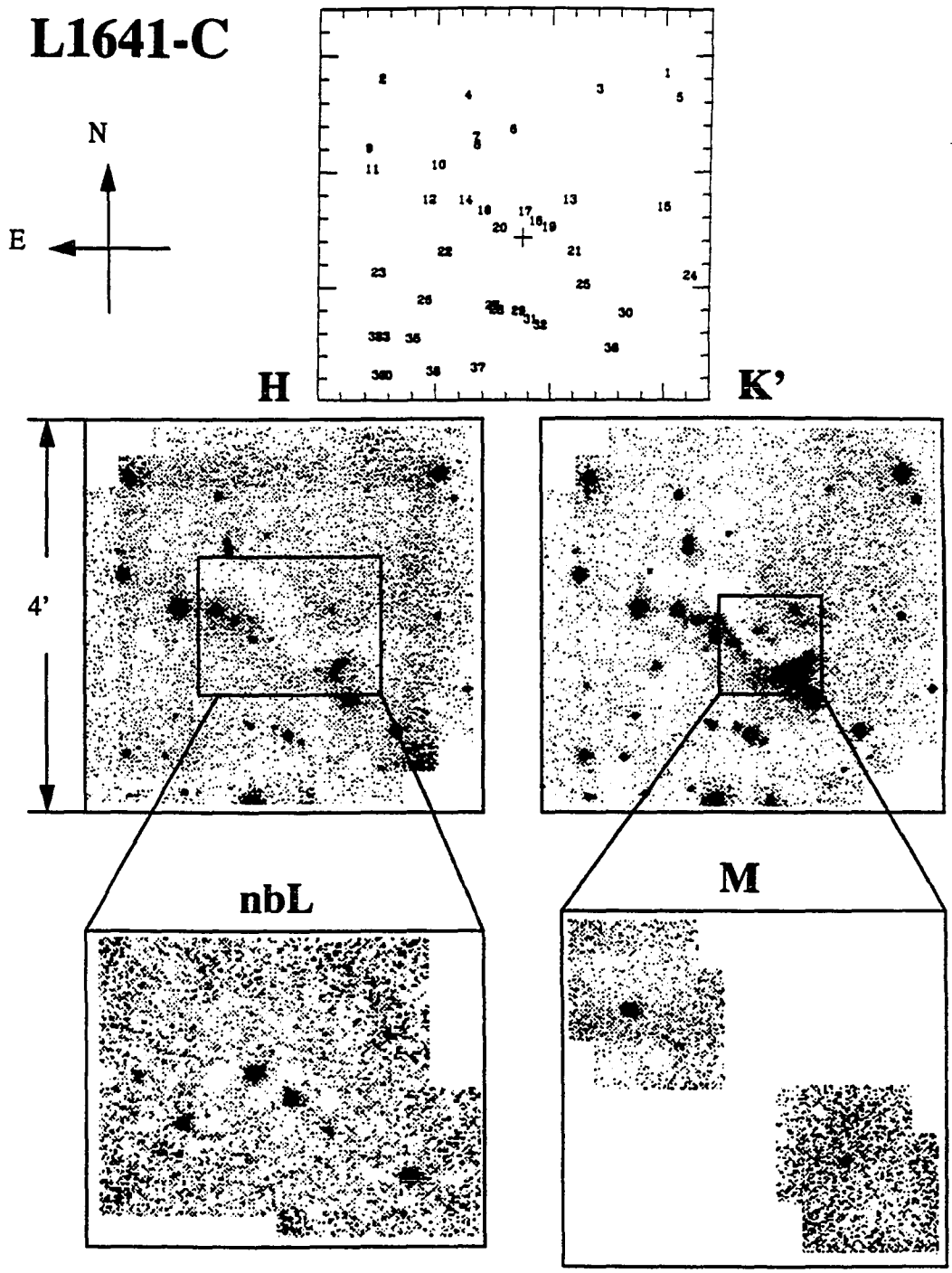

Figure 5.3 *H*, *K'*, *nbL*, and *M* images of L1641-Center. The *H* and *K'* images cover a 4' × 4' arcmin region at the same scale. The *nbL* and *M* images cover much smaller areas and are shown at an enlarged scale. The figure on top shows the source numbers used in Table 5.3. The *IRAS PSC* position is marked by the cross.

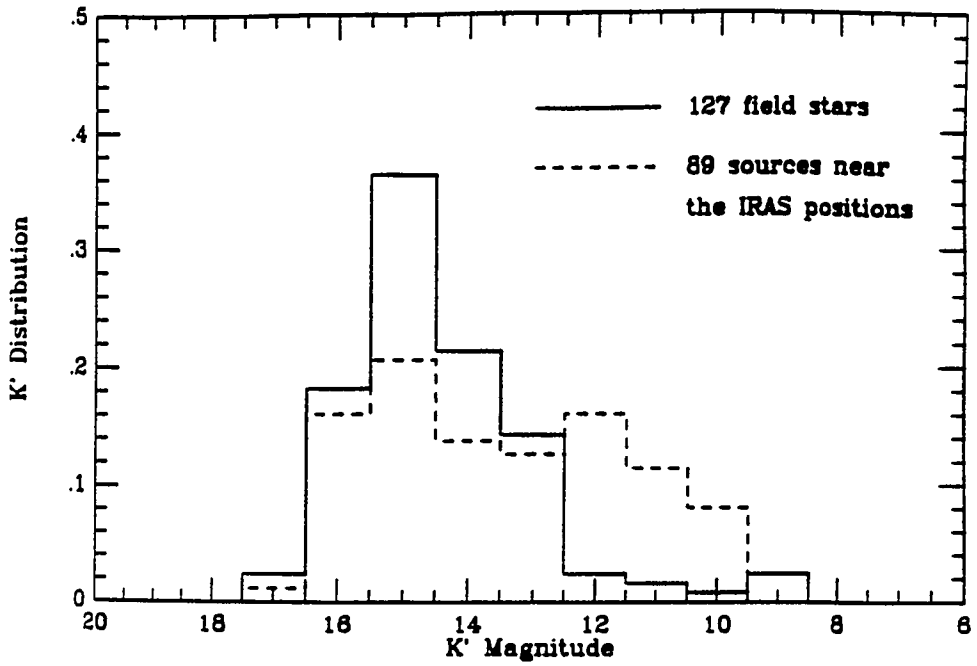

Figure 5.4 Histograms of the observed K' magnitude of 127 field stars and 89 sources detected in the vicinity of the three *IRAS* sources.

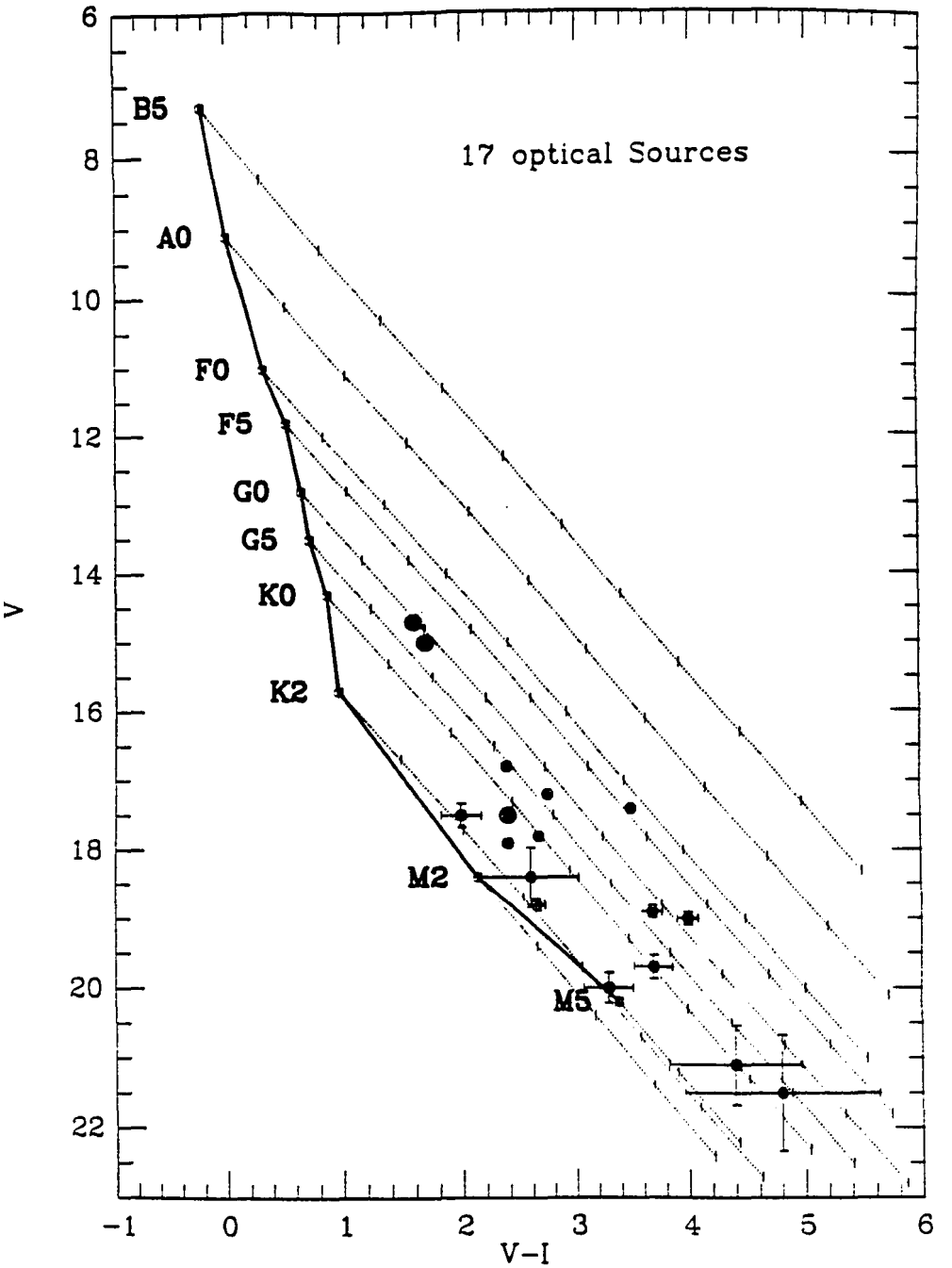

Figure 5.5 *V* vs. *V* - *I* diagram of the 17 optical sources that are detectable in *V*. The open squares and the thick line indicate the loci of B5-M5 main-sequence dwarfs at the distance of 480 pc. The dotted lines are extinction track. The extinction increases toward the lower-right corner with each tick mark indicating A_V = 1.0 mag. The sources detected in this study are shown as filled circles. The three larger filled circles indicate the sources whose spectral type was known previously.

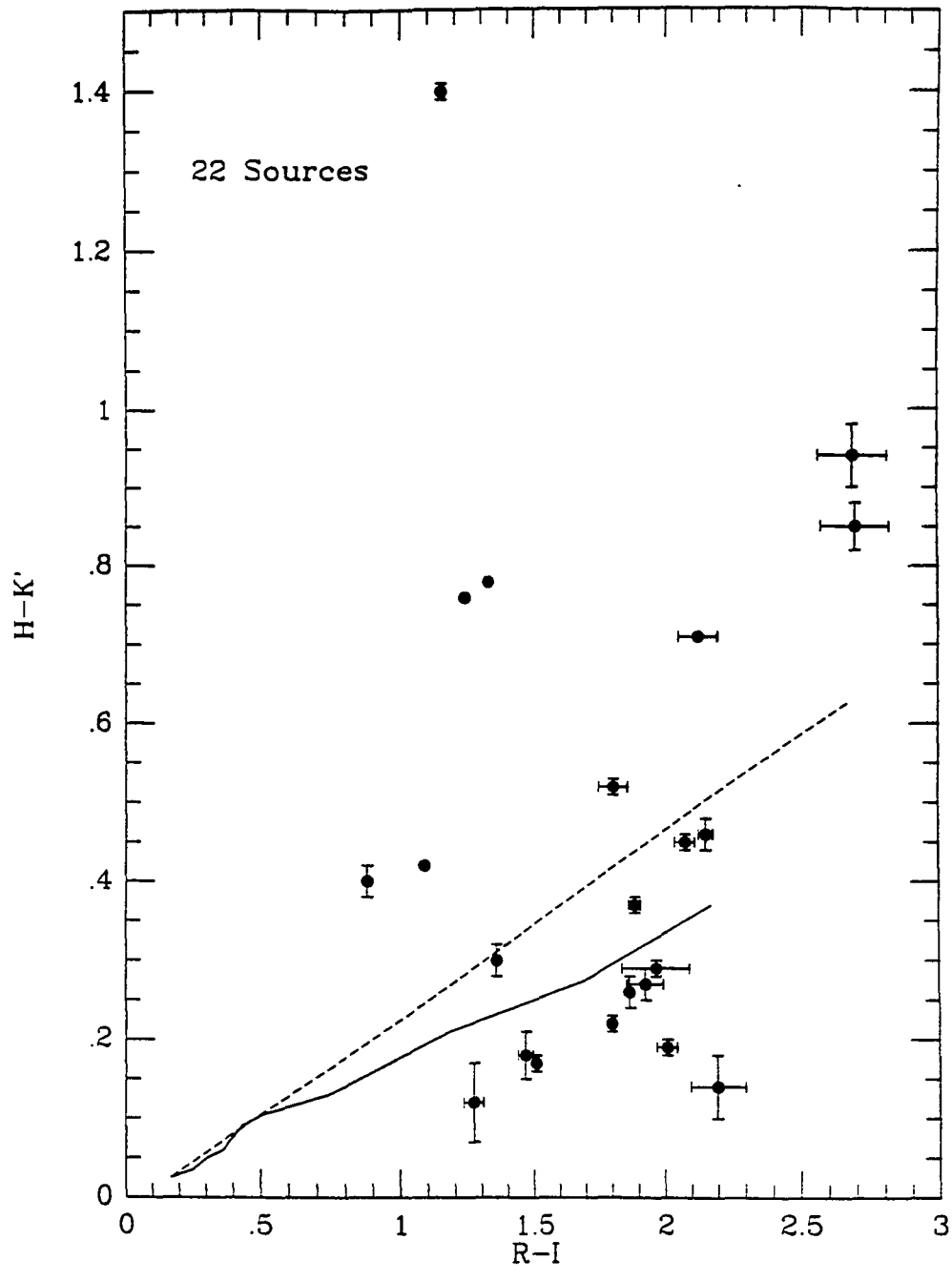

Figure 5.6. *R - I* vs *H - K'* diagram of 22 sources. The solid line represents the loci of main-sequence dwarfs. The dashed line indicates the extinction vector.

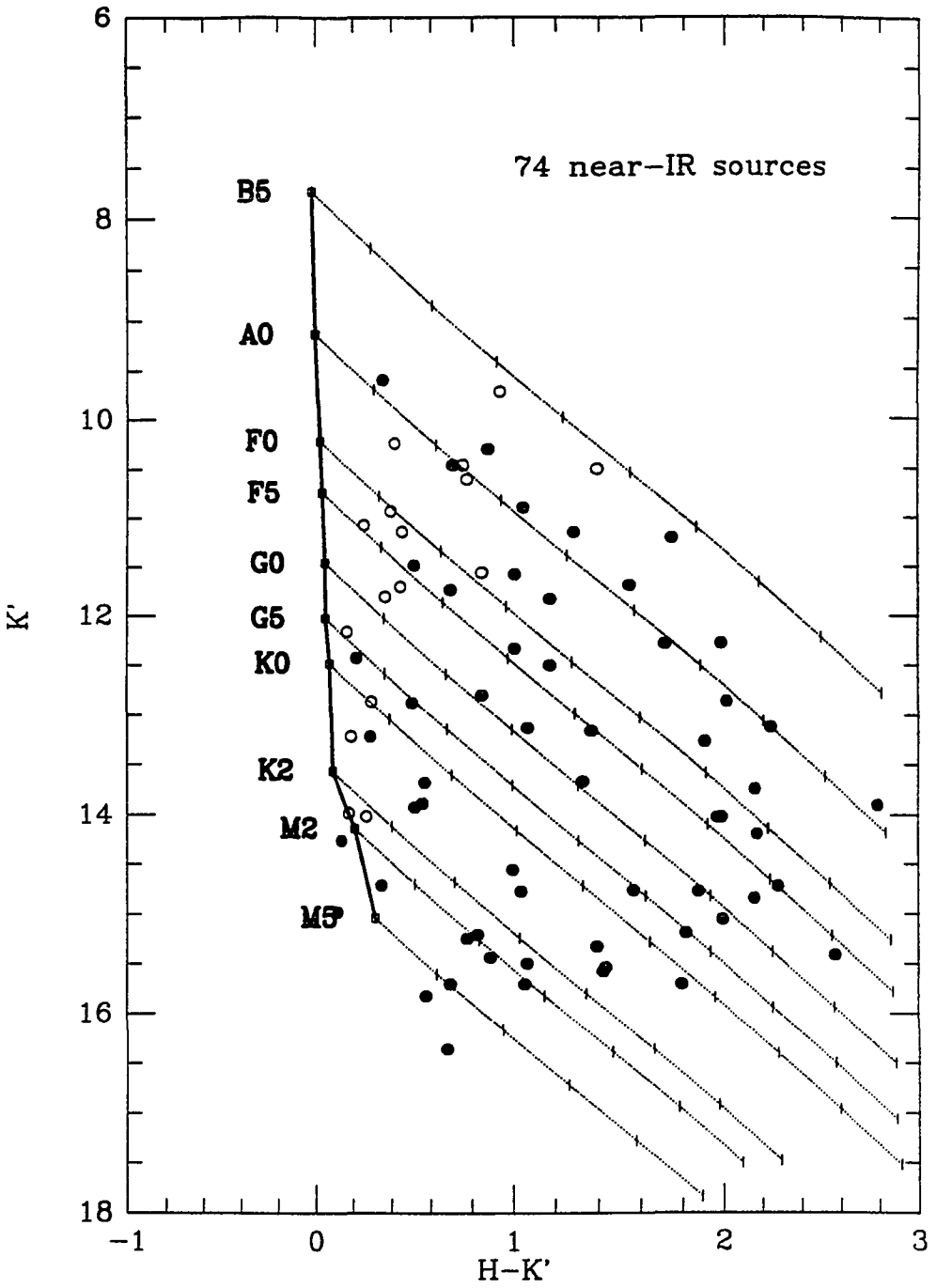

Figure 5.7. *K'* vs. *H* - *K'* diagram of 74 sources detected in *H* and *K'* around the three *IRAS* sources. The symbols for the main-sequence dwarfs are the same as Fig 5.5, except each tick mark is A_V = 5.0 mag. The open circles are the optical sources, and the filled ones are only detectable in *H* and *K'*. The maximum uncertainty in the *K'* mag is 0.1 mag and in the *H* - *K'* it is 0.14 mag.

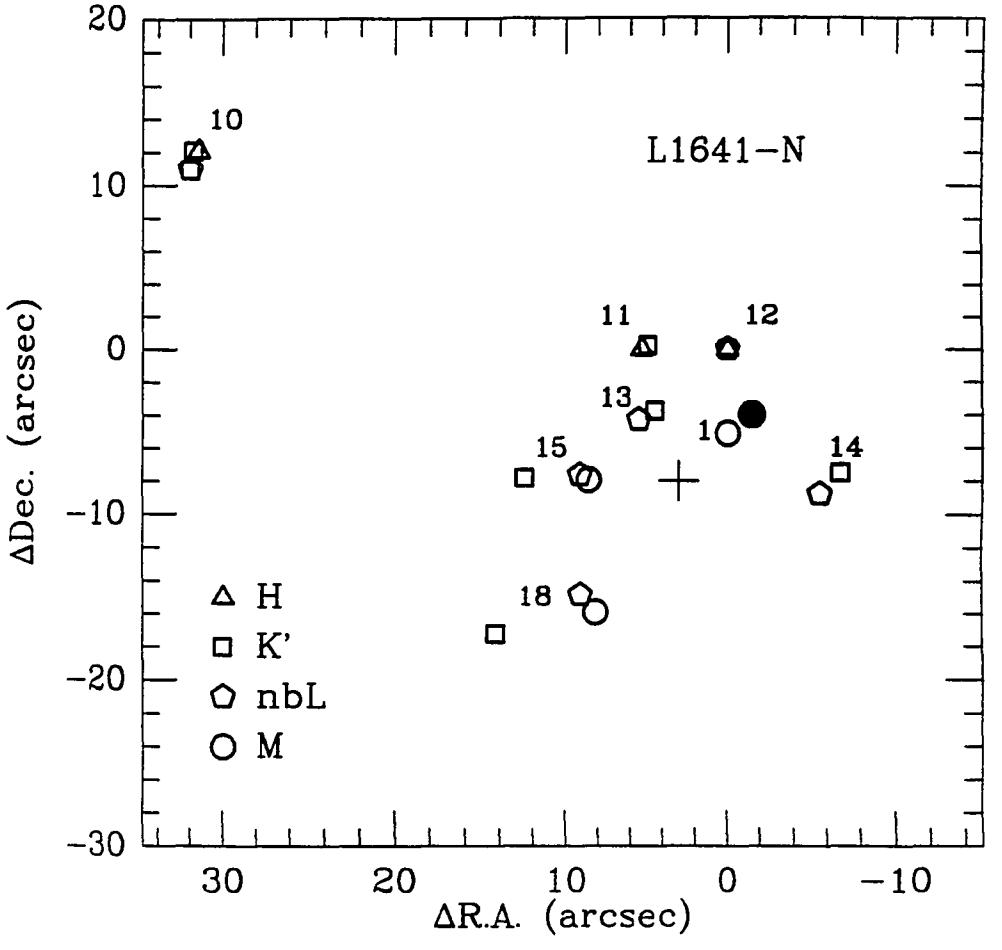

Figure 5.8. Map of the near-IR sources near L1641-N. The *IRAS* position is indicated by the cross. The filled circle denotes the position of the 2.7 mm continuum source. Source positions determined from *H*, *K'*, *nbL* and *M* are plotted. All positions are offset from N12, an optical star with low extinction.

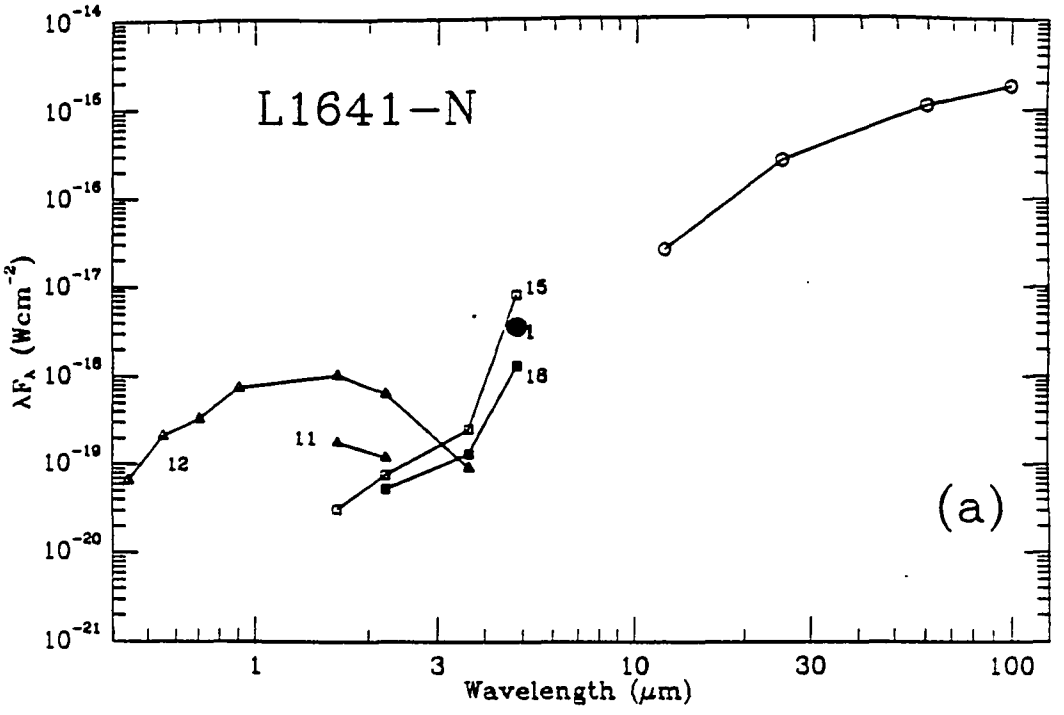

Figure 5.9a The spectral energy distributions of the selected near-IR sources near L1641-N.

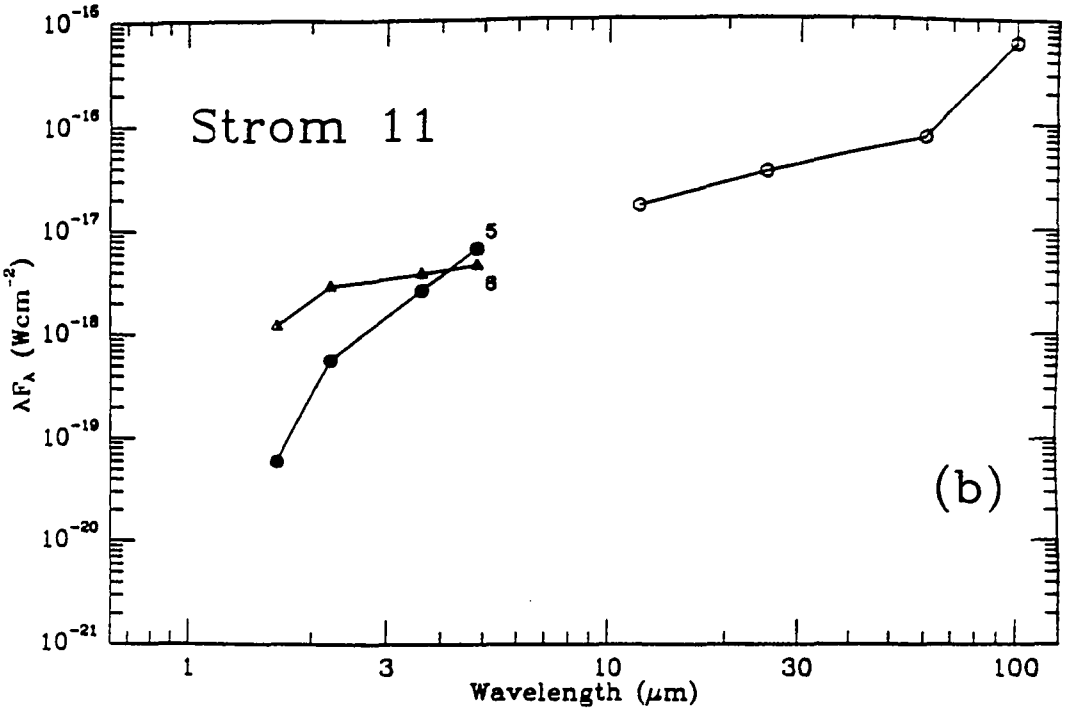

Figure 5.9b The spectral energy distributions of the selected near-IR sources near Strom 11.

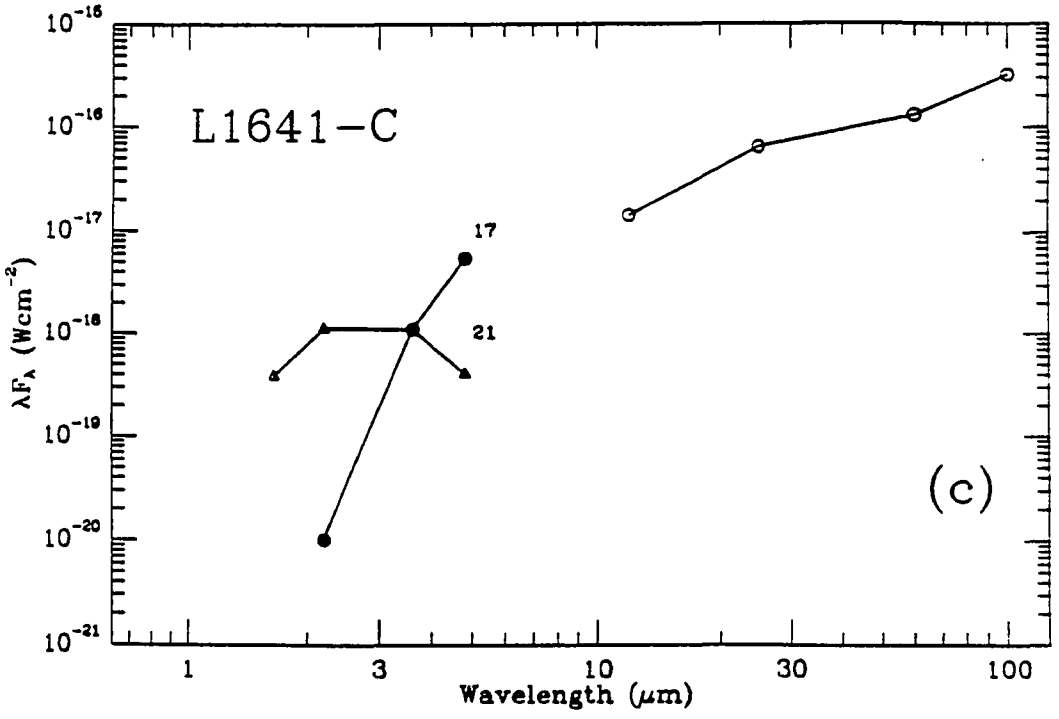

Figure 5.9c The spectral energy distributions of the selected near-IR sources near L1641-C.

CHAPTER 6
STELLAR DENSITY ENHANCEMENT: A REVISIT

6.1. INTRODUCTION

As discussed in Chapters 4 and 5, the spatial distribution of young stars in L1641 can be characterized by a range of surface density, from large cluster to stellar density enhancement and to individual stars. The formation of the Trapezium Cluster might be triggered by the external force, while the SDEs and individual star formation occur spontaneously throughout the L1641.

Figure 6.1 shows the spatial distribution of the 59 *IRAS* sources we imaged in this study (the filled circles). The 14 *IRAS* sources that are associated with the SDEs are shown by the larger open circles. Evidently the 14 sources with SDEs and the 45 sources without SDEs are almost evenly distributed in the L1641. Our near-IR imaging shows, however, that *IRAS* sources with and without SDEs have a very different near-IR source distribution in their vicinity. The 14 sources in the SDEs are associated with 5-17 bright ($K' < 11$) sources while the 45 sources not in SDEs have only 2-3 such sources. The difference is unlikely caused by extinction, because the sources in SDEs are generally redder than those in isolation. If corrected for extinction, there would be many more bright near-IR sources in the SDEs than those not in the SDEs. In this chapter, we want to understand why these otherwise very similar *IRAS* sources have such different near-IR source distributions in their vicinity. In section 6.2 we study the association of SDEs with dense molecular cores. We will then examine the necessary conditions for SDE formation in section 6.3. We discuss two mechanisms of forming individual stars in section 6.4. In section 6.5, we will discuss the possible impact of the SDEs on the star

formation theory, mainly on the initial mass function and the interaction among the young stars within a dense core.

6.2. SDES AND DENSE CORES

In the last two chapters, we suggest that the SDEs indicate a continuous star formation within the molecular dense cores. It is therefore interesting to see whether we can find the association of the SDEs with observed molecular dense cores. Table 6.1 summarizes the information obtained in various millimeter survey for dense cores in L1641. The HCO^+ and ^{13}CO mapping data were obtained in this study, as presented in Chapter 3. The NH_3 data were obtained by Wouterloot, Henkel & Walmsley (1989) and by Harju, Walmsley, & Wouterloot (1992), using the 100 m telescope in Effelsberg. The most comprehensive data came from a CS (J = 1-0) survey for dense cores in Orion A molecular cloud by Tatematsu, Umemoto and their co-workers (Tatematsu et al. 1992, Umemoto et al. 1992). The survey used the Nobeyama 45 m millimeter telescope that has a beamsize of 36" at 49 GHz. Table 6.1 lists the dense cores that are associated with the *IRAS* sources that we imaged in the near-IR, and all of these dense cores were detected > 5 σ at 49 GHz.

Table 6.2 illustrates the association of the CS cores with the SDEs. Of 59 *IRAS* sources we imaged in H and K', 47 were mapped in CS, and 27 of them are associated with a CS core. A contingency table statistical test (see Appendix C) shows that the *IRAS* sources that are in SDEs also are most likely to be in a CS core. A similar conclusion can be drawn from our ^{13}CO data. Twenty-five *IRAS* sources were both imaged in near-IR and mapped in ^{13}CO. Of 8 sources that are located inside ^{13}CO molecular cores, 6 of them are associated with SDEs. We therefore suggest that the SDEs are closely associated with molecular dense cores.

The physical parameters of the dense cores with and without the SDEs are also very different. In Figure 6.2 we plot the CS J = 1-0 linewidth and mass of the 27 CS cores listed in Table 6.1. These data were kindly provided to us by Dr. T. Umemoto. The cores that contain SDEs are obviously more massive and have a higher velocity dispersion (or larger line width) than those without SDEs. The CS cores with SDEs have an average mass of 220 $M_{\odot}$, nearly four times higher than that of those without SDEs. They are also more turbulent with an average velocity dispersion of 1.47 km s^{-1}, compared to 1.01 km s^{-1} for the cores without SDEs.

The above results can be understood if the star formation is a continuous process within the SDE. The more massive cores have a reservoir that is large enough to form new stars continuously, while the less massive ones are capable of forming only a few stars before being dissipated by the outflows from the young stars. This explains why the SDEs are predominantly seen in the more massive cores. For a more massive core, a higher velocity dispersion is needed to maintain the virial equilibrium. As to be discussed in section 6.5.2., the collective effect of the outflows from newly formed young stars within the dense core may provide enough turbulence to enhance the velocity dispersion.

It is important to note that the continuous star formation within the dense cores does not conflict with our discussion of dense core dissipation by molecular outflows. The star formation within the dense cores may have begun a few million years ago. The CO outflow we observe today represents the latest event of star formation. Once the dense core is gradually consumed by (individual or continuous) star formation, the star forming activity will cease and we can then no longer detect any CO molecular outflows. There is therefore a close association between the dense cores and the CO outflows. If the core mass is only a few $M_{\odot}$, it can probably form 1-2 stars before being dissipated by the outflows from the stars. If the core is more massive, and is capable of producing

continuous star formation, it takes several outflows to dissipate. In either case, the dense cores are closely associated with CO outflows, and the CO outflow is a main agent in dissipating the dense cores.

6.3. FORMATION OF SDES

Besides the more massive dense cores, what are the other conditions that are necessary to form a SDE? Our multi-wavelength observations provided some clues:

(1) For young stars continuing to form within a dense core, it is essential that all the previously formed stars in the SDE are low-mass stars. Otherwise the "first generation" young stars would be too destructive to the dense core, prohibiting the new stars from forming later. This is consistent with our optical and near-IR analysis of the sources in three SDEs, which shows that most of them are probably late-type low-mass PMS stars (Chapter 5). It is also consistent with the results of a near-IR spectroscopic observations of the sources near L1641-N (Hodapp & Deane 1992).

(2) 7 of the 11 sources with CO molecular outflows are associated with SDEs, compared with only 7 of 45 non-outflow sources. This suggests that the SDEs are associated with the most recent on-going star formation. At this stage, the previously formed stars have not yet moved away from their birthplace, resulting in the pile-up of PMS stars in cores. It is easier to detect an SDE when its age span is a few Myr.

(3) When a massive core encounters an external event (such as cloud-cloud collision, or nearby supernova explosion), it is likely that the molecular gas of the whole core will be disturbed, and a cluster can be expected to form coevally. This may explain the large-scale cluster in the Trapezium Cluster. External triggering may not play an important role in forming SDEs, because the *IRAS* sources in SDEs and not in SDEs are evenly distributed throughout the L1641. It is highly unlikely that all of them are triggered by

an external force, although it is possible that they may be related to local triggering, such as clump-clump collision or the twisting of the molecular filaments.

In summary, it is easier to detect an SDE in a relatively isolated region where massive dense cores can continuously form low-mass stars.

6.4. FORMATION OF INDIVIDUAL STARS

If the SDE is the result of a continuous star formation with the dense cores, how were the isolated individual stars formed? Were they formed in a different mechanism from the SDEs, or they were also formed in the SDE, and later were dispersed? In the following we discuss these two possibilities:

(1) *Stars were formed by different mechanisms.* Shu (1991) suggests that the different YSO distributions can be understood in the context of the balance between the magnetic field and self-gravity of the molecular dense cores. If gravity is dominant, the dense core will quickly collapse to form a group of stars within a short period. On the other hand, if the magnetic field can support the dense core against the collapse, the core can maintain in equilibrium until ambipolar diffusion gradually weakens the magnetic field. This could result in an individual star formation. As shown in Figure 6.1, the SDE sources and non-SDE sources are distributed evenly throughout molecular cloud, and they should have very similar global environments. The molecular dense cores at scales of $<<$ 1 pc are therefore important in determining whether stars are formed in SDE or not.

(2) *Stars are formed in form of SDEs which disperses quickly.* In this scenario, most stars were formed in dense cores in the form of SDEs. When the age span is small, the "first generation" young stars do not have enough time to move away from their birthplace. This will result in a temporary grouping near the dense cores, seen as the

SDE. The SDE then represents a phenomenon that can only be found in the early stage of star formation. This is supported by the fact that 7 of 11 CO outflow sources are associated with SDEs. The detailed study of three sources (8, 18, and 75) show that the age span with SDEs might be 1-3 Myr (Chapter 5). As time goes by, the star formation activity ceases due to the depletion of dense cores. Because the SDE has many fewer stars than the large scale cluster, it can never be gravitationally bound, the "first generation" stars may move away from their birthplace. The SDE is then dispersed into individual stars.

To discriminate between these two possibilities, we need to (1) study the physical parameters of molecular dense cores, and (2) study the nature of the sources within the SDEs. We will discuss several possible follow-up observations in Chapter 7.

6.5. IMPLICATIONS TO STAR FORMATION THEORY

In our near-IR images, the number of young stars in the SDEs is at least compatible to those not in SDEs, suggesting that SDE is an important form of star formation in L1641. We found that the young stars in L1641 are formed in a range of stellar densities, rather than in two discrete modes: cluster and isolation. If this is proved to be common, the SDEs we detected in this study can have some impact on our understanding of the star formation process. We discuss in the following sections the initial mass function and the interaction among the young stars.

6.5.1. *The Initial Mass Function*

Since stars are formed within the dense cores, one might expect to see some relationship between the core mass distribution and initial mass function of the stars.

However only very recently has the high-resolution survey for dense cores in an entire molecular cloud become feasible thanks to the advance of the millimeter technology. ^{13}CO mapping in Rossett Molecular Cloud (Blitz et al. 1991), in M17 SW (Stutzki & Gusten 1990) and in Ophiuchus (Nozawa et al. 1991) all showed that the mass distribution of the molecular clumps can be fit by a power-law: $dN(m) \sim M^{-p} dM$, where $dN(m) / dM$ is the number of clumps per solar mass interval, and the index $p = 1.5$-1.7. A recent high-resolution CS survey for dense cores in L1641 gave $p = 1.8$ (Tetematsu & Umemoto 1991). On the other hand the initial mass function determined by Salpeter (1955) has an index of $p = 2.35$.

Several factors may result in the different slopes of the core mass distribution and the initial stellar mass function: (1) the star formation efficiency may be different for the massive cores and the low-mass cores; and (2) the more massive cores may further fragment into many less massive cores. Our detection of the SDEs at least qualitatively supports the latter. If the SDE is a common phenomenon, a massive core is capable of making many low-mass stars, giving a steeper rise to the low-mass stars than the high-mass stars in the initial mass distribution. A quantitive explanation requires a careful comparison of SDEs with their associated dense cores.

6.5.2. *Interaction Among Young Stars*

If all young stars have to go through the outflow stage, what is the effect of the previously formed stars on the most recent star formation within the same dense core? The CO molecular outflow has a spatial scale of a few parsecs. It is usually larger than the scale of the observed NH_3, HCO^+ and CS cores, and is probably comparable to the ^{13}CO cores. This suggests that the outflow may have substantial influence on the dense

cores. Our discussion in Chapter 3 showed that a single outflow is capable of dissipating a core of a few solar masses.

We now use the three HCO^+ dense cores we mapped in chapter 3 to see if the outflows are capable to supply the turbulence within the dense core. The observed HCO^+ line width consists of both thermal and non-thermal components. We can obtain an upper limit of the turbulent velocity dispersion, Δv_{core}, by assuming the whole line width is nonthermal. The turbulence momentum of the core can then be calculated as $P_{core} = M_{core} \times \Delta v_{core}$, where M_{core} is the total mass of the core. The momenta for the 3 dense cores are listed in Table 6.3. When compared with the momentum of the CO molecular outflow, clearly 3 - 12 outflows should be enough to account for the turbulence in the dense cores. We therefore suggest that the continuous star formation within a dense core will considerably increase the turbulence of the core. This is also consistent with Figure 6.2 in which the CS cores with SDEs have large velocity dispersion than those without SDEs.

If the turbulence in the dense core increases with the star formation activity, the stars that are formed later will have a more turbulent environment than the previously formed stars. Myers and Fuller (1992) suggested that the increased non-thermal motion can be translated into a higher mass accretion rate, using the formula given by Shu et al. (1987):

$$\dot{M} = \frac{0.975\, a^3}{G}$$

and

$$a^2 = a^2_{th} + a^2_{nt}$$

where the sound speed a is the sum of thermal (a_{th}) and non-thermal (a_{nt}) motion. The stars that are formed later will experience higher mass accretion rate than the "first generation" stars. Whether this enhanced accretion rate will result a higher mass star or

form a low-mass star more quickly is a subject of future study; the star formation within the SDE is probably more complicated than the standard isothermal model can account for.

TABLE 6.1 ASSOCIATION OF SDES WITH DENSE CORES

No.	ID	SDE	HCO^+	CS	NH_3	^{13}CO	No.	ID	SDE	HCO^+	CS	NH_3	^{13}CO
8	L1641-N	Y	Y	Y	Y	IC	108	L1641-S3	N		Y	Y	OC
18	MSSB 8	Y		Y			119		N		N		
25	V801 Ori	N		Y			120		N		N		
29		N		Y			133		N				
32	V846 Ori	N		Y			134		N		N		
34		N		N			146		N		Y	Y	
36	MSSB 18	N		Y			150		N		N		
41		N					160		Y		N	Y	OC
42		N		N			163		N		N	N	OC
46	HD 37357	N		N	N		168		N		N		OC
47	V380 Ori	Y		Y		IC	171		N			N	OC
49		N		Y			177		N		Y		OC
50		Y		Y		IC	181		N		N		OC
51	HH 1-2	Y		Y		IC	186		N		N		
62		N		N	N		187		Y		N		
71	T456	Y		Y		IC	191		N		Y		OC
72		N		N			193		Y		Y		
75	L1641-C	Y	Y	Y	Y	IC	194	L1641-S4	Y		Y	Y	IC
78		N		Y			198		N		Y		
79	Haro 13a	N		N	N	OC	211		N				
83	Haro 14a	N		Y			216	L1641-S2	N		Y	Y	IC
85		N		Y		OC	224		N				
87		N		Y			237		N				
93		N		N			243		Y				
95	V599	N		N		OC	245		Y				
99		N		N		IC	246		N				
101		N		N			256		N				OC
104	H 4-255	Y	Y	Y	Y	IC	270		N				
105	Re50	N		Y	N	IC	280		N			N	N
106		N		Y		OC							

Note: the blank entries indicate that there is no data available.

TABLE 6.2 SDE AND CS CORES

		CS cores?		
		Yes	No	Total
SDE?	Yes	10	2	12
	No	17	18	35
	Total	27	20	47

TABLE 6.3 CORE TURBULENCE AND CO OUTFLOW

No.	M_{core} $M_\odot$	Δv_{core} (km s^{-1})	P_{core} ($M_\odot$ km s^{-1})	$P_{outflow}$* ($M_\odot$ km s^{-1})
8	30	1.9	51	4
75	3	1.0	3	1
104	8	2.2	18	6

* Calculated from the data presented in Fukui (1989)

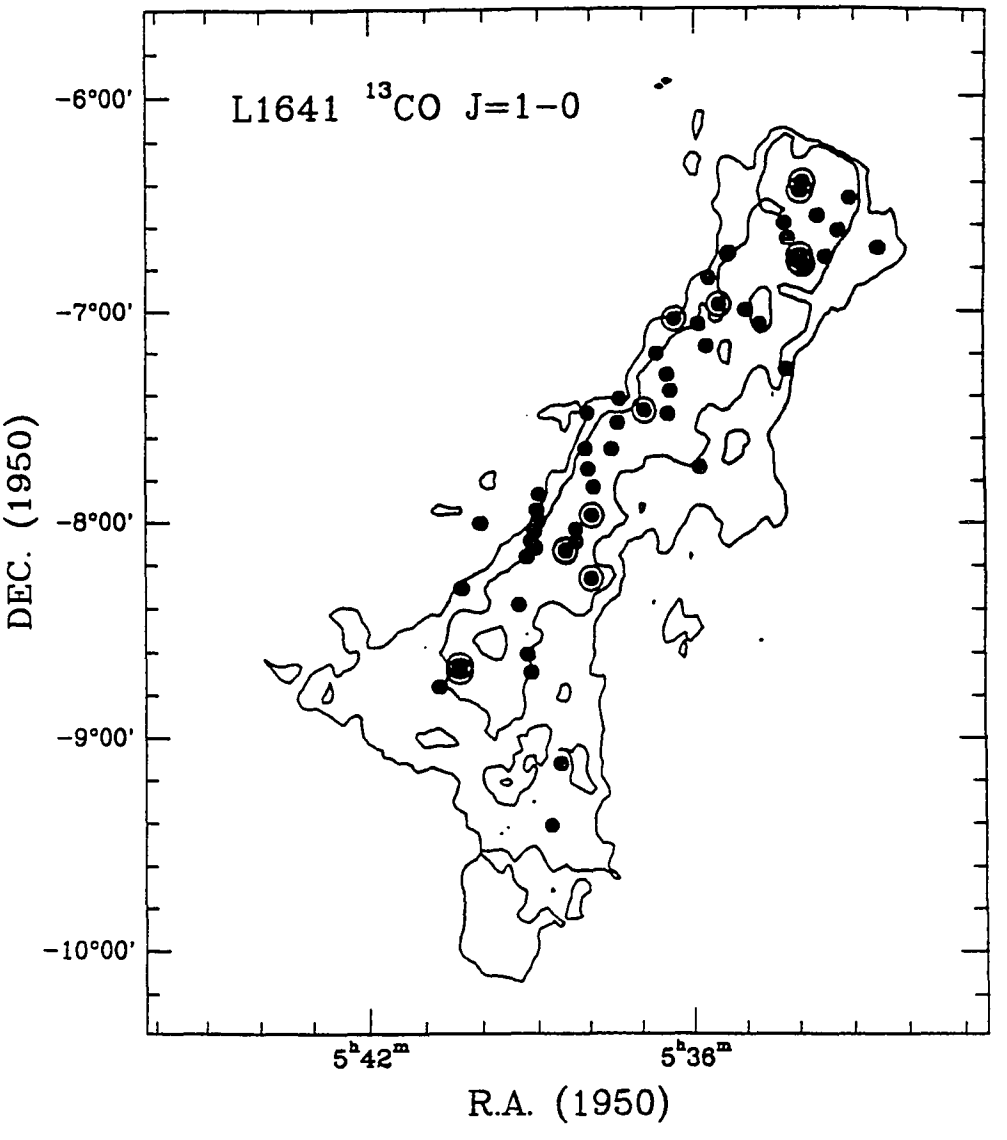

Figure 6.1 The spatial distribution of the 59 *IRAS* sources in L1641 that we imaged in the near-IR. The 14 sources with the SDEs are indicated by the large open circles.

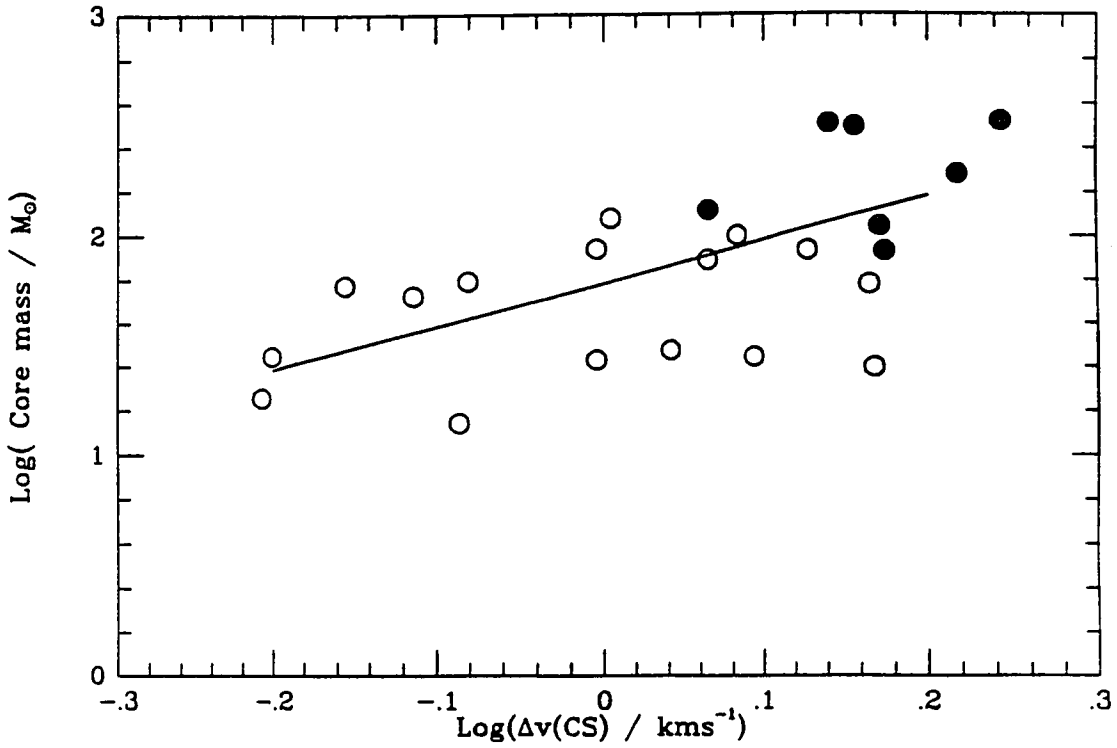

Figure 6.2 The log-log plot of CS line width vs. the mass of the CS cores. The data were obtained in a CS survey for dense cores with Nobeyama 45 m telescope by Tatematsu et al. (1992) and Umemoto et al. (1992). All 27 sources are imaged in the near-IR in this study. The filled circles denote the *IRAS* sources with SDEs, and the open ones are the *IRAS* sources without SDEs.

CHAPTER 7
SUMMARY

7.1. WHAT HAVE WE OBSERVED?

For the last three years, we have carried out a comprehensive millimeter, far-IR and near-IR study of young stellar objects in the dark cloud L1641. The details of the results from this study have been presented in Chapters 2-6. The major observational results can be summarized as the follows:

(1) We selected a sample of 224 *IRAS* sources from the *IRAS* co-added images in the L1641. The enhanced sensitivity of the coadded images over that of the PSC allows us to expand the source sample and to improve the detection quality. By analyzing the spatial distribution, the *IRAS* color-color diagram, and the dust emission mechanism, we conclude that most of the *IRAS* sources located inside the L1641 are self-heated embedded young stellar objects, while most of the sources outside of the contour are probably infrared cirrus heated by the interstellar radiation field. The following studies are therefore concentrated on the 122 sources that are located inside the L1641.

(2) From ^{13}CO mapping of 40 *IRAS* sources, we found 7 of 9 *IRAS* sources with CO molecular outflows are associated molecular cores, compared to only 4 of 31 non-outflow sources. We have also mapped 3 outflow sources in HCO^+, and all of them show well-defined dense cores with size of 0.1 pc and mass of 3-30 $M_\odot$.

(3) We found a correlation between the molecular column density and the *IRAS* 12-25 μm flux ratio. The correlation is much better for high-resolution HCO^+ data than the moderate-resolution ^{13}CO data.

(4) We imaged 59 *IRAS* sources in H and K', some of them were also imaged in nbL and M. For 55 of 59 *IRAS*, we were able to identify the near-IR counterpart of the *IRAS*

sources, although 9 of them may be multiple sources. With these identifications, we discussed the spectral energy distribution of the sources. Forty-five sources are classified as class I sources, including 10 of 11 outflow sources. The 10 sources are class II sources.

(5) The distribution of the mean-frequency of the *IRAS* sources in L1641 is very similar to those in Perseus, but it is different from those in Taurus. This indicates that the *IRAS* sources in L1641 and Perseus are embedded in dense cores larger and more massive than the cores in Taurus.

(6) 14 sources imaged in H and K' are associated with small (but statistically significant) groupings of near-IR sources, which we defined as stellar density enhancements (SDEs). Most of the near-IR sources within SDEs are probably young stellar objects physically associated with the *IRAS* sources.

(7) A detailed optical and near-IR study of three *IRAS* sources with SDEs show that at least 60% of the near-IR sources in the vicinity of the *IRAS* positions are pre-main-sequence stars. Star formation within SDEs is a continuous process with an age span of 1-3 Myr.

7.2. WHAT HAVE WE LEARNED?

We started this thesis by asking three questions: (1) what are the key indicators of the evolutionary states of young stellar objects? (2) when and how are the molecular dense cores dissipated? and (3) how are young stars distributed in a single molecular cloud? Although the answers seem much more complicated than we first thought, the following summarizes what we have learned from the results listed in the preceding section:

(1) *Outflow as an early stage of star formation* The *IRAS* sources associated with CO molecular outflows are significantly different from those without the outflow. They tend to be colder and more luminous. Most of them are associated with dense molecular cores. All of them show nebulosity in the near-IR images. Ten of 11 outflow sources are class I sources. It is also found 7 of 11 *IRAS* sources are associated with the SDEs. These observations add additional support to the suggestion that the outflow sources are at a earlier evolutionary stage prior to the pre-main-sequence stars.

(2) *The dissipation of molecular dense cores by outflow or accretion* We found that most of outflow sources are associated with molecular dense cores, and most of non-outflow sources are not. It was also found that the outflow sources tend to have colder color temperature, and are associated with higher column density of the molecular gas. This indicates that the molecular dense cores may have dissipated by the time the molecular outflow has terminated. The mass-loss rate of the outflow is compatible to the dissipation rate required to dissipate a core with a few solar masses within 10^6 yr.

(3) *Young Stellar Population in L1641* The full coverage of our *IRAS* source selection and the extensive near-IR imaging provides thus far the most comprehensive census of young stellar population in L1641. Using the *IRAS* data, we found that most of the *IRAS* sources are almost indistinguishable from the *IRAS* counterpart of the known T Tauri stars. The near-IR imaging of the 59 *IRAS* sources and the optical and near-IR photometric data of the 89 near-IR sources near three *IRAS* sources suggest that most of the near-IR sources are late-type pre-main-sequence stars. We therefore suggest that the major young stellar population in L1641 is low-mass PMS stars.

(4) *Distribution of young stars in L1641* The spatial distribution of young stellar objects in L1641 can be characterized by a range of surface density, from a large cluster (the Trapezium Cluster) to SDEs and to individual stars. The cluster and isolated star

formation modes may be the high and low ends of a continuous stellar density distribution.

(5) *The cause of star formation* The formation of the Trapezium Cluster may be triggered by the external force, while the formation of SDEs and individual stars may be caused by their self-gravity, and occur spontaneously.

7.3. FUTURE STUDIES

I consider the discovery of SDEs as the most important result in this thesis. The SDEs are potentially important for us to understand the physical process of star formation. The followings are the questions we would like to pursue in the future study:

(1) Is the SDE a common phenomenon, or it is unique to the L1641? How does it compared to the distribution of young stars in the typical isolated star formation region, like the Taurus dark cloud?

(2) What determines the degree of young star aggregation? Do different stellar densities indicate different star formation mechanisms?

(3) What is the relationship between the mass spectrum of the dense cores and the initial mass function of the stars?

(4) If young stars are continuously formed with an SDE, is there any difference between the "first generation" stars and the stars that are formed later?

To address these questions in future study, we suggest three follow-up observations:

(1) *High -resolution survey for molecular dense cores* An unbiased census of molecular dense cores will allow us to compare the star formation activity as a function of core masses. In addition, we can compare the velocity distribution within the dense cores with and without SDE to understand the effect of SDE on the non-thermal velocity

of the dense cores. Similar core comparison should also be made for different molecular clouds that have different characteristics of star formation.

(2) *Near-IR survey for SDEs* At present L1641 is the only molecular cloud in which the *IRAS* sources have been extensively imaged with high sensitivity (K' = 17.5) and large spatial coverage (4' × 4'). The similarity between Perseus and L1641 (section 4.5.2) suggests that the Perseus molecular cloud is a logical choice for such survey with near-IR cameras. The survey should be carried out in at least three wavelengths (i.e. H, K and L) so that the near-IR color information can be used to determine the nature of the sources.

(3) *Infrared spectroscopic observations* The spectroscopic information of the sources within the SDEs will provide more definitive identification of their nature than the broadband imaging can. It will also provide the dynamical properties of the individual stars. With the information, we can more precisely constrain the age span of the stars within the SDEs. The newly commissioned infrared spectrographs, such as KSPEC on the UH 2.2 m telescope and CSHELL on the IRTF, are the ideal instruments for such studies.

APPENDIX A

TABLE OF 224 *IRAS* SOURCES IN L1641

In this section, we present the complete source sample of the 224 *IRAS* sources selected from the coadded *IRAS* images in L1641. The source selection and flux determination are explained in Chapter 2. In Table A1, column [1] gives the source number; [2] is the source number used in Strom's catalog (Strom et al. 1989b); [3] and [4] are the coordinates of the sources at 1950 epoch, determined from the *IRAS* coadded images (see section 2.2 for discussion); [5]-[8] are the source flux densities at 12, 25, 60 and 100 μm respectively. If there is no detection, a 5 σ upper limit is given with a flag U; The uncertainties of the flux densities are flagged in the following convention: A, 4%; B, 4-8%; C, 8-12%; D, 12-16%; E, 16-20%; F, 20-50%; G, 50%; and H, 100%; [9] is the far-infrared luminosity integrated from 7 μm to infinity (section 2.3.2); [10] indicates source's angular size: "p" for point source (FWHM > 1'.1, see section 2.2.2), and "e" for extended source; [11] shows whether a source is outside (o) or inside (i) the L1641, which is defined by the lower ^{13}CO integrated intensity contour in Figure 2.1; [12] gives the ^{13}CO column density toward the source. The data were obtained using the 4 m telescope in Nagoya University (section 2.3.3); [12] gives source identification; [13] shows if the source is associated with a known young stellar object: "O" is for outflow, "E" for emission line stars, "T" for T Tauri star; [14] gives references as follows: (1) Fukui (1989), (2) Morgan et al. (1991), (3) Herbig & Bell (1988) and (4) Strom et al. 1989b.

TABLE A1. 224 IRAS SOURCES FROM COADDED IMAGES

No.	SN	α (1950) 5^h		δ (1950)			$f12$ (Jy)	$f25$ (Jy)	$f60$ (Jy)	$f100$ (Jy)	L_{FIR} ($L_\odot$)	p-e	o-i	N(^{13}CO) 10^{16} cm^{-2}	ID	YSO	Ref
[1]	[2]	[3]		[4]			[5]	[6]	[7]	[8]	[9]	[10]	[11]	[12]	[13]	[14]	[15]
2	2	37^m	43^s	-6^o	20'	7"	0.32 D	0.91 C	3.9 U	15.6 U	1.4	e	o	0.09			
3	3	39	38	-6	20	7	0.46 U	0.52 U	3.8 U	23.8 D	6.0	e	o	0.38			
4		35	0	-6	21	7	0.37 D	0.57 C	3.9 C	16.1 U	3.0	e	i	0.11			
6		36	29	-6	22	37	2.81 B	3.59 B	23.8 B	134.6 A	48.5	e	o	0.00			
7	4	34	31	-6	23	22	0.63 U	0.65 E	3.7 E	39.0 F	11.5	e	i	1.15			
8	6	33	56	-6	24	7	1.08 D	21.9 A	213.4 A	601.2 A	238.5	p	i	5.22	L1641-N	O	1
9	5	37	2	-6	24	7	2.14 B	3.0 D	18.3 A	105.9 A	38.0	e	o	0.09			
11		32	22	-6	25	22	0.97 C	0.9 B	13.7 C	120.0 A	37.0	e	o	0.35			
12	8	35	15	-6	25	37	0.37 D	0.36 D	1.9 E	35.5 U	1.8	e	i	0.13			
13		35	46	-6	25	45	0.88 C	1.0 B	8.3 C	12 F	7.8	e	o	0.12			
14		37	10	-6	25	45	3.38 A	5.54 A	26.7 A	78.6 C	37.2	e	o	0.08			
15	10	36	10	-6	26	7	3.03 A	3.29 B	23.4 A	119.4 A	44.7	e	o	0.00			
17	9	33	4	-6	26	22	3.07 C	5.0 U	22.5 U	15.5 U	7.8	e	i	1.20			
18	11	33	58	-6	26	37	0.70 D	3.0 D	15.0 C	200. F	58.5	e	i	3.77	MSSB-8	O	2
20		37	59	-6	26	37	1.58 A	2.02 A	8.0 A	17.0 A	10.6	e	o	0.09			
21		38	29	-6	26	52	0.94 B	0.86 B	3.6 C	14.6 C	6.8	e	o	0.00			
22		34	36	-6	27	15	0.20 F	0.33 F	3.0 E	10.0 F	4.0	e	i	0.27			
23		32	8	-6	27	22	0.87 B	1.0 C	5.6 C	364.8 A	96.2	e	o	0.40			
25	12	33	3	-6	28	37	1.15 A	8.60 A	36.0 A	100.7 A	44.3	p	i	2.52	V801 Ori	T	3
26		35	17	-6	30	22	1.31 C	2.16 A	10.8 B	18.0 E	11.4	e	i	0.19			
27	13	35	3	-6	31	52	0.73 E	0.90 D	6.2 E	42.8 U	5.0	e	i	0.20			
28	15	39	18	-6	32	52	1.51 A	2.25 B	7.2 C	32.9 D	14.3	e	o	0.08			
29		33	39	-6	33	37	3.92 A	4.88 A	26.5 B	57.4 C	32.2	e	i	2.61			
30		35	52	-6	33	52	1.28 A	1.26 D	6.3 C	12.0 H	7.8	e	n	0.00			
31	16	34	37	-6	35	7	1.07 B	1.07 B	4.9 U	37.1 U	2.8	p	i	1.60	BE Ori	T	3
32	17	34	15	-6	35	37	0.33 A	0.76 B	4.8 U	110.1 U	1.3	p	i	1.04	V846 Ori		4

TABLE A1. - *Continued*

No.	SN	α (1950) 5^h		δ (1950)			*f*12 (Jy)	*f*25 (Jy)	*f*60 (Jy)	*f*100 (Jy)	L_{FIR} ($L_\odot$)	p-e	o-i	N(^{13}CO) 10^{16} cm^{-2}	ID	YSO	Ref
[1]	[2]	[3]		[4]			[5]	[6]	[7]	[8]	[9]	[10]	[11]	[12]	[13]	[14]	[15]
33	18	34	52	-6	36	37	1.06 C	1.07 D	4.0 F	20.0 F	8.6	p	i	0.63	BF Ori	T	3
34	19	33	16	-6	37	37	0.22 F	0.36 D	6.8 D	18.7 U	4.2	e	i	1.30			
35	20	31	52	-6	37	52	0.35 C	0.92 E	3.5 D	41.4 U	3.0	p	o	0.38			
36	22	34	11	-6	39	52	5.58 A	6.05 B	18.0 C	120.0 D	48.4	e	i	0.53	MSSB-18	O	2
37	23	34	4	-6	40	37	5.87 A	8.12 A	13.2 E	191.6 U	20.7	e	i	0.99			
38	24	39	7	-6	41	22	0.28 E	0.24 E	1.9 E	47.3 U	1.6	p	o	0.00			
39	25	32	42	-6	42	15	0.30 D	0.32 E	3.0 C	37.5 U	2.3	e	i	0.64			
40		39	57	-6	42	22	0.72 D	1.04 D	3.9 D	10.2 E	5.6	p	o	0.00			
41		32	32	-6	42	37	0.24 D	0.30 C	2.5 E	11.0 H	4.2	p	n	0.65			
42	26	34	27	-6	43	22	0.40 F	0.90 F	7.6 G	32.0 D	11.8	p	i	1.01			
44		32	54	-6	43	52	1.14 B	1.56 B	5.7 B	11.8 F	7.5	e	i	0.43			
46	27	35	20	-6	44	7	2.10 A	2.92 A	5.0 D	20.2 D	11.7	p	i	0.27	HD37357		4
47	28	33	58	-6	44	37	8.58 B	7.35 C	27.0 C	150.0 U	31.9	p	i	3.92			
49	30	33	30	-6	45	7	0.96 B	1.94 B	29.7 A	154.9 B	51.9	p	i	2.93			
50	31	33	58	-6	46	22	1.80 C	10.00 H	60.0 B	280.0 B	99.6	p	y	4.90			
51	32	33	56	-6	47	7	0.70 D	5.00 E	80.7 C	261.5 A	97.5	p	i	4.66	MSSB-21	O	2
52		32	14	-6	47	52	0.36 E	0.55 U	5.3 A	42.0 A	13.3	e	o	0.08			
53		34	44	-6	48	45	2.40 B	3.98 A	9.2 D	37.8 U	10.9	e	i	0.63			
54		31	20	-6	48	52	0.77 A	1.15 B	6.1 A	24.4 B	10.1	e	o	0.00			
56	33	35	24	-6	48	52	0.38 U	0.59 C	3.1 C	14.6 U	2.0	p	i	0.83			
57		39	5	-6	50	7	0.33 E	0.43 E	2.7 E	11.2 C	4.5	p	o	0.00			
58		31	51	-6	50	37	0.96 A	1.22 B	6.2 A	31.1 B	12.1	e	o	0.00			
59		36	32	-6	50	37	0.64 B	0.60 B	1.4 D	12.6 E	5.0	e	o	0.07			
62	34	35	41	-6	50	52	2.82 A	3.11 A	7.1 B	55.9 A	22.6	p	i	0.99			
64		37	0	-6	51	52	0.71 B	0.69 C	3.1 C	29.6 C	10.0	e	o	0.15			
65		35	14	-6	53	15	0.85 U	0.85 U	5.3 C	10.0 D	4.3	e	i	0.14			
68		34	38	-6	55	45	1.70 A	2.37 A	7.4 D	23.3 U	7.9	e	i	0.46			

TABLE A1. - *Continued*

No.	SN	α (1950) 5^h		δ (1950)			*f*12 (Jy)	*f*25 (Jy)	*f*60 (Jy)	*f*100 (Jy)	L_{FIR} ($L_\odot$)	p-e	o-i	N(^{13}CO) 10^{16} cm^{-2}	ID	YSO	Ref
[1]	[2]	[3]		[4]			[5]	[6]	[7]	[8]	[9]	[10]	[11]	[12]	[13]	[14]	[15]
70		33	15	-6	58	22	0.34 E	1.10 F	8.3 A	56.0 B	18.1	e	i	0.21			
71	35	35	29	-6	58	22	0.24 U	0.51 C	5.3 C	12.0 H	5.1	p	i	1.75	T456		4
72	37	34	59	-6	59	52	0.74 C	1.34 B	2.4 D	33.6 U	3.2	p	i	1.64			
73	36	36	16	-6	59	52	2.14 B	5.31 A	20.5 A	44.7 B	24.5	p	i	0.46			
74	38	39	42	-7	2	7	0.47 C	0.60 C	2.2 D	17.3 B	6.2	e	o	0.04			
75	39	36	21	-7	2	22	0.57 C	5.34 A	26.1 A	106.5 A	39.7	p	i	1.96	L1641-C	O	1
76		33	34	-7	2	52	1.00 B	1.06 A	5.2 B	26.9 D	10.7	e	o	0.59			
77		31	38	-7	3	22	1.18 A	0.25 C	0.6 U	4.1 U	2.1	p	o	0.00			
78		34	43	-7	3	52	0.38 E	0.36 H	4.3 U	7.3 U	1.0	p	n	1.47			
79	40	35	53	-7	3	52	53.7 A	124.6 A	168.8 A	127.0 A	241.0	p	i	1.02	V883 Ori	E	3
80	41	39	36	-7	6	52	0.16 C	0.24 C	1.0 C	7.0 H	2.5	p	n	0.00			
81		36	54	-7	7	15	0.51 U	0.39 U	4.5 B	29.6 C	9.0	e	i	0.59			
83	42	35	44	-7	10	7	0.39 E	0.98 B	4.0 C	21.0 U	3.3	p	i	2.25	Haro 14a		4
84	43	32	10	-7	10	22	0.23 E	0.43 C	3.5 A	13.4 B	5.2	e	o	0.00			
85	44	36	42	-7	12	7	0.50 D	3.11 A	9.6 C	20.0 H	10.8	p	n	0.87			
87		36	41	-7	12	37	0.49 C	2.93 A	9.6 C	18.0 H	10.2	p	n	0.80			
89	47	36	18	-7	14	7	2.22 B	3.18 B	3.1 C	44.1 U	6.9	p	i	0.66	H 2-249	T	4
90		33	33	-7	15	52	0.76 C	1.06 B	7.8 A	45.1 B	15.8	e	o	0.06			
91		34	19	-7	16	22	0.21 U	0.43 D	1.3 E	11.8 E	3.7	e	i	0.85			
92		33	0	-7	16	37	0.59 D	1.00 E	5.0 H	10.0 H	5.7	o	n	0.00			
95	49	36	30	-7	18	7	1.05 B	3.57 B	9.8 B	46.0 U	8.9	p	i	0.33	V599 Ori		4
96		36	8	-7	18	22	0.89 B	1.42 A	8.3 B	23.4 C	10.9	e	i	1.36			
97		37	12	-7	20	22	0.29 D	0.31 D	2.0 E	15.2 E	5.1	e	i	0.75			
99	51	36	26	-7	22	37	0.79 D	1.43 C	5.3 C	18.0 H	8.4	p	y	1.75			
100		31	21	-7	24	22	4.91 U	0.36 C	0.9 C	5.9 E	2.0	e	o	0.00			
101	52	37	25	-7	24	52	0.54 U	0.50 E	3.9 U	15.1 U	0.5	p	i	1.20			
102		35	53	-7	25	37	0.88 B	1.28 A	4.8 B	6.1 U	4.7	e	i	0.73			

TABLE A1. - *Continued*

No.	SN	α (1950) 5^h		δ (1950)			*f*12 (Jy)	*f*25 (Jy)	*f*60 (Jy)	*f*100 (Jy)	L_{FIR} ($L_\odot$)	p-e	o-i	N(^{13}CO) 10^{16} cm^{-2}	ID	YSO	Ref
[1]	[2]	[3]		[4]			[5]	[6]	[7]	[8]	[9]	[10]	[11]	[12]	[13]	[14]	[15]
103		32	23	-7	27	52	0.58 D	1.16 D	3.6 C	9.1 D	5.1	e	o	0.00			
104	54	36	56	-7	28	7	0.89 B	4.62 A	68.1 A	122.9 B	58.2	p	i	1.83	H 4-255	OT	1, 3
105	55	38	2	-7	28	52	29.59 A	88.46 A	182.2 A	219.2 A	211.9	p	i	1.40	L1641-S	OE	1, 3
106	57	36	29	-7	29	7	0.45 U	0.45 D	1.5 U	39.4 U	0.5	p	i	1.26			
107		33	14	-7	30	37	0.19 E	0.69 B	1.2 U	7.7 U	1.0	e	o	0.00			
108	59	37	27	-7	31	37	0.30 U	8.99 A	128.6 A	219.9 A	14.3	p	i	1.60	L1641-S3	O	1
113	61	36	44	-7	34	52	1.54 A	2.17 A	6.2 B	14.1 E	9.2	e	i	0.50			
114		39	24	-7	35	37	0.50 U	0.32 B	0.7 U	0.6 U	0.3	p	o	0.00			
116		36	55	-7	36	22	0.78 B	1.76 A	5.8 B	11.5 D	7.0	e	i	0.59			
117		45	19	-7	38	15	0.14 U	0.12 U	0.7 C	1.9 D	0.7	e	o	0.00			
118		32	56	-7	38	22	0.23 D	0.41 B	0.8 D	7.0 U	1.0	p	o	0.00			
119	62	38	4	-7	38	52	0.11 U	0.78 B	2.0 D	18.4 U	1.5	p	i	1.38			
120	63	37	34	-7	39	7	0.45 D	0.81 C	1.4 U	24.7 U	1.5	p	i	0.76			
122		41	21	-7	39	37	0.16 U	0.12 D	1.0 B	3.0 H	1.2	e	o	0.00			
123		35	20	-7	39	45	0.74 B	0.84 B	4.7 B	21.6 C	8.7	e	i	0.20			
124		34	46	-7	39	52	0.34 D	0.22 U	1.2 U	6.9 U	0.9	p	i	0.54			
126		40	24	-7	41	7	0.14 U	0.23 U	1.0 C	13.8 D	3.8	e	o	0.09			
127		40	37	-7	42	7	0.13 U	0.12 E	1.3 F	10.1 B	3.1	e	o	0.00			
128		41	43	-7	42	15	0.13 U	0.10 U	0.5 C	6.4 U	0.3	e	o	0.06			
131	66	34	10	-7	42	52	0.85 A	1.62 A	5.2 U	23.0 D	9.8	e	o	0.00			
133		35	52	-7	44	7	0.20 U	0.57 C	3.0 C	11.0 D	4.1	e	i	0.53			
134	67	38	1	-7	44	37	0.20 U	0.43 D	2.1 D	10.0 U	1.4	p	i	1.30			
136		33	36	-7	45	22	0.20 U	0.15 E	0.9 C	11.4 U	0.6	e	o	0.00			
138		35	15	-7	46	52	0.70 D	1.33 B	2.0 C	15.6 U	2.9	e	i	0.41			
141		32	53	-7	48	7	0.14 U	0.15 E	0.4 F	5.2 D	1.5	e	o	0.00			
142		36	28	-7	48	7	0.48 B	0.50 C	4.7 A	37.1 C	12.0	e	i	0.49			
143		33	2	-7	48	15	0.33 B	0.19 U	0.4 G	7.2 C	2.6	p	y	0.00			

TABLE A1. - *Continued*

No.	SN	α (1950) 5^h		δ (1950)			*f*12 (Jy)	*f*25 (Jy)	*f*60 (Jy)	*f*100 (Jy)	L_{FIR} ($L_\odot$)	p-e	o-i	N(^{13}CO) 10^{16} cm^{-2}	ID	YSO	Ref
[1]	[2]	[3]		[4]			[5]	[6]	[7]	[8]	[9]	[10]	[11]	[12]	[13]	[14]	[15]
146	68	37	55	-7	49	52	0.98 B	3.87 A	9.7 B	9.5 U	8.9	p	i	1.22			
149	69	36	11	-7	51	52	0.13 C	0.31 C	1.5 D	9.6 U	1.2	p	i	0.20	Haro 7-1	T	3
150	70	38	58	-7	51	52	0.18 C	0.60 C	1.0 E	38.7 U	1.2	p	i	1.07			
151		41	43	-7	52	22	0.14 U	0.17 E	0.4 D	8.8 U	0.3	e	o	0.02			
154		35	10	-7	54	37	0.59 C	0.67 D	1.7 E	15.0 F	5.6	e	i	0.56			
155		34	59	-7	54	52	0.21 U	0.25 E	1.1 F	15.0 H	4.3	e	n	0.65			
156		42	25	-7	54	52	0.12 U	0.14 U	0.5 D	4.5 B	1.3	e	o	0.00			
158		38	24	-7	56	15	0.20 U	0.26 U	1.1 D	7.0 U	0.6	p	i	1.18			
160	72	39	1	-7	56	22	0.37 B	3.44 B	13.1 A	30.9 E	14.8	p	i	1.23			
161		34	46	-7	57	22	0.18 U	0.32 E	2.2 C	37.0 C	10.3	e	i	0.39			
162		36	9	-7	57	52	0.90 B	0.42 D	0.6 H	1.9 U	1.9	e	n	0.16			
163	73	37	57	-7	57	52	0.96 B	2.48 A	5.6 A	16.2 E	8.9	p	i	0.90			
164		43	50	-7	57	52	0.16 U	0.16 U	1.1 B	3.6 H	1.3	e	n	0.04			
167		43	41	-7	59	15	0.25 U	0.29 U	0.9 C	4.2 D	1.4	e	o	0.00			
168	74	38	59	-7	59	22	0.36 C	0.95 A	3.5 U	32.5 U	1.5	p	i	1.42			
169		43	53	-7	59	37	0.10 U	0.17 U	1.5 B	4.3 D	1.6	e	o	0.00			
171	76	40	2	-8	0	7	0.48 C	0.98 B	2.1 D	20.0 U	2.4	p	i	0.10			
172		34	17	-8	0	22	0.20 D	0.21 C	0.7 D	10.0 U	0.8	p	i	0.17			
173		35	20	-8	0	37	0.21 D	0.20 E	2.1 D	8.1 F	3.2	e	i	0.40			
174		34	4	-8	0	45	0.45 B	0.76 B	1.8 B	6.9 U	2.1	e	o	0.19			
176		31	25	-8	1	52	0.12 E	0.17 U	0.3 U	5.2 U	0.3	p	o	0.00			
177	78	38	16	-8	1	52	0.20 U	0.32 C	1.9 D	10.0 U	1.2	p	i	1.43			
178	77	39	26	-8	1	52	0.80 B	1.69 B	4.9 A	10.0 U	4.8	p	i	0.93	Haro 7-2	T	3
180		36	32	-8	2	15	0.41 U	0.32 U	7.8 B	52.0 B	15.8	e	i	0.35			
181	79	39	3	-8	2	22	0.20 U	0.41 C	2.8 U	28.7 U	0.4	p	i	1.15			
183		36	11	-8	4	7	0.34 U	0.26 D	1.1 E	14.1 U	0.7	p	o	0.08			
185		35	32	-8	5	7	0.37 C	0.39 B	1.0 B	5.0 U	1.3	e	o	0.17			

TABLE A1. - *Continued*

No.	SN	α (1950) 5^h		δ (1950)			*f*12 (Jy)	*f*25 (Jy)	*f*60 (Jy)	*f*100 (Jy)	L_{FIR} ($L_\odot$)	p-e	o-i	N(^{13}CO) 10^{16} cm^{-2}	ID	YSO	Ref
[1]	[2]	[3]		[4]			[5]	[6]	[7]	[8]	[9]	[10]	[11]	[12]	[13]	[14]	[15]
186	81	39	7	-8	5	7	0.89 B	3.18 B	8.2 D	8.7 U	7.6	p	i	1.35			
187	82	38	15	-8	5	22	2.09 A	4.72 A	3.0 H	13.2 U	7.5	p	n	1.07			
188		45	7	-8	5	22	0.11 U	0.12 U	0.4 D	8.4 A	2.3	e	o	0.12			
191	83	39	2	-8	7	7	1.87 A	3.62 A	6.0 C	7.0 U	8.1	p	i	1.59	DL Ori	T	3
192		35	58	-8	7	37	0.31 D	0.50 B	0.6 U	10.4 U	1.0	e	o	0.37			
193	84	38	27	-8	7	37	0.57 D	2.19 D	15.0 H	25.0 H	13.5	p	i	1.52			
194	85	38	27	-8	8	7	0.60 D	1.80 D	12.0 H	20.0 H	11.1	p	i	1.37	L1641-S4	O	1
196	86	38	1	-8	8	52	0.43 B	0.55 B	0.8 C	28.0 U	1.4	p	i	0.70	Haro 7-4	T	3
197	89	40	12	-8	9	22	18.01 A	15.24 A	123.6 A	378.9 A	173.9	e	o	0.30			
198	87	39	12	-8	9	37	0.27 C	1.34 C	2.2 C	11.2 E	4.7	p	i	1.56			
200		31	40	-8	10	7	0.13 U	0.13 U	0.3 E	4.4 B	1.2	e	o	0.00			
203		42	22	-8	11	7	0.49 B	0.71 B	3.7 A	25.8 A	8.9	e	o	0.04			
204		35	16	-8	11	45	0.13 U	0.13 E	1.2 B	10.1 U	0.7	e	o	0.00			
205		42	8	-8	12	22	0.82 A	0.86 A	3.7 A	26.9 A	9.8	e	o	0.14			
206		42	39	-8	13	22	0.16 U	0.24 U	4.7 B	14.6 E	5.3	e	o	0.14			
207		43	16	-8	13	22	0.19 D	0.23 C	1.2 U	15.0 U	0.5	e	o	0.17			
209		42	9	-8	13	45	0.85 B	0.82 A	5.6 A	27.3 A	10.6	e	o	0.23			
211	91	37	58	-8	15	37	0.46 B	1.14 A	2.7 C	8.4 E	4.4	p	i	0.68			
214		44	31	-8	17	45	0.21 U	0.15 U	0.4 D	1.2 F	0.4	e	o	0.16			
215		33	4	-8	18	7	0.36 D	0.57 C	3.7 A	8.1 A	4.2	e	o	0.00			
216	93	40	22	-8	18	22	0.94 B	4.41 A	15.1 B	50.0 F	21.7	p	i	0.42	L1641-S2	O	1
217		38	42	-8	18	45	0.21 U	0.40 B	1.6 B	3.4 D	1.6	e	i	0.91			
218		36	33	-8	18	52	0.19 U	0.24 E	1.8 U	11.9 U	0.3	e	o	0.00			
219		37	25	-8	21	7	0.24 D	0.14 U	0.5 U	10.2 U	0.6	p	o	0.08			
220		36	57	-8	21	22	0.14 U	0.69 B	0.3 F	16.3 U	0.5	e	o	0.05			
222		42	58	-8	22	22	0.22 U	0.40 C	1.5 E	20.1 D	5.8	e	o	0.19			
224	94	39	21	-8	22	52	0.37 C	0.62 B	1.0 D	10.5 U	1.5	p	i	0.91			

TABLE A1. - *Continued*

No.	SN	α (1950) 5^h		δ (1950)			*f*12 (Jy)	*f*25 (Jy)	*f*60 (Jy)	*f*100 (Jy)	L_{FIR} ($L_\odot$)	p-e	o-i	N(^{13}CO) 10^{16} cm^{-2}	ID	YSO	Ref
[1]	[2]	[3]		[4]			[5]	[6]	[7]	[8]	[9]	[10]	[11]	[12]	[13]	[14]	[15]
228		45	19	-8	28	52	0.13 E	0.10 U	0.3 D	9.1 U	0.4	p	i	0.00			
229	95	40	46	-8	30	37	0.13 F	0.52 B	1.1 E	5.4 U	1.1	p	i	0.29			
230	96	44	11	-8	33	7	0.17 U	0.24 U	2.6 A	5.2 D	2.2	p	o	0.24			
232	98	40	33	-8	33	52	0.24 U	0.48 D	1.6 D	2.4 H	1.4	p	y	0.30			
233		40	44	-8	33	52	0.17 U	0.19 E	0.8 U	5.0 U	0.2	p	i	0.20			
234	97	40	10	-8	34	7	0.16 U	0.23 D	1.0 C	11.3 E	3.3	p	i	0.54			
235		42	58	-8	35	7	0.21 D	0.21 U	1.1 U	23.8 U	0.5	p	i	0.29			
237	99	39	11	-8	36	37	0.40 C	1.97 A	5.3 B	15.0 H	7.3	p	n	0.62			
238		37	57	-8	37	52	0.19 D	0.18 U	0.7 U	6.4 U	0.5	p	o	0.00			
240	100	39	19	-8	38	22	0.35 B	0.50 E	0.5 U	7.3 U	1.1	p	i	0.63			
242		42	11	-8	39	7	0.10 U	0.35 E	0.2 U	8.0 U	0.4	e	i	0.32			
243	101	40	24	-8	39	52	0.80 A	1.20 E	1.4 E	10.0 H	4.9	p	n	0.95			
244	102	44	16	-8	40	22	0.28 C	0.57 D	1.3 D	7.0 F	3.0	e	o	0.13			
245	103	40	24	-8	41	22	0.70 A	1.33 A	1.9 B	10.0 H	5.0	p	y	0.99			
246	104	39	7	-8	41	37	0.26 D	0.73 B	3.5 B	16.8 B	6.2	p	i	0.70			
247		36	59	-8	41	45	0.15 U	0.16 U	1.2 C	3.0 E	1.2	e	o	0.09			
249		37	29	-8	42	15	0.19 D	0.22 U	0.8 U	6.4 U	0.5	e	o	0.15			
250		41	31	-8	43	22	0.12 U	0.12 U	0.5 E	17.0 F	4.5	e	i	0.48			
251	105	39	8	-8	44	22	0.22 U	0.99 B	4.1 C	19.6 U	2.8	p	i	0.48			
252		39	39	-8	44	37	0.28 C	0.17 U	0.8 U	10.3 U	0.7	p	i	0.43			
256	106	40	45	-8	45	37	0.17 U	0.77 B	4.0 B	15.5 A	5.7	p	i	0.97			
257		43	15	-8	46	52	0.12 U	0.14 U	0.7 C	4.6 H	1.4	e	n	0.19			
258	107	40	46	-8	47	22	0.14 U	0.40 B	3.2 D	15.8 D	5.3	p	i	0.16			
261		40	5	-8	51	45	0.16 U	0.12 U	0.4 D	6.9 E	1.9	e	i	0.64			
263		42	13	-8	54	7	0.13 E	0.13 U	0.6 U	10.1 U	0.3	e	o	0.26			
264	108	38	15	-8	54	45	0.16 E	0.22 E	1.5 C	6.8 A	2.6	p	i	0.00			
266	110	37	32	-8	58	7	0.41 C	0.19 U	0.7 U	7.7 U	1.0	p	i	0.10			

TABLE A1. - *Continued*

No.	SN	α (1950) 5^h		δ (1950)			*f*12 (Jy)	*f*25 (Jy)	*f*60 (Jy)	*f*100 (Jy)	L_{FIR} ($L_\odot$)	p-e	o-i	N(^{13}CO) 10^{16} cm^{-2}	ID	YSO	Ref
[1]	[2]	[3]		[4]			[5]	[6]	[7]	[8]	[9]	[10]	[11]	[12]	[13]	[14]	[15]
267	111	38	49	-8	58	45	0.10 U	0.36 B	6.2 A	7.8 U	3.6	p	i	0.34			
269		42	47	-9	0	15	0.21 U	0.10 U	1.4 B	6.2 D	2.0	e	o	0.00			
270	113	38	33	-9	7	22	0.95 B	2.14 A	1.9 D	8.3 E	5.4	p	i	0.64			
272		43	34	-9	7	52	0.61 B	0.15 U	0.4 C	4.9 A	2.4	e	o	0.00			
273		43	7	-9	8	15	0.11 U	0.17 U	1.2 C	7.2 C	2.2	e	o	0.10			
276	114/ 115	38	23	-9	20	52	6.15 A	10.00 U	30.0 E	185.3 F	72.1	e	i	0.42			
277	116	39	5	-9	21	45	0.99 B	1.71 A	5.9 C	86.9 A	26.5	e	i	0.44			
280	118	38	44	-9	24	37	0.79 B	3.04 A	19.1 B	40.0 E	19.5	p	i	0.09			
281	119	38	13	-9	29	37	1.71 B	1.47 B	7.5 U	105.0 U	4.2	e	i	0.34			
282		44	43	-9	31	7	0.20 E	0.12 U	0.5 U	1.9 U	0.5	p	o	0.00			
283		45	19	-9	32	7	0.33 B	0.15 D	0.1 D	3.8 U	0.6	p	o	0.00			
286		40	42	-9	37	52	0.23 C	0.21 U	3.1 U	10.2 U	0.6	p	o	0.19			
287	121	45	20	-9	41	7	3.91 A	1.22 A	0.5 U	0.9 U	7.3	p	o	0.00			
288	123	37	52	-9	43	37	0.88 A	1.70 A	1.2 D	9.0 U	2.9	p	I	0.19	V350 Ori	T	3
289		40	27	-9	46	22	0.20 D	0.50 D	0.5 U	6.7 U	0.8	p	i	0.48			
292		41	35	-6	30	29	0.35 C	0.36 D	1.8 E	13.4 U	1.7	e	o				
295		41	59	-6	51	59	0.19 U	0.20 U	2.9 B	11.0 D	3.8	e	o				
297		43	23	-6	35	59	0.51 C	1.17 A	8.3 A	23.0 B	10.1	e	o				
298		42	21	-6	37	59	0.28 D	0.40 C	3.5 B	39.3 B	11.8	e	o				
300		42	57	-6	46	0	0.77 B	1.03 B	5.1 B	36.6 A	12.8	e	o				
301		44	7	-6	48	59	0.58 B	0.73 B	3.7 A	36.0 A	11.7	e	o				
302		43	17	-6	48	59	0.23 U	0.47 B	3.7 B	22.2 C	7.1	e	o				
303		44	53	-6	51	29	0.52 B	0.56 B	4.6 A	15.0 A	6.5	e	o				
305		45	17	-7	3	30	0.30 U	0.41 C	2.1 C	10.5 U	1.4	e	o				
306		54	39	-7	5	59	0.45 C	0.83 B	3.0 A	7.7 C	4.1	e	o				
307		45	19	-7	9	59	1.07 B	0.41 U	1.8 U	10.0 U	2.7	p	o				

TABLE A1. - *Continued*

No.	SN	α (1950) 5^h		δ (1950)			*f*12 (Jy)	*f*25 (Jy)	*f*60 (Jy)	*f*100 (Jy)	L_{FIR} ($L_\odot$)	p-e	o-i	N(^{13}CO) 10^{16} cm^{-2}	ID	YSO	Ref
[1]	[2]	[3]		[4]			[5]	[6]	[7]	[8]	[9]	[10]	[11]	[12]	[13]	[14]	[15]
308		44	43	-7	9	59	0.16 U	0.19 U	3.6 B	6.6 E	2.9	e	o				
310		44	47	-7	19	29	0.17 U	0.20 U	1.5 C	7.9 U	0.8	e	o				
311		45	51	7	20	30	0.39 B	0.38 C	1.3 D	9.6 C	3.7	e	o				
312		36	5	-8	32	58	0.37 B	0.45 B	1.6 C	22.7 C	7.1	e	o				
313		36	43	-8	40	58	0.28 D	0.18 U	1.1 C	9.3 A	3.3	e	o				
315		36	35	-9	2	28	0.36 C	0.89 B	4.0 A	22.5 A	8.1	e	o				
316		35	57	-9	7	28	1.63 A	1.85 A	5.8 A	12.5 D	8.7	e	o				
317		35	0	-9	27	28	0.59 C	1.94 A	8.9 A	41.3 A	15.5	e	o				
318		35	25	-9	40	28	1.24 B	1.60 B	3.8 E	86.5 A	26.0	e	o				

APPENDIX B

COLUMN DENSITIES OF MOLECULAR GAS

The observed line profile is usually expressed as the corrected antenna temperature as a function of frequency (or velocity), $T^*_A(\upsilon)$. If the profile is gaussian, it can be characterized by three parameters: peak temperature T_p, line width (or velocity dispersion Δv), and line center (or velocity of local standard of rest) V_{LSR}. In the following, we show that these observed parameters can be used to calculate the column density of the observed molecules, the total number of molecules between the emitter and observer per unit area. A more detailed discussion can be found in Yang (1991)

The formal solution of radiative transfer equation can be written as:

$$I_\upsilon = [B_\upsilon(T_{ex}) - B_\upsilon(T_{bg})]\,(1-\exp(-\tau_\upsilon)) \qquad \text{(A1)}$$

where I_υ is the radiation intensity; $B_\upsilon(T)$ is the Planck function at a temperature T; T_{ex} and T_{bg} are the gas excitation temperature and background temperature (T_{bg} = 2.7 K), respectively. τ_υ is the optical depth of the molecular line at υ. In millimeter wavelength, it is convenient to write I_υ in term of radiative temperature T_R by

$$T_R = \frac{h\upsilon}{k}\frac{c2}{2h\,\upsilon^3} I_\upsilon \qquad \text{(A2)}$$

where h is Planck constant, k is Boltzman constant, and c is the speed of light. T_R in turn can be related to the observed antenna temperature T^*_A, which has been corrected for atmospheric attenuation and ohmic loss (Ulich & Haas 1976),

$$T_R = \frac{T^*_A}{\eta_{fss}\,\eta_c} \qquad \text{(A3)}$$

where η_{fss} gives correction for the forward spillover, and η_c for coupling efficiency between the antenna beam patten and source brightness distribution (Kutner & Ulich 1981). Both ηfss and ηc are very difficult to determine, and they are close to unity for most of the sources we observed in this study, we assume $T_R = T^*_A$.

Combining equation (A1)-(A3), we have

$$T_R = [J_\upsilon(T_{ex}) - J_\upsilon(T_{bg})] [1-\exp(-\tau_\upsilon)] \qquad (A4)$$

where $J_\upsilon(T) = (h\upsilon_0/k) / [\exp(h\upsilon_0/kT)-1]$, and υ_0 is the rest frequency of the line. For an optically thick line, $\tau_\upsilon >> 1$, the above equation gives $T_R = T_{ex}$. This is the reason ^{12}CO J = 1-0, an optically thick line in most dense cores, can be used as a temperature tracer. For optically thin line, τ is proportional to the number of molecules in the line of sight, the line therefore can be used to obtain the column density.

For a transition J = 1-0, the optical depth can be calculated by

$$\tau_\upsilon = (h\upsilon_0/c) [B_{01} N_0 - B_{10} N_1] \varphi(\upsilon-\upsilon 0) \qquad (A5)$$

where N_0 and N_1 are the column densities of the molecules at J = 0 and J = 1, respectively; B_{ij} is the Einstein coefficients, $\varphi(\upsilon)$ is the line profile. In A5 we assumed that the excitation temperature T_{ex} does not change in the line of sight. Using the relations between the Einstein coefficients to eliminate N_1, A5 can be rewritten as

$$\tau_\upsilon = \frac{8\pi^3 \upsilon_0}{3hc} |\mu^2| [1-\exp(-h\upsilon_0/kT_{ex})] N_0 \varphi(\upsilon-\upsilon 0) \qquad (A6)$$

The total column density N of the molecules can then be calculated using $N = N_0 (2kT_{ex}/h\upsilon_0)$. The term in the parenthesis is the partition function given by Dickman (1978). Using equation A6 we have

$$N = \frac{3k\,T_{ex}}{(4\pi^3 \upsilon_0)\,|\mu^2|}\left[\frac{\tau_\upsilon\, c}{\upsilon_0\,\varphi(\upsilon-\upsilon 0)}\right]\frac{1}{1-\exp(-h\upsilon_0/kT_{ex})}) \qquad \text{(A7)}$$

If the velocity of molecular gas has a Maxwellian distribution, its line profile should be gaussian, term in the square parenthesis in (A7) approximately equals to $\tau_0\,\Delta v$, where τ_0 is optical depth at the line center (v_{LSR}), and Δv is the full-width-half-maximum (FWHM) of the observed line profile.

For J = 1-0 transition of the CO, ^{13}CO and HCO^+ molecules used in this study, the rest frequency of the transition, the dipole moment μ of the molecules are given in Table A2. Using these data, the column density of the molecular gases can be written as

$$N(^{13}CO) = 2.49 \times 10^{14} \cdot \frac{T_{ex} \cdot \tau_0{}^{13} \cdot \Delta v_{13}}{1 - \exp(-5.31/T_{ex})} \qquad (cm^{-2}) \qquad \text{(A9)}$$

$$N(HCO^+) = 1.87 \times 10^{11} \cdot \frac{T_{ex}\, T_p\, \Delta v}{1 - \exp(-4.3/T_{ex})} \qquad (cm^{-2}) \qquad \text{(A10)}$$

where T_p and T_{ex} are in K, and Δv in km s^{-1}. These two equations are used in section 3.3 to calculate the column densities of the two molecules at the *IRAS* sources.

TABLE A2 MOLECULAR CONSTANTS

Transition	Frequency (GHz)	μ debye	Reference
^{12}CO J = 1-0	115.271204	0.1098	Chackerian & Tipping 1983
^{13}CO J = 1-0	110.201307	0.1101	Chackerian & Tipping 1983
HCO^+ J = 1-0	98.188523	4.48	Haese & Woods 1975

APPENDIX C

CONTINGENCY TABLE

In this thesis we used a statistical test called contingency table to test (1) the association of the point-like *IRAS* sources with the L1641 in Chapter 2 and (2) the association of the stellar density enhancements with CS molecular dense cores in Chapter 6. The principle of this test is can be found in Hoel (1947). In this section, we use the data in Chapter 2 as an example to explain how the test was carried out.

A contingency table is usually constructed for studying the relationship between two variables. We want to test whether the point-like *IRAS* sources are exclusively associated with L1641. We started the test by setting up the hypothesis that there is no such association.

Using the data in Table 2.2, we can summarize the spatial distribution of the 224 *IRAS* sources into the contingency table (Table A3). The sources are divided into different categories depending whether they are inside or outside the L1641, and whether they are point sources or the extended sources.

TABLE A3 CONTINGENCY TABLE

		Point source?		
		Yes	No	Total
Inside L1641?	Yes	79 (53)	43 (68)	122 (54%)
	No	20 (46)	82 (58)	102 (46%)
	Total	99	125	224

We now calculate the expected frequencies based on the no-association hypothesis. Since 122 of 224 *IRAS* sources (54%) are inside the L1641, the same percentage of the point sources should be expected inside L1641, if there is no particular relationship between the point sources and the L1641. The resulting expecting

frequency, 53 and 46, corrected to the nearest integer, for the point sources inside and outside L1641 can be obtained. They are inserted in parentheses in Table A3 next to their corresponding observed frequency (79 and 20, respectively). The expecting frequency of the extended sources can obtained similarly.

χ^2, a measure of the compatibility of the observed and expected frequency can be calculated as:

$$\chi^2 = \sum_{i=1}^{k} \frac{(o_i - e_i)^2}{e_i}$$

where k is the number of pairs of frequencies to be compared, o_i and e_i denote these frequencies, and $\Sigma\, o_i = \Sigma\, e_i = n$. Using the data in Table A3 ($k = 4$, and $n = 224$), we obtained $\chi^2 = 46.6$. The number of degrees of freedom in this case is $(2-1) \times (2-1) = 1$. From the χ^2 distribution table, we found, for degree of freedom of 1, $\chi_0^2 = 6.6$ at a probability < 0.01. This means that the chance for the no-association hypothesis to be true is much less than 1%. We therefore conclude that the point-like *IRAS* sources are spatially associated with the L1641.

APPENDIX D

NEAR-IR IMAGING OF INDIVIDUAL SOURCES

In this section, we discuss the near-IR images of the individual sources. The *H* and *K'* images of the 59 *IRAS* sources are presented in Figure A1. In the images, the coadded *IRAS* positions are marked by the crosses. If more than one *IRAS* source presents in one image, the *IRAS* source numbers are given. The near-IR sources identified as the probable counterpart of the *IRAS* sources are indicated by the arrows. The near-IR sources mentioned in the following discussion are marked by the "#" sign followed by the source number used in the discussion. The spectral energy distributions of 55 *IRAS* sources are presented in Figure A2. We now discuss each individual source in turn.

008 (L1641-N) This is the most complicate source associated with a SDE and the diffuse nebulosity. There are 5 sources within 30" from the *PSC* position. All of them are very red ($H - K' > 3$) and are associated with nebulosities. #1 can only be detected in *M* and are located with 3" from the *IRAS PSC* position and the 2.6 mm continuum source. #1 is therefore identified as the counterpart, although other sources also may have significant emission in the *IRAS* bands. This is consistent with the fact that the 12 μm *IRAS* image shows the multiple sources. See Chapter 5 for a detailed discussion.

018 (MSSB 8) Although both #5 and #8 have a very red $H - K'$ color, #5 becomes much brighter in *nbL*. It is the brightest source in *M*, making it the most probable candidate for the *IRAS* counterpart. The nebulosity originated from #5 shows a spiral structure. It is also interesting that the other sources within the central 40" × 40" region have an average $H\text{-}K' < 1.0$, compared with $H\text{-K} = 3.3$ for #5. This suggests that the

reddening of #5 is mostly due to the circumstellar material. See Chapter 5 for a detailed discussion.

025 (near HH 34) Several sources are associated with nebulosity. #8 is the reddest, and the brightest in *nbL*. Examining the R band CCD imaging (Strom et al. 1986), we found that #8 corresponds to an optical source from which an optical jet is ejected. This source is probably the driving source of HH 34.

029 Although not listed in the *PSC*, #10 is red and bright.

032, (V846 Ori) Although not the reddest, #5 lies within 10" from the *IRAS* position. It is the brightest in *K'*. The other two redder sources are too faraway.

034 #6 appears to be red ($H - K' > 1.5$), and none of the other sources in the field is embedded.

036 (MSSB11) Although all other sources in the field are not very red, #1 has $H - K > 3$, making it the prime candidate. As shown in the *K'* image, it is located at the center of a bipolar infrared nebulosity. This highly elongated structure is parallel to a highly collimated CO molecular outflow detected by Morgan et al. (1991). It is too faint to be detected in *nbL* and *M*.

041 All stars have little extinction. Considering its *IRAS* fluxes are very low (f_{12} = 0.24 Jy), the near-IR counterpart may be difficult to detect. We have no identification for this source.

042 #11 is the reddest and brightest, and it is close to the *IRAS* position.

046 This is only one bright source (#1) near the *IRAS* position. It is HD 37357.

047 (V380 Ori), *050*, *51*, (HH 1-2) Source 47 is V380 Ori (#1) which illuminates NGC 1999. The triangle obscuration is visible, although it is much less obscured than in the optical (Herbig 1974), due to the relatively low extinction in infrared. There are also 5 faint sources to the southwest, aligning in the direction of the 3 HH objects found by Strom et al. (1986). #2 is a bright source which lies within 20" from the source 50, and is likely its near-IR counterpart. The bright source (#3) associated with the elongated nebulosity is the C-S star with HH 1 and HH 2 (at the bottom of the image). Although the C-S star is the brightest in the HH 1-2 region, it is probably not the counterpart of the *IRAS* source, because its fluxes at *H* and K are too high to match the *IRAS* fluxes at 12 μm. The other two candidates are the VLA source and the H_2O maser (#3), both are detected in our *K'* image. The mapping with Kuiper Airborne Observatory showed the latter has stronger far-IR emission at 50 and 100 μm (Harvey et al. 1986). The maser source is also much closer to the *IRAS PSC* position ($\Delta\alpha$ = 5", $\Delta\delta$ = -13"). #3 is therefore identified as the *IRAS* counterpart, although the *IRAS* source may be multiple heating sources.

049 The two sources (#1 and #2) are close to the *IRAS* position and are equally red. Both of them are selected as the *IRAS* counterpart.

062, #10 is the only bright source close to the *IRAS* position.

071 (T456) A good example of stellar density enhancement. The *IRAS* source is associated with a group of bright sources all of which have low extinction. #5 is chosen because it lies within 4" from *IRAS* position, and because it is the brightest. It corresponds to an optical star T456.

072 There is only one source (#3) within 30" from *IRAS* position. It is bright and reasonably red.

075 (L1641-C) There are many deeply embedded sources with high extinction in this region, as many sources have H-K > 2.0. Although #20 is the brightest source in K' with a bipolar shape nebulosity, #17 is much redder and becomes the dominate source in M. It also lies within 10" from the *IRAS* position. The extinction the this region is relatively higher than the other fields. As the result, there are more red sources in the image. See Chapter 5 for a detailed discussion.

078 The bright source in the field is too bright to match the *IRAS* flux at 12 μm. We have no identification for this *IRAS* source.

079 (Haro 13a) #1 is the brightest source near the *IRAS* position with a large-scale nebulosity.

083 (Haro 14a) #9 is very red (H - K' = 2.0). The highly elongated nebulosity can be seen in the southeast.

085, 087 The two *IRAS* sources are very close. It is marked as non-point source in Strom et al. (1989b). Source 85 is listed in *PSC* while source 87 is not. #1 is a very red

source, and associated with cone-shape nebulosity. For source 87, #4 can be easily identified. Also noticeable is the faint spiral-shaped nebulosity near #4.

093 All sources in the field have a low extinction. We have no identification.

095 (V599) There is only one bright source, and it is V599.

099 (H4-254) The star in the east of the *IRAS* position is too bright at H and K' to match the *IRAS* fluxes. The source in the west (#1) is very red (H - K' = 1.4), and it corresponds to T489. This source is identified as the *IRAS* counterpart.

101 Most of the sources in the field are red. #12 is chosen because it has H - $K' > 2$, and is close to the *IRAS* position. Other sources also may have emission in *IRAS* bands

104 (H 4-255) There are 2 red and bright sources in the field (#2 and #3). #2 is the reddest, and is also associated with an extended nebulosity. It is therefore likely the *IRAS* counterpart. #3 is the brightest in K', but not as red. #3 and #2 correspond to positions of H4-255 and H 4-255 FIR, given by Leverault (1988).

105 (Re50) #1 (H - K' = 1.7) is embedded inside a huge nebulosity.

106 #11 is chosen because it is red and close to the *IRAS* position. None of the other sources in the field is as red (H - $K' < 0.2$).

108 (L1641-S3) Of the several red sources near the *IRAS* position, #7 is the reddest, and is therefore chosen to be the *IRAS* counterpart.

119 Two sources (#4 and #5) are close to the *IRAS* position and both of them are red.

120 Although not very red, the bright source #16 lies within 5" from the *IRAS* position, and is therefore chosen.

133 No identification.

134 #9 is the only red ($H - K' > 2$) source in the field, and it is near the *IRAS* position.

146 #7 has $H - K' > 1.8$, and it is close to the *IRAS* position.

150 Both #11 is extremely red ($H - K' = 3.5$), and is close to the *PSC* position (<10").

160 #15 is extremely red ($H - K' = 3.0$), and lies within 10" from the *IRAS* position. Although associated with a very elongated nebulosity in the north, #5 is not as red.

163 Three sources (#7, #8 and #11) are red and close to the *IRAS* position, but #7 is the brightest source in *M*, and is therefore chosen. Note the spiral-shaped nebulosity.

168 Three sources (#4, #5, #7) are very red and lie within 60" from the *IRAS* position, but #4 is the brightest and the closest to the *IRAS* position.

171 The double stars (#12, #14) are almost identical. Both could be the counterparts.

177 There is only one source that is close to the *PSC* position.

181 #8 is very red (H - K' > 1.5) and is associated with jet-like nebulosity. However it is too faint to be detected in M.

186 #4, #5, and #6 are all very red (H-K > 2.5), but #6 is the brightest in K' and is also much closer to the *IRAS* position.

187 #8 is very red and bright.

191 #4 is the reddest with H - K' = 0.8, but it lies too far from either the *IRAS* position or the *PSC* position. Although not the reddest, #5 is the brightest and is very close to the *IRAS* position. #5 is therefore chosen to the counterpart.

193 and 194 (L1641-S4) Two *IRAS* sources are located very closely. #8 is the reddest (*nbL* - M = 2.9), and is chosen as counterpart of source 193. However the nearby sources are also very red with H - K' > 2, they also may contribute to the *IRAS* fluxes. #15, although weak in K', has a unipolar nebulosity and is very red, and is probably the near-IR counterpart of source 194.

198 #5 is a red source with nebulosity at two opposite directions, and it is very close to the *IRAS* position.

211 #15 is the only red source (H - K' = 2.0) in the field. All three nearby sources are associated with nebulosity.

216 (L1641-S2) #17 is clearly the counterpart: it is the only red source in the field, and it is associated with a jet-like nebulosity which ended with several knots in the east of the *IRAS* position. The extended structure coincides the blue lobe of the CO molecular outflow mapped by Wouterloot et al. (1989).

224 There is only one source (#6) near the *IRAS* position.

237 There are only two sources near the *IRAS* position, the fainter source is not as red, and the brighter one (#2) has $H - K' = 2.2$) and is associated with nebulosity. #2 is therefore chosen.

243 and 245 The two *IRAS* sources are close to each other, and are associated with a large group of bright sources. #3 is much redder than the others, and it is also very close to source 243's *PSC* position. There are three sources near source 245's *IRAS* position. The binary (#22 and #23) are the reddest, and chosen to be the counterpart of source 245.

246 #2 and #3 are both extremely red. Both could be the counterparts of the *IRAS* source. This may be a multiple source.

256 None of the bright sources in the field is red. The very faint source (#16) with extended structure is probably the counterpart.

270 All sources within 40" are red, but #8 is several magnitude brighter than the others, and it is also very close to the *PSC* position.

280 #18 is closed to the *PSC* position, but has a low extinction.

Figure A1 The H and K' images of 59 *IRAS* sources. Each image covers a 4' × 4' region unless a scale is given. The north is up, and the east is to the left. The limiting magnitudes are approximately $H = 17.5$ and $K' = 17.5$. The *IRAS* positions are marked by the cross. If more than one *IRAS* source presents in an image, the *IRAS* source numbers are given. The near-IR sources identified as the most probable counterparts of the *IRAS* sources are indicated by the arrows. The near-IR sources mentioned in the discussions are marked by the "#" sign followed by the source number used in the discussion.

Source 8

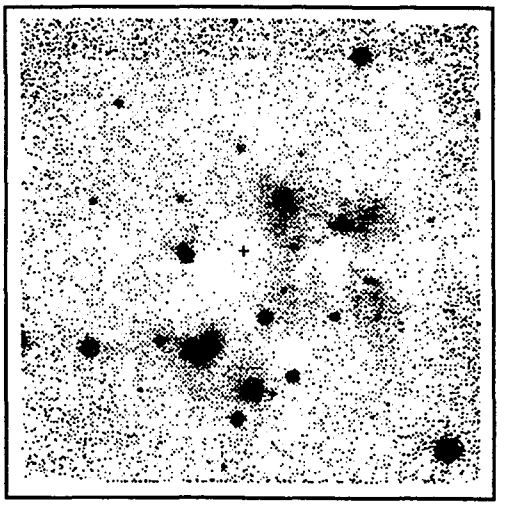

H

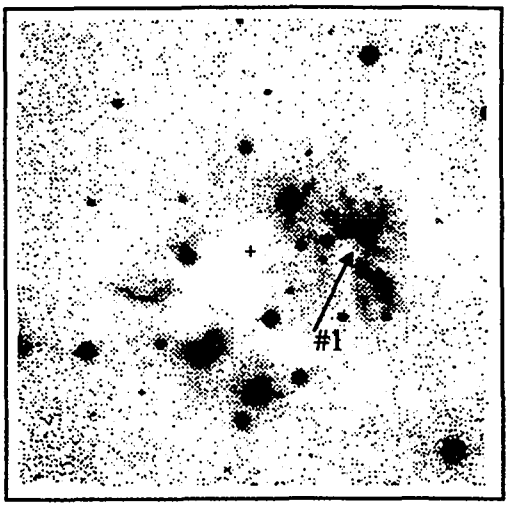

K′

Source 18

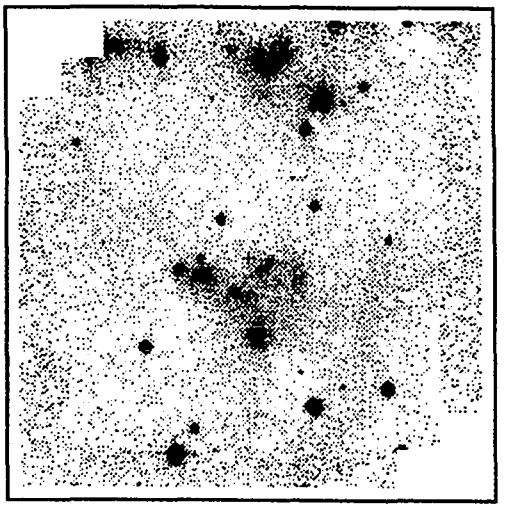

H

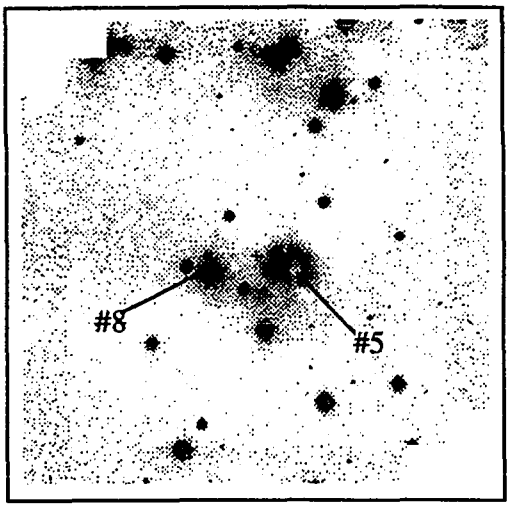

K′

Source 25

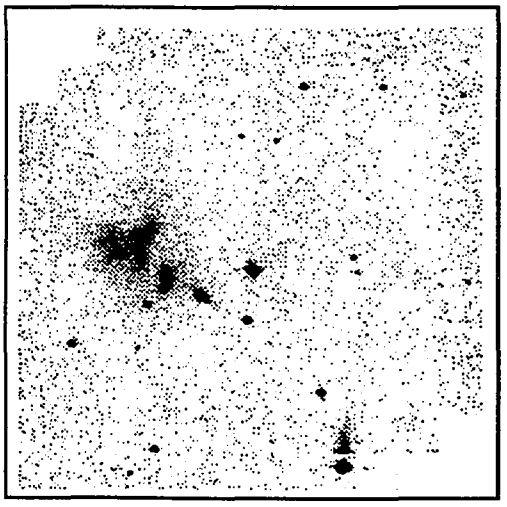

H

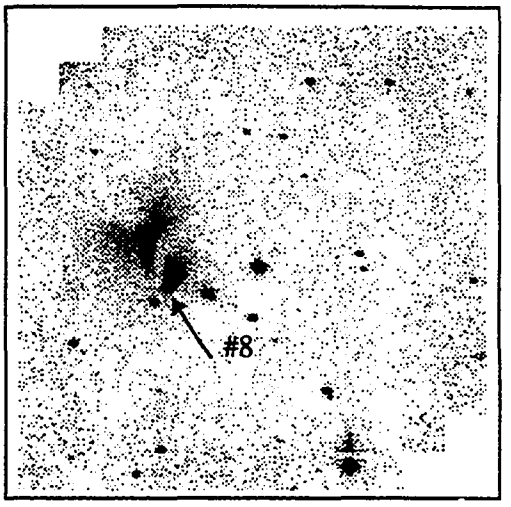

K′

Source 29

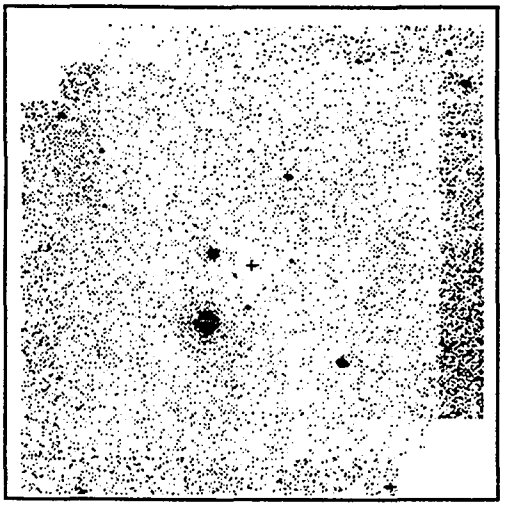

H

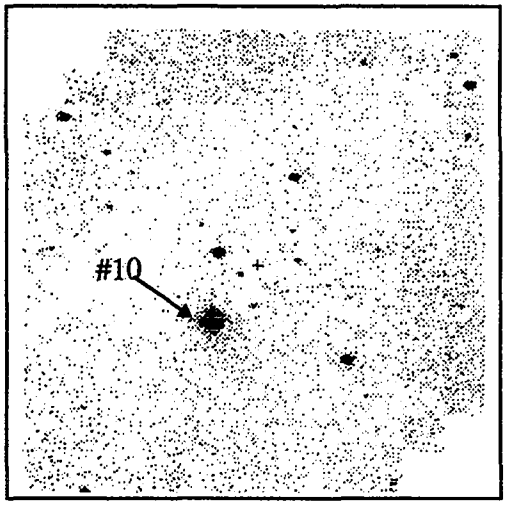

K′

Source 32

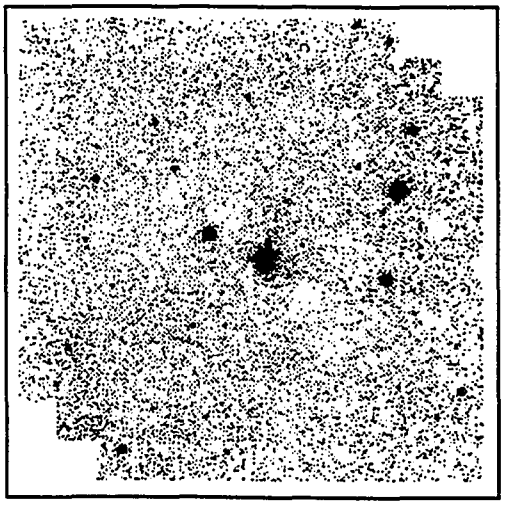

H

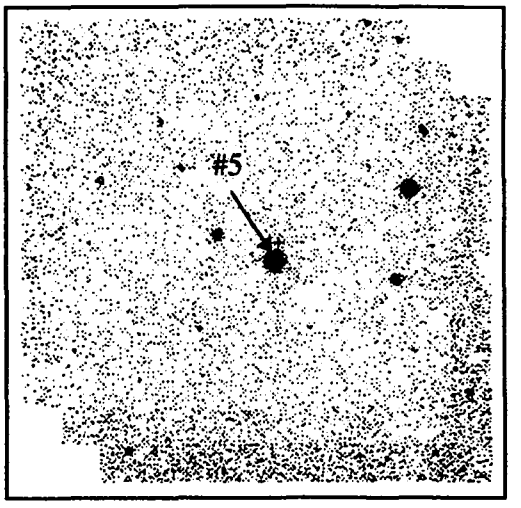

K′

Source 34

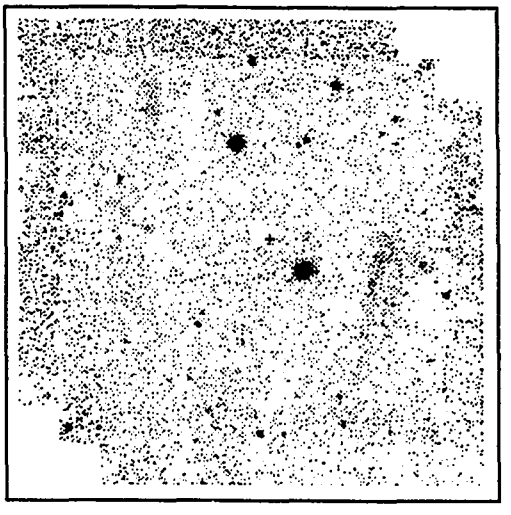

H

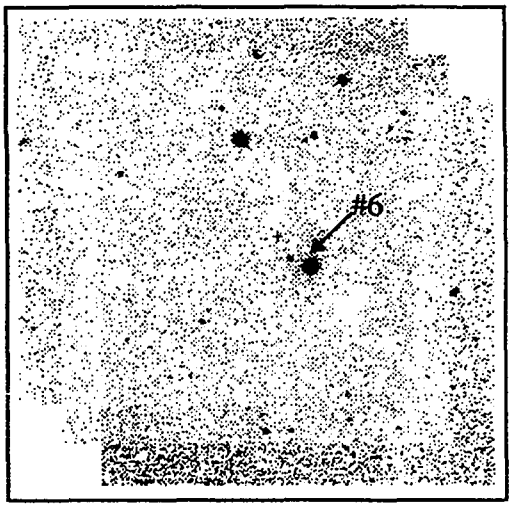

K′

Source 36

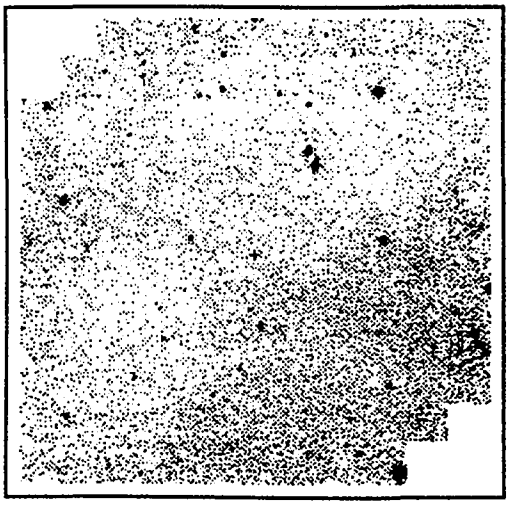

H

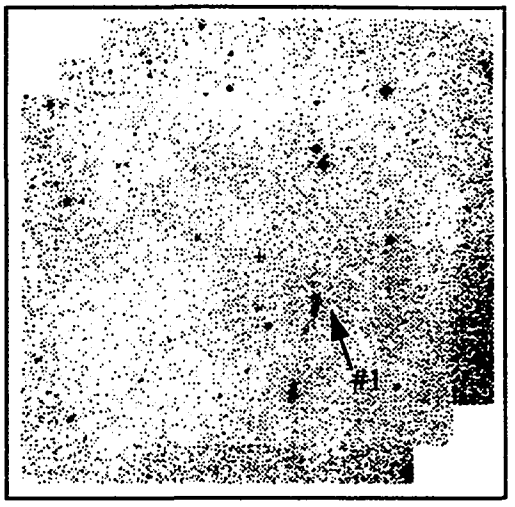

K′

Source 41

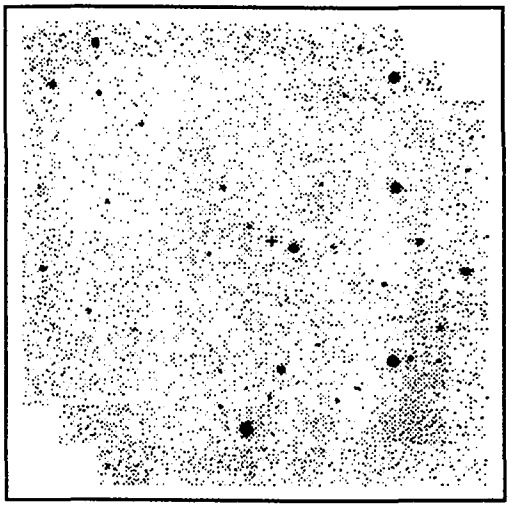

H

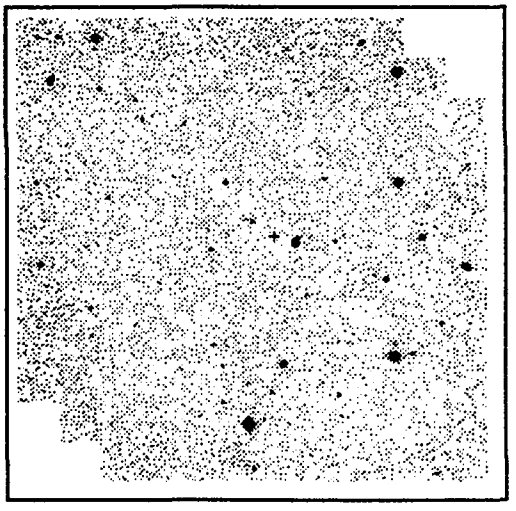

K′

Source 42

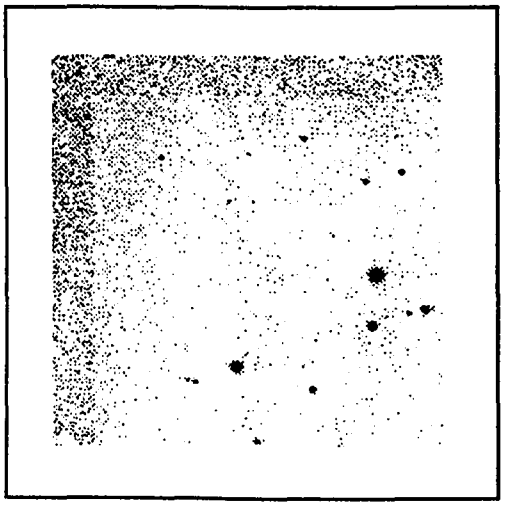

H

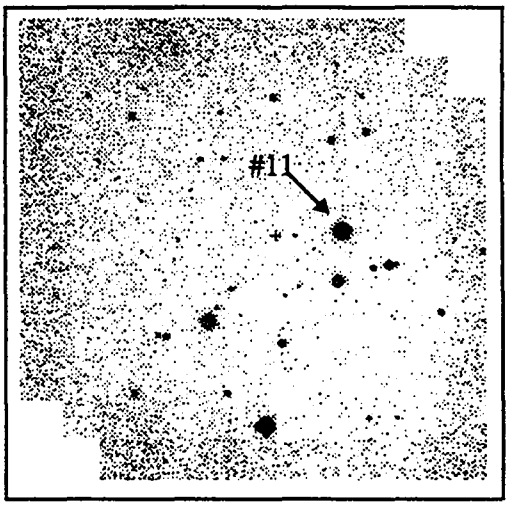

K′

Source 46

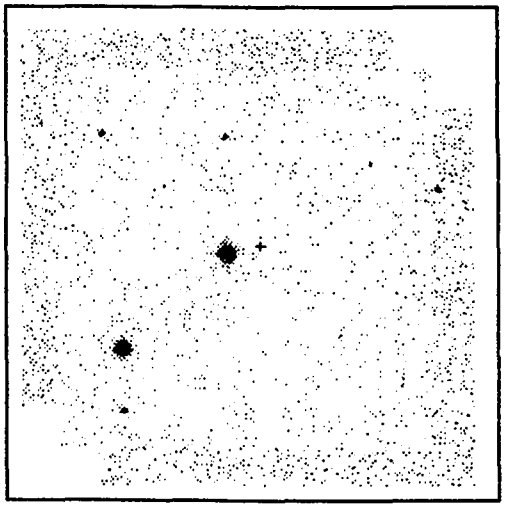

H

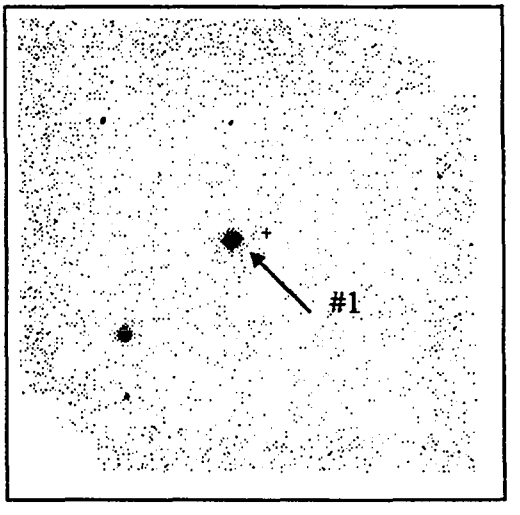

K′

Sources 47, 50, 51

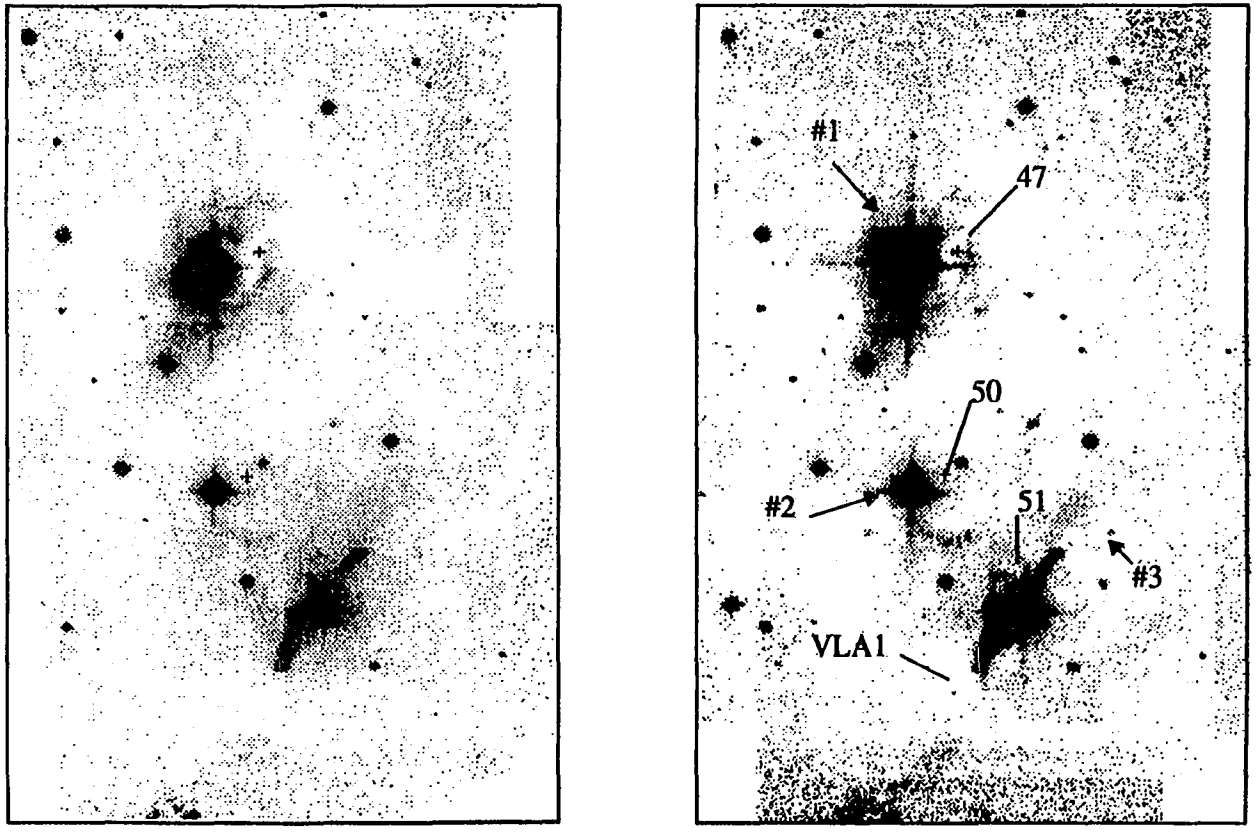

Source 49

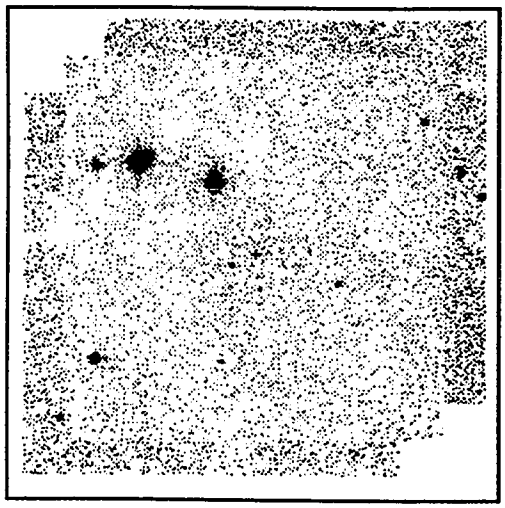

H

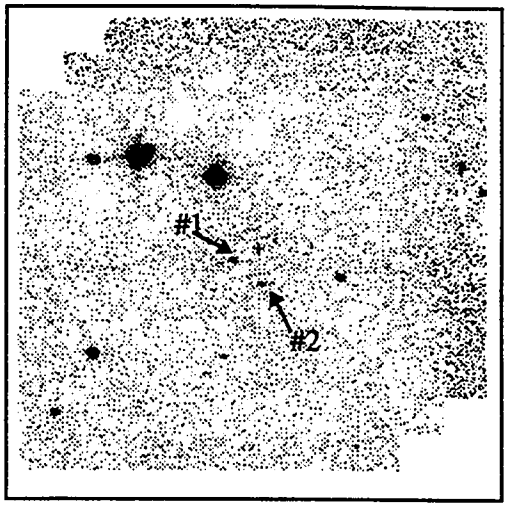

K′

Source 62

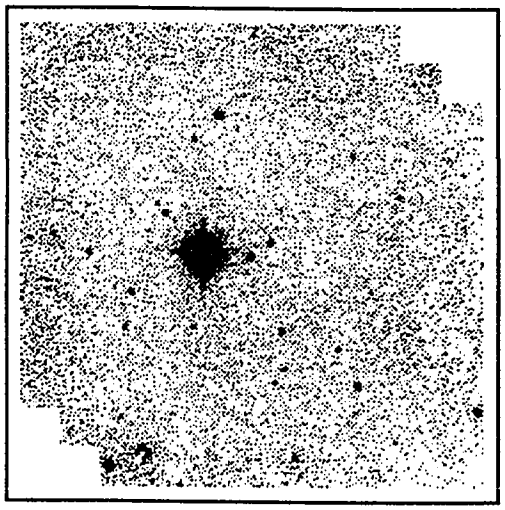

H

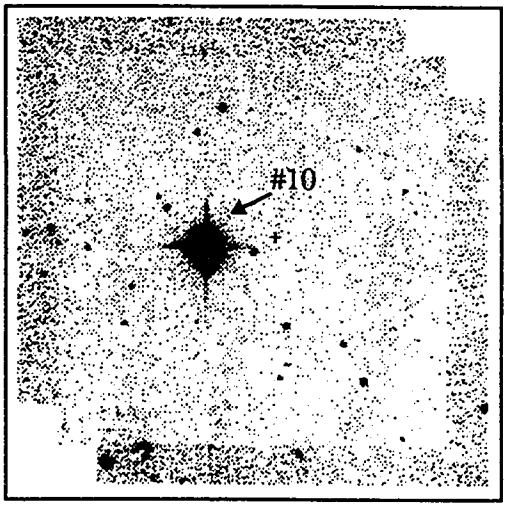

K′

Source 71

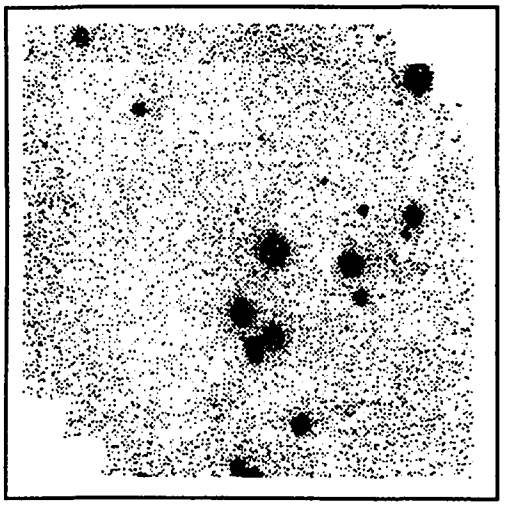

H

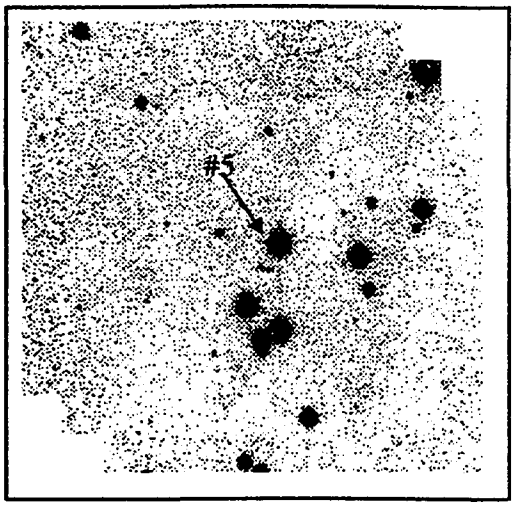

K′

Source 72

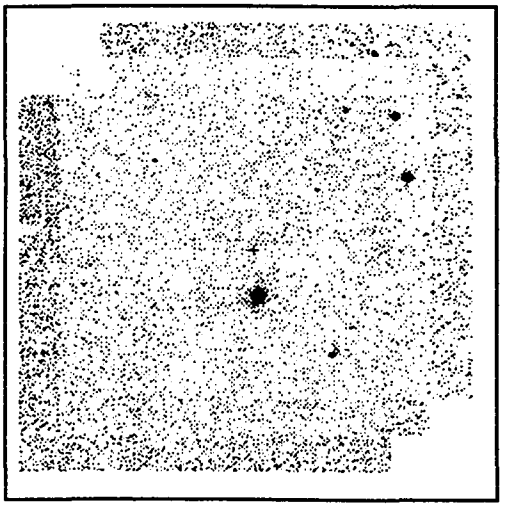

H

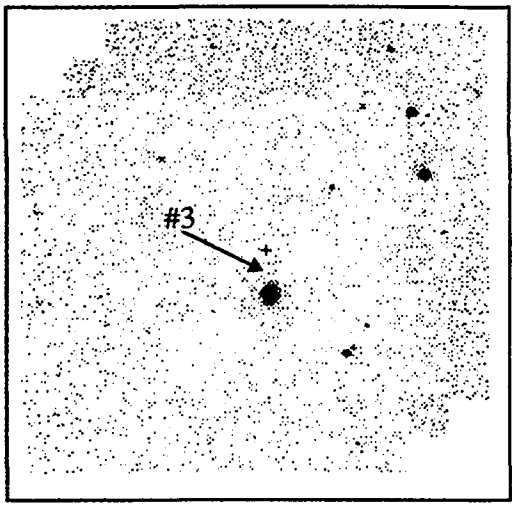

K′

Source 75

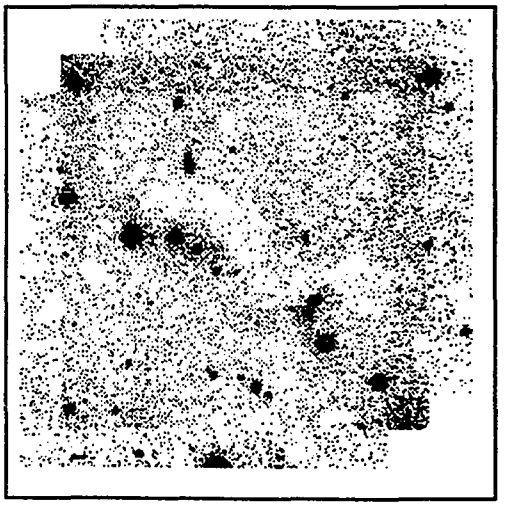

H

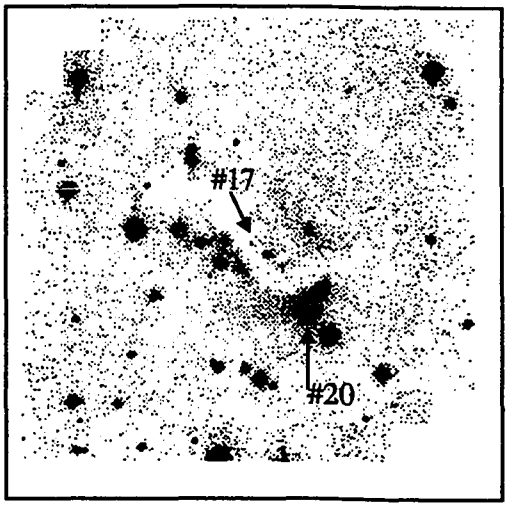

K′

Source 78

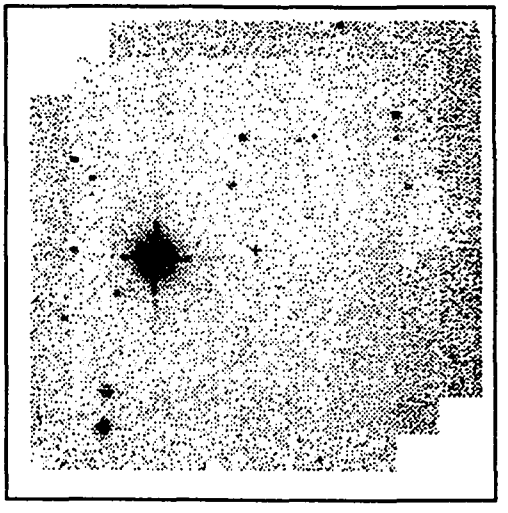

H

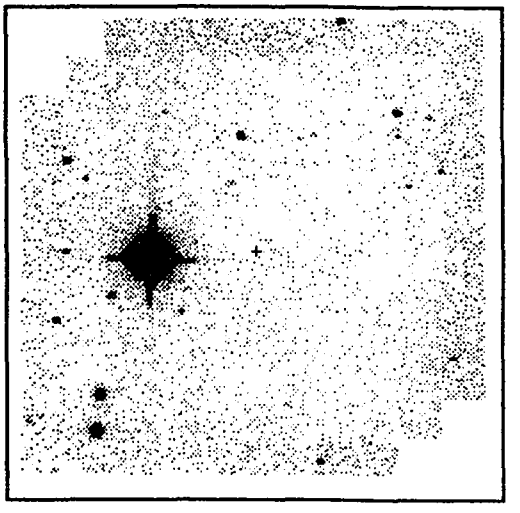

K′

Source 79

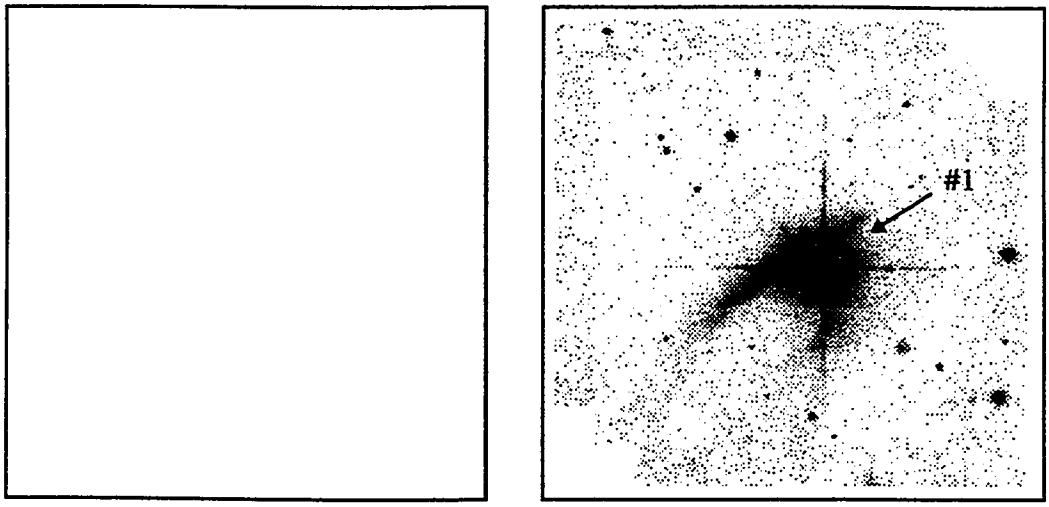

H K′

Source 83

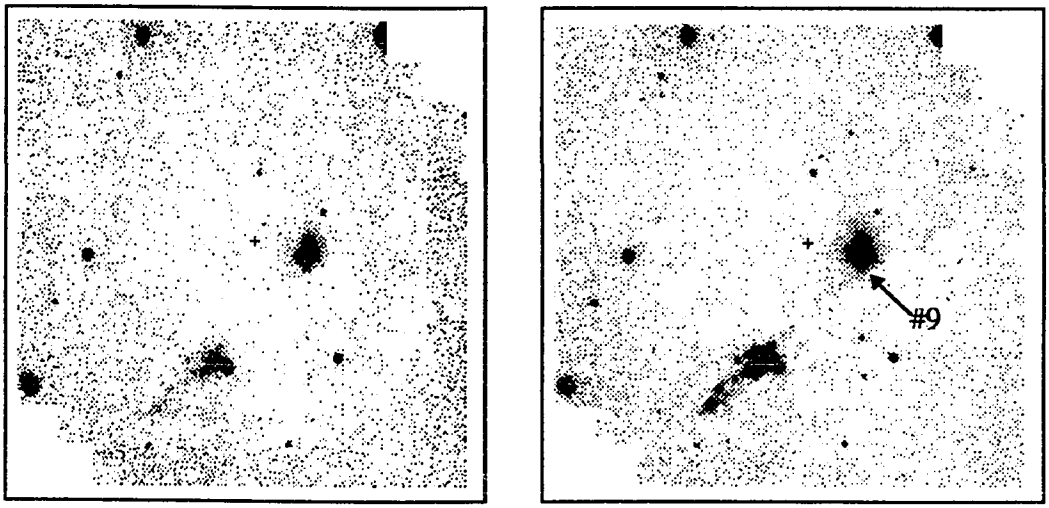

H K′

Sources 85, 87

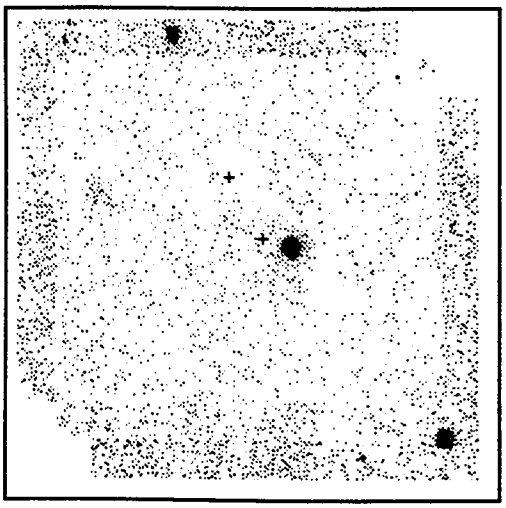

H

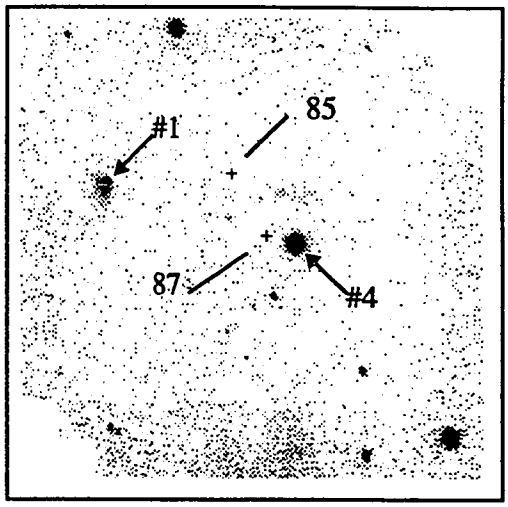

K′

Source 93

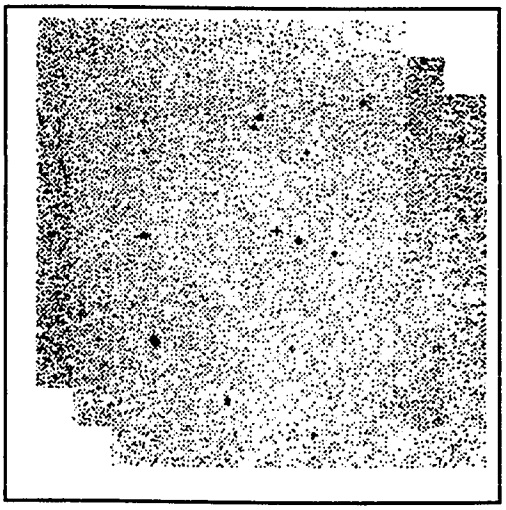

H

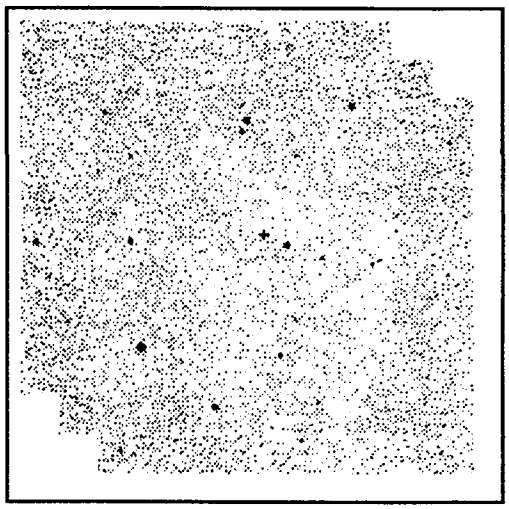

K′

Source 95

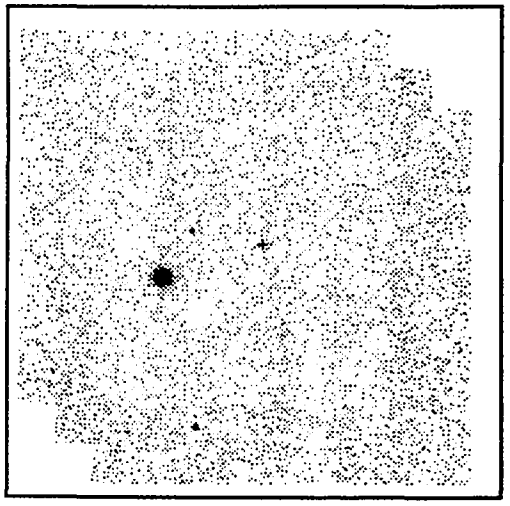

H

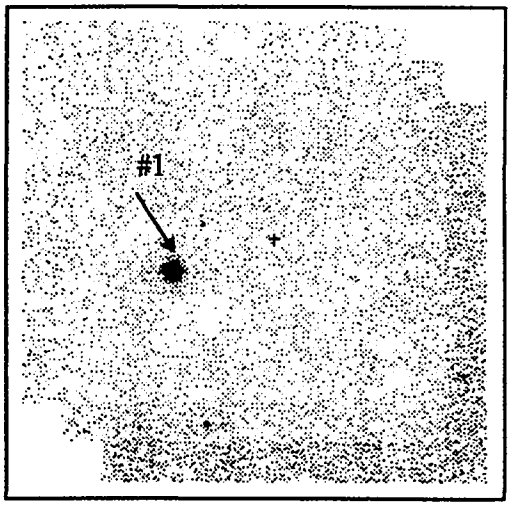

K′

Source 99

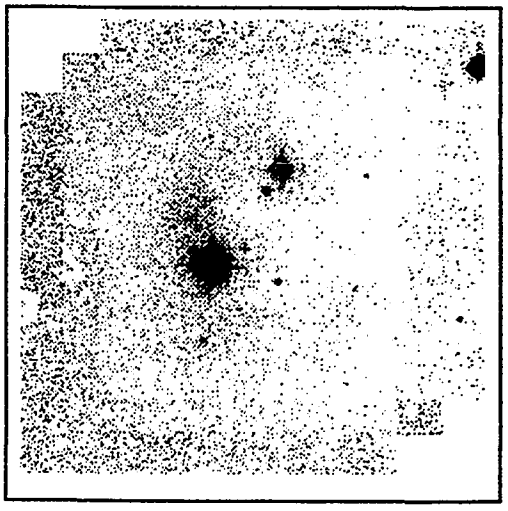

H

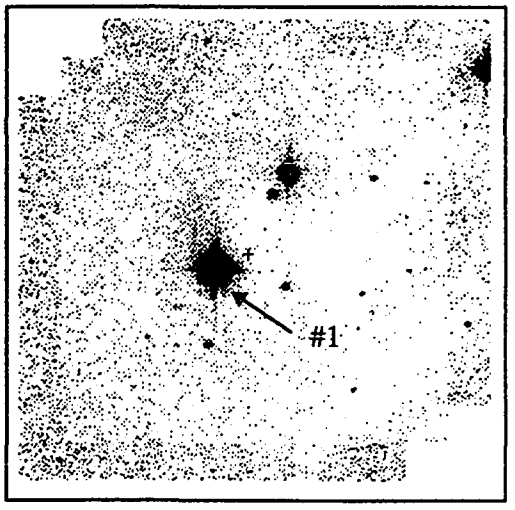

K′

Source 101

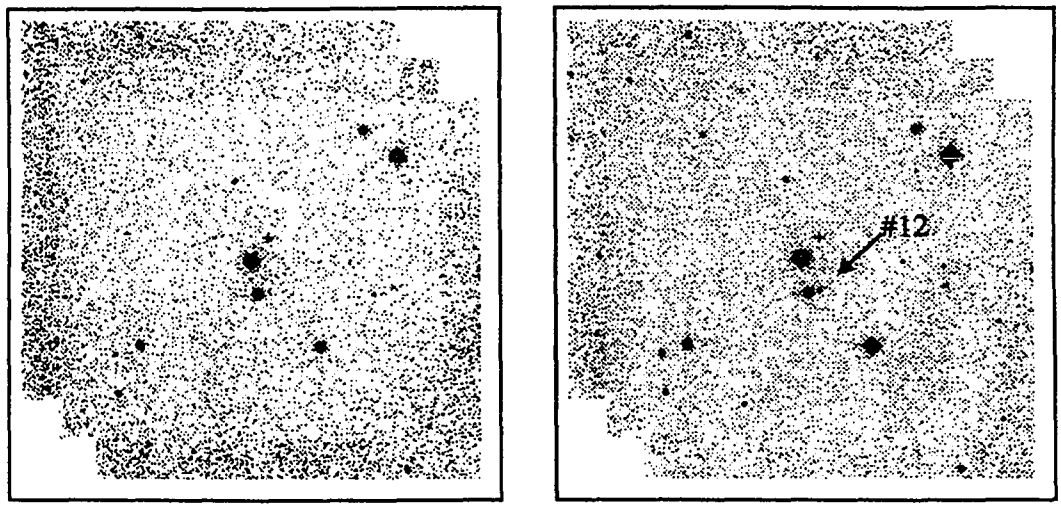

H K′

Source 104

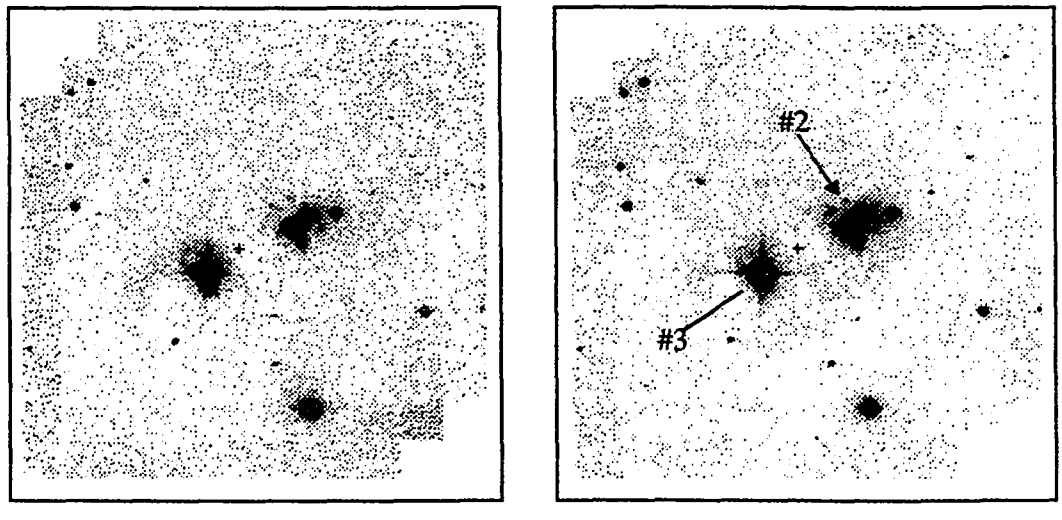

H K′

Source 105

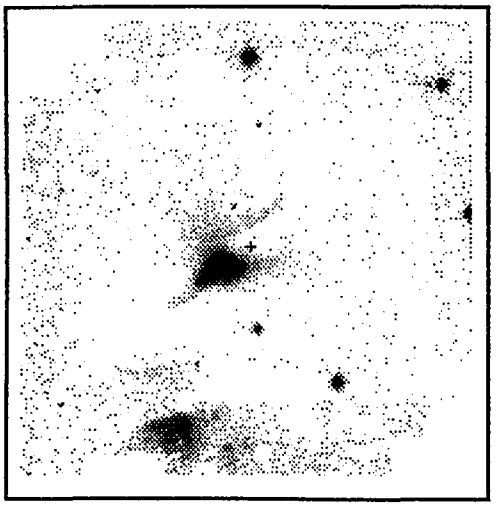

H

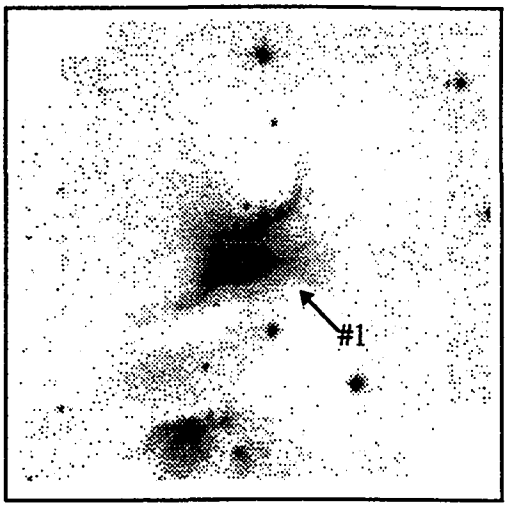

K′

Source 106

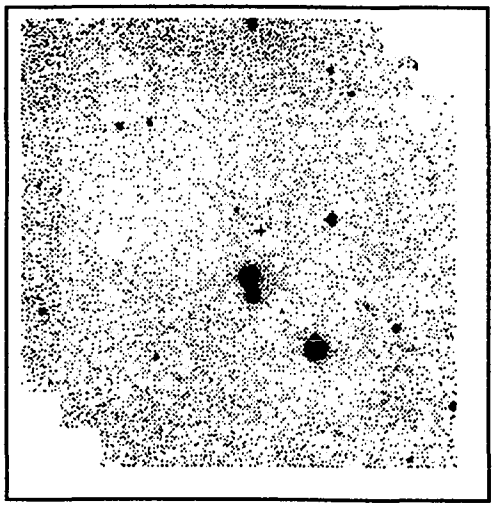

H

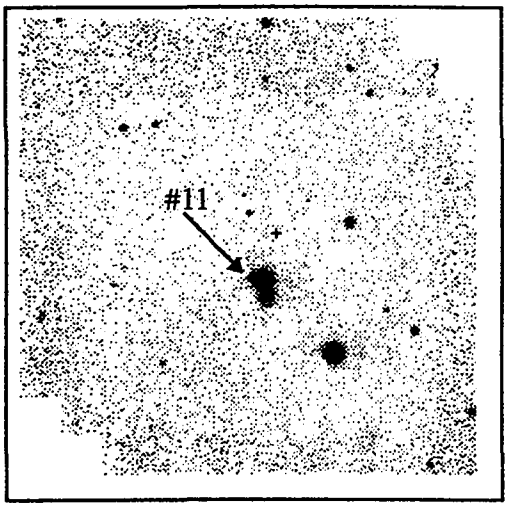

K′

Source 108

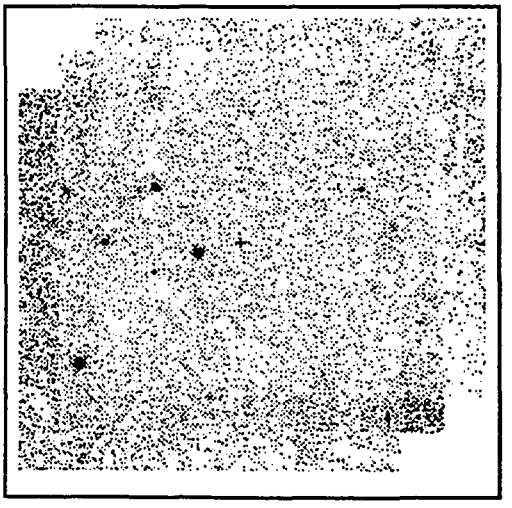

H

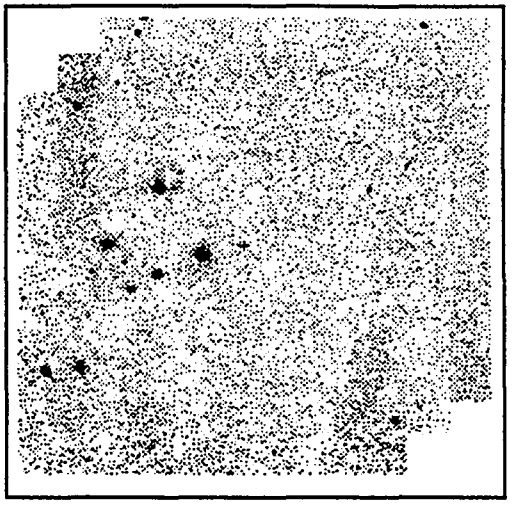

K′

Source 119

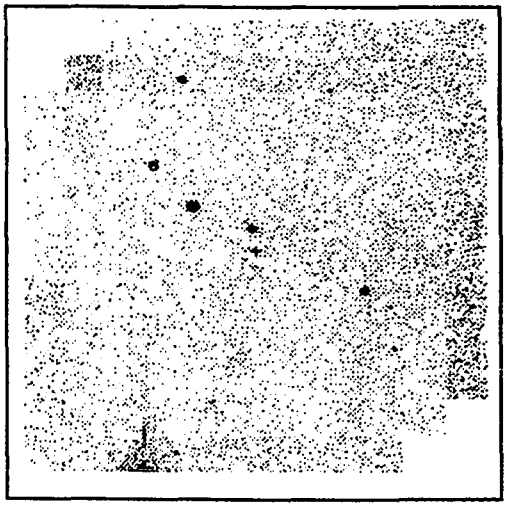

H

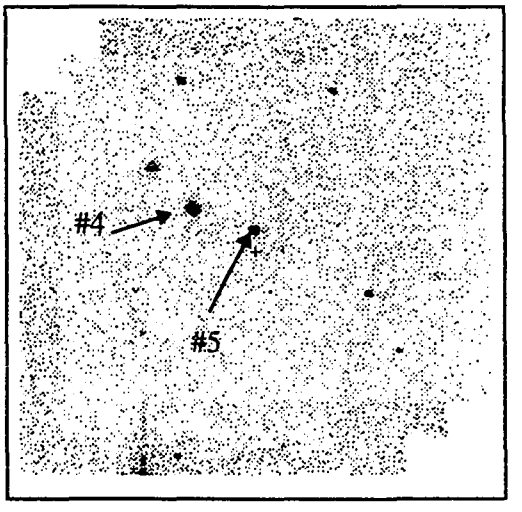

K′

Source 133

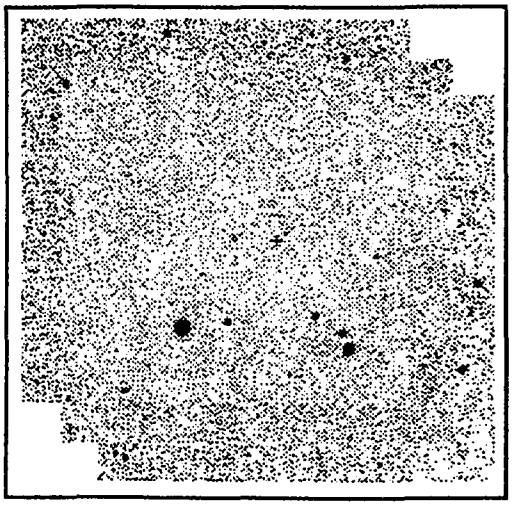

H

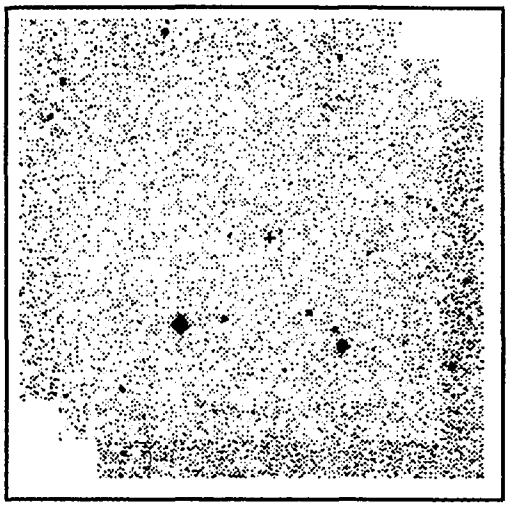

K′

Source 134

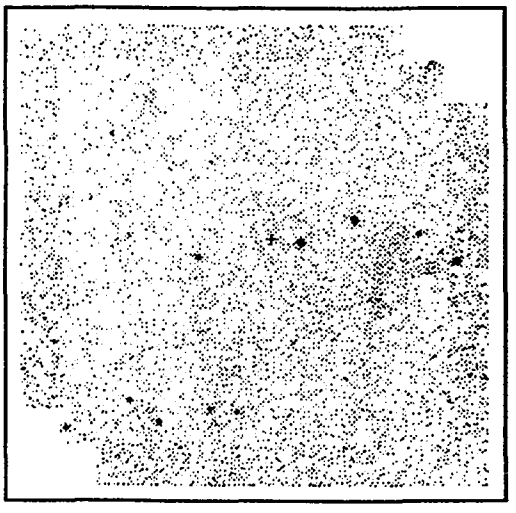

H

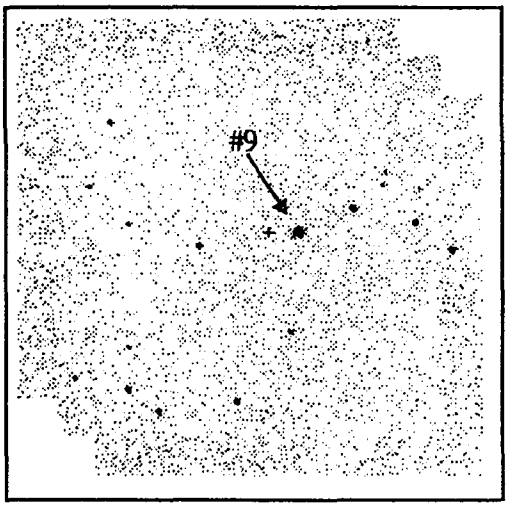

K′

Source 146

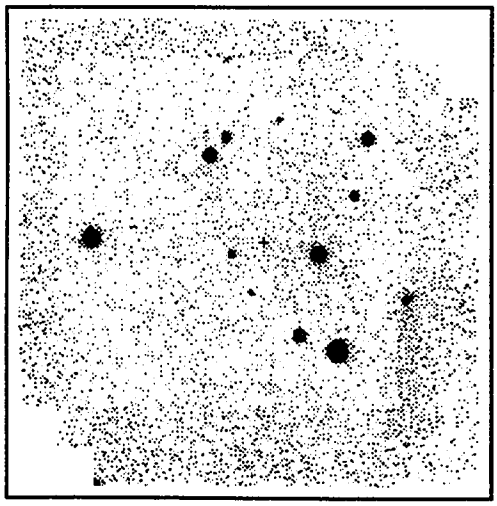

H

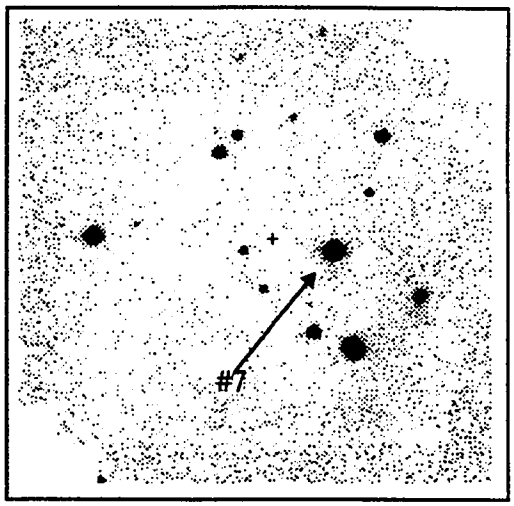

K′

Source 150

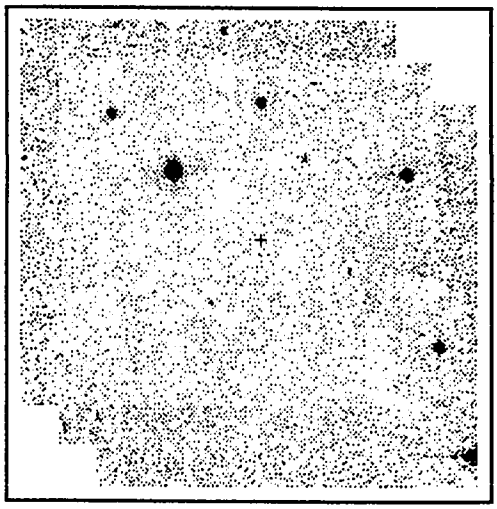

H

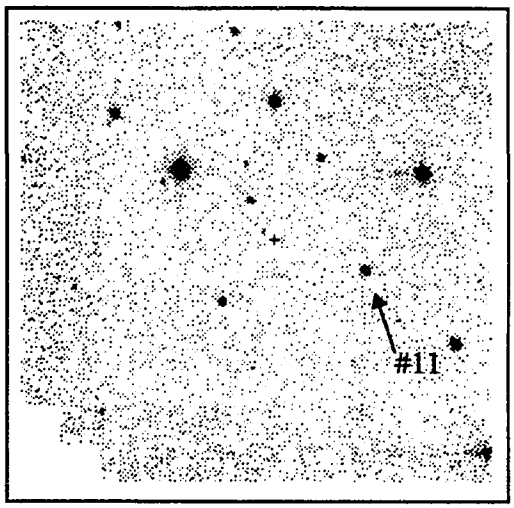

K′

Source 160

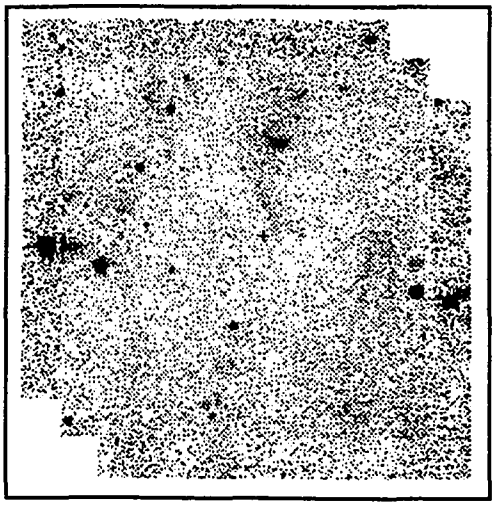

H

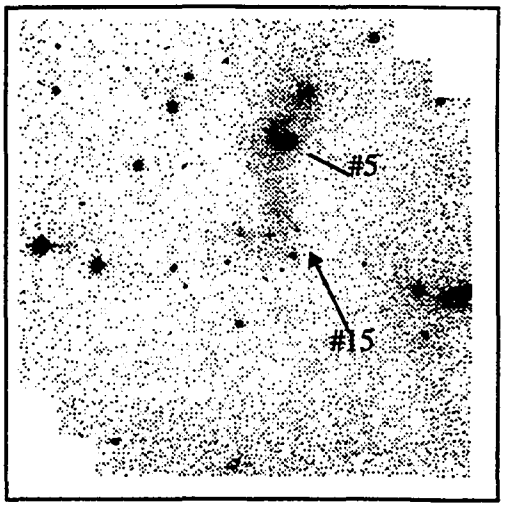

K′

Source 163

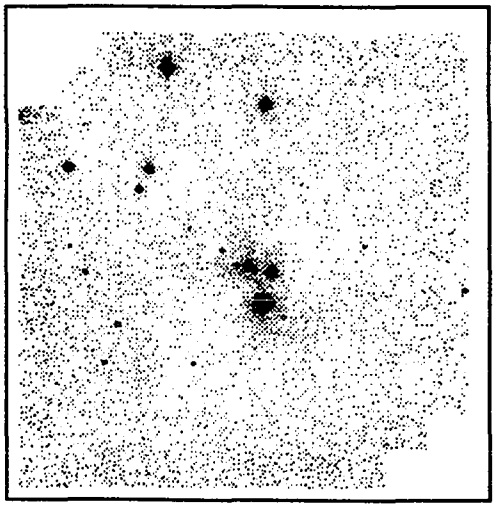

H

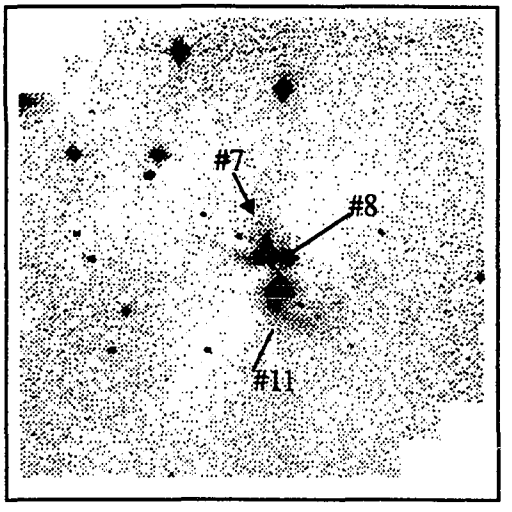

K′

Source 168

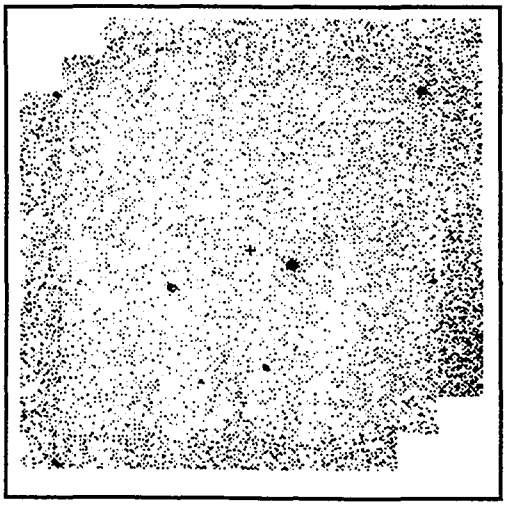

H

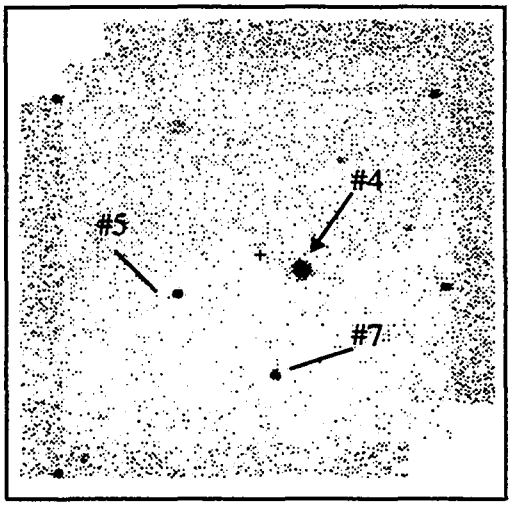

K′

Source 171

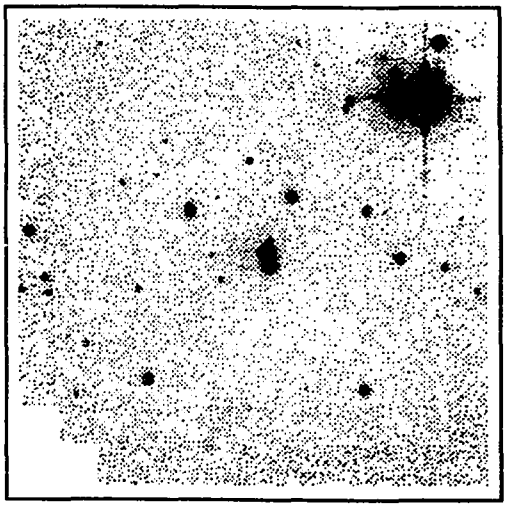

H

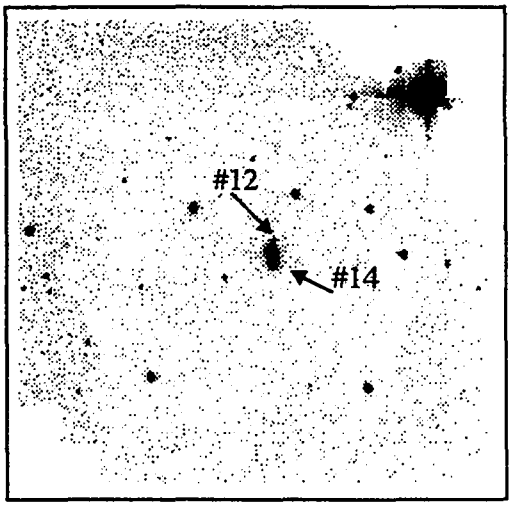

K′

Source 177

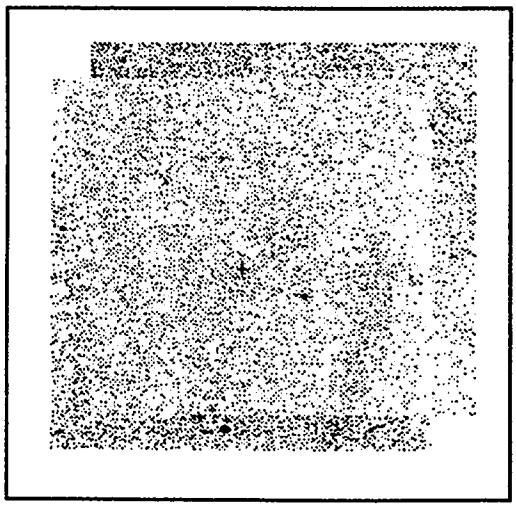

H

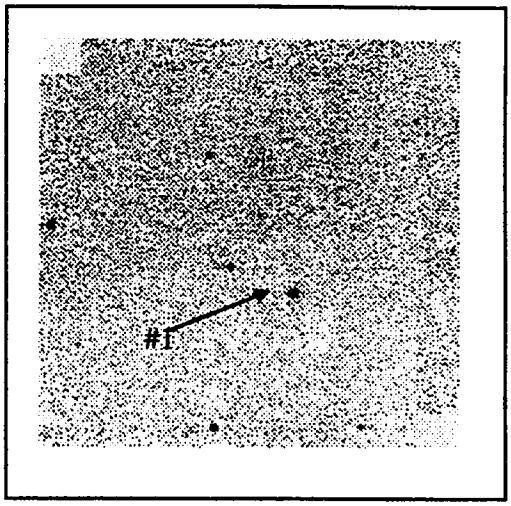

K′

Source 181

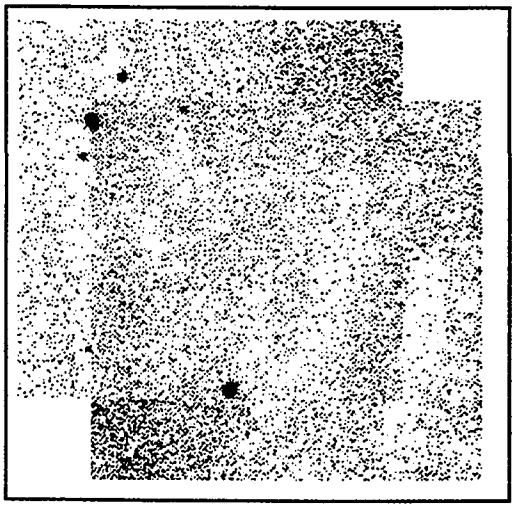

H

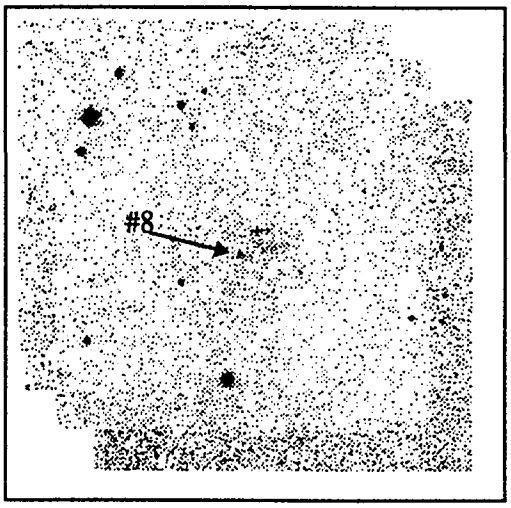

K′

Source 186

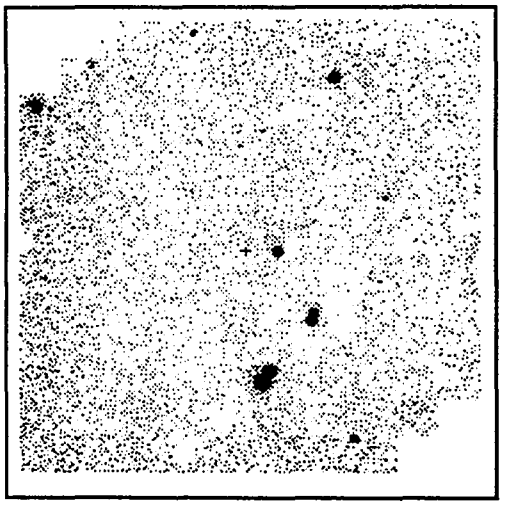

H

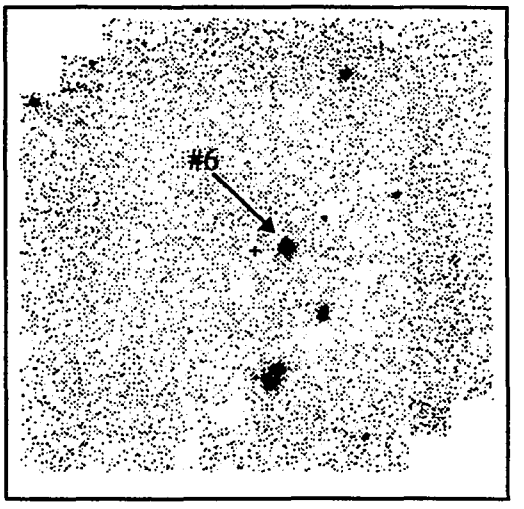

K′

Source 187

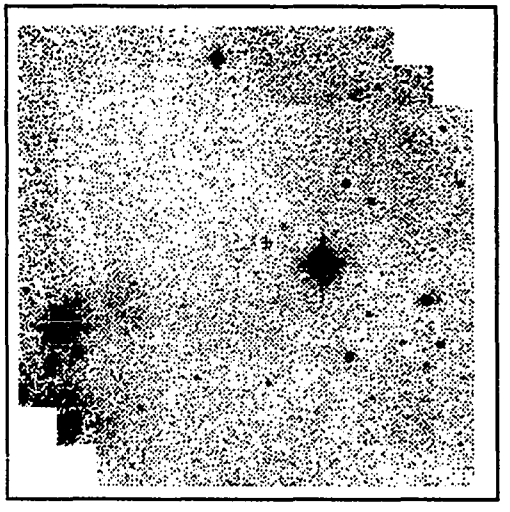

H

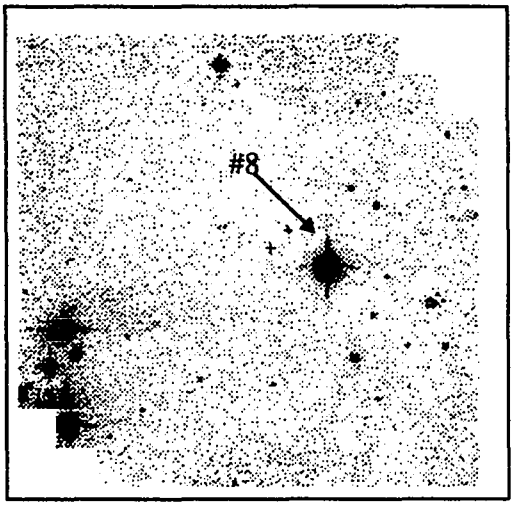

K′

Source 191

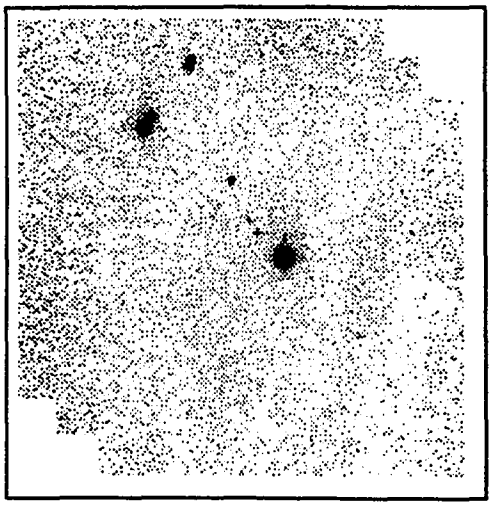

H

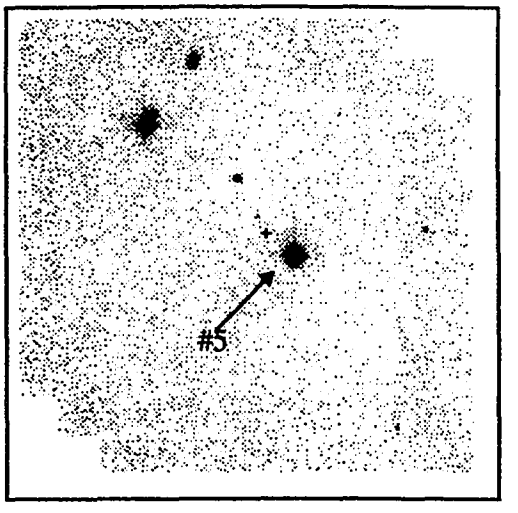

K′

Source 198

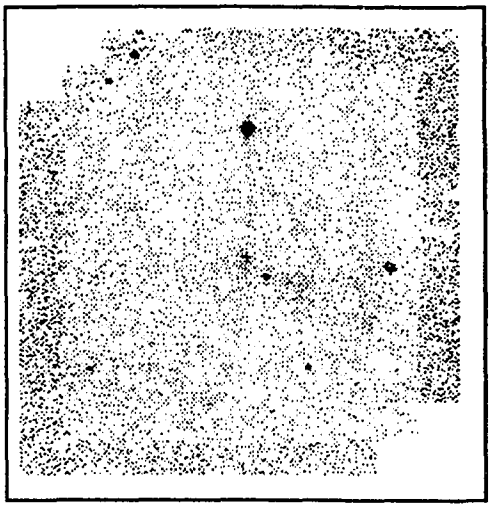

H

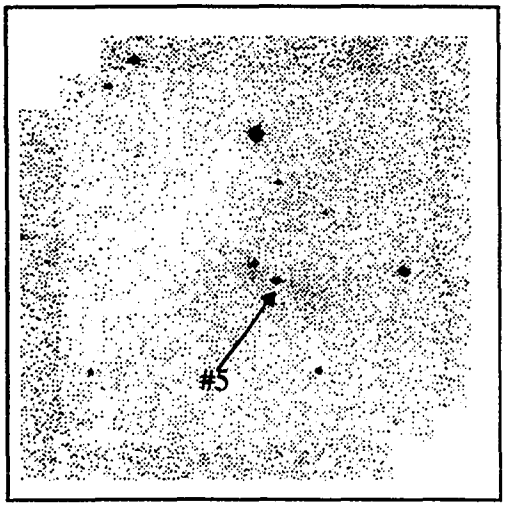

K′

Sources 193, 194

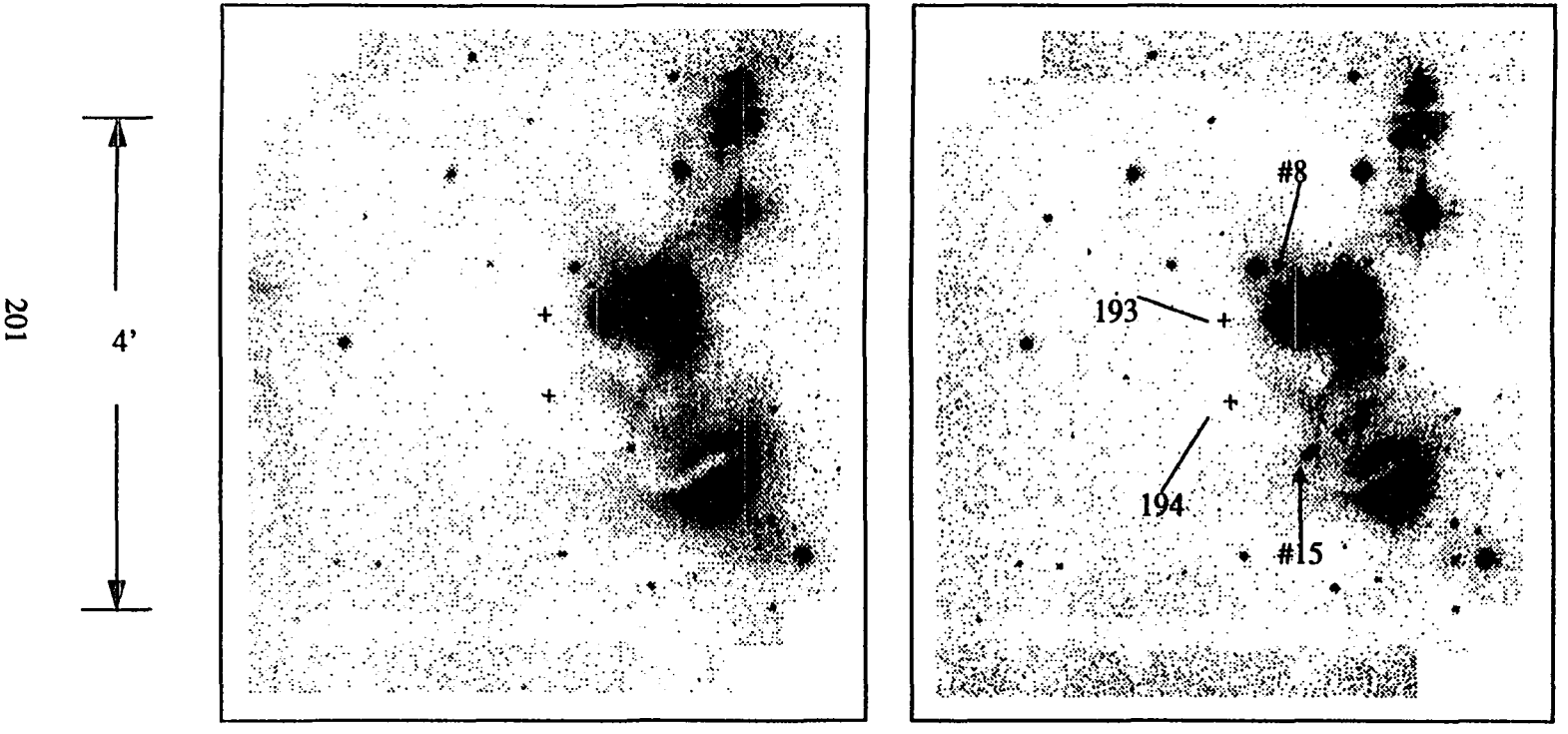

Source 211

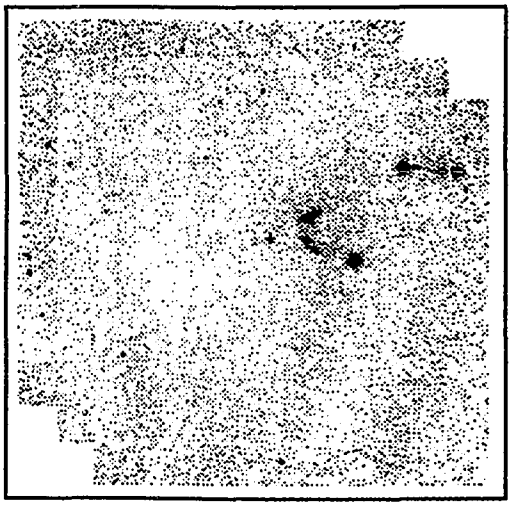

H

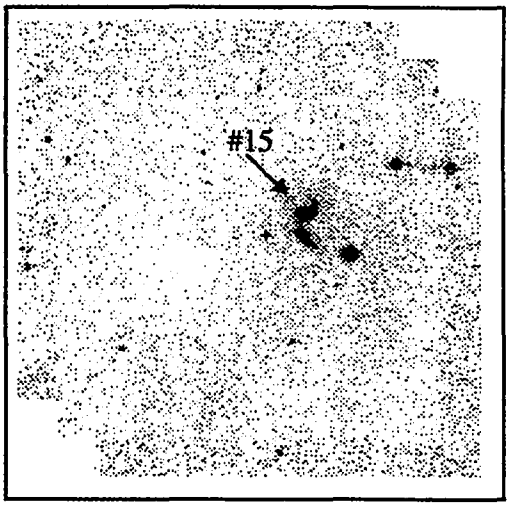

K′

Source 216

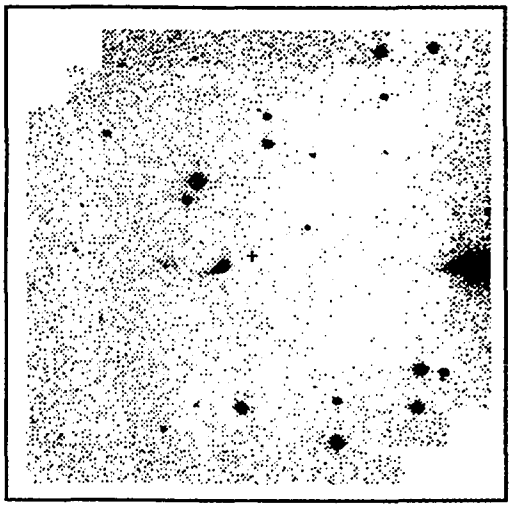

H

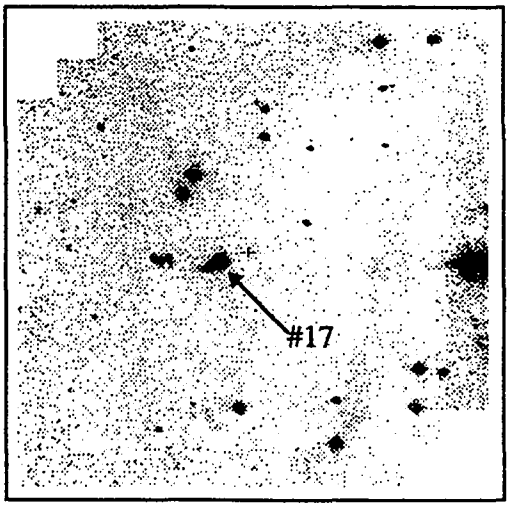

K′

Source 224

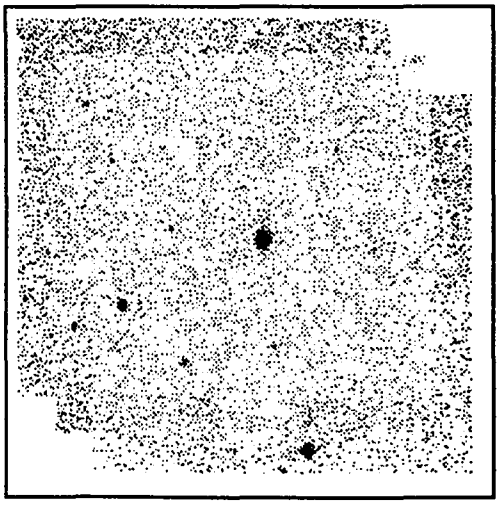

H

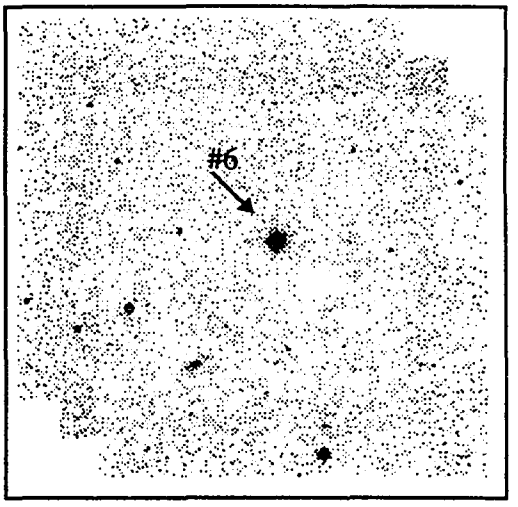

K′

Source 237

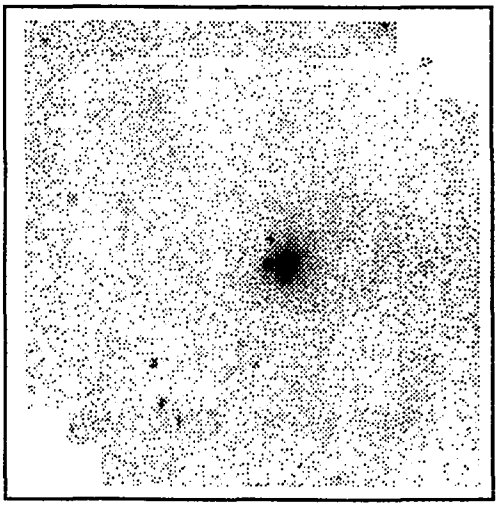

H

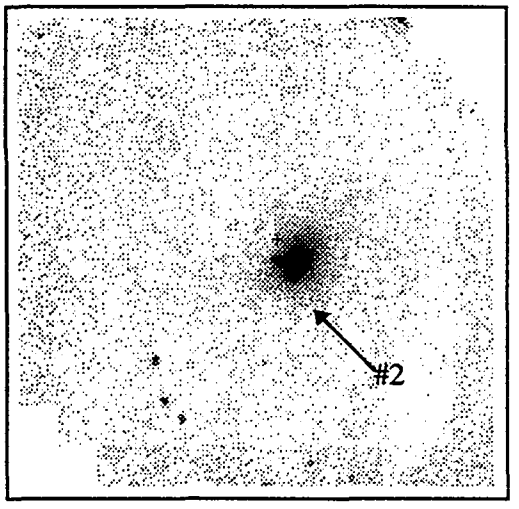

K′

Sources 243, 245

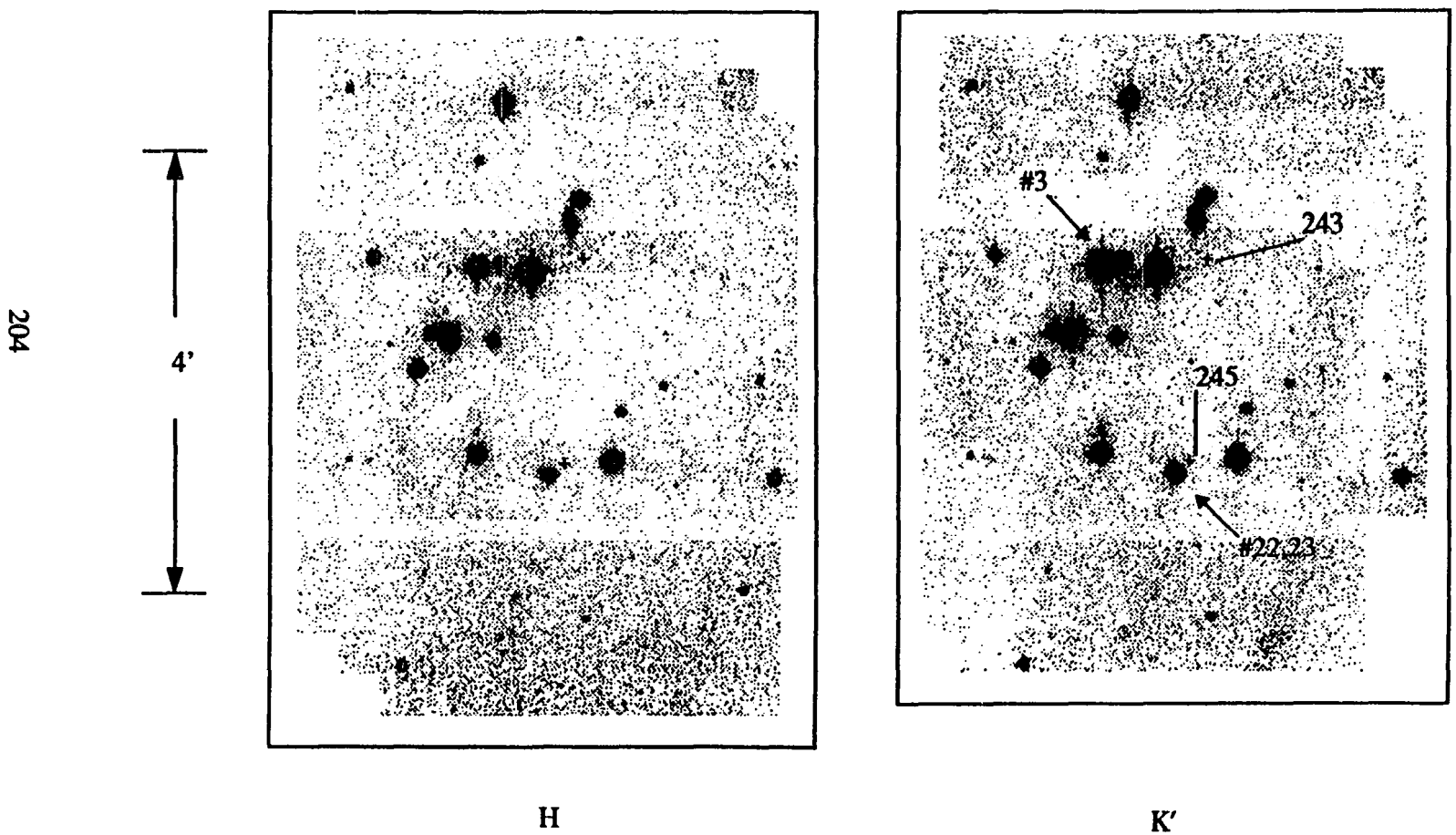

Source 246

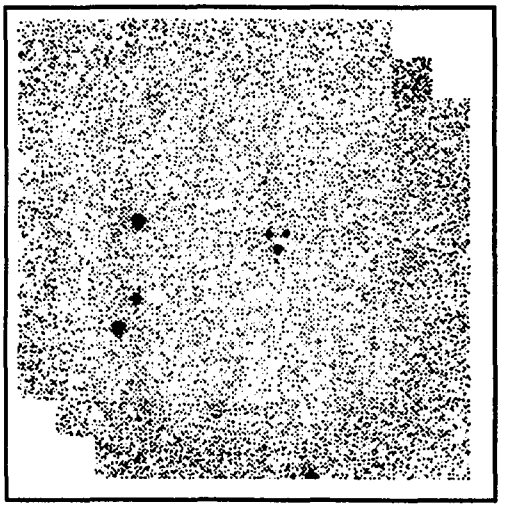

H

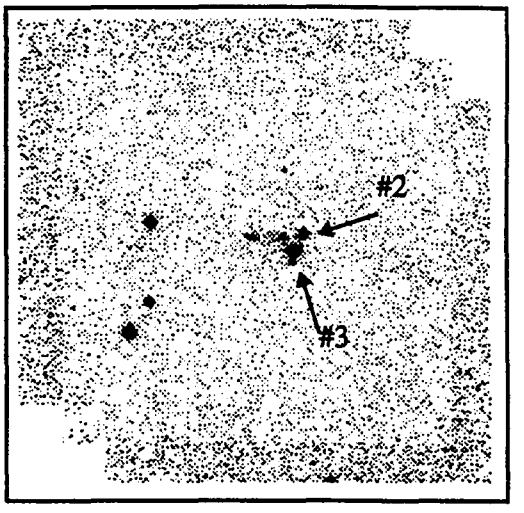

K′

Source 256

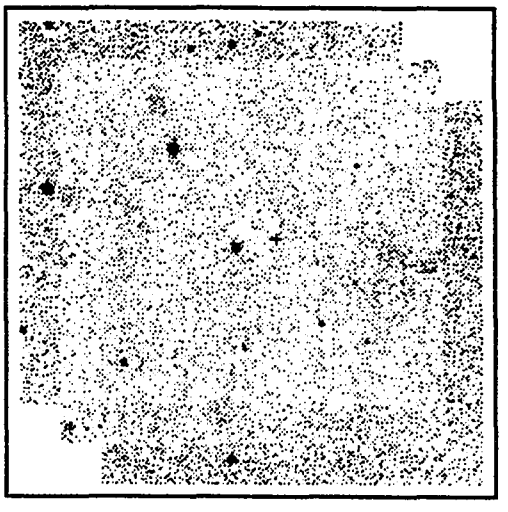

H

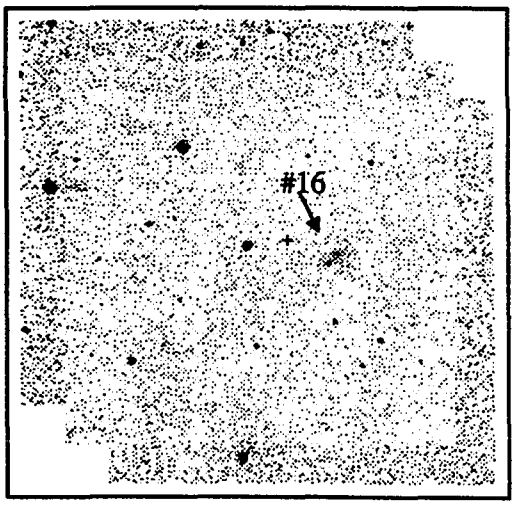

K′

Source 270

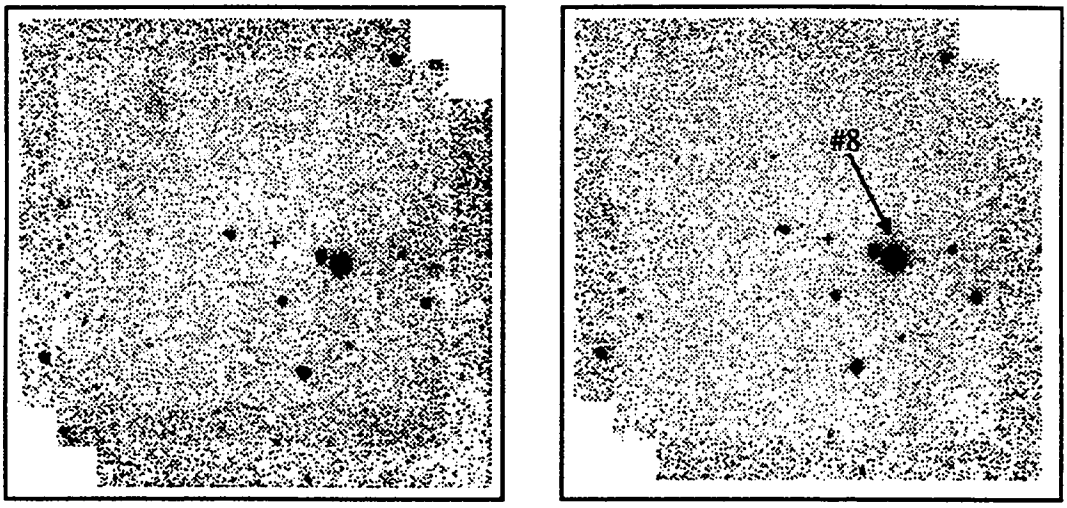

H K′

Source 280

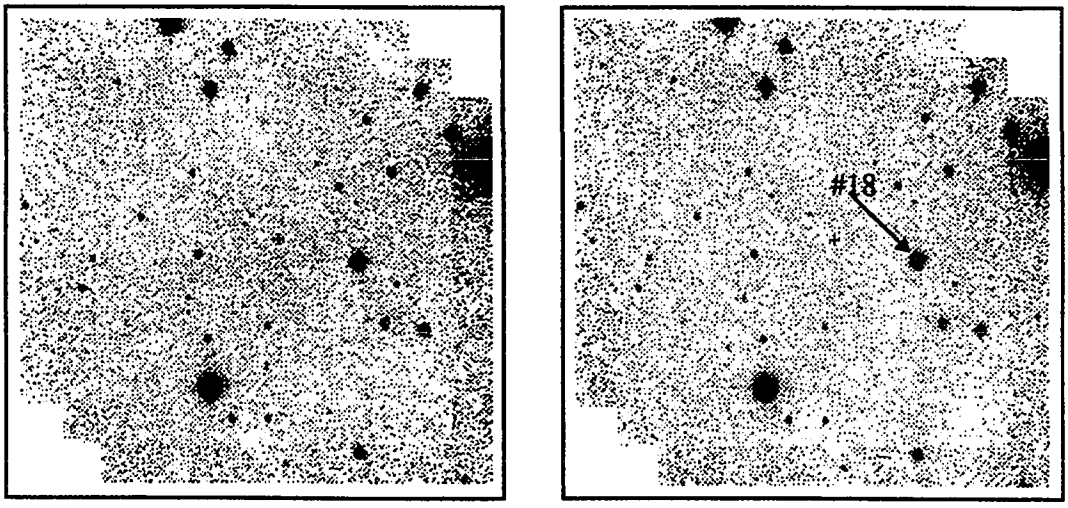

H K′

Figure A2 The spectral energy distributions of 55 *IRAS* sources that we have found the most probable near-IR counterparts. The downward arrows indicate the 5 σ upper limits at respective wavelengths.

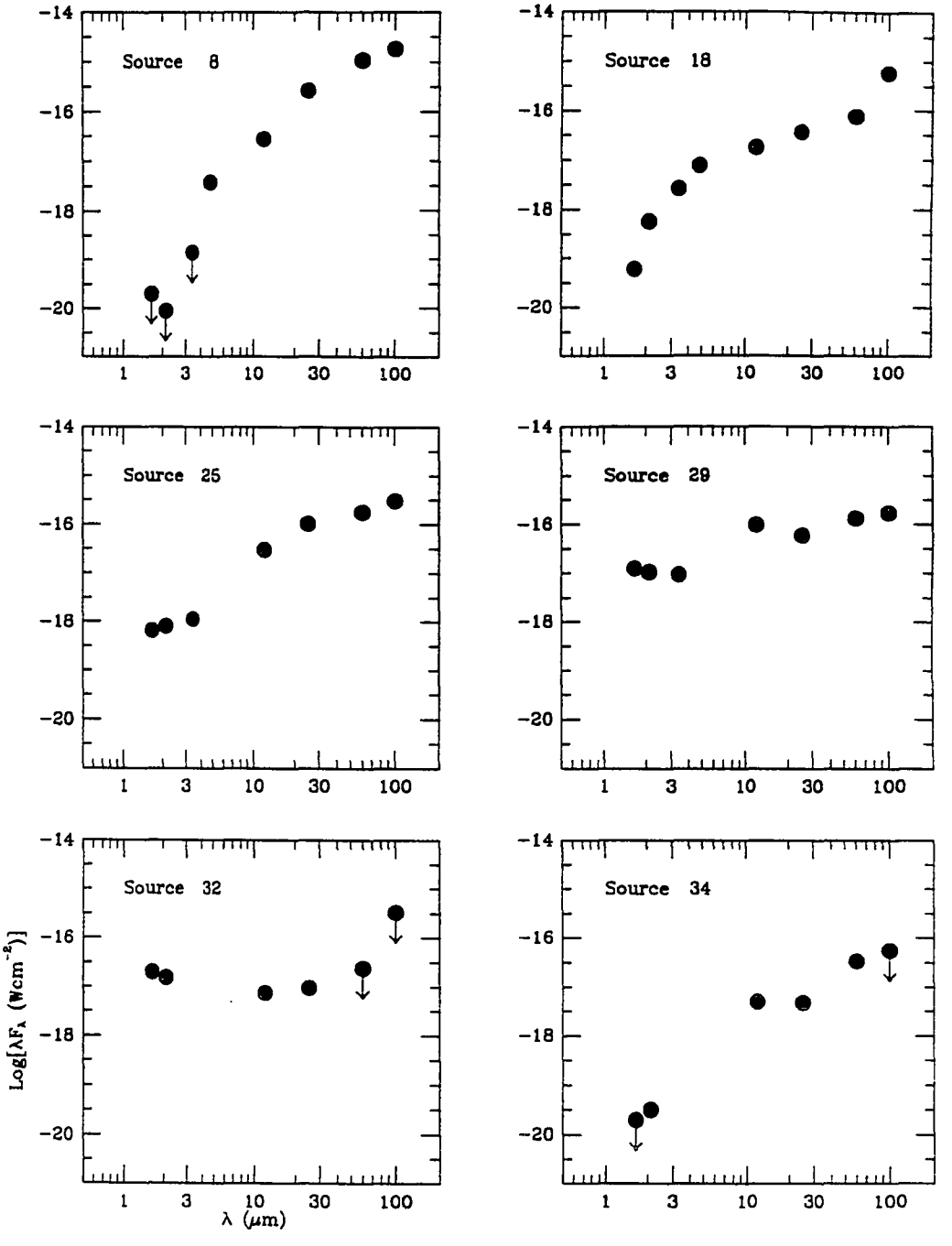
Source 8
Source 18
Source 25
Source 29
Source 32
Source 34
-14
-16
-18
-20
1
3
10
30
100
Log[λF_λ (Wcm^-2)]
λ (μm)

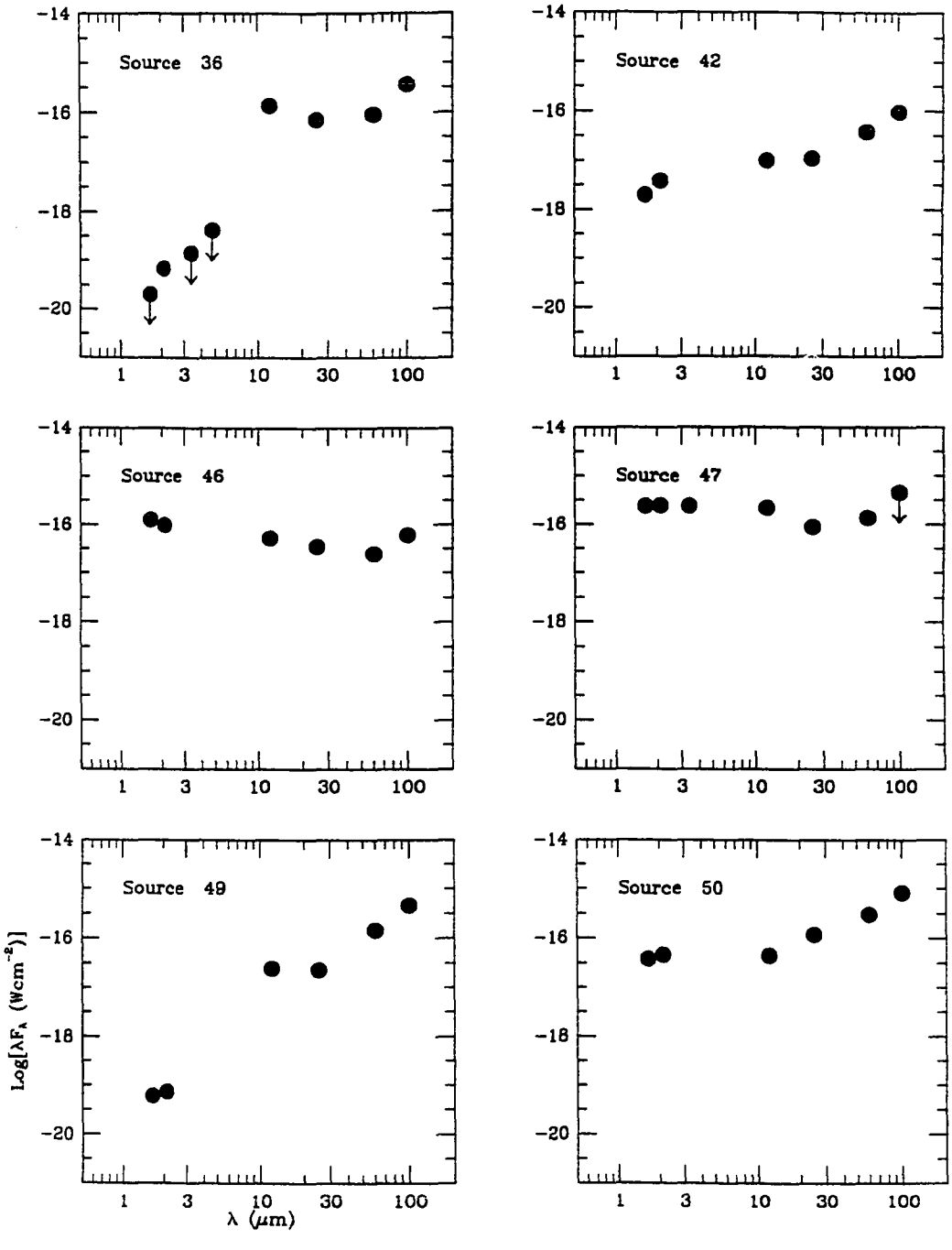
Source 36
Source 42
Source 46
Source 47
Source 49
Source 50
-14
-16
-18
-20
1
3
10
30
100
Log[λF_λ (Wcm^-2)]
λ (μm)

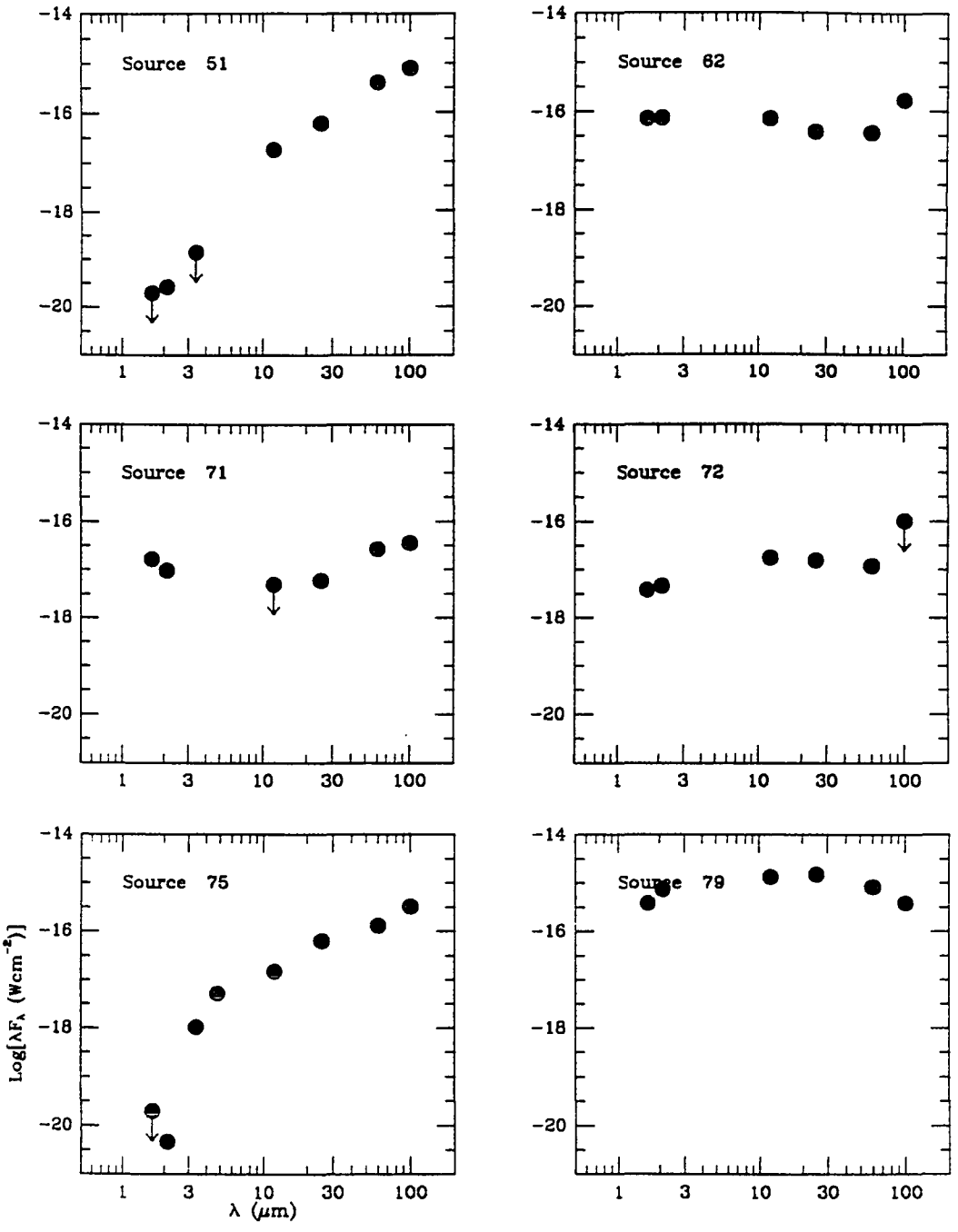
Source 51
Source 62
Source 71
Source 72
Source 75
Source 79
-14
-16
-18
-20
1
3
10
30
100
λ (μm)
Log[λF_λ (Wcm^-2)]

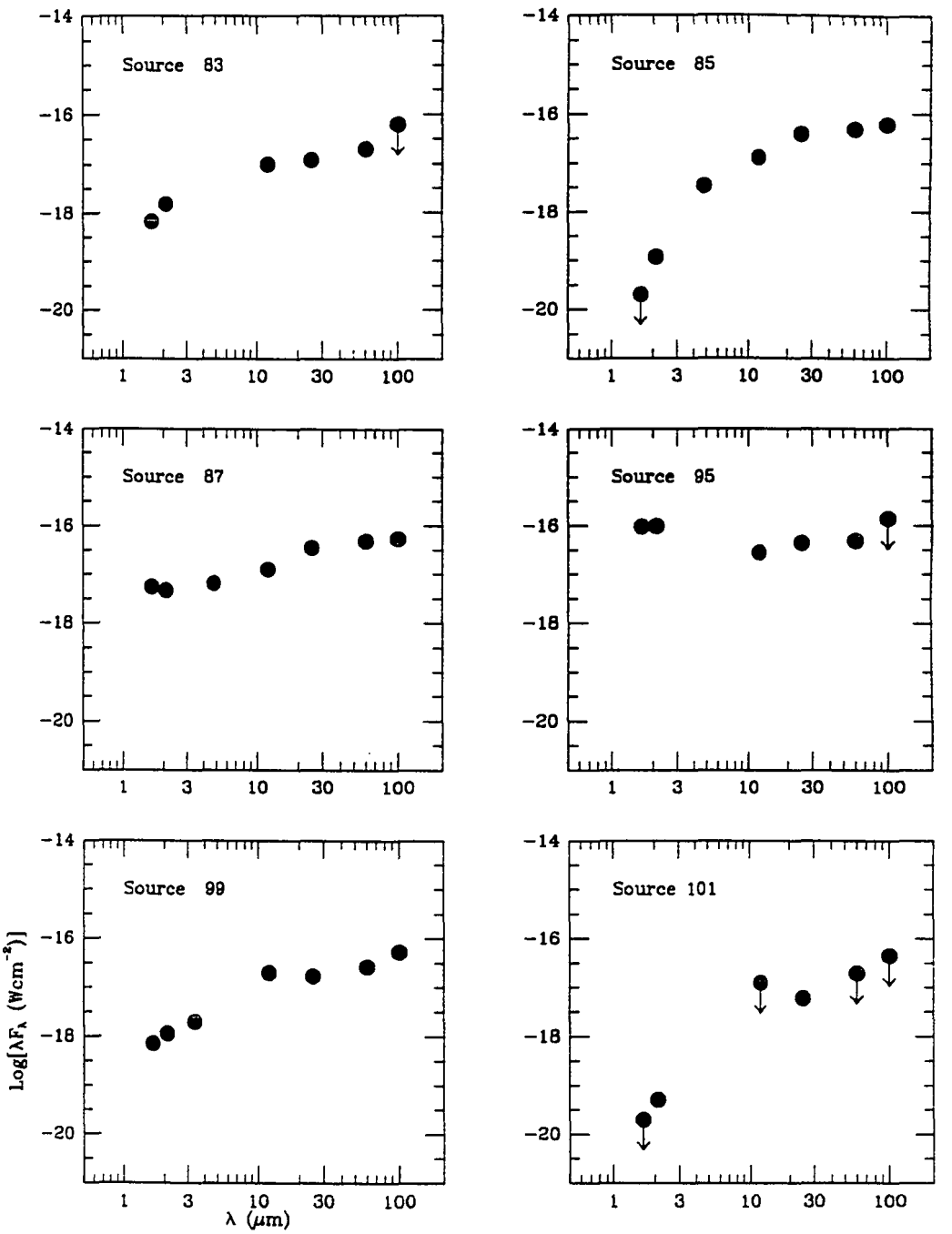
Source 83
Source 85
Source 87
Source 95
Source 99
Source 101
-14
-16
-18
-20
1
3
10
30
100
λ (μm)
Log[λF_λ (Wcm^-2)]

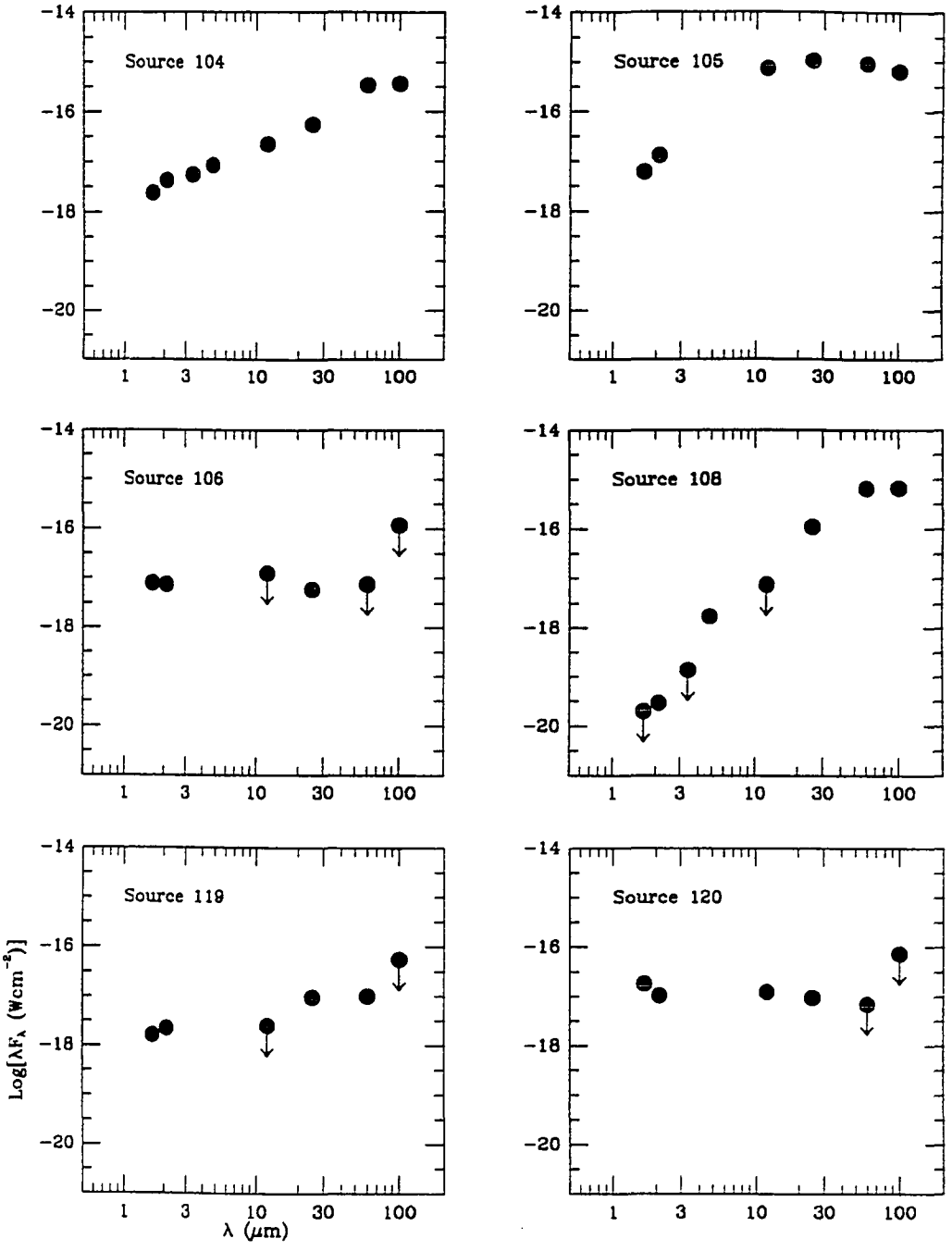
Source 104
Source 105
Source 106
Source 108
Source 119
Source 120
Log[λF_λ (Wcm^-2)]
λ (μm)
-14
-16
-18
-20
1
3
10
30
100

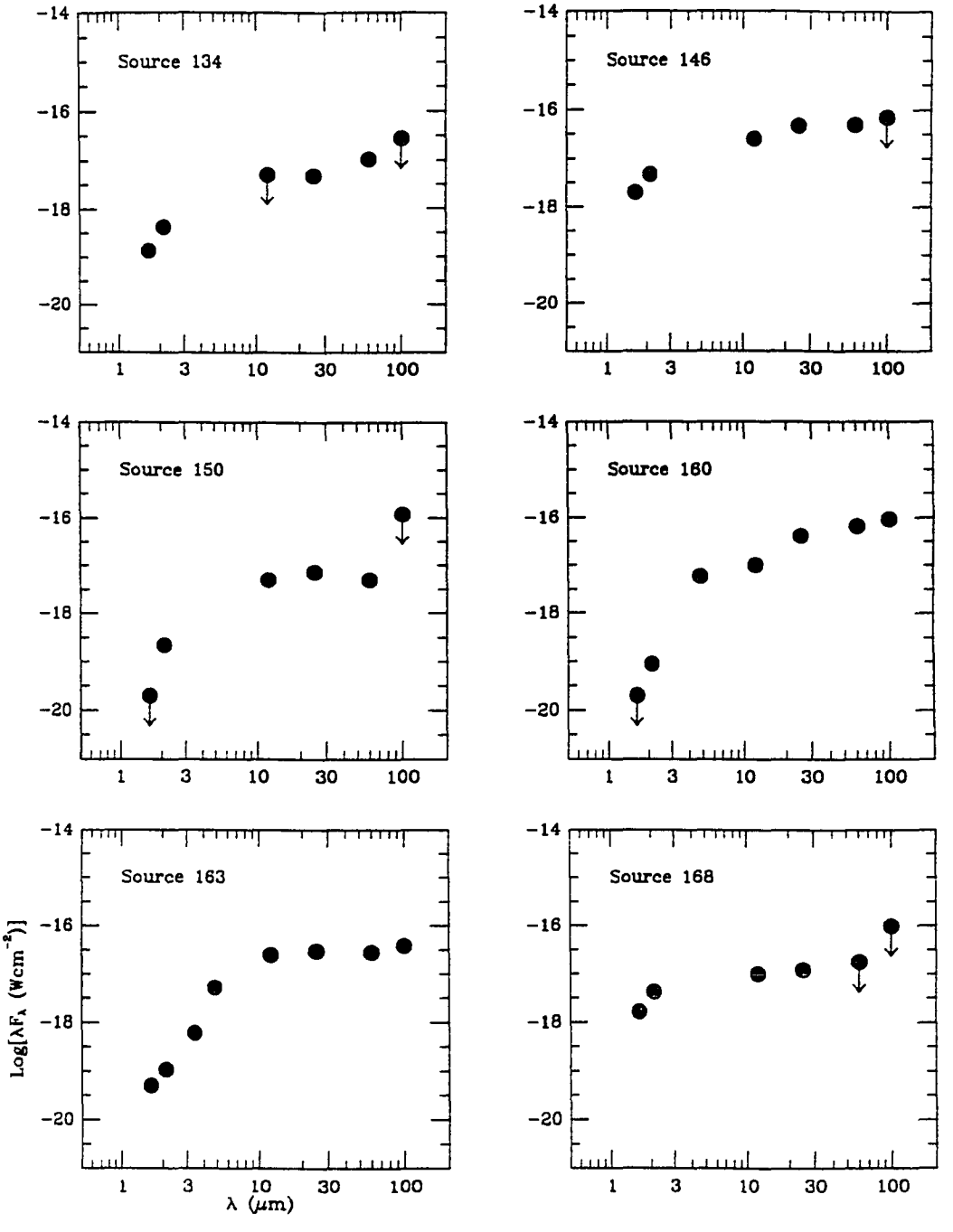
Source 134
Source 146
Source 150
Source 160
Source 163
Source 168
Log[λF_λ (Wcm^-2)]
λ (μm)
-14
-16
-18
-20
1
3
10
30
100

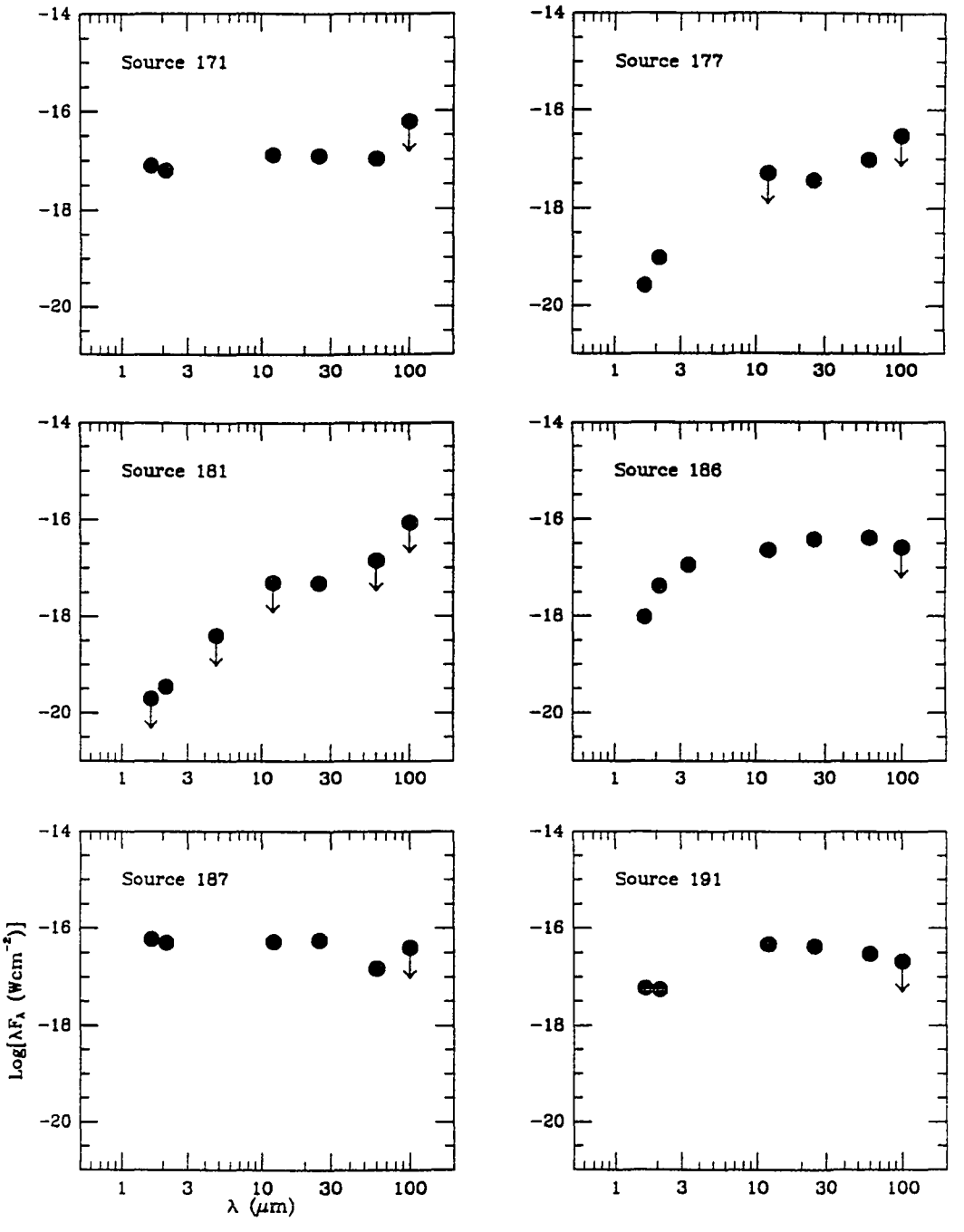
Source 171
Source 177
Source 181
Source 186
Source 187
Source 191
-14
-16
-18
-20
1
3
10
30
100
λ (μm)
Log[λF_λ (Wcm^-2)]

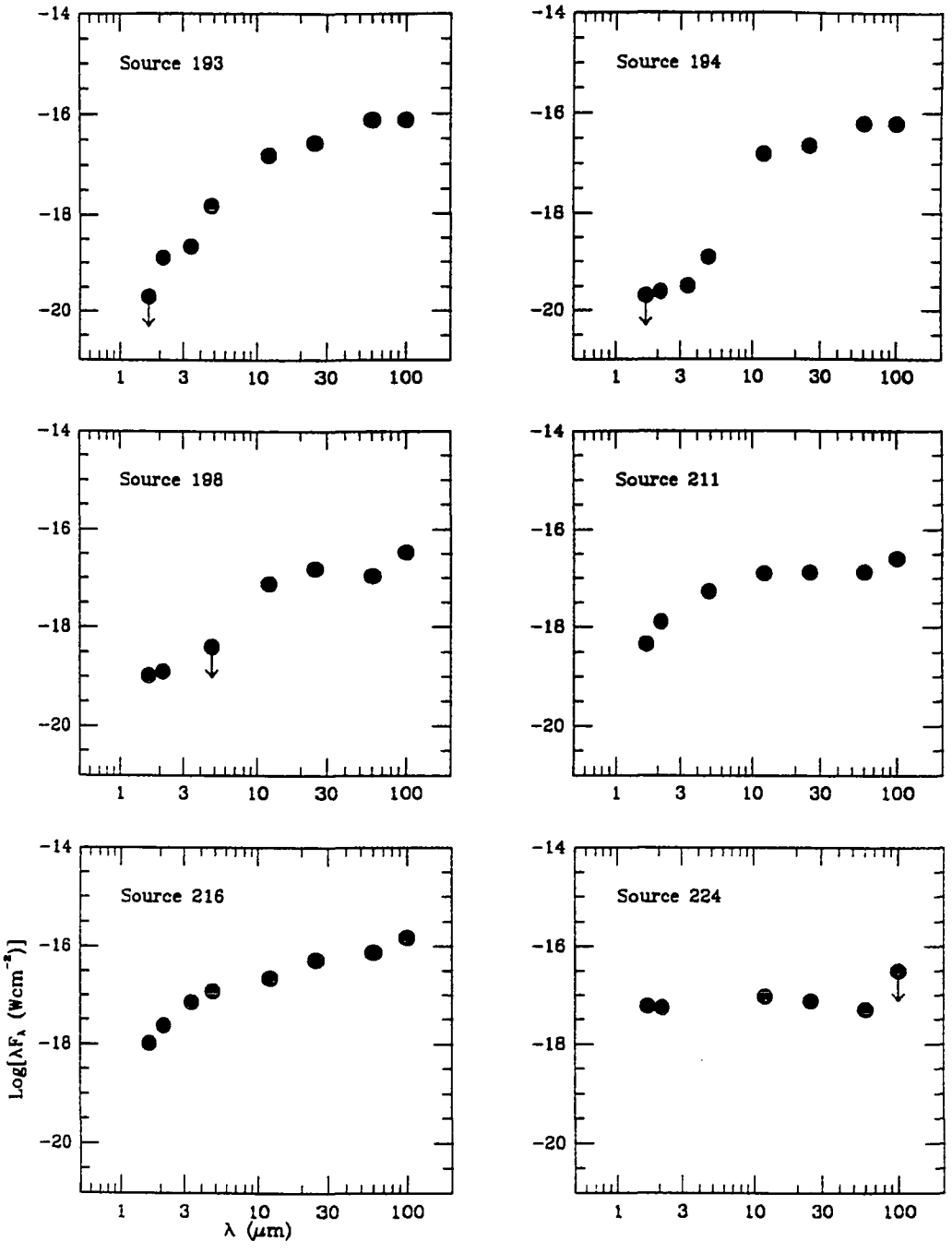
Source 193
Source 194
Source 198
Source 211
Source 216
Source 224
-14
-16
-18
-20
1
3
10
30
100
λ (μm)
Log[λF_λ (Wcm^-2)]

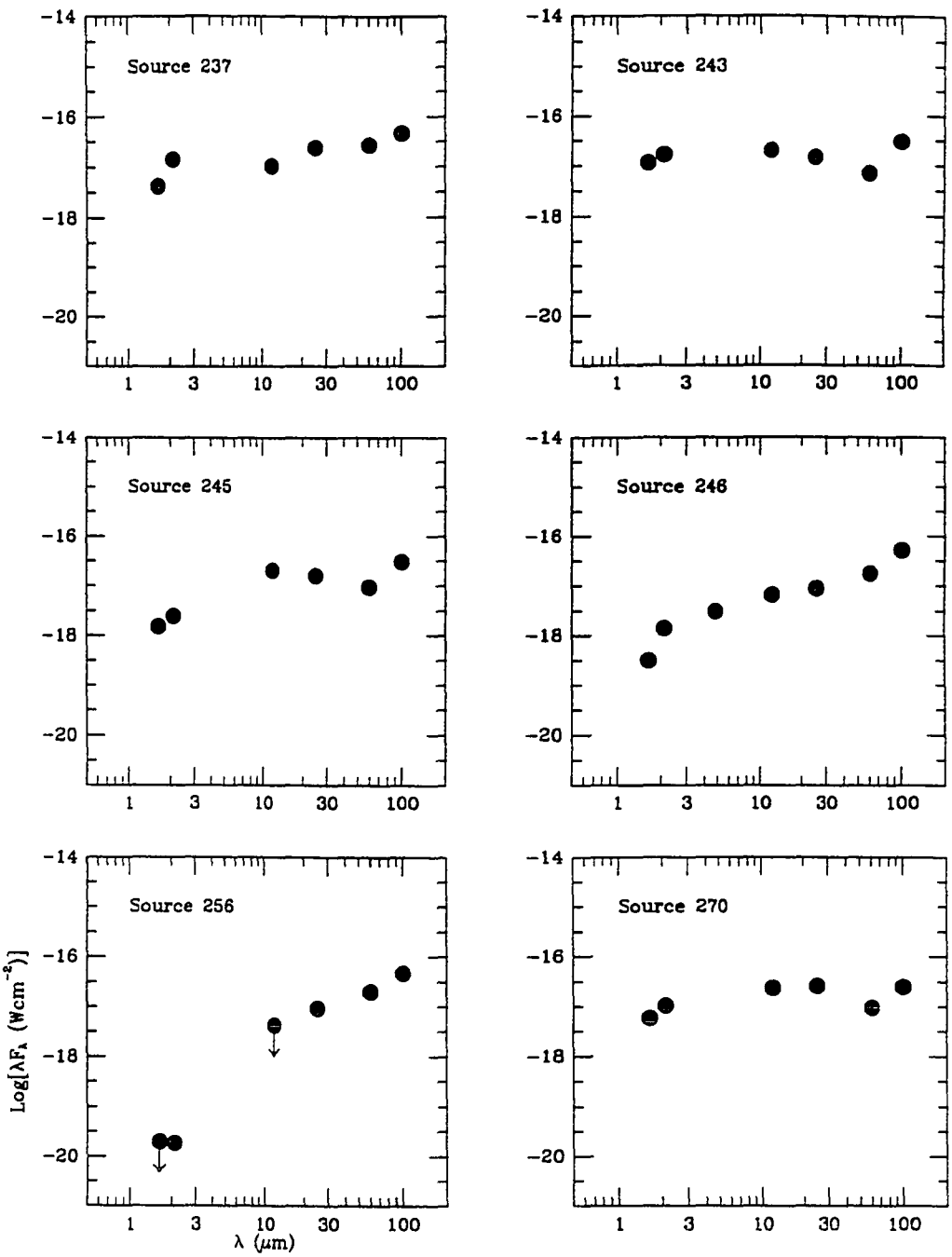
Source 237
Source 243
Source 245
Source 246
Source 256
Source 270
-14
-16
-18
-20
1
3
10
30
100
λ (μm)
Log[λF_λ (Wcm^-2)]

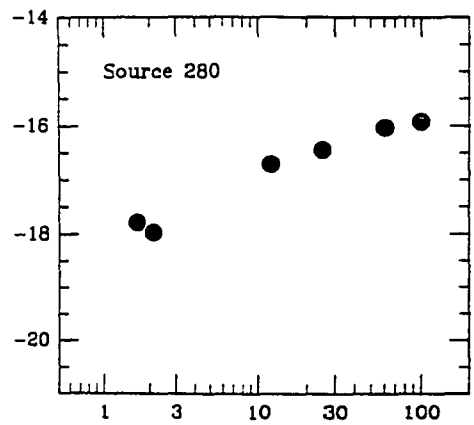
Source 280
-14
-16
-18
-20
1
3
10
30
100

REFERENCES

Adams, F. C. 1990, ApJ, 363, 578

Adams, F. C., Lada, C. J., & Shu, F. H. 1987, ApJ, 312, 788

Allen, C. W. 1973, in Astrophysical Quantities (London: Athlone)

Bally, J., & Lada, C. J. 1983, ApJ, 265, 578

Bally, J., Langer, W. D., Stark, A. A., & Wilson, R. W. 1987, ApJ, 173, 324

Beichman, C. A. 1985 in Light on Dark Matter ed. F.P. Israel, (Reidel: Holland), 279

Beichman, C. A. 1987, ARA&A, 25, 523

Beichman, C. A., Neugebauer, G., Habing, H. J., Clegg, P. E. & Chester, T. J. 1988, *Infrared Astronomical Satellite Catalogs and Atlases*. Vol. 1. *Explanatory Supplement* (Washington: GPO)

Beichman, C. A., Myers, P. C., Emerson, J. P., Harris, S., Mathieu, R., Benson, P. J., & Jennings, R. E. 1986, ApJ, 307, 337

Benson, P. J., & Myers, P. C. 1989, ApJS, 71, 89

Bertout, C. 1989, ARA&A, 27, 351

Bessell, *M.* S. 1989, in Infrared Extinction and Standardization, ed E. F. Milone (Berlin: Springer), 61

Blaauw, A. 1991, in The Physics of Star Formation and Early Stellar Evolution, ed. C. J. Lada, & N. D. Kylafis (Dordrecht: Kluwer), 125

Blitz, L., 1991, in The Physics of Star Formation and Early Stellar Evolution, ed. C. J. Lada, & N. D. Kylafis (Dordrecht: Kluwer), 3

Boulanger, F., Beichman, C. A., Desert, J. P., Helou, G., Perault, M., & Ryter, C. 1988, ApJ, 333, 328

Campbell, B., Persson, S. E., Strom, S. E., & Grasdalen, G. L. 1988, AJ, 95, 1173

Chackerian, C., & Tipping, R. H. 1983, J. Molec. Spectrosc. 99, 431

Chen, H., Fukui, Y., & Iwata, T. 1992, ApJ, submitted

Chen, H., Fukui, Y., & Yang, J. 1992, ApJ, 398, 544

Chen, H., Tokunaga, A. T., & Hodapp, K.-W. 1991, in Proc. Vulcano Workshop on Young Star Clusters and Early Stellar Evolution, ed. F. Palla, P. Persi & H. Zinnecker, 737

Chen, H., Tokunaga, A. T., Strom, K. M., & Hodapp, K.-W., 1992, ApJ, in press (April 30, 1993)

Cohen, M., & Kuhi, L. O. 1979, ApJS, 41, 743

Cowie, L. L., Songaila, A., & York, D. G. 1979, ApJ, 230, 469

Dickman, R. L. 1978, ApJS, 37, 407

Dickman, R. L., & Herbst, W. 1990, ApJ, 357, 531

Draine, B. T., & Lee, H. M. 1984, ApJ, 285, 494

Emerson, J. P. Harris, S., Jennings, R. E., Beichman, C. A. Baud, B., Beintema, D. A., Marsden, P. L. & Wesselius, P. R. 1984, ApJ, 278, L49

Emerson, J. P., 1988, in Formation and Evolution of Low Mass Stars, ed. Dupree, A. K., & Lago, M. T. V. T. (Dordrecht: Kluwer) 193

Evans II, N. J., Leverault, R. M., & Harvey, P. M. 1986, ApJ, 301, 894

Fukui, Y. 1989, in Proc. ESO Workshop on Low-Mass Star Formation and Pre-Main Sequence Objects, ed. B. Reipurth (Garching: ESO), 95

Fukui, Y., Iwata, T., Takaba, H, Mizuno, A., Ogawa, H., Kawabata, K., & Sugitani, K. 1989, Nature, 342, 161

Fukui, Y., & Mizuno, A. 1991, in IAU Symposium 147, Fragmentation of Molecular Clouds and Star Formation, ed E. Falgarone, F., Boulanger, & G. Duvert (Dordrecht: Kluwer), 275

Fukui, Y., Sugitani, K., Takaba, H., Iwata, T., Mizuno, A., Ogawa, H., & Kawabata, K. 1986, ApJ, 311, L85

Fuller, G. 1992, in Proceedings of a Graudate Workshop on Star Formation, ed J.-P. Arcoragi, P. Bastien, & R. Pudritz, in press

Genzel, R., & Stutzki, J. 1989, ARA&A, 27, 41

Goldreich, P., & Kwan, J. 1974, ApJ, 189, 441

Guide Star Catalog 1989, (Baltimore: Space Telescope Science Institute) CD-ROM

Haese, N. N., & Woods, R. C. 1979, Chem. Phys. Letters, 61, 396

Harju, J., Walmsley, C. M., & Wouterloot, J. G. A. 1992, A&A Suppl. in press

Hartigan, P., Hartmann, L., Kenyon, S., Hewett, R., & Stauffer, J. 1989, ApJS, 70, 899

Hartmann, L., Hewett, R., Stahler, S., & Mathieu, R. D. 1986, ApJ, 309, 275

Harvey, P. M., Marshall, J., & Lester, D. F. 1986, ApJ, 301, 346

Herbig, G. H. 1962, Adv. Astr. Ap. 1, 47

Herbig, G. H., and Bell, K. R. 1988, Lick Obs. Bull., No. 1111

Herbig, G. H., & Terndrup, D. M. 1986, ApJ, 307, 609

Heyer, M. H., Ladd, E. F., Myers, P. C., & Campbell, B. 1990, AJ, 99, 1585

Hoel, P. G. 1947, in Introduction to Mathematical Statistics (New York: John Wiley & Sons), 191

Hodapp, K.-W. 1992, private communication

Hodapp, K.-W., Rayner, J., & Irwin, E. 1992, PASP, 104, 441

Hodapp, K.-W. & Deane, J. 1992, in preparation

Jones, B. F., & Herbig, G. H. 1979, AJ, 84, 1872

Keynon, S. J., Hartmann, L. W., Strom, K. M., & Strom S. E. 1990, AJ, 99, 869

Koornneef, J. 1983, A&A, 128, 84

Kutner, M. L., Tucker, K. D., Chin, G., & Thaddeus, P. 1979, ApJ, 215, 521

Kutner, M. L., & Ulich, B. L. 1981, ApJ, 250, 341

Lada, C. J. 1985, ARA&A, 23, 267

Lada, C. J. 1991, in The Physics of Star Formation and Early Stellar Evolution, ed. C. J. Lada & N. D. Kylafis (Dordrecht: Kluwer) 329

Lada, C. J. & Wilking, B. A. 1984, ApJ, 287, 610

Lada, E. A. 1990, Ph.D. thesis, University of Texas at Austin

Ladd, E. F. 1991, Ph.D. thesis, Harvard University

Ladd, E. F., Lada, E. A., & Myers, P. C. 1992, ApJ. submitted

Landolt, A. U. 1983, AJ, 88, 439

Larson, R. B., 1969a, MNRAS, 145, 271

Larson, R. B., 1969b, MNRAS, 145, 297

Leverault, R. M. 1988, ApJS, 67, 283

Lynds, B. T. 1962, ApJS, 7, 1

McCaughrean, M. J. 1988, Ph.D. thesis, University of Edinburgh, Scotland

Morgan, J., Snell, R. L., & Strom, K. M., 1990, ApJ, 362, 274

Morgan, J. A., Schloerb, F. P., Snell, R. L., & Bally, J. 1991, ApJ, 376, 618

Mundt, R., & Fried, J. W. 1983, ApJ, 274, L83

Myers, P. C., & Benson, P. J. 1983, ApJ, 266, 309

Myers, P. C., Heyer, M., Snell, R., & Goldsmith, P. F. 1988, ApJ 324 908

Myers, P. C., Fuller, G. A. 1992, ApJ, (Sptember 10)

Myers, P. C., Fuller, G. A., Mathieu, R. D., Beichman, C. A., Benson, P. J., Schild, E., & Emerson, J. P. 1987, ApJ, 319, 340

Myers, P. C., Linke, R. A., & Benson, P. J. 1983, ApJ, 264, 517

Nakajima, T., Nagata, T., Nishida, M., Sato, S., & Kawara, K. 1986, MNRAS, 221, 483

Nozawa, S., Mizuno, A., Teshima, Y., Ogawa, A., & Fukui, Y., 1991, ApJS, in press

Ohashi, N., 1992, Ph. D. thesis, Nagoya University, Japan

Parsamian, E. S., & Chavira, E. 1982, Bol. Inst. Tonantzintla, 3, 69

Reike, G. H., & Lebofsky, M. J. 1985, ApJ, 288, 618

Ressler, M. E., & Shure, M. 1991, AJ, 102, 1398

Schwartz, R. D., Gyuludaghian, A. L., & Wilking, B. A., 1991, ApJ, 370, 263

Scoville, N. Z., Sargent, A. I., Sanders, D. B., Claussen, M. J., Masson, C. R., Lo, L., K. Y., & Philips, T. G. 1986, ApJ., 303, 416

Sellgren, K. 1985, ApJ 277, 623

Shu, F., 1991, in Physics of Star Formation and Early Stellar Evolution, eds. C. J. Lada & N. J. Kylafis (Dorechet: Kluwer), 365

Shu, F. H., Adams, F.C., & Lizano, S. 1987, ARA&A, 25, 23

Strom, K. M., Margulis, M., & Strom, S. E. 1989a, ApJ, 346, L33

Strom, K. M., Newton, G., Strom, S. E., Seaman, R. L., Carrasco, L., Cruz-Gonzalez, I., Serrano, A., & Grasdalen, G. L. 1989b, ApJS, 71, 183

Strom, K. M., et al. 1990, ApJ, 362, 168

Strom, K. M., Strom, S. E., Wolff, S. C., Morgan, J., Wenz, M., 1986, ApJS, 62, 39

Stutzki, J., & Gusten, R., 1990, ApJ, 356, 513

Sugitani, K., et al. 1992, in preparation

Takaba, H. 1986, Ph. D. thesis, Nagoya University, Japan

Takaba, H., Fukui, Y., Fujimoto, Y., Sugitani, K., Ogawa, H., & Kawabata, K. 1986, A&A, 166, 276

Tatematsu, K. et al. 1991, Ap.J. in press

Tereby, S. 1991, in Proc. Vulcano Workshop on Young Star Clusters and Early Stellar Evolution, eds. F. Palla, P. Persi & H. Zinnecker, 823

Ulich, B. L., & Haas, R. W. 1976, ApJS, 30, 247

Umemoto, T. et al. 1992, in preparation

Wainscoat, R. J., Cohen, M., Volk, K. Walker, H. J., & Schwartz, D. E., 1992, ApJS, in press

Wainscoat, R. J., & Cowie, L. L. 1992, AJ, 103, 332

Wilking, B. A. 1989, PASP, 101, 229

Wilking, B. A., Blackwell, J. H., & Mundy, L G. 1990, AJ, 100, 758

Willking, B. A., Lada, C. J., & Young, E. T. 1989, ApJ, 340, 823

Wotten, A., Snell, R., & Evans II, N. J. 1980, ApJ, 240, 532

Wouterloot, J. G. A. & Brand, J. 1992, preprint

Wouterloot, J. G. A., Henkel, C., & Walmsley, C. M., 1989, A&A, 215, 131

Wynn-Williams, C. G. 1982, ARA&A, 20, 587

Yang, J., Umemoto, T., Iwata, T., & Fukui, Y. 1991, ApJ, 373, 137

Yang, J. 1990, Ph.D. thesis, Nagoya University

Zinnecker, H., McCaughrean, M. J., & Wilking, B. A. 1991, in Protostars and Planets III, in press

Zuckerman, B., & Palmer, P. 1974, ARA&A, 12, 279